

**EFFECT OF LONG DURATION MOTIONS ON THE STRUCTURAL RESPONSE OF
RC SHEARWALL BUILDINGS**

by

MICHAEL FAIRHURST

B.A., The University of British Columbia, 2012

M.A.Sc., The University of British Columbia, 2014

A DISSERTATION SUBMITTED IN PARTIAL FULFILLMENT OF
THE REQUIREMENTS FOR THE DEGREE OF

DOCTOR OF PHILOSOPHY

in

THE FACULTY OF GRADUATE AND POSTDOCTORAL STUDIES

(Civil Engineering)

THE UNIVERSITY OF BRITISH COLUMBIA

(Vancouver)

December 2021

© Michael Fairhurst, 2021

The following individuals certify that they have read, and recommend to the Faculty of Graduate and Postdoctoral Studies for acceptance, the dissertation entitled:

Effect of Long Duration Motions on the Structural Response of RC Shearwall Buildings

submitted by Michael Fairhurst in partial fulfillment of the requirements for

the degree of Doctor of Philosophy

in Civil Engineering

Examining Committee:

Carlos E. Ventura, Professor, Department of Civil Engineering, UBC

Supervisor

Armin Bebamzadeh, Department of Civil Engineering, UBC

Supervisory Committee Member

Terje Haukaas, Professor, Department of Civil Engineering, UBC

University Examiner

Annalisa Meyboom, Associate Professor, School of Architecture and Landscape Architecture, UBC

University Examiner

Additional Supervisory Committee Members:

Perry Adebar, Professor, Department of Civil Engineering, UBC

Supervisory Committee Member

Liam Finn, Emeritus Professor, Department of Civil Engineering, UBC

Supervisory Committee Member

Farzad Naeim, MNI Corp

Supervisory Committee Member

Ronald DeVall, RJC Engineers

Supervisory Committee Member

Abstract

This dissertation investigates the effect of ground motion duration on the seismic performance and safety of reinforced concrete (RC) shearwall buildings. Long duration ground motions are characteristic of recordings from subduction tectonic regimes – such as the Cascadia Subduction Zone off of the Pacific Northwest coast of North America. However, current North American building code provisions use design spectra to quantify seismic demands on structures - this method does not account for the effect of shaking duration.

This dissertation is primarily focused on the impact ground motion duration has on the performance of RC shearwall buildings. 2-dimensional and 3-dimensional numerical models of RC shearwall structures are developed and analyzed using suites of motions with different duration characteristics. It is found that code-level performance (ground motions with a 2% in 50 year probability of exceedance) of these structures is not significantly affected by the duration of the input motions. However, the collapse capacities (ability to withstand shaking levels above the design level) of the structures are impacted by ground motion duration: short duration ground motion suites tended to require higher shaking intensity levels (~20% higher; quantified through response spectral values) to induce collapse, compared to longer duration record suites.

A method was developed to develop suites of ground motion records that match a target response spectrum, as well as the variability of that spectrum. The method relies on spectral matching techniques and is a modification of the variable target spectrum (VTS) method for matching the mean of a suite of motions to a target. Using this method, suites of motions are developed for use in risk-based analysis – which requires prediction of structural response and the variability of that response.

Using four mean and variance matched motion suites, the reliability of current code design provisions is investigated. It is concluded that current code seismic (R , R_dR_o) factors should be decreased by $\sim 1/1.25$ for structures subjected to long duration subduction motions in order to achieve similar collapse risks compared to similar analyses using shorter, crustal recordings. Current component factors appear to be suitable despite the increased demand variability from the longer motion suites.

Lay Summary

The effect of the duration of ground motion shaking on the performance and safety of building systems has been a long-standing area of research. Typically, shaking duration has been correlated with damage induced into the structures, potentially effecting their safety against excessive damage or collapse. However, currently, there is limited information into the potential effects of ground motion duration on the performance of Reinforced Concrete (RC) shearwall structures. This type of structure is very common for mid- and high-rise building construction in Vancouver, BC, and other highly seismically active locations along the West Coast of North America. The findings of this work provide information regarding the behavior of RC shearwall structures subjected to long duration ground motions, including the effect this might have on current North American building standards.

Preface

This dissertation is the original work of Michael Fairhurst, conducted at the University of British Columbia in Vancouver, under the supervision of Professor Carlos E. Ventura.

A version of Chapter 4 has been published. Fairhurst, M., Bebamzadeh, A., & Ventura, C. E. (2019). Effect of ground motion duration on reinforced concrete shear wall buildings. *Earthquake Spectra*, 35(1), 311-331. I developed the numerical models, prepared the ground motion suites, and wrote the majority of the manuscript. Drs. Ventura and Bebamzadeh provided advice and suggestions throughout the work and contributed to the preparation of the manuscript.

Table of Contents

- Abstract iii**
- Lay Summary v**
- Preface vi**
- Table of Contents..... vii**
- List of Tables xiii**
- List of Figures..... xvi**
- Acknowledgements xxxiv**
- Dedication..... xxxvi**
- Chapter 1: Introduction 1**
 - 1.1 Background 1
 - 1.2 Objectives 3
 - 1.3 Organization..... 4
- Chapter 2: Literature Review..... 7**
 - 2.1 Seismic Provisions in North America 7
 - 2.1.1 National Building Code of Canada (NBCC)..... 8
 - 2.1.2 ASCE 7 9
 - 2.1.3 FEMA P695 10
 - 2.1.4 Performance-based Design Standards 11
 - 2.1.5 Limitations 12
 - 2.2 Seismicity in Southwestern BC 13
 - 2.2.1 Seismic Background 13

2.2.2	Southwestern Canada Seismic Hazard Model	15
2.2.2.1	Introduction	15
2.2.2.2	Shallow Crustal Sources	16
2.2.2.3	Subduction Intraslab Sources	17
2.2.2.4	Subduction Interface Sources.....	18
2.2.2.5	Ground Motion Prediction	19
2.2.2.6	Treatment of Uncertainty	20
2.2.3	Ground Motion Duration Prediction	21
2.2.3.1	Duration Modelling.....	24
2.3	Coupled RC Shearwall Buildings	27
2.3.1	Conventionally Reinforced Coupling Beams	28
2.3.2	Ductile Coupling Beams	29
2.3.3	Coupled Shearwall Behavior	31
2.4	Effect of Ground Motion Duration	33
Chapter 3: Mechanism and Effect of Ground Motion Duration		35
3.1	Physical mechanisms	35
3.1.1	Cyclic Degradation	35
3.1.2	Ratcheting	40
3.2	Intensity Measures.....	43
3.3	Intensity Metric Study	47
3.3.1	Ground Motion Database	47
3.3.2	Ground Motion Selection and Scaling.....	51
3.3.3	SDOF Model.....	52

3.3.4	Analysis and Results	53
3.4	Effect of Ductility	59
3.4.1	Ground Motion Selection and Scaling	59
3.4.2	SDOF Model	61
3.4.3	Analysis and Results	61
3.5	Conclusions	78
Chapter 4: Effect of Ground Motion Duration on RC Shearwall Buildings		80
4.1	Archetype Buildings	80
4.2	Numerical Modelling	86
4.2.1	Shearwall Model	86
4.2.1.1	Material Models	87
4.2.2	Header Beam Model	88
4.2.2.1	Calibration	89
4.2.3	P-Delta Effects	91
4.2.4	Damping	92
4.3	Ground Motion Suites	93
4.4	Code Level Analysis	98
4.5	Collapse Level Analysis	103
4.6	Conclusions	109
Chapter 5: An Algorithm to Match a Target Mean Spectrum and Variation		111
5.1	Background	111
5.1.1	Variable Target Spectra	112
5.1.2	Conditional Spectrum	114

5.1.3	Subduction Interface Records	116
5.2	Methodology	118
5.2.1	Application to CS	121
5.2.2	Modification of Outliers	122
5.3	Example Suite Development	126
5.3.1	Target Conditional Spectra	126
5.3.2	Comparison to Traditional Spectral Matching	133
5.4	Other Considerations	137
5.4.1	Correlation of Spectral Values in Subduction Earthquake Events	138
5.4.1.1	Spectral Correlation Calculations	139
5.4.1.2	Results	140
5.4.1.3	Combining GMMs	148
5.4.1.4	Observations	153
5.4.2	Period Range of Interest.....	153
5.4.2.1	Analysis.....	155
5.4.2.2	Results	156
5.5	Conclusions	164
Chapter 6: RC Shearwall Model 3D Analysis		166
6.1	Archetype Buildings	166
6.1.1	Conventional Construction	167
6.1.2	Ductile Design.....	168
6.2	Numerical Modelling.....	170
6.2.1	Header Beam Shear Hinges.....	170

6.2.1.1	Ductile Header Calibration	171
6.2.2	Gravity System.....	172
6.2.3	Foundation Model.....	174
6.2.4	Model Summary	175
6.3	Ground Motion Suites.....	178
6.4	Analysis Results	188
6.4.1	Ductile Design.....	188
6.4.1.1	Code Level Analysis	188
6.4.1.2	Collapse and Life Safety Analysis.....	199
6.4.2	Conventional Construction.....	203
6.4.2.1	Code Level Analysis	203
6.4.2.2	Collapse and Life Safety Analysis.....	213
6.5	Conclusions.....	217
Chapter 7: Effect of Ground Motion Duration on Prescriptive Building Codes.....		219
7.1	Modern Standards.....	219
7.2	Reduction Factor Calibration	220
7.2.1	Record-to-record Variability	220
7.2.2	R-Factor Calibration	221
7.2.3	Collapse Risk Check.....	225
7.2.4	Implications for NBCC and ASCE 7	229
7.3	Component Factor Calibration	230
7.3.1	Force Controlled.....	231
7.3.2	Deformation Controlled	234

7.4	Conclusions	238
Chapter 8: Conclusion.....		240
8.1	Research gaps.....	240
8.2	Summary and Conclusions.....	241
8.3	Recommended Research.....	244
Bibliography		248
Appendix A: Ground Motion Suite Metadata for Duration Intensity Metric Study		262
Appendix B: Additional Plots for 6 and 30 Story Models for Period Elongation Study ...		267
Appendix C: Flexure-shear Coupling.....		278
Appendix D: Additional Code-level Analysis Results for 2D Models.....		288

List of Tables

Table 2.1 GSC 2015 seismic hazard model GMM summary.....	20
Table 3.1 Subduction zone database event summary.	49
Table 3.2 Subduction zone database event owners and providers.....	50
Table 3.3 Crustal suite metadata.....	60
Table 3.4 Subduction interface suite metadata.	61
Table 4.1 First three elastic periods of the 5 RC shearwall archetype building numerical models.	93
Table 4.2 Long duration suite summary.	95
Table 4.3 Short duration suite summary.....	96
Table 4.4 Mean of maximum interstory drifts summary for all archetype models at the 2% in 50 year shaking level.....	99
Table 4.5 Median collapse scaling level for all archetype models.	105
Table 4.6 Collapse probability at the 2% in 50 year shaking level and CMRs for all archetype models.	107
Table 5.1 Subduction earthquake events greater than magnitude 8.0 with time history data available by the CESMD (https://www.strongmotioncenter.org/ , accessed 07/18) and K-Net/KiK- Net (Kinoshita, 1998) databases.	118
Table 5.2 Subduction seed record metadata.	128
Table 5.3 Summary of modern subduction zone GMMs considered.....	146
Table 5.4 Summary of GSC (2015) and USGS (2014) subduction intraslab GMM weights.	148
Table 5.5 Summary of GSC (2015) and USGS (2014) subduction interface GMM weights.	148

Table 5.6 First three elastic periods of the three RC shearwall prototype buildings.....	155
Table 5.7 Metadata for the three input time series scaled to the 2015 Vancouver 2% in 50 year UHS.....	156
Table 5.8 Period elongation summary for the 6 story model subjected to three records at three scaling levels.....	158
Table 5.9 Period elongation summary for the 18 story model subjected to three records at three scaling levels.....	159
Table 5.10 Period elongation summary for the 30 story model subjected to three records at three scaling levels.....	159
Table 6.1 First nine elastic periods of the 18 story RC shearwall archetype building numerical models.....	177
Table 6.2 Crustal seed record metadata.....	182
Table 6.3 Subduction interface seed record metadata.....	183
Table 6.4 Median collapse scaling level and probability of collapse at the 2% in 50 year shaking level for the 18 story ductile models.....	201
Table 6.5 Median life safety exceedance scaling level and probability of life safety exceedance at the 2% in 50 year shaking level for the 18 story ductile models.....	201
Table 6.6 Median collapse scaling level and probability of collapse at the 2% in 50 year shaking level for the 18 story CC models.....	215
Table 6.7 Median life safety exceedance scaling level and probability of life safety exceedance at the 2% in 50 year shaking level for the 18 story CC models.....	215
Table 7.1 Modern North American seismic design standard summary.....	219

Table 7.2 Collapse statistics for the 3D ductile and conventional construction (CC) 3D models.	222
Table 7.3 ASCE 7-16 assumed variability and uncertainty values for component force demand (reproduced from ASCE/SEI, 2016, Table C 16-3).	231
Table 7.4 ASCE 7-16 assumed variability and uncertainty values for component capacity (reproduced from ASCE/SEI, 2016, Table C 16-3).	232
Table 7.5 Demand dispersion (β_D) at the 100% shaking level (2% in 50 year probability of exceedance) for wall shear in the ductile and CC models subjected to four suites of motions. ...	234
Table 7.6 Demand dispersion (β_D) at the 100% shaking level (2% in 50 year probability of exceedance) for column rotation in the ductile and CC models subjected to four suites of motions.	234
Table 7.7 ASCE 7-16 assumed variability and uncertainty values for component deformation demand (reproduced from ASCE/SEI, 2016, Table C16-5).....	235
Table 7.8 ASCE 7-16 assumed variability and uncertainty values for component deformation (reproduced from ASCE/SEI, 2016, Table C 16-5).	235
Table 7.9 Demand dispersion (β_D) at the 100% shaking level (2% in 50 year probability of exceedance) for wall plastic hinge rotation in the ductile and CC models subjected to four suites of motions.	237
Table 7.10 Demand dispersion (β_D) at the 100% shaking level (2% in 50 year probability of exceedance) for header deformation in the ductile and CC models subjected to four suites of motions.	238
Table C.1 Long and short duration records selected for SFI vs fiber element study.....	281

List of Figures

Figure 2.1 Southwestern BC seismic sources (source: United States Geological Survey).	13
Figure 2.2 Historic earthquakes near Southwestern BC (source: Natural Resources Canada).	15
Figure 2.3 2015 GSC seismic hazard model shallow crustal sources in Southwestern BC (source: VC Structural Dynamics, 2019).	17
Figure 2.4 2015 GSC seismic hazard model subduction intraslab sources in Southwestern BC (source: VC Structural Dynamics, 2019).	18
Figure 2.5 2015 GSC seismic hazard model subduction interface sources in Southwestern BC (source: VC Structural Dynamics, 2019).	19
Figure 2.6 2015 Source duration vs. moment magnitude estimations with: a) three different shear wave velocities and constant stress drop of 150 bars; and, b) three different stress drop and constant source shear wave velocity of 3.7 km/s.	24
Figure 2.7 2015 Ground motion median duration (5-95% significant duration) predictions from the Afshari and Stewart (2016) GMM for: a,c) $V_{s30} = 250$ m/s; and, b,d) $V_{s30} = 1100$ m/s.	26
Figure 2.8 Acceleration time histories from three recordings: a) Northridge, 1994 station: STM-360. $M_w = 6.7$, distance = 26 km; b) Hokkaido, Japan, 2003 station: HKD125-NS. $M_w = 8.0$, distance = 134 km; c) Tohoku, 2011, station: MYG009-NS, $M_w = 9.1$, distance = 111 km.	27
Figure 2.9 Ductility capacity vs. aspect ratio for conventional coupling beams from various testing programs.	29
Figure 2.10 Ductility capacity vs. aspect ratio for diagonally reinforced coupling beams from various testing programs with: linear fit (dotted; $R^2 = 0.57$), and logarithmic fit (solid; $R^2 = 0.70$).	31

Figure 2.11 Force distribution in a coupled wall system.	32
Figure 2.12 Yielding mechanism in a coupled wall system with well-detailed header beams.	32
Figure 3.1 Simple bilinear backbone (pushover) curve with in-cycle strength degradation.	36
Figure 3.2 Simple bilinear backbone curve with strength and stiffness degradation.	37
Figure 3.3 Cyclic pushover with strength and stiffness degradation.	38
Figure 3.4 Hysteretic models: a) bilinear; b) peak-orientated (Clough); and c) pinching.	40
Figure 3.5 Ratcheting example: a) input acceleration time history; b) SDOF drift response time history (moving average in red); and c) SDOF drift vs. base shear response.	42
Figure 3.6 Illustration of significant duration (d5-95) for Tohoku, 2011; station: MYG009-NS; $M_w = 9.1$; distance = 111 km; d5-95 = 104.3 s.	45
Figure 3.7 Illustration of significant duration (d5-95) for Northridge, 1994; station: STM-360; $M_w = 6.7$; distance = 26 km; d5-95 = 10.7 s.	46
Figure 3.8 Suite of 200 motions linearly scaled to the 2% in 50 year Victoria Site Class C UHS.	52
Figure 3.9 Degrading bilinear backbone curve used in the SDOF model.	53
Figure 3.10 Collapse scaling level for bilinear degrading system with different duration metrics; from top left to bottom right: Arias intensity, number of cycles, Housner intensity, RMS acceleration, specific energy density, and 5-95% significant duration	56
Figure 3.11 Collapse scaling level for peak-orientated degrading system with different duration metrics; from top left to bottom right: Arias intensity, number of cycles, Housner intensity, RMS acceleration, specific energy density, and 5-95% significant duration	57

Figure 3.12 Collapse scaling level for pinching degrading system with different duration metrics; from top left to bottom right: Arias intensity, number of cycles, Housner intensity, RMS acceleration, specific energy density, and 5-95% significant duration58

Figure 3.13 Two suites of 20 linearly scaled motions; a) crustal suite; and b) subduction suite. .60

Figure 3.14 IDA curves for bilinear degrading system with ductility = 8: a) crustal suite; and b) subduction suite results.64

Figure 3.15 Empirical and lognormal cumulative distribution functions for bilinear degrading system with ductility = 8: a) crustal suite; and b) subduction suite results.64

Figure 3.16 Collapse CDF for bilinear degrading system with (from top left to bottom right) ductility = 3, 4, 5, 6, 7, 8.65

Figure 3.17 Mean collapse scale level for bilinear degrading system vs. level of ductility.66

Figure 3.18 100% shaking level probability of collapse for bilinear degrading system vs. level of ductility.....66

Figure 3.19 Collapse CDF for bilinear20 degrading system with (from top left to bottom right) ductility = 3, 4, 5, 6, 7, 8.67

Figure 3.20 Median collapse scale level for bilinear20 degrading system vs. level of ductility. ..68

Figure 3.21 100% shaking level probability of collapse for bilinear20 degrading system vs. level of ductility.....68

Figure 3.22 Collapse CDF for bilinear50 degrading system with (from top left to bottom right) ductility = 3, 4, 5, 6, 7, 8.69

Figure 3.23 Median collapse scale level for bilinear50 degrading system vs. level of ductility. ..70

Figure 3.24 100% shaking level probability of collapse for bilinear50 degrading system vs. level of ductility.....70

Figure 3.25 Collapse CDF for bilinear non-degrading system with (from top left to bottom right) ductility = 3, 4, 5, 6, 7, 8.	71
Figure 3.26 Median collapse scale level for bilinear non-degrading system vs. level of ductility.	72
Figure 3.27 100% shaking level probability of collapse for bilinear non-degrading system vs. level of ductility.....	72
Figure 3.28 Cyclic pushover curves for bilinear systems with $\lambda =$ a) infinity, b) 20, c) 35, and d) 50, and e) cyclic loading protocol.	73
Figure 3.29 Collapse CDF for peak-orientated degrading system with (from top left to bottom right) ductility = 3, 4, 5, 6, 7, 8.....	74
Figure 3.30 Median collapse scale level for peak-orientated degrading system vs. level of ductility.	75
Figure 3.31 100% shaking level probability of collapse for peak-orientated degrading system vs. level of ductility.	75
Figure 3.32 Collapse CDF for pinching degrading system with (from top left to bottom right) ductility = 3, 4, 5, 6, 7, 8.	76
Figure 3.33 Median collapse scale level for pinching degrading system vs. level of ductility.	77
Figure 3.34 100% shaking level probability of collapse for pinching degrading system vs. level of ductility.....	77
Figure 3.35 Cyclic pushover curves for a) peak-orientated model with $\lambda = 35$; b) pinching model with $\lambda = 35$; and c) cyclic loading protocol.	78
Figure 4.1 Archetype building floor plan.	82
Figure 4.2 Reinforcement details of 6 and 12 story shearwall buildings.	83

Figure 4.3 Reinforcement details of 18 story shearwall building.	84
Figure 4.4 Reinforcement details of 24 and 30 story shearwall buildings.	85
Figure 4.5 Elevation view of slabs and header beams.	86
Figure 4.6 Material models: 1) confined concrete (<i>Concrete02</i>); b) unconfined concrete (<i>Concrete02</i>); c) steel (<i>ReinforcingSteel</i>).	89
Figure 4.7 Specimen P2 elevation and cross section (Galano and Vignoli, 2000).	90
Figure 4.8 Nonlinear shear hinge model for header beams vs experimental results (Galano and Vignoli, 2000).	91
Figure 4.9 Illustration of a typical story of the 2D OpenSees numerical models.	92
Figure 4.10 Example of spectrally equivalent record acceleration response spectra and time histories.	97
Figure 4.11 Spectra of (a) the long duration suite and (b) the short duration suite compared to the Vancouver 2% in 50 year design spectrum.	97
Figure 4.12 Long and short duration suite significant duration (d_{5-95}) comparison.	98
Figure 4.13 Interstory drift results for the 30 story model at the code shaking level for (a) the long duration suite and (b) the short duration suite.	100
Figure 4.14 Interstory drift results for the 24 story model at the code shaking level for (a) the long duration suite and (b) the short duration suite.	100
Figure 4.15 Interstory drift results for the 18 story model at the code shaking level for (a) the long duration suite and (b) the short duration suite.	101
Figure 4.16 Interstory drift results for the 12 story model at the code shaking level for (a) the long duration suite and (b) the short duration suite.	101

Figure 4.17 Interstory drift results for the 6 story model at the code shaking level for (a) the long duration suite and (b) the short duration suite.....	102
Figure 4.18 Energy demand statistics for the 30 story model at the code shaking level.	103
Figure 4.19 CDF results for the long and short duration suites for the 6 story model including (a) RTR variability only, and (b) total variability.	108
Figure 4.20 CDF results, including total variability, for the long and short duration suites for: (a) the 12 story; (b) the 18 story model; (c) the 24 story model; and (d) the 30 story model.	109
Figure 5.1 VTS method illustration: a) sample seed suite linearly scaled to a target CMS from 0.3-3.0 s, b) resulting FF(T), c) suite of VTS, and d) suite of records matched to their individual VTS targets (matched from 0.3-3.0 s).....	114
Figure 5.2 Algorithm for developing a suite of records matched to a target conditional mean spectrum and standard deviation.....	122
Figure 5.3 Algorithm for developing a suite of records matched to a target conditional mean spectrum and standard deviation (with outlier modification).....	125
Figure 5.4 (a) Source-specific subduction UHS with $AEF = 1/2475$ and CMS with $TC = 1.0$ s; and (b) Vancouver subduction hazard magnitude and distance deaggregation for $SA(Tc = 1.0) = 0.277g$ (mean magnitude, $M_w = 8.82$; mean distance, $R_{CD} = 137.5km$).....	127
Figure 5.5 Seed record suite: (a) acceleration spectra vs. target CMS (conditioned to $SA(Tc = 1.0) = 0.277g$); and, (b) lognormal standard deviation vs. target conditional standard deviation.	128
Figure 5.6 Seed record suite: (a) FF(T); and, (b) target VTS.	129
Figure 5.7 Matched (to VTS from 0.3-3.0s) record suite: (a) acceleration spectra vs. target CMS (conditioned to $SA(Tc = 1.0) = 0.277g$); and, (b) lognormal standard deviation vs. target conditional standard deviation.	130

Figure 5.8 Target VTS* suite: (a) acceleration spectra vs. target CMS (conditioned to $SA(T_c = 1.0) = 0.277g$); and, (b) lognormal standard deviation vs. target conditional standard deviation. 131

Figure 5.9 Matched (to VTS* from 0.3-3.0s) record suite: (a) acceleration spectra vs. target CMS (conditioned to $SA(T_c = 1.0) = 0.277g$); and, (b) lognormal standard deviation vs. target conditional standard deviation. 131

Figure 5.10 Matched (to VTS* from 0.3-3.0s, with outliers modified) record suite: (a) acceleration spectra vs. target CMS (conditioned to $SA(T_c = 1.0) = 0.277g$); and, (b) lognormal standard deviation vs. target conditional standard deviation. 132

Figure 5.11 ϵ_{sjT} for record suite matched to VTS* from 0.3-3.0s (a) without outlier modification; and, (b) with outlier modification ($\epsilon_{lim} = 2.0$). 133

Figure 5.12 Matched (using traditional spectral matching from 0.3-3.0s) record suite: (a) acceleration spectra vs. target subduction source-specific UHS (1/2475 annual exceedance frequency); and, (b) lognormal standard deviation vs. target conditional standard deviation. ... 134

Figure 5.13 Example Tohoku, Japan record matched (from 0.3-3.0s) to: (a) the target CMS; and, (b) its target VTS*. 135

Figure 5.14 Example Tohoku, Japan seed and matched record (from 0.3-3.0s) to the target UHS, from top to bottom: acceleration; velocity; displacement; and, Arias intensity time histories. ... 136

Figure 5.15 Example Tohoku, Japan seed and matched record (from 0.3-3.0s) to its target VTS*, from top to bottom: acceleration; velocity; displacement; and, Arias intensity time histories. ... 137

Figure 5.16 Plots of epsilon correlation coefficients, $\rho_{\epsilon T1, \epsilon(T2)}$, between T2 and T1 estimated using residuals of the Zhao et al. (2006) GMM for (a) the entire record database and (b) predicted by the Baker and Jayram (2008) correlation model. 141

Figure 5.17 Plots of epsilon correlation coefficients, $\rho_{\epsilon T1, \epsilon(T2)}$, between T2 and T1 estimated using residuals of the Zhao et al. (2006) GMM for (a) the interface records and (b) the intraslab records. 142

Figure 5.18 Plots of epsilon correlation coefficients, $\rho_{\epsilon T1, \epsilon(T2)}$, between T2 and T1 estimated using residuals of the Zhao et al. (2006) GMM for the subduction interface database compared to the Baker and Jayram (2008) predictions for (a) T2 = 0.05 s, (b) T2 = 0.5 s, (c) T2 = 2.0 s, and (d) T2 = 5.0 s. Also included is the 95% confidence interval (CI). 144

Figure 5.19 Plots of epsilon correlation coefficients, $\rho_{\epsilon T1, \epsilon(T2)}$, between T2 and T1 estimated using residuals of the Zhao et al. (2006) GMM for the subduction intraslab database compared to the Baker and Jayram (2008) predictions for (a) T2 = 0.05 s, (b) T2 = 0.5 s, (c) T2 = 2.0 s, and (d) T2 = 5.0 s. Also included is the 95% confidence interval (CI). 145

Figure 5.20 Plots of epsilon correlation coefficients, $\rho_{\epsilon T1, \epsilon(T2)}$, between T2 and T1 estimated using residuals of the (a) Atkinson and Macias (2009), (b) Ghofrani and Atkinson (2014), (c) Abrahamson et al. (BC Hydo, 2016), and (d) Atkinson and Boore global GMM (2003). 147

Figure 5.21 Epsilon correlation coefficient, $\rho_{\epsilon(T1), \epsilon(T2)}$, plots between T2 and T1 calculated using residuals of the (a) GSC 2015 intraslab GMM and (b) USGS 2014 intraslab GMM. 149

Figure 5.22 Epsilon correlation coefficient, $\rho_{\epsilon(T1), \epsilon(T2)}$, plots between T2 and T1 calculated using residuals of the (a) GSC 2015 interface GMM and (b) USGS 2014 interface GMM. 150

Figure 5.23 Epsilon correlation coefficient, $\rho_{\epsilon(T1), \epsilon(T2)}$, plots between T2 and T1 calculated using the Baker and Jayaram (2008) predictions for compared to (a) GSC 2015 GMM for the intraslab database at T2 = 0.2 s, and (b) T2 = 2.0 s; (c) USGS 2014 GMM for the intraslab database at T2 = 0.2 s, and (d) T2 = 2.0 s. Also included is the 95% confidence interval (CI). 151

Figure 5.24 Epsilon correlation coefficient, $\rho_{\epsilon(T1),\epsilon(T2)}$, plots between T2 and T1 calculated using the Baker and Jayaram (2008) predictions for compared to (a) GSC 2015 GMM for the interface database at T2 = 0.2 s, and (b) T2 = 2.0 s; (c) USGS 2014 GMM for the interface database at T2 = 0.2 s, and (d) T2 = 2.0 s. Also included is the 95% confidence interval (CI). 152

Figure 5.25 First three periods of 18 story RC shear wall model subjected to the Tohoku-MYG009 NS ground motion; from top to bottom: scaled to 100%, 150%, and 200%; roof drift time history response under the 200% shaking level; and input acceleration time history scaled to 100% Vancouver 2% in 50 year target UHS. 160

Figure 5.26 First three periods of 18 story RC shear wall model subjected to the Hokkaido-HKD125 NS ground motion; from top to bottom: scaled to 100%, 150%, and 200%; roof drift time history response under the 200% shaking level; and input acceleration time history scaled to 100% Vancouver 2% in 50 year target UHS. 161

Figure 5.27 First three periods of 18 story RC shear wall model subjected to the Northridge-STM360 ground motion; from top to bottom: scaled to 100%, 150%, and 200%; roof drift time history response under the 200% shaking level; and input acceleration time history scaled to 100% Vancouver 2% in 50 year target UHS. 162

Figure 5.28 (a) First three period cumulative distribution function; and, (b) power spectral density of roof drift of 18 story RC shear wall model subjected to the Tohoku-MYG009 NS ground motion scaled to 100%. 163

Figure 5.29 (a) First three period cumulative distribution function; and, (b) power spectral density of roof drift of 18 story RC shear wall model subjected to the Hokkaido-HKD125 NS ground motion scaled to 100%. 163

Figure 5.30 (a) First three period cumulative distribution function; and, (b) power spectral density of roof drift of 18 story RC shear wall model subjected to the Northridge-STM360 ground motion scaled to 100%. 164

Figure 6.1 Reinforcement details of 18 story ductile shearwall building. 169

Figure 6.2 Ductile header beam detailing: stories 1-6 Avd = 8-35M bars; stories 7-13 Avd = 6-35M bars; and stories 14- 18 Avd = 6-30M bars..... 170

Figure 6.3 Specimen CB24F-RC: a) elevation; and b) cross section (from: Naish, 2010). All units are in inches. 171

Figure 6.4 Nonlinear shear hinge model for ductile header beams vs experimental results (Naish, 2010). 172

Figure 6.5 Generic bilinear moment-rotation ($M-\theta$) spring with in-cycle strength loss. 173

Figure 6.6 Material models for the zero-length base section: 1) confined concrete (*Concrete02*); b) unconfined concrete (*Concrete02*); c) steel bond-slip material (*Bond-SPI*). 175

Figure 6.7 Illustration of a typical story of the 3D OpenSees numerical models. 177

Figure 6.8 18 story ductile vs. conventional construction (CC) base shear vs story drift pushover curves. 178

Figure 6.9 a) Crustal hazard deaggregation and, b) subduction interface deaggregation for 2% in 50 year hazard at $T = 0.75$ s for Vancouver, BC; c) 2% in 50 year UHS vs CMS targets; and, d) CS target lognormal standard deviations. 180

Figure 6.10 LONG075 suite: a) seed record suite spectra; b) seed record suite lognormal standard deviation; c) matched (from 0.2-4.0 s) record suite spectra; and, d) matched record suite lognormal standard deviation. 184

Figure 6.11 LONG20 suite: a) seed record suite spectra; b) seed record suite lognormal standard deviation; c) matched (from 0.2-4.0 s) record suite spectra; and, d) matched record suite lognormal standard deviation..... 185

Figure 6.12 SHORT075 suite: a) seed record suite spectra; b) seed record suite lognormal standard deviation; c) matched (from 0.2-4.0 s) record suite spectra; and, d) matched record suite lognormal standard deviation..... 186

Figure 6.13 SHORT20 suite: a) seed record suite spectra; b) seed record suite lognormal standard deviation; c) matched (from 0.2-4.0 s) record suite spectra; and, d) matched record suite lognormal standard deviation..... 187

Figure 6.14 Coupled-direction interstory drift results for the ductile 18 story model at the code shaking level for: a) the SHORT075; b) LONG075; c) SHORT20; and, d) LONG20 ground motion suites..... 190

Figure 6.15 Wall direction interstory drift results for the ductile 18 story model at the code shaking level for: a) the SHORT075; b) LONG075; c) SHORT20; and, d) LONG20 ground motion suites. 191

Figure 6.16 Header rotation results for the ductile 18 story model at the code shaking level for: a) the SHORT075; b) LONG075; c) SHORT20; and, d) LONG20 ground motion suites. 192

Figure 6.17 Reinforcement strain results for the ductile 18 story model at the code shaking level for: a) the SHORT075; b) LONG075; c) SHORT20; and, d) LONG20 ground motion suites. . 193

Figure 6.18 Story shear results for the ductile 18 story model at the code shaking level for: a) the SHORT075; b) LONG075; c) SHORT20; and, d) LONG20 ground motion suites. 195

Figure 6.19 Story overturning moment results for the ductile 18 story model at the code shaking level for: a) the SHORT075; b) LONG075; c) SHORT20; and, d) LONG20 ground motion suites. 196

Figure 6.20 Column hinge results for the ductile 18 story model at the code shaking level for: a) the SHORT075; b) LONG075; c) SHORT20; and, d) LONG20 ground motion suites. 198

Figure 6.21 Collapse results for the ductile 18 story model: a) SHORT075 and LONG075 suites lognormal CDFs with total vs. RTR variability; and, b) SHORT20 and LONG20 suites lognormal CDFs with total vs. RTR variability. 202

Figure 6.22 LS exceedance results for the ductile 18 story model: a) SHORT075 and LONG075 suites lognormal CDFs with total vs. RTR variability; and, b) SHORT20 and LONG20 suites lognormal CDFs with total vs. RTR variability. 202

Figure 6.23 Coupled-direction interstory drift results for the CC 18 story model at the code shaking level for: a) the SHORT075; b) LONG075; c) SHORT20; and, d) LONG20 ground motion suites. 204

Figure 6.24 Wall direction interstory drift results for the CC 18 story model at the code shaking level for: a) the SHORT075; b) LONG075; c) SHORT20; and, d) LONG20 ground motion suites. 205

Figure 6.25 Header rotation results for the CC 18 story model at the code shaking level for: a) the SHORT075; b) LONG075; c) SHORT20; and, d) LONG20 ground motion suites. 206

Figure 6.26 Wall strain results for the CC 18 story model at the code shaking level for: a) the SHORT075; b) LONG075; c) SHORT20; and, d) LONG20 ground motion suites. 207

Figure 6.27 Story shear results for the CC 18 story model at the code shaking level for: a) the SHORT075; b) LONG075; c) SHORT20; and, d) LONG20 ground motion suites. 209

Figure 6.28 Story overturning moment results for the CC 18 story model at the code shaking level for: a) the SHORT075; b) LONG075; c) SHORT20; and, d) LONG20 ground motion suites. .210

Figure 6.29 Column hinge rotation results for the CC 18 story model at the code shaking level for: a) the SHORT075; b) LONG075; c) SHORT20; and, d) LONG20 ground motion suites.212

Figure 6.30 Collapse results for the CC 18 story model: a) SHORT075 and suites lognormal CDFs with total vs. RTR variability; b) SHORT20 and LONG20 suites lognormal CDFs with total vs. RTR variability.....216

Figure 6.31 LS exceedance results for the CC 18 story model: a) SHORT075 and suites lognormal CDFs with total vs. RTR variability; b) SHORT20 and LONG20 suites lognormal CDFs with total vs. RTR variability.216

Figure 7.1 Theoretical CDFs for two systems of different variability with: a) same P[Collapse] at the MCE shaking level; and, b) same CMR.221

Figure 7.2 CDFs of 1) a system designed for 10% P[Collapse] at the design shaking level subjected to short duration records ($\beta_{TOT,SHORT} = 0.35$); and, 2) the same system subjected to long duration records ($\beta_{TOT, LONG} = 0.40$; $\mu_{LONG} = \mu_{SHORT}/1.2$).....224

Figure 7.3 CDFs of 1) a system designed for 10% P[Collapse] at the design shaking level subjected to short duration records ($\beta_{TOT,SHORT} = 0.35$); and, 2) a system designed for 10% P[Collapse] at 125% of the design shaking level subjected to long duration records ($\beta_{TOT, LONG} = 0.40$). 225

Figure 7.4 Subduction interface, crustal (combined crustal + intraslab), and total hazard curves for Vancouver, BC, for $T = 2.0$ s. Shaking level is expressed the percentage of the 2% in 50 year hazard level.226

Figure 7.5 Crustal and subduction interface CDFs for a system calibrated to a) $P[\text{Collapse} \mid \text{Design Shaking}] = 10\%$ for crustal records; and, b) $P[\text{Collapse} \mid \text{Design Shaking}] = 10\%$ for subduction interface records.....228

Figure 7.6 . Illustration of lognormal PDFs for component force capacity and demand (normalized to an average capacity of 1.0); the average component capacity is calibrated to achieve a probability of collapse = 10% at the MCE_R233

Figure 7.7 . Illustration of lognormal PDFs for component deformation capacity and demand (normalized to an average capacity of 1.0); the average component capacity is calibrated to achieve a probability of collapse = 25% at the MCE_R236

Figure B.1 First three periods of 6 story RC shear wall model subjected to the Tohoku-MYG009 NS ground motion; from top to bottom: scaled to 100%, 150%, and 200%; roof drift time history response under the 200% shaking level; and input acceleration time history scaled to 100% Vancouver 2% in 50 year target UHS.....268

Figure B.2 First three periods of 6 story RC shear wall model subjected to the Hokkaido-HKD125 NS ground motion; from top to bottom: scaled to 100%, 150%, and 200%; roof drift time history response under the 200% shaking level; and input acceleration time history scaled to 100% Vancouver 2% in 50 year target UHS.....269

Figure B.3 First three periods of 6 story RC shear wall model subjected to the Northridge-STM360 ground motion; from top to bottom: scaled to 100%, 150%, and 200%; roof drift time history response under the 200% shaking level; and input acceleration time history scaled to 100% Vancouver 2% in 50 year target UHS.....270

Figure B.4 (a) First three period cumulative distribution function; and, (b) power spectral density of roof drift of 6 story RC shear wall model subjected to the Tohoku-MYG009 NS ground motion scaled to 100%.271

Figure B.5 (a) First three period cumulative distribution function; and, (b) power spectral density of roof drift of 6 story RC shear wall model subjected to the Hokkaido-HKD125 NS ground motion scaled to 100%.271

Figure B.6 (a) First three period cumulative distribution function; and, (b) power spectral density of roof drift of 6 story RC shear wall model subjected to the Northridge-STM360 ground motion scaled to 100%.272

Figure B.7 First three periods of 30 story RC shear wall model subjected to the Tohoku-MYG009 NS ground motion; from top to bottom: scaled to 100%, 150%, and 200%; roof drift time history response under the 200% shaking level; and input acceleration time history scaled to 100% Vancouver 2% in 50 year target UHS.273

Figure B.8 First three periods of 30 story RC shear wall model subjected to the Hokkaido-HKD125 NS ground motion; from top to bottom: scaled to 100%, 150%, and 200%; roof drift time history response under the 200% shaking level; and input acceleration time history scaled to 100% Vancouver 2% in 50 year target UHS.274

Figure B.9 First three periods of 30 story RC shear wall model subjected to the Northridge-STM360 ground motion; from top to bottom: scaled to 100%, 150%, and 200%; roof drift time history response under the 200% shaking level; and input acceleration time history scaled to 100% Vancouver 2% in 50 year target UHS.275

Figure B.10 (a) First three period cumulative distribution function; and, (b) power spectral density of roof drift of 30 story RC shear wall model subjected to the Tohoku-MYG009 NS ground motion scaled to 100%.276

Figure B.11 (a) First three period cumulative distribution function; and, (b) power spectral density of roof drift of 30 story RC shear wall model subjected to the Hokkaido-HKD125 NS ground motion scaled to 100%.276

Figure B.12 (a) First three period cumulative distribution function; and, (b) power spectral density of roof drift of 30 story RC shear wall model subjected to the Northridge-STM360 ground motion scaled to 100%.277

Figure C.1 Material models: 1) confined concrete (*ConcreteCM*); b) unconfined concrete (*ConcreteCM*); c) steel (*ReinforcingSteel*).....280

Figure C.2 Roof drift time history responses of the SFI_MVLEM and Fiber models subjected to the Chi-Chi CHY028 record at: a) 100% shaking level; and, b) 150% shaking level.282

Figure C.3 Roof drift time history responses of the SFI_MVLEM and Fiber models subjected to the Tohoku TKY016 record at 100% shaking level.283

Figure C.4 Roof drift time history responses of the SFI_MVLEM and Fiber models subjected to the Northridge CCN090 record at: a) 100% shaking level; and, b) 150% shaking level.284

Figure C.5 Roof drift time history responses of the SFI_MVLEM and Fiber models subjected to the Superstition Hills PTS315 record at: a) 100% shaking level; and, b) 150% shaking level. ..285

Figure C.6 Roof drift time history responses of the SFI_MVLEM and Fiber models subjected to the Hokkaido HKD127 record at: a) 100% shaking level; and, b) 150% shaking level.286

Figure C.7 Roof drift time history responses of the SFI_MVLEM and Fiber models subjected to the Kobe SKI000 record at: a) 100% shaking level; and, b) 150% shaking level.287

Figure D.1 Coupling beam rotation results for the 6 story model at the code shaking level for (a) the long duration suite and (b) the short duration suite.289

Figure D.2 Coupling beam rotation results for the 12 story model at the code shaking level for (a) the long duration suite and (b) the short duration suite.289

Figure D.3 Coupling beam rotation results for the 18 story model at the code shaking level for (a) the long duration suite and (b) the short duration suite.290

Figure D.4 Coupling beam rotation results for the 24 story model at the code shaking level for (a) the long duration suite and (b) the short duration suite.290

Figure D.5 Coupling beam rotation results for the 30 story model at the code shaking level for (a) the long duration suite and (b) the short duration suite.291

Figure D.6 Story shear results for the 6 story model at the code shaking level for (a) the long duration suite and (b) the short duration suite.....292

Figure D.7 Story shear results for the 12 story model at the code shaking level for (a) the long duration suite and (b) the short duration suite.....292

Figure D.8 Story shear results for the 18 story model at the code shaking level for (a) the long duration suite and (b) the short duration suite.....293

Figure D.9 Story shear results for the 24 story model at the code shaking level for (a) the long duration suite and (b) the short duration suite.....293

Figure D.10 Story shear results for the 30 story model at the code shaking level for (a) the long duration suite and (b) the short duration suite.....294

Figure D.11 Story moment results for the 6 story model at the code shaking level for (a) the long duration suite and (b) the short duration suite.....295

Figure D.12 Story moment results for the 12 story model at the code shaking level for (a) the long duration suite and (b) the short duration suite.....295

Figure D.13 Story moment results for the 18 story model at the code shaking level for (a) the long duration suite and (b) the short duration suite.....296

Figure D.14 Story moment results for the 24 story model at the code shaking level for (a) the long duration suite and (b) the short duration suite.....296

Figure D.15 Story moment results for the 30 story model at the code shaking level for (a) the long duration suite and (b) the short duration suite.....297

Acknowledgements

First, I would like to thank my supervisor: Professor Carlos E. Ventura for giving me the opportunity to conduct this research and for his guidance along the way. His discussions and questions were always valuable and thought-provoking, and not only helped refine and improve my research, but gave me a deeper understanding of earthquake engineering in general. He always gave me the freedom to explore my own topics and ideas and was patient when I got off track. My appreciation of his support throughout my graduate work cannot be overstated.

I would also like to thank my supervisory committee member Professor Liam Finn for his help and knowledge relating to seismic hazard and ground motions. Our discussions, whether we agreed or disagreed, were always pleasant and I always came away more knowledgeable than before. Thanks to Professor Perry Adebar for his detailed review of my dissertation and the knowledge and expertise he imparted on me relating to the design and analysis of concrete structures. And thanks to Professor Farzad Naeim for his encouragement and guidance in shaping this dissertation. Special thanks to Dr. Ron DeVall, it was always a pleasure working with him and he contributed greatly to shape this dissertation. He will be deeply missed.

Thanks to my coworkers at BC Hydro, especially my managers Brent Bergman and Dr. Soheil Razavi-Darbar, who were extremely patient and accommodating, allowing me to gain valuable work experience while having enough time to complete my research and dissertation. Thanks to Jeff Yathon and Dr. Osmar Penner for helping me get started with BC Hydro, and to Drs. Behzad Hassani and Seku Catacoli for their friendship and invaluable advice along the way.

I also have to give thanks to my parents: Donna, Bob, and Nancy, for their support and encouragement throughout my years of education; to my siblings; my grandparents; and to the rest of my family. Special thanks to my aunt Deborah for always believing in me.

I must also thank my friends, who have made my time in Vancouver much more enjoyable. Thanks to Professor Lisa Tobber for the inspiration and everlasting friendship, no matter how uncool we became. Thanks to Dr. Yuxin Pan for all the fun times traveling. Thanks, Sharon Sendjaya, for the long and thoughtful talks - one day we will follow through on one of our schemes and make it big. Thanks Jasmine and Mike Dupuis for always being there and saving me from homelessness (more than once). And thanks to Shawn Adair for his encouragement and motivation on all my endeavors outside of academia.

Finally, my sincerest thanks to Dr. Armin Bebamzadeh. Armin went above and beyond his role as a supervisory committee member. Despite being possibly the busiest person I know, Armin made time, every week, to schedule a meeting to discuss my research progress. He pushed me more than anyone else to finish my work, no matter how frustrated or disheartened I become. I can honestly say that I would never have made it this far with his support and friendship. For all of this and more, I cannot thank Armin enough; but I hope (finally) finishing this dissertation is a start.

Dedication

I dedicate this dissertation to Ron Fairhurst and Gordon Hoover, both who passed away during its completion. These were two of the most admirable and kind-hearted men I have known, and I am blessed to have had them both as grandfathers and to have had the opportunity to spend so much time with them while they were here.

Chapter 1: Introduction

1.1 Background

The seismicity in Southwestern BC is dominated by the subduction of the oceanic Juan de Fuca plate beneath the continental North American plate occurring about 100 km west of Southern Vancouver Island in what is called the Cascadia Subduction Zone. Many major population centers in BC, such as Vancouver and Victoria, are susceptible to subduction megathrust earthquakes from the rupture of the Cascadia Subduction Zone – what are colloquially referred to as “Big Ones”. Such earthquakes have occurred in the past and are capable of reaching a moment magnitude (M_w) of 9.0 or higher (Goldfinger et al., 2012). Recent earthquakes located in similar subduction zones, such as Tohoku, Japan (M_w 9.1, 2011), El Maule, Chile (M_w 8.8, 2010), and Sumatra, Indonesia (M_w 9.1, 2004) have produced very strong levels of shaking, as well as records with very long durations, and caused severe amounts of damage over very large areas.

Recent research has indicated that the duration of shaking of a ground motion can impact the safety and ultimate collapse risk of different structural systems such as steel moment frames (Chandramohan et al., 2016b), concrete moment frames (Chandramohan et al., 2016a; Raghunandan and Liel, 2013), and timber structures (Pan, 2018). These studies indicate that longer ground motions tend to increase the levels deformation demands and damage to these structures, compared to shorter records of similar intensity. If the structural effect of this damage (such as component strength and stiffness degradation) is properly modelled, this damage can potentially induce collapse at lower shaking levels than would be predicted from analysis using shorter records. This tends to match both real-world observations made during post-earthquake reconnaissance missions and results from laboratory testing programs (Hancock and Bommer,

2006). However, this effect has not been thoroughly investigated for RC shearwall buildings using state-of-the-art numerical models.

Moreover, modern design standards in Canada (the National Building Code of Canada, NBCC; NRCC, 2015) and the United States (ASCE 7; ASCE/SEI, 2016) develop design earthquake loads using the response spectrum of a linear single-degree-of-freedom (SDOF) system and the assumed ductility and overstrength of the structural system. This method does not account for the duration of shaking of potential earthquake events. Other, performance-based standards, such as the Los Angeles Tall Building Structural Design Council (LATBSDC) alternative design procedure (LATBSDC, 2017) and the Pacific Earthquake Engineering Center (PEER) Tall Building Initiative (PEER TBI; PEER, 2017), do require a detailed seismic hazard assessment as well as sophisticated nonlinear dynamic analysis of the design structure. These standards attempt to account for appropriate shaking characteristics (such as duration) by requiring the selection of ground motions with geophysical parameters (e.g. magnitude, distance, and soil conditions) similar to that anticipated at the building site; however, duration is not explicitly accounted for. Also, since traditional seismic hazard analysis does not consider duration, the duration of the selected motions is still somewhat arbitrary.

One of the challenges of studying ground motion duration is preparing ground motion record suites that both reflect the seismic hazard of the region and appropriately capture the correct duration characteristics. To investigate the isolated effect of shaking duration, it is essential to use record suites that reflect the duration levels being compared, but that do not contain confounding variables such as shaking intensity or record spectral variation. To assess the safety of a structural system, the record suites used should be consistent with the seismic hazard of the system's location including mean spectral values, spectral dispersion, and geophysical parameters. This is

particularly difficult to obtain for long duration subduction interface record suites due to the lack of records from such events. Typical methods used to develop hazard-consistent suites of earthquake records (e.g. condition spectra; CS; Lin et al., 2013) typically rely on large databases of candidate records such as the PEER NGA-West2 database (Ancheta et al., 2013) for shallow crustal events. However, such a comprehensive database of subduction interface records currently does not exist.

Due to these difficulties, the impact of ground motion duration on prescriptive building codes has not been adequately assessed. Such studies require sophisticated nonlinear structural models able to simulate the response quantities associated with ground motion duration. Also, properly selected and modified ground motion suites, consistent with the total seismic hazard, are required to assess the collapse risk and safety of structures subjected to different types of shaking. This dissertation focuses on RC coupled shearwall buildings, which make up a large proportion of tall buildings in Vancouver's downtown core.

1.2 Objectives

The main objective of this research is to add to the state-of-knowledge on the effect of ground motion duration on structural systems by studying RC shearwall buildings, which, as of yet, has not been adequately assessed. The region of interest for this study in Southwestern BC, particularly Vancouver, since it has the potential to receive shaking from both short crustal and long duration subduction interface events. Both existing (constructed using conventional methods) and modern, more ductile, structures are considered.

This will require, first, identifying the potential mechanism(s) by which ground motion duration can affect the response of RC shearwall buildings. Next, numerical models of this system

can be developed. These models must be able to adequately simulate the mechanisms and effects of ground motion duration on the system.

Development of a representative suite of ground motions is an essential part of any structural time history analysis. When comparing the effect of two motion types, or using the motions to assess the safety of a system, the properties of the input motions becomes even more important. Thus, a methodology for preparing suitable ground motion record suites is another important objective of this work. Such suites of motions can be used to assess the effect of ground motion duration on the performance of RC shearwall structures.

Finally, the implication of these results on the safety of RC shearwall systems will be investigated. The objective is to use results from this work to assess structures designed to modern standards and propose modifications if the current provisions do not entail designs with sufficiently low collapse risk probabilities.

1.3 Organization

To achieve the objectives outlined in the previous section, this dissertation is organized as follows:

Chapter 2 provides a literature review of the studies and standards related to the effect of ground motion duration. First, modern North American seismic design standards are reviewed in order to identify where they lack pertaining to the consideration of ground motion duration. Next, the seismic background of Southwestern BC is described including a description of the Geological Survey of Canada (GSC) seismic hazard model for Western Canada. This section also considers the modeling and prediction of ground motion duration. Next, the performance and testing of RC

shearwall buildings and their components is reviewed. Finally, recent studies related to the structural effect of ground motion duration are reviewed.

Chapter 3 provides background information on the effect of ground motion duration on the performance of structural systems and the mechanism(s) by which it imparts these effects. These effects are important to identify and describe as they will influence the numerical model development of the subsequent chapters. Also included is a study intended to define an appropriate duration metric since the term “duration” is arbitrary and can be quantified in many ways.

Chapter 4 investigates the effect of ground motion duration on concrete shearwall buildings using simplified 2D nonlinear models. This chapter considers existing, conventionally designed structural systems, which are expected to be most vulnerable to shaking duration. Results from physical component tests are used to calibrate the components of the numerical models. These models are used to efficiently perform a large amount of time analyses using spectrally equivalent record suites in order to isolate and study the effect of shaking duration.

Chapter 5 proposes a methodology for developing ground motion suites that can be used for both comparing the difference in structural response between two suites (e.g. long vs. short duration suites) and providing results from nonlinear time history analysis (NTHA) that can be used in seismic risk assessment.

Chapter 6 extends the conclusions of Chapter 4 using sophisticated 3D models subjected to hazard-consistent ground motion suites. This chapter considers both existing (similar to Chapter 4) and modern (designed with a larger ductility capacity) structural systems. Four hazard-consistent record suites (two with shorter, crustal motions; the other two comprising long duration subduction interface records) are developed and used to analyze the structures and assess the differences between the two shaking types.

Chapter 7 investigates the effect of ground motion duration on modern, prescriptive building codes and aims to provide recommendations for the design of RC shearwall buildings in subduction zones (e.g. Southwestern BC). This chapter uses the results from Chapter 6 to quantify the performance of this type of structure.

Chapter 8 summarizes the findings and contributions of this work including the research gaps it fills and proposes recommendations for future studies.

Chapter 2: Literature Review

This literature review is discretized into four main sections relating to the impact of ground motion duration on the design and performance of RC shear wall buildings:

1. **Modern seismic provisions in North America.** It is first important to understand the current design provisions including their intent and limitations, particularly when it pertains to ground motion duration.
2. **Seismicity in Southwestern BC.** Before delving into the effect of ground motion duration on structural response, it is necessary to understand the seismicity behind the events capable of producing long and short duration recordings. Thus, this section introduces the seismic setting of Southwestern BC, the area of focus of this research, including the current modelling of this seismic regime. A brief discussion on ground motion duration and the different factors that may influence it is also presented.
3. **Coupled RC shear wall buildings.** Next, coupled RC shear wall buildings are introduced, including header types and system behavior. This type of structure is the primary focus of this research.
4. **Ground motion duration.** Finally, the current state-of-knowledge of the impact of ground motion duration on the response structural systems is discussed. This is a long-standing area of research that includes physical testing, numerical modelling, and site investigation. However, not until recently has computational power and numerical modelling frameworks allowed for more detailed studies conducted through numerical simulations.

2.1 Seismic Provisions in North America

This section provides a brief history of the Canadian seismic provisions, as well as introduces other commonly used provisions from the United States (US). A discussion of the

limitations of these provisions is discussed with particular emphasis on the effect of ground motion duration.

2.1.1 National Building Code of Canada (NBCC)

Seismic provisions were first introduced into the NBCC in 1941, based on the Uniform Building Code at that time (NRCC, 1941; Mitchell et al., 2010). For seismic design, an equivalent lateral force procedure (ELFP) was adopted where the lateral force the building must be designed to resist was computed based and a factor multiplied by the weight of the structure. The factor was initially based solely on the soil type, and later modified based on the expected level of shaking at the site in 1953 (defined by a broad “seismic category”; NRCC, 1953). These provisions have gone through several major revisions since then, as has the Canadian seismic hazard model used to define seismic demands.

In 1965, a “C” factor was introduced to modify base shear demand based on the type of construction ($C = 0.75$ for moment resisting frames and concrete shearwalls with adequate reinforcement to achieve ductile behavior; and $C = 1.25$ for all other construction types). This factor introduced the concept that ductile systems could yield to dissipate seismic energy, and thus, could be designed for lower base shears (NRCC, 1965). This factor was reintroduced as “K” in 1970, and was further defined for a wider variety of building systems in this edition (NRCC, 1970). In 1995, the seismic force reduction factor: “R”, was first introduced into the NBCC (NRCC, 1995). In 2005, this was replaced with the modern $R_d R_o$, where R_d is a ductility related factor that reduces seismic demand due to the system’s ability to dissipate seismic energy, and R_o is an overstrength factor that accounts for the dependable reserve strength in a building designed to code standards (NRCC, 2005, 2010). The use of these factors recognizes that modern buildings are expected to undergo damage under design level earthquakes, and through this damage, will

dissipate seismic energy. More ductile systems, such as ductile coupled RC shearwalls and ductile RC moment frames, are specified larger R_d factors, which allows them to be designed for lower base shears compared to less ductile systems, such as conventionally constructed RC walls or frames. The intent of these force reduction factors is to provide building systems that protect the life safety of the building occupants under the considered seismic load – not to prevent damage to the building itself. Currently the NBCC specifies a design earthquake with a 2% in 50 year probability of exceedance; the design values for this shaking level come from the current GSC seismic hazard model (see: Section 2.2.2).

2.1.2 ASCE 7

The American Society of Civil Engineering (ASCE) publishes the standard for new building design, including seismic provisions, for the US: ASCE 7. This standard uses a system-specific R factor to reduce seismic base shear demands - similar to the NBCC's R_dR_o . This factor includes both ductility and overstrength. ASCE 7-16 (ASCE/SEI, 2016) uses a risk-targeted Maximum Considered Earthquake (MCE_R) to define seismic demands. The MCE_R is similar to a 2% in 50 year event – however, it is modified to produce designs with a uniform seismic collapse risk across the country (Luco et al., 2017).

The ASCE explicitly lays out their performance criteria for regular (Type I and II) new structures:

1. Maximum of 10% probability of collapse when subjected to MCE_R shaking, and
2. Maximum of 1% probability of collapse in 50 years.

The first criterion can be checked explicitly through nonlinear time history analysis of a structural model subjected to a suite of MCE_R level motions. The second is implicitly assumed to be met if the building is properly designed to modern code standards and (1) is met.

2.1.3 FEMA P695

These seismic force reduction factors (R and R_dR_o from ASCE 7 and the NBCC, respectively) have largely been assigned by building code committees based on expert experience and knowledge. To provide a more reproducible and systemized approach to developing these factors, in 2009, the Applied Technology Council (ATC) prepared a report for the Federal Emergency Management Agency (FEMA) proposing a method to quantify building seismic performance factors: FEMA P695 (FEMA, 2009).

The FEMA P695 methodology can be used to evaluate R factors for existing structural systems and develop them for novel systems. The basis of the method is to develop R factors that give a building system a sufficient margin against collapse against larger than expected shaking (greater than the MCE_R), as well as a sufficiently low probability of collapse at the maximum considered, or MCE_R , level of shaking (FEMA, 2009). This involves nonlinear incremental dynamic analysis (IDA; Vamvatsikos and Cornell, 2002) of a suite of numerical structural models that represent extent of the design space for the new or existing system.

The FEMA P695 methodology has been widely adopted in the US and worldwide to develop and assess seismic reduction factors. Zareian et al. (2010) used the methodology to evaluate the performance of special steel frames. Gogus and Wallace (2015) adopted the methodology to assess the seismic safety of RC walls. Outside of the US, Hossain (2013) was the first to adopt the methodology in Canada in order to assess the seismic performance of concrete buildings reinforced with superelastic shape memory alloys. Similar studies were performed by Shahnewaz et al. (2020) for cross-laminated timber platform buildings.

In this report, a suite of 22 earthquake motions are adopted for the time history analyses. While these are all short recordings from shallow crustal events, others have proposed alternative suites of subduction motions (e.g. Estrella et al., 2019).

2.1.4 Performance-based Design Standards

For the design of new structures that fall outside of the building code scope, two alternative design standards were introduced for Los Angeles, and then, later, the US as a whole: the Los Angeles Tall Building Structural Design Council (LATBSDC) alternative design procedure (LATBSDC, 2005) and the Pacific Earthquake Engineering Center (PEER) Tall Building Initiative (PEER TBI; PEER, 2010), respectively. These two documents were primarily focused on the design of tall RC shearwall buildings using a performance-based procedure. Both of these documents have undergone several revisions since they were first introduced.

Performance-based design following the LATBSDC and PEER documents involves five main steps:

1. definition of seismic hazard/ground motion selection and scaling,
2. development of a numerical building model,
3. nonlinear time history analysis (NTHA),
4. performance assessment, and
5. peer review.

Following this procedure, new designs are analyzed to ensure they meet certain performance objectives (e.g. levels of damage) at one or more seismic hazard levels (typically the serviceability level of shaking and the MCE_R level of shaking). The performance objectives and hazard levels are selected to ensure that new buildings designed with this method meet or exceed

standard building code requirements. The entire procedure is subject to extensive peer review (LATBSDC, 2005; PEER, 2010).

2.1.5 Limitations

Currently, the seismic force reduction factors (R and R_dR_o from ASCE 7 and the NBCC, respectively) are selected through the judgement of expert committees and do not consider the duration of expected ground motions at the building site. This is a potential problem since these factors include an energy dissipation component, and longer duration motions may produce much larger seismic energy demands on structures.

The FEMA P695 methodology is becoming more common to calibrate seismic force reduction factors for novel systems. As previously mentioned, this methodology requires nonlinear time history analyses of a suite of structural models; however, the proposed records are all from short, shallow crustal earthquake events. Thus, even seismic factors calibrated through the FEMA P695 methodology may not be suitable for structures to be constructed in regions where long duration earthquakes are possible (Estrella et al., 2019).

The current PEER TBI (PEER, 2017) and LATBSDC (LATBSCD, 2017) standards require nonlinear time history analysis to explicitly meet certain performance objectives. Both the 2015 NBCC and ASCE 7-16 also both allow nonlinear time history analysis to be used for structural design and assessment. These standards do not explicitly account for ground motion duration; however, attempt to do so by requiring the selection of ground motions with geophysical parameters (e.g. magnitude, distance, and soil conditions) similar to that anticipated at the building site (from PSHA) when performing time history analyses. Since traditional PSHA does not consider duration, the duration of the selected motions is still somewhat arbitrary.

2.2 Seismicity in Southwestern BC

The following sections introduce the seismic background of Southwestern BC. This includes a discussion of the potential seismic sources in this region and the Geological Survey of Canada (GSC) seismic hazard model for Western Canada.

2.2.1 Seismic Background

Southwestern BC has a unique seismic setting that includes earthquakes from three sources: shallow crustal events, which occur along shallow faults in the Earth's crust; subduction intraslab events, which occur deep within subducting tectonic plates; and subduction interface events, which are caused by slip between subducting tectonic plates (Figure 2.1)

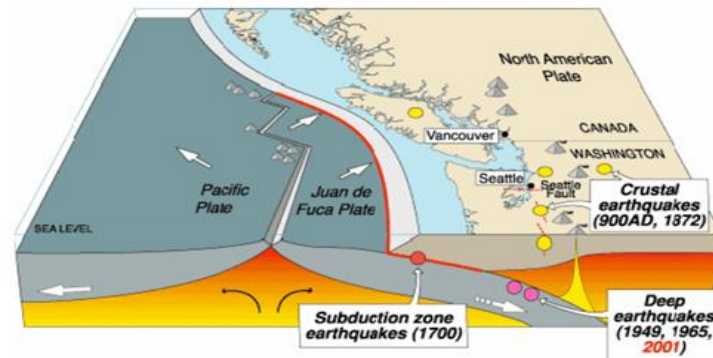


Figure 2.1 Southwestern BC seismic sources (source: United States Geological Survey).

The seismicity in Southwestern BC is dominated by the Cascadia Subduction Zone, where the oceanic Juan de Fuca plate is being subducted beneath the continental North American plate occurring about 100 km west of Southern Vancouver Island. This regime is capable of producing earthquakes with a moment magnitude (M_w) of 9.0 or higher (Goldfinger et al., 2012). The last large interface event in the Cascadia subduction zone was approximately 300 years ago (~1700 A.D.).

Subduction intraslab earthquakes can occur deep below the surface in faults along the Juan de Fuca plate, between 20 and 100 km deep. The most recent major intraslab event in the Cascadia region was the 2001 Nisqually earthquake, which was a magnitude 6.8 event that occurred 50 km beneath Seattle, Washington. Other historic intraslab events in the Pacific Northwest include the 1949 Puget Sound event (magnitude = 7.1), and the 1965 Olympia, Washington (magnitude = 6.9) earthquakes.

Earthquakes from shallow faults, typically less than 20 km deep, in the crust of the North American plate are also possible. These types of events are frequently recorded in Southwestern BC - around 200-300 per year (earthquakescanada.nrcan.gc.ca). The vast majority of these events are very small, however larger magnitude events are also possible. In the past 70 years, more than 100 magnitude 5 or greater earthquakes have been recorded in Southwestern BC. The largest recorded crustal event was the magnitude 8.1 event near Queen Charlotte Island Earthquake in 1949. Several other significant events (magnitude 7.3 in 1946 and magnitude 7.0 in 1918) have been recorded on or near Vancouver Island; and a magnitude 7.4 event was recorded near the Washington border in 1872.

Figure 2.2 illustrates the historic earthquake events that have occurred in or near Southwestern BC in the past ~390 years including the magnitude ~9 Cascadia subduction zone rupture from ~1700.

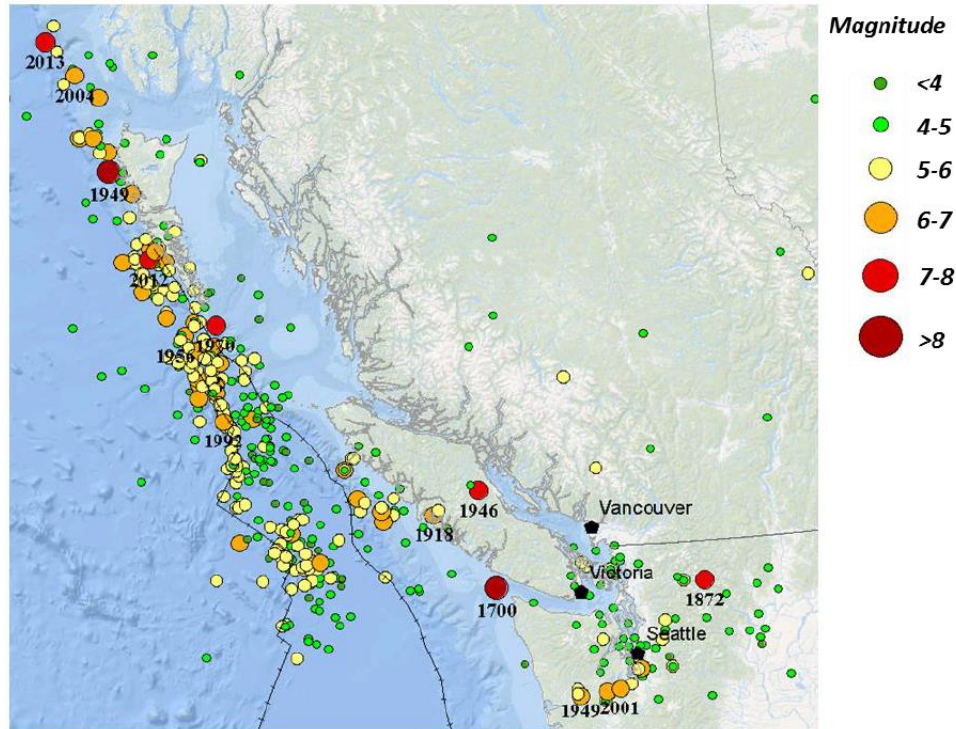


Figure 2.2 Historic earthquakes near Southwestern BC (source: Natural Resources Canada).

2.2.2 Southwestern Canada Seismic Hazard Model

This section introduces the 2015 GSC seismic hazard model sources for Southwestern Canada (Halchuk et al., 2014), which was developed to compute seismic hazard values for use in the 2015 National Building Code of Canada (NBCC).

2.2.2.1 Introduction

The 2015 GSC seismic hazard model consists of both Cornell-type area sources and discrete fault sources. Area sources are defined by their coordinates, depth, minimum and maximum magnitudes, and a magnitude-reoccurrence (M-R) relationship. Fault sources are defined in a similar manner except with a surface trace and depths/dip angles instead of an area and depth, respectively. Area sources are used to capture the seismicity of an area where the exact

faulting is unknown or ill-defined, but earthquake events have been observed. Fault sources are modeled where a faulting location is known or can be well estimated.

M-R for each source is described in terms of an asymptotically truncated Gutenberg-Richter magnitude-frequency distribution following:

$$N(m) = N_o e^{-\beta m} [1 - e^{-\beta(M_{max}-m)}]$$

where $N(m)$ is the cumulative number of earthquakes greater than magnitude m ; N_o is the total number of earthquakes per year; M_{max} is the maximum magnitude considered possible for the source; and β is a constant that describes the relative number of small-to-large earthquakes, where $\beta = b \ln(10)$, and b is the Gutenberg-Richter (1944) b-value.

2.2.2.2 Shallow Crustal Sources

Figure 2.3 illustrates the 2015 GSC crustal sources in Southwestern BC. There are 14 areal crustal sources within a 500 km radius from Vancouver, BC. These sources include (in no particular order):

- Offshore (OFS)
- Explorer Plate Bending (EXP)
- Brooks Peninsula (BRO)
- Coastal Mountains (CST)
- Nootka Fault (NOFR)
- Vancouver Island Coast Mountains (VICM)
- Juan de Fuca Plate Bending, Offshore (JDFF)
- Olympic Mountains (OLM)
- Puget Sound, Shallow (PGT)
- Cascade Mountains (CAS)
- Northern British Columbia (NBC)

- Southern British Columbia (SBC)
- Rocky Mountain Fold/Thrust Belt, North (ROCN)
- Rocky Mountain Fold/Thrust Belt, South (ROCS)

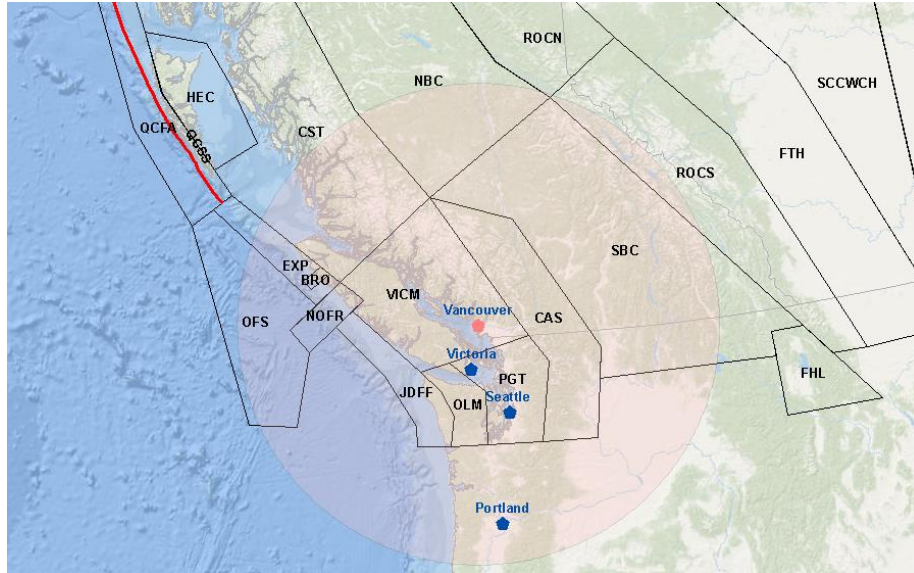


Figure 2.3 2015 GSC seismic hazard model shallow crustal sources in Southwestern BC (source: VC Structural Dynamics, 2019).

2.2.2.3 Subduction Intraslab Sources

Two subduction intraslab area sources are included in the GSC model to capture the seismicity that occurs in the subducting Juan de Fuca plate:

1. The Juan de Fuca Plate Bending (JDFN) area source captures the band of earthquakes about 100 km wide that straddles the west coast of Vancouver Island. The earthquakes are within the Juan de Fuca plate and occur in the 25 to 35 km depth range in a 10 km thick band that dips to the east.
2. The Georgia Strait/Puget Sound (GTP) area source captures the deep seismicity within the east dipping Juan de Fuca Plate. Most of the seismicity occurs at depths between 40 km and 70 km and is confined to a band about 10 km thick.

These sources are illustrated in relation to Vancouver, and other major population centers in the area, in Figure 2.4.

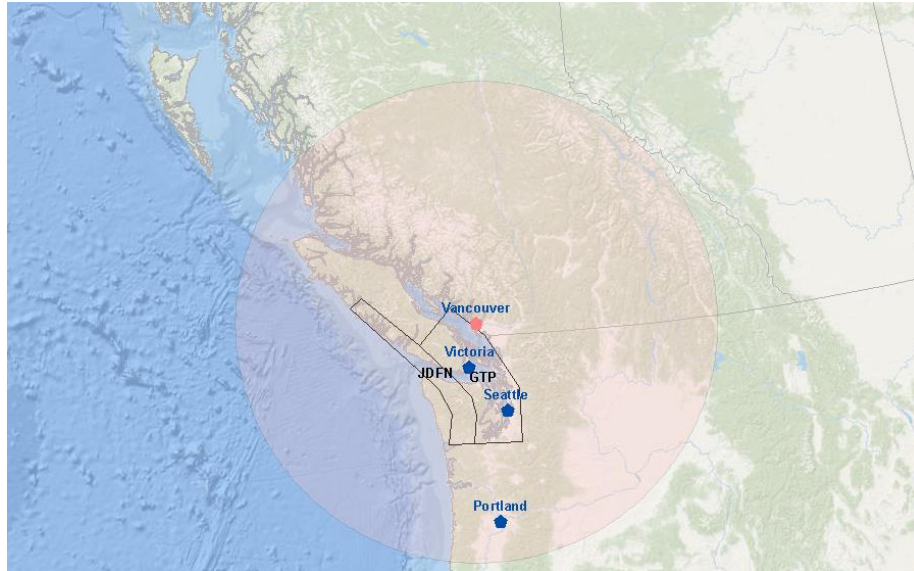


Figure 2.4 2015 GSC seismic hazard model subduction intraslab sources in Southwestern BC (source: VC Structural Dynamics, 2019).

2.2.2.4 Subduction Interface Sources

The Juan de Fuca subduction zone was modeled with a series of finite fault models which include the Juan de Fuca segment of the Cascadia subduction zone (termed Cascadia Interface Subduction or CIS source) and the Explorer segment of the Cascadia subduction zone (termed Explorer Interface Subduction or EIS source). The CIS zone was modeled as a characteristic source capable of generating earthquakes of magnitudes from 8.5 to 9.2.

Also included along with the interface sources are two thrust fault sources: the Winona Thrust Fault (WIN) and Haida Gwaii Thrust Fault (HGT). Although these are not true interface sources, they are modeled in the same fashion and use the same ground motion intensity prediction

models as the other interface sources. The HGT source is too far from Vancouver to significantly affect its seismic hazard. These sources are shown in Figure 2.5.

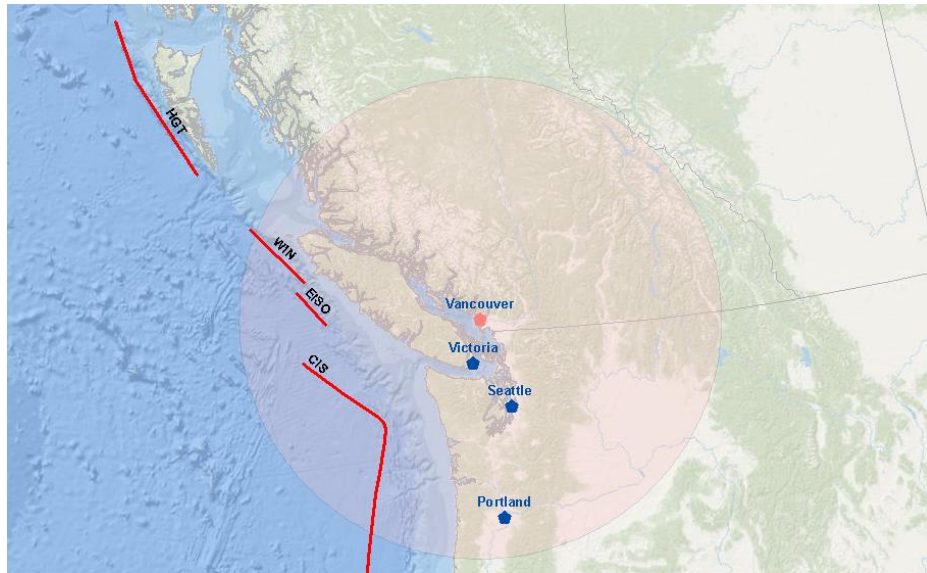


Figure 2.5 2015 GSC seismic hazard model subduction interface sources in Southwestern BC (source: VC Structural Dynamics, 2019).

2.2.2.5 Ground Motion Prediction

Ground motion models (GMMs) are used to predict shaking intensity (mean and standard deviation) from different earthquake scenarios (magnitude, distance, site class, etc.). Table 2.1 summarizes the GMMs used in the 2015 GSC seismic hazard model for the different source types. The GSC uses a weighted logic tree approach for predicting shaking intensity – the weights of the GMMs used for each source are also included in Table 2.1.

Source Type	GMM Reference	Weight	Shorthand
Crustal (Areal Sources)	Boore and Atkinson (2008)	1.0	BA08
Crustal (Fault Sources)	Boore and Atkinson (2008)	1.0	BA08
Crustal Offshore	Boore and Atkinson (2008)	1.0	BA08
Intraslab (30km Depth)	Zhao et al. (2006) (BA08 for 10s)	1.0	Z06
Intraslab (50km Depth)	Zhao et al. (2006) (BA08 for 10s)	1.0	Z06
Subduction Interface	Atkinson and Macias (2009)	0.5	AM09
	Ghofrani and Atkinson (2014)	0.2	GA14
	Abrahamson et al. (2016)	0.2	A16
	Zhao et al. (2006)	0.1	Z06

Table 2.1 GSC 2015 seismic hazard model GMM summary.

2.2.2.6 Treatment of Uncertainty

Uncertainty is a very important consideration in any probabilistic seismic hazard model. There are two main sources of uncertainty inherit in any seismic hazard analysis: aleatory uncertainty, which due to randomness in natural processes, such as weather or earthquakes; and epistemic uncertainty, which results from uncertainty in knowledge. The former cannot be reduced by collecting additional information, but the latter can be.

Aleatory uncertainty arises from physical variability that is inherent in the unpredictable nature of future events. An example is the random component of earthquake source and propagation processes which will cause a scatter of amplitudes about the median values, even if the median were known with perfect accuracy. The Cornell-McGuire approach, as implemented

in the 2015 GSC seismic hazard model, includes aleatoric uncertainty by incorporating the standard deviation (scatter of data about the median) of the GMMs into the computation.

Epistemic uncertainty arises from the differences in expert specification of modelling assumptions, unknown or only partially known parameters, and extrapolation beyond observed range of data. The 2015 GSC model adopted a “logic tree” approach to account for this type of uncertainty. Several of the source modelling parameters in the model use a three-branch model (best, lower bound, and upper bound estimates) to capture epistemic uncertainty – these include: M-R parameters, depth, and maximum magnitude. For some sources, up to three alternative source models were also considered.

To capture the epistemic uncertainty in ground motion prediction, a three-branch logic tree was also implemented. To do this, several possible GMMs were considered for each source - then a representative, or “central”, GMM was selected (Table 2.1). The upper and lower bounds were then derived to encompass the other possible models. For example: for crustal sources, the suite of four PEER Next Generation Attenuation models for Western North America (NGA-West) were considered. Ultimately, BA08 was selected as a central GMM, as it was the simplest to implement, and the upper and lower branch GMMs were drawn around the other three models (Atkinson and Adams, 2013).

2.2.3 Ground Motion Duration Prediction

The length of strong shaking, or duration, of a ground motion record depend on the characteristics of the source of the event, the travel path to site, and of the site of the recording.

The primary variables for predicting ground motion duration are:

1. event type (e.g. subduction interface vs. shallow crustal),
2. event magnitude,

3. distance from event source to recording site,
4. soil conditions at the event source, and
5. soil conditions at the recording site.

Recordings from larger subduction interface events, especially at sites far from the source and/or on soft soil, typically have longer durations and more energy than those from close, small magnitude crustal events.

One way to simply quantify this is to consider the following approximation for earthquake source duration (Beresnev, 2002):

$$T_s \approx \frac{0.6}{f_c} \quad (2-1)$$

where T_s is the earthquake source duration, and f_c is the corner frequency used to define a Brune (1970) source spectrum.

To estimate the corner frequency of an earthquake, consider the equation for stress drop based on corner frequency (Eshelby, 1957):

$$\Delta\sigma = \frac{7M_o}{16} \frac{f_c^3}{(k\beta)^3} \quad (2-2a)$$

where $\Delta\sigma$ is the stress drop of the event, M_o is the event's seismic moment (a measure of the total energy of the event), k is a constant that depends on source type, and β is the shear wave velocity at the source. The stress drop is the amount of stress difference in a fault pre- to post-rupture and typically drops with increasing magnitude.

Rearranging Equation 2-2a for corner frequency yields:

$$f_c = \sqrt[3]{\frac{16\Delta\sigma}{7M_o}} (k\beta)^3 \quad (2-2b)$$

The definition of moment magnitude, which is typically used to define the magnitude of earthquakes, can be used to compute the seismic moment (Kanamori, 1977):

$$M_w = \frac{2}{3} \log_{10} M_o + 10.7 \quad (2-3a)$$

Or,

$$M_o = 10^{(M_w+10.7)*2/3} \quad (2-3b)$$

where M_w is the moment magnitude and M_o is measured in dyne-cm (10^{-7} N-m).

Combining Equations 2-1, 2-2b, and 2-3b, yields a simple method for estimating source duration based on magnitude if the stress drop of an event and shear wave velocity at the event source are known.

In Figure 2.6a, the source duration is estimated over a wide range of magnitude ranges using $\beta = 2, 3,$ and 4 km/s, with a constant stress drop of 150 bars, and assumed k of 0.3 (Chen and Abercrombie, 2020). In Figure 2.6b, the source duration is estimated using $\Delta\sigma = 50, 150,$ and 250 bars, with a constant $\beta = 3.7$ km/s. From these figures, it can be seen that source duration increases exponentially with magnitude and increases with decreasing stress drop and/or source shear wave velocity. Larger magnitude earthquakes typically have larger ruptures areas (Strasser et al., 2010) and lower stress drops – both the large magnitudes and the low stress drops tend to increase source duration.

Note that this is only an estimation of source duration – the duration of an earthquake recording will depend on the travel path of the seismic waves from the source to the recording site and of the soil conditions at the recording site. To include path duration, for the Western United States, Atkinson and Boore (1995) recommend the following equation:

$$T_{path} \approx 0.05R \quad (2-4)$$

where R is the distance in km. This can be added to Equation 2-1 to get an estimate of the complete shaking duration, T_{GM} :

$$T_{GM} = T_s + T_{path} \quad (2-5)$$

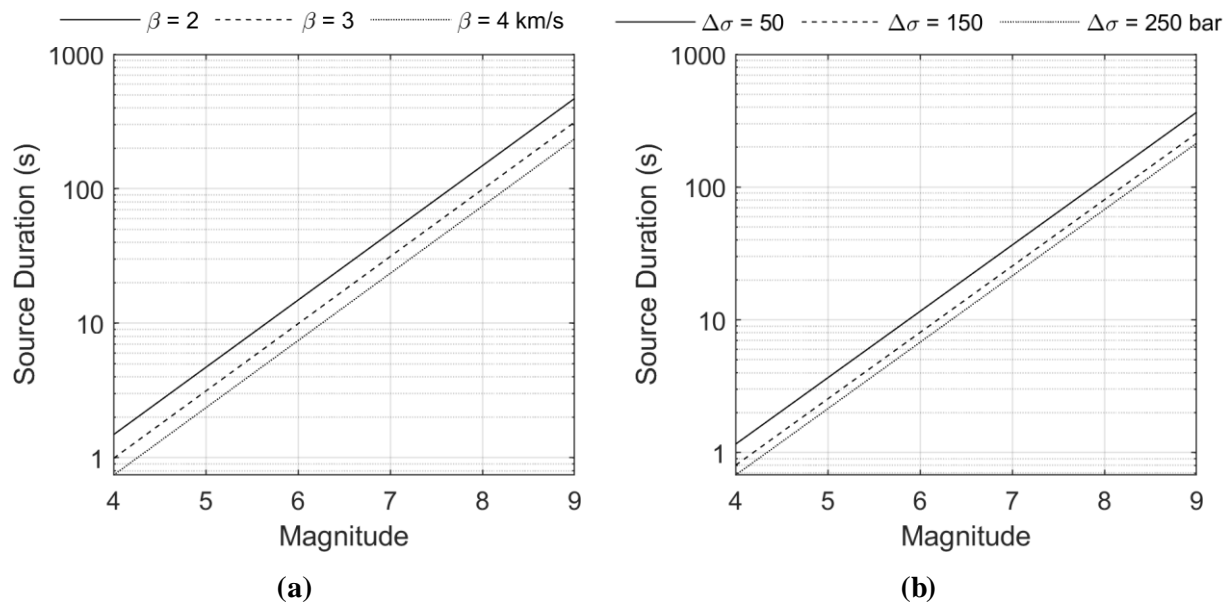


Figure 2.6 2015 Source duration vs. moment magnitude estimations with: a) three different shear wave velocities and constant stress drop of 150 bars; and, b) three different stress drop and constant source shear wave velocity of 3.7 km/s.

2.2.3.1 Duration Modelling

There are many metrics to quantify ground motion duration (see Section: 3.2) – most of these are based on the duration, or time, of “strong” shaking or the amount of energy in a recording. The amount of energy is of particular importance for the response of structures, since this seismic energy will need to be dissipated through the structure (typically through damping and damage/deformation of ductile building components).

One commonly used metric for the duration of an earthquake recording is the significant duration, which is related to the time of significant energy accumulation in the record (see Section: 3.2). Afshari and Stewart (2016) developed a GMM for significant duration using the PEER NGA-West2 database for magnitude 3.0-7.9 crustal events. The resulting median 5-95% significant duration (d_{5-95} ; this refers to the time between 5 and 95% of the total energy accumulation in the recording) predictions from this model are illustrated in Figure 2.7 for a range of distances and magnitudes for both site time averaged 30 m shear wave velocity (V_{s30}) = 250 and 1100 m/s. Note that the significant duration increases with both magnitude and distance, and is uniformly lower for the higher V_{s30} .

Figure 2.8 illustrates three acceleration time histories from three different events: Northridge, 1994 ($M_w = 6.7$, distance = 26 km, $d_{5-95} = 10.7$ s); Hokkaido, Japan, 2003 ($M_w = 8.0$, distance = 134 km, $d_{5-95} = 40.9$ s); and Tohoku, Japan, 2011 ($M_w = 9.1$, distance = 111 km, $d_{5-95} = 104.3$ s). Both Japanese events are from subduction interface ruptures, while the Northridge event was a shallow crustal earthquake. Both the subduction records have much longer significant durations compared to the crustal; and the larger magnitude Tohoku recording is much longer than that from the Hokkaido recording, despite have similar station-to-rupture distances. All recordings were from stations on NEHRP Site Class C soil ($V_{s30} = 360-760$ m/s) and all recordings had similar peak ground accelerations and 1.0 s spectral values ($S_a(1.0$ s)).

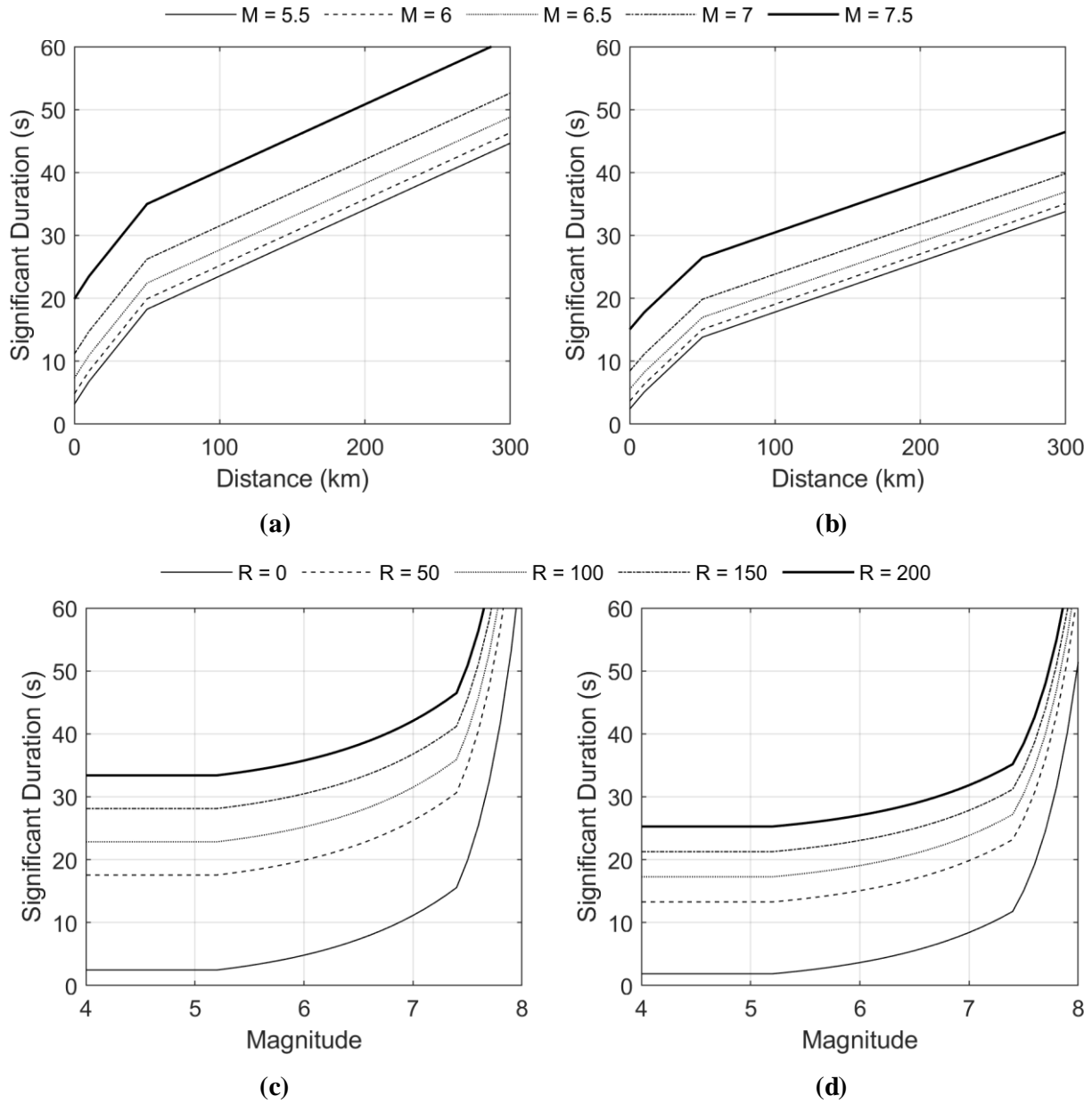


Figure 2.7 2015 Ground motion median duration (5-95% significant duration) predictions from the Afshari and Stewart (2016) GMM for: a,c) $V_{s30} = 250$ m/s; and, b,d) $V_{s30} = 1100$ m/s.

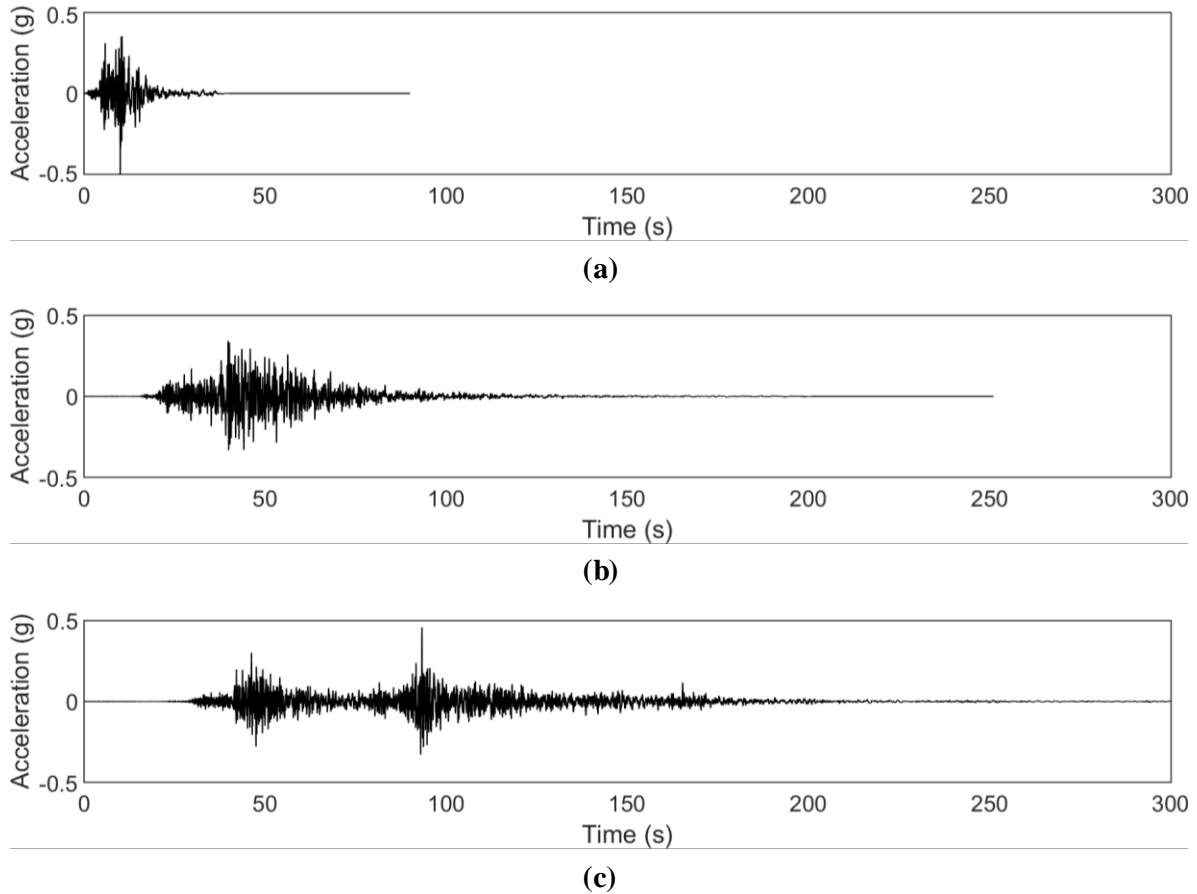


Figure 2.8 Acceleration time histories from three recordings: a) Northridge, 1994 station: STM-360. $M_w = 6.7$, distance = 26 km; b) Hokkaido, Japan, 2003 station: HKD125-NS. $M_w = 8.0$, distance = 134 km; c) Tohoku, 2011, station: MYG009-NS, $M_w = 9.1$, distance = 111 km.

2.3 Coupled RC Shearwall Buildings

The following sections provide a brief introduction to the performance and history of coupled RC shearwall buildings. These systems comprise two or more shearwalls (typically in the core of the building) connected at each level through coupling, or “header” beams, which couple the walls by allowing the transfer of vertical forces between them.

2.3.1 Conventionally Reinforced Coupling Beams

Conventional coupling beams are deep beams that link and transfer shear between two adjacent shearwalls. Due to their small aspect ratio (length/depth), these beams are typically governed by shear. These beams are reinforced with longitudinal reinforcement and transverse reinforcement in the form of traditional stirrups.

Many testing programs have been carried out in order to study the behavior of this type of beam including their strength and ductility capacity. Barney et al. (1980) tested two beams with aspect ratios of 2.5 and 5 and observed ductility tolerances of 7.8 and 10, respectively. Kwan and Zhao (2002) tested 5 specimens with different aspect ratios ranging from 1.17 to 2.0. They observed ductility capacities from 4 to 6, increasing with increases in aspect ratio. Galano and Vignoli (2000) tested a suite of short coupling beams – four of which were conventionally reinforced. These beams had aspect ratios of 1.5 and ductility capacities of ~6. Xiao et al. (1999) subjected conventional coupling beams with high strength concrete to reverse-cyclic loading. They observed ductilities of 6 and 6.2 from beams with aspect ratios of 3 and 4, respectively.

In Figure 2.9, the ductility vs. aspect ratio results from the 10 samples included in these four testing programs is plotted. A nearly linear relationship ($R^2 = 0.69$) is observed between ductility and aspect ratio with a slope of 1.13 and y-intercept at ductility = 3.36. For typical residential construction with header beams with aspect ratios of ~2.4 (Naish, 2010) a ductility capability of ~6.1 would be expected from these results.

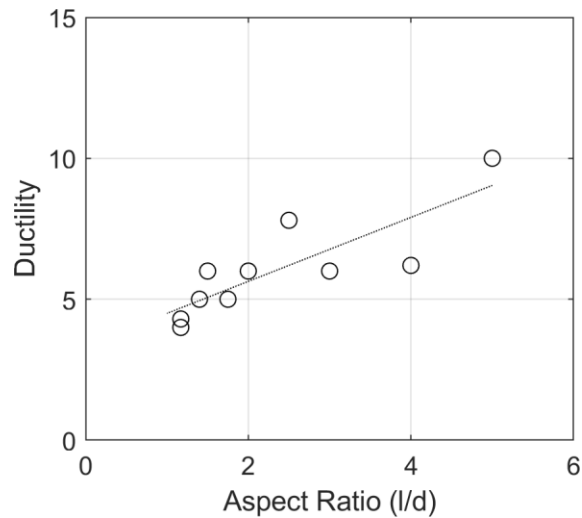


Figure 2.9 Ductility capacity vs. aspect ratio for conventional coupling beams from various testing programs.

2.3.2 Ductile Coupling Beams

Paulay and Binney (1974) introduced the concept of diagonal reinforcement in coupling beams to increase the performance of these beams when subjected to high shear loads. The purpose of the diagonal bars was to act as a truss to resist lateral loads, with one group of bars in tension, and the other in compression. This way, the strength and ductility capacity of the steel bars could be exploited, producing a shear failure mechanism with significant ductility and energy dissipation capacity. The bar groups, however, must be adequately tied to resist buckling under compression – this is one of the main detailing provisions (Paulay and Binney, 1974).

Since the 1970s, when they were first introduced, several testing programs have been conducted on diagonally reinforced coupling beams. Barney et al. (1980) tested two diagonally reinforced beams. These beams had aspect ratios of 2.5 and 5, and achieved ductility capacities of 9.2 and 10, respectively. Another two beams were tested by Tassios et al. (1996) – these beams had aspect ratios of 1 and 1.66 and achieved ductility capacities of 5.6 and 5.2, respectively.

Galano and Vignoli (2000) also tested several diagonally reinforced beams with an aspect ratio of 1.5. Ductility capacities from 5 to 7 were observed, with ductility capacity increasing with the amount of longitudinal steel. The hysteretic behavior of these beams was also less pinched compared to similar conventionally reinforced beams, resulting in much more energy dissipation in each nonlinear loading cycle.

More recently, Naish (2010) tested eight diagonally reinforced coupling beams. Five of these beams had aspect ratios of 2.4, while the remaining 3 had ratios of 3.33. Different steel layouts and type of confinement were tested. The beams with aspect ratios of 2.4 reached ductility capacities from ~8.2-10.2; the beams with aspect ratios of 3.33 reached ductility capacities from ~8.8-9.8. The largest ductility capacity of 10.25 was measured in a specimen with an aspect ratio of 2.4, full section confinement, and a RC slab cast with the beam.

In Figure 2.10, the ductility capacity vs. aspect ratio results from the 15 samples included in these four testing programs is plotted. Fitting a linear relationship to the data ($R^2 = 0.57$) yields slope of 1.49 and y-intercept at ductility = 4.39. However, the data is better fit with a logarithmic curve ($R^2 = 0.70$) with the form: $\mu = 3.96 \ln(l/d) + 4.83$; where μ is ductility and l/d is the beam aspect ratio (length/depth). For a header beam with an aspect ratio of 2.4, a ductility capability of 8.0 or 8.3 would be expected from these results, depending on the form of the fitted curve (linear or logarithmic, respectively).

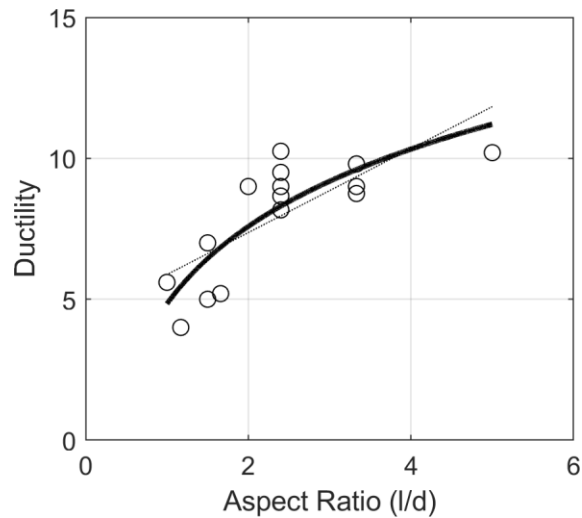


Figure 2.10 Ductility capacity vs. aspect ratio for diagonally reinforced coupling beams from various testing programs with: linear fit (dotted; $R^2 = 0.57$), and logarithmic fit (solid; $R^2 = 0.70$).

2.3.3 Coupled Shearwall Behavior

In RC coupled shearwall systems, coupling beams are used to connect shearwalls to add strength and stiffness to the system. These beams transfer vertical forces between two walls, allowing them to resist a portion of the overturning moment induced by a lateral load(s) through frame-like coupling action (Figure 2.11). This reduces the moments that must be resisted by individual walls and adds significantly more lateral stiffness to the system.

In well-detailed systems, these coupling beams are also intended to provide the majority of the energy dissipation of the system. Ideally, the beams should develop plastic hinges nearly simultaneously, distributing energy dissipation over the height of the structure, rather than concentrating it in plastic hinges at the bases of the walls. Under extreme lateral loading demands, the walls may also form plastic hinges at their bases, further adding to the energy dissipation capacity of the system, as shown in Figure 2.12.

Paulay (1980) studied the design and behavior of coupled wall systems, considering the novel use of diagonal reinforcement in header beams proposed by Paulay and Binney (1974). This reinforcement detailing allowed squat coupling beams to achieve the ductility required to dissipate a majority of the seismic energy demands on the system.

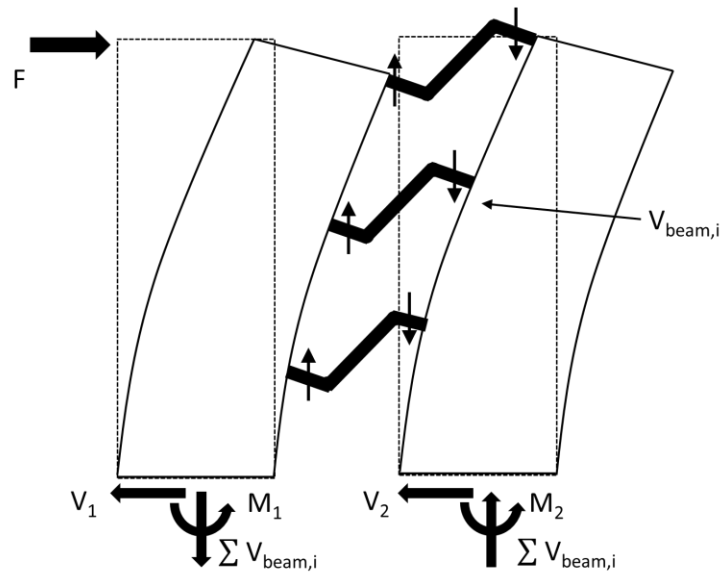


Figure 2.11 Force distribution in a coupled wall system.

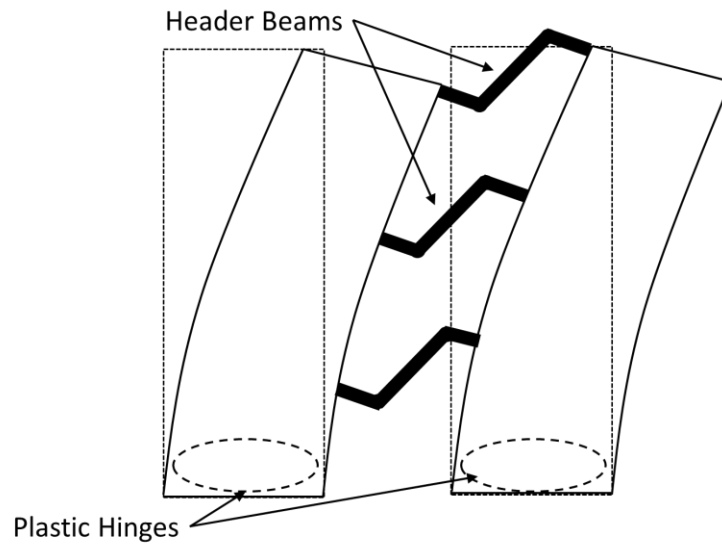


Figure 2.12 Yielding mechanism in a coupled wall system with well-detailed header beams.

2.4 Effect of Ground Motion Duration

A comprehensive state-of-knowledge review on the effect of ground motion duration on structural damage was compiled by Hancock and Bommer (2006). In this review, it was noted that the majority of experimental tests showed a high correlation between number of loading cycles and specimen damage (e.g.: Calado et al., 2002; Dutta and Mander, 2001; Manfredi and Pecce, 1997). In studies that rely on numerical methods, the conclusions were less clear: most studies using cumulative damage measures found a correlation between ground motion duration and structural damage (e.g.: Tang and Yao, 1972; Stephens and Yao, 1986; Chai, 2005); however, studies that used extreme responses (such as maximum interstory drift or displacement) generally did not find strong correlations between duration and damage (e.g.: Rahnema and Manuel, 1996; Iervolino et al., 2006; Cosenza et al., 2004). These results may be due to limitations in the numerical models used, which did not always properly account for cyclic strength and stiffness degradation.

More recently, several studies conducted in the OpenSees framework (McKenna et al., 2000) using models with strength and stiffness degrading plastic hinges, along with “leaning” P-Delta columns, have indicated that ground motion duration has a high importance when predicting structural collapse or damage. Two of these studies considered concrete moment frames (Chandramohan et al., 2016a; Raghunandan and Liel, 2013), while another used steel moment frames modeled with degrading plastic hinges (Chandramohan et al., 2016b). In the study done by Chandramohan et al. (2016b), spectrally equivalent long and short duration record pairs were considered in order to isolate the effect of duration from spectral shape. The results of these recent studies indicate that ground motion duration does have a large impact of structural collapse and

damage; however, these studies have focused on moment-resisting frames and the results have not been generalized for other structural systems.

Chapter 3: Mechanism and Effect of Ground Motion Duration

This chapter provides background information on the effect of ground motion duration on the performance of structural systems and the mechanism(s) by which it imparts these effects. The effect on different structural models and various deformation capacities is also considered. Also included is a review of different metrics that can be used to quantify ground motion duration, as well as a study intended to define an appropriate duration metric for use in later work.

3.1 Physical mechanisms

The physical mechanisms by which ground motion duration may affect the response of structures can be summarized into two main categories: cyclic degradation and ratcheting. These mechanisms are explained in the following sections.

3.1.1 Cyclic Degradation

The term “cyclic” in “cyclic degradation” comes from the fact that damage (and the resulting degradation) accumulates as a specimen is loaded, unloaded, and reloaded cyclically. This contrasts with “in-cycle” degradation in which degradation occurs during a single loading cycle as a specimen is displaced through yielding, peak strength (or “capping” strength), post-capping, and ultimately collapse or failure (see Figure 3.1).

Cyclic degradation can be broadly summarized into two types: strength and stiffness. Strength degradation refers to a systems loss in ability to resist peak loads after multiple cycles of damage. Stiffness degradation refers to a loss of stiffness (i.e. a constant force will produce larger displacement demands) that occurs due to damage. Most materials and systems exhibit some form of cyclic degradation. For example, cracking in reinforced concrete may cause stiffness degradation, while concrete loss due to spalling will cause both strength and stiffness degradation.

Nail pullout in plywood walls will lead towards a loss of both strength and stiffness as the structure becomes further damaged.

Ibarra et al. (2005) further subclassify cyclic degradation into four categories:

1. basic strength,
2. post-capping strength,
3. unloading stiffness, and
4. accelerated reloading stiffness degradation.

To describe the first two mechanisms, refer to the simple backbone curve (force vs. deformation) illustrated in Figure 3.1. Basic strength loss refers to the loss of peak (or “capping”) strength (force F_c), while post-capping strength loss refers to strength loss after the displacement at which peak force occurs (displacement Δ_c) is exceeded.

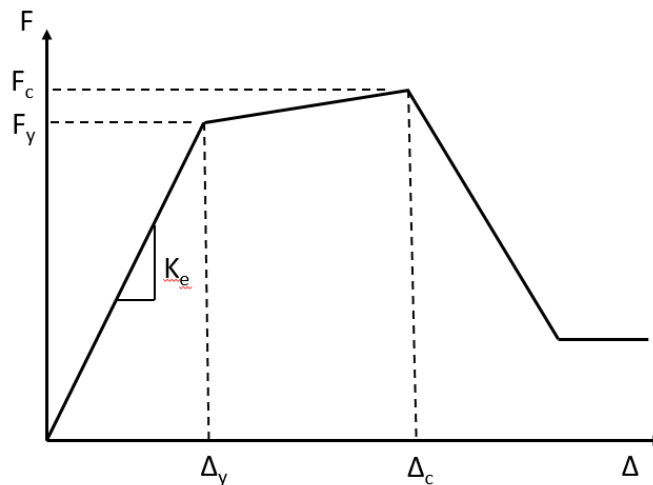


Figure 3.1 Simple bilinear backbone (pushover) curve with in-cycle strength degradation.

Next, consider the same system in Figure 3.2, which has been loaded until a displacement just past its capping displacement, unloaded, and then reloaded. The loss in unloading stiffness (K_u to K_u') from the first to second loading cycle illustrates unloading stiffness degradation. That is, as damage accumulates, the system will become softer when it is unloaded. The shift in yield

displacement (Δ_y to $\Delta_{y'}$) and resulting stiffness loss illustrates reloading stiffness degradation. As more damage accumulates the system will soften at an accelerated rate, hence the name: “accelerated reloading stiffness degradation”.

Additional loading and unloading cycles will result in further strength and stiffness degradation as shown in Figure 3.3.

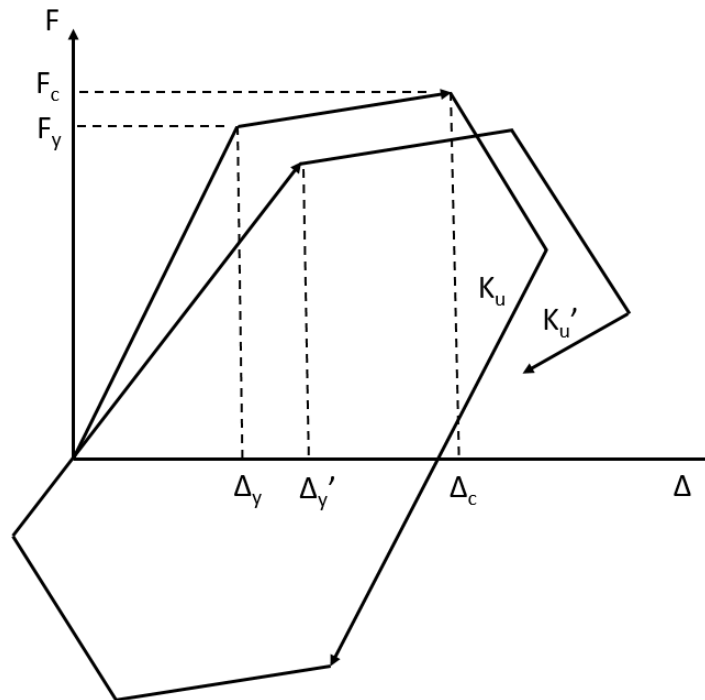


Figure 3.2 Simple bilinear backbone curve with strength and stiffness degradation.

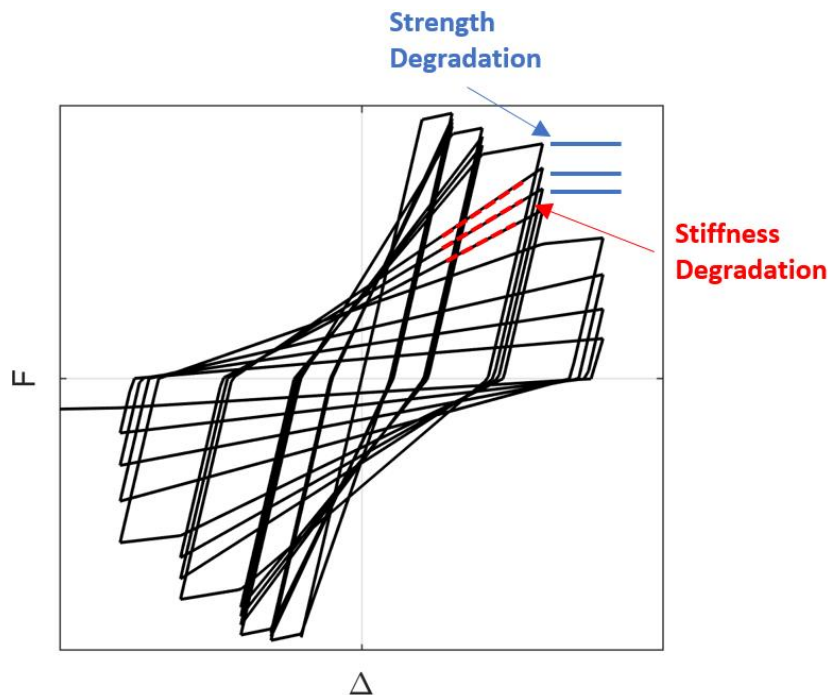


Figure 3.3 Cyclic pushover with strength and stiffness degradation.

Ibarra et al. (2005) used these parameters to develop three models: 1) a basic bilinear model; 2) a peak-orientated model; and 3) a pinching model. The bilinear model is a standard bilinear response with an elastic stiffness (K_e), a reduced post-yield stiffness to represent strain hardening, followed by a negative post-capping stiffness. The peak oriented model (often called a “Clough” model), proposed by Clough and Johnson (1966), is similar to a bilinear model, except that when reloading the system will tend towards the previous maximum displacement. This produces a stiffness loss dependent on maximum displacement rather than damage. Finally, the pinching model is like the peak-oriented model except that reloading consists of two parts with two stiffnesses and a break point in the middle. See Figure 3.4 for illustrations of these three basic models. These models have been incorporated into the OpenSees framework under the material models *Bilin*, *Clough*, and *ModIMKPinching*, respectively. Lignos (2008) and Ibarra and Krawinkler (2005) have successfully used these models to capture the experimental response of

reinforced concrete beams; Ibarra et al. (2005) also present calibrations to steel, reinforced concrete, and plywood experimental results.

Comparable hysteretic models have also been proposed by Sivaselvan and Reinhorn (2000) and Song and Pincheria (2000). These models typically base the amount of degradation on the total accumulated hysteretic energy through loading in both positive and negative directions (i.e. the total area under the force displacement curve, considering all cycles, to that point).

Lowes et al. (2003) developed a similar model to simulate the behavior of reinforced concrete frames under earthquake loading. Their model considers unloading, reloading, and strength degradation and uses either energy (area under the force-displacement curve) or cycles (total number of loading/unloading cycles) to define damage. This model uses a pinched backbone curve and is commonly used to simulate the behavior of reinforced concrete frames and other systems which exhibit a pinching behavior (Noh et al., 2017; Shen et al., 2013.; Ab-Kadir et al., 2014). It has been implemented into the OpenSees framework as the *Pinching4* material model.

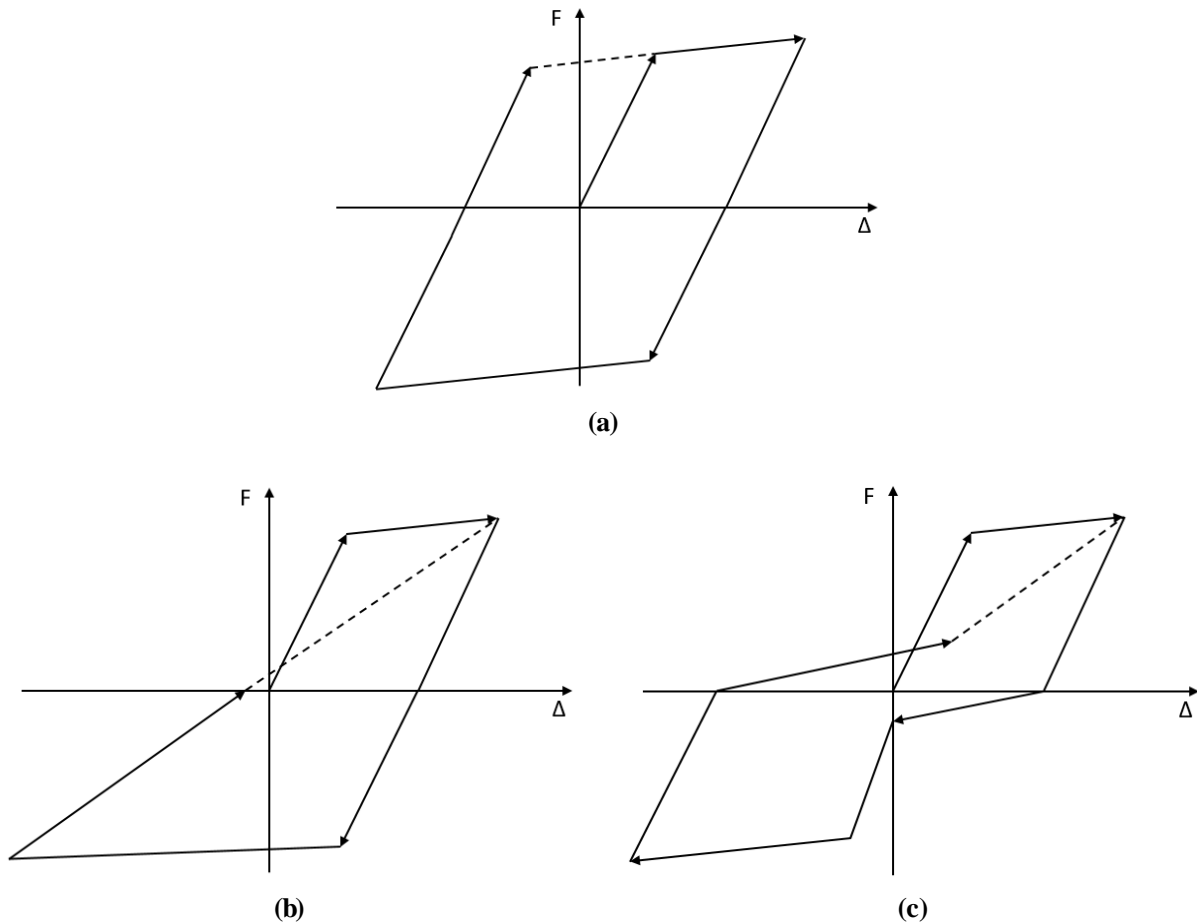


Figure 3.4 Hysteretic models: a) bilinear; b) peak-orientated (Clough); and c) pinching.

3.1.2 Ratcheting

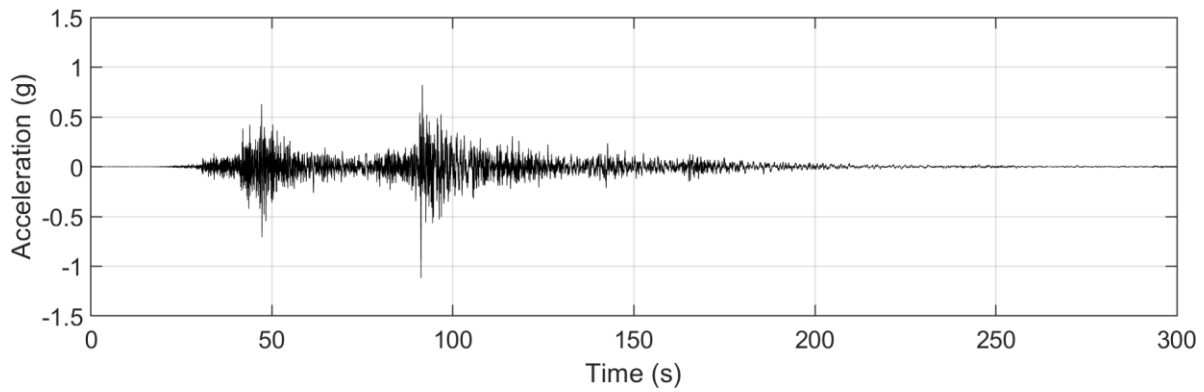
Another important contribution to cyclic degradation is the accumulation of displacement due to inelastic excursions in one direction combining throughout a loading cycle or length of earthquake shaking. This is commonly referred to as “ratcheting” (displacements tend to ratchet in one direction).

There are many physical mechanisms that can cause potential ratcheting. For example: slip in rebar at the foundation of a concrete wall. If a concrete wall is pushed past the point of foundation rebar slip, when the load is removed the wall will not center at its starting point. The

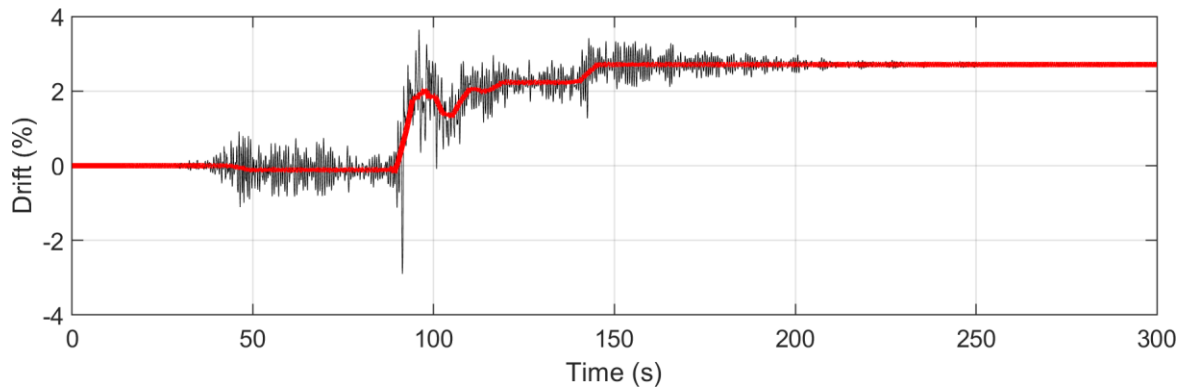
next loading cycle will then begin with an initial displacement. As the specimen continues to be loaded/unloaded these initial displacements will accumulate in one direction if the wall is not loaded symmetrically (such as under earthquake excitation).

Another example is slip along the failure plane of a concrete dam under earthquake loading. Since a dam has a constant water reservoir applying hydrostatic pressure in one direction, as it is excited during an earthquake, it will tend to slip in the direction of the reservoir pressure. Second order displacement (P-Delta) effects will amplify the accumulated ratcheting deformations.

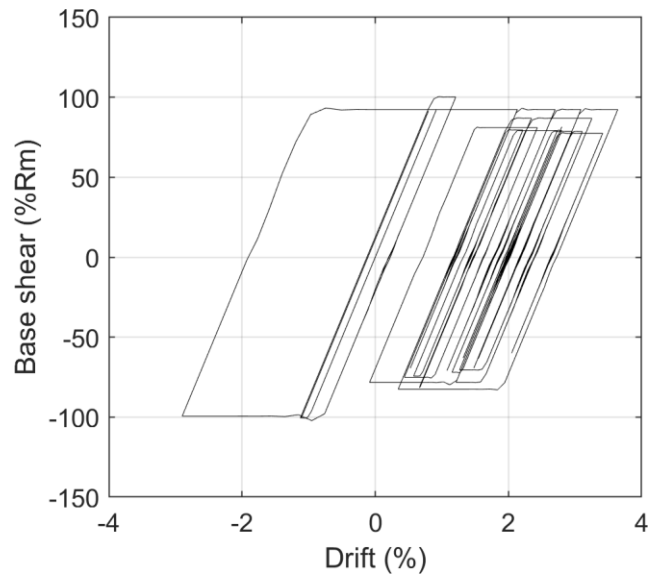
In Figure 3.5, a simple single degree of freedom (SDOF) numerical model of a concrete column was subjected to a motion from the 2011 Tohoku, Japan, earthquake (Figure 3.5a). The column was modelled with a rotational base hinge with a bilinear backbone curve. Second order effects were included through the use of a leaning (or “P-Delta”) column. Figure 3.5b illustrates the top drift time history response of the model; a moving mean of the response is highlighted in red. Figure 3.5c shows the drift vs. base shear (expressed as a percentage of the resistance, R_m , of the model) hysteretic response. Note that after the first major acceleration pulse in the motion (around 50 seconds into the shaking), the model does not return to baseline (zero displacement). With the P-Delta effect now acting on this displaced model, each further pulse (at ~100 and ~150 s) continue to push the model in this direction. The result is a much higher displacement demand than if the model was allowed to return to its baseline after each of the three major shaking pulses.



(a)



(b)



(c)

Figure 3.5 Ratcheting example: a) input acceleration time history; b) SDOF drift response time history (moving average in red); and c) SDOF drift vs. base shear response.

3.2 Intensity Measures

When defining “ground motion duration”, it is essential to determine an appropriate intensity metric to quantify the duration. Raw record length is arbitrary and is dependent on the trigger thresholds of the recording instrument; thus, a more appropriate metric should be selected. The duration metric and structural performance will be highly correlated. Many metrics have been proposed and utilized to quantify ground motion duration including:

- **Arias intensity (Ai):** a measure of the total energy contained in an accelerogram computed using integration of acceleration squared over the length of the record as:

$$Ai = \frac{\pi}{2g} \int_0^{t_{max}} a^2 dt$$

where g is acceleration due to gravity, t_{max} is the record length, and a is the acceleration time series (Arias, 1970). Arias Intensity involves computing an integral over the length of the record, and thus, is expected to relate to the length of strong shaking in the record.

- **Number of cycles:** a simple count of the number of direction reversal cycles in the complete time series. Directly related to the length of shaking.
- **Housner Intensity ($SI(\zeta)$):** a measure of earthquake intensity computed using the integral of the spectral velocity proposed by Housner (1952). Computed as:

$$SI(\zeta) = \int_0^{10} S_v(T, \zeta) dT$$

where $S_v(T, \zeta)$ is the spectral velocity, ζ is the level of damping used to compute the spectral velocity (usually taken as 5% critical damping), and T is the period of shaking. The integral is performed from $T = 0$ to 10 s.

Although the Housner Intensity does not integrate over time, longer duration records are expected to produce more shaking in the longer periods (which have more time to allow for the accumulation of more long period cycles), and thus, Housner Intensity may be indirectly related to shaking duration.

- **Root mean square (RMS) acceleration (a_{RMS}):** the square root of the area under the acceleration spectral density vs. frequency curve. The a_{RMS} is typically used as a measure of the energy contained in a random vibration event as is calculated as:

$$a_{RMS} = \sqrt{\frac{1}{f} \int_0^{f_{max}} ASD(f)^2 df}$$

where f is the frequency, f_{max} is the maximum useable frequency in the recording, and ASD is the acceleration spectral density.

Since the RMS acceleration is a measure of energy, it is expected to correlate to the length of shaking in a record.

- **Specific Energy Density (SED):** the integral of the velocity squared of the record computed over the record length; computed as:

$$SED = \int_0^{t_{max}} v(t)^2 dt$$

where v is the record velocity, and the other variables have been previously defined. Similar to Arias Intensity, it is computed using an integral over the record length; thus, it is expected to be highly correlated to the length of strong shaking of the record.

- **Significant duration:** the length of time over which a specific amount of energy in the record is accumulated, where energy is quantified as the integral of acceleration squared

(normalized Arias Intensity): $\int a^2 dt$. Commonly, ranges of 5 to 95% (d_{5-95}), 5 to 75% (d_{5-75}), or 25 to 75% (d_{25-75}) are used.

Figure 3.6 illustrates the 5-95% significant duration from a recording from the 2011 Tohoku, Japan, subduction interface earthquake. Figure 3.7 illustrates the significant duration for a recording from the 1994 Northridge shallow crustal earthquake.

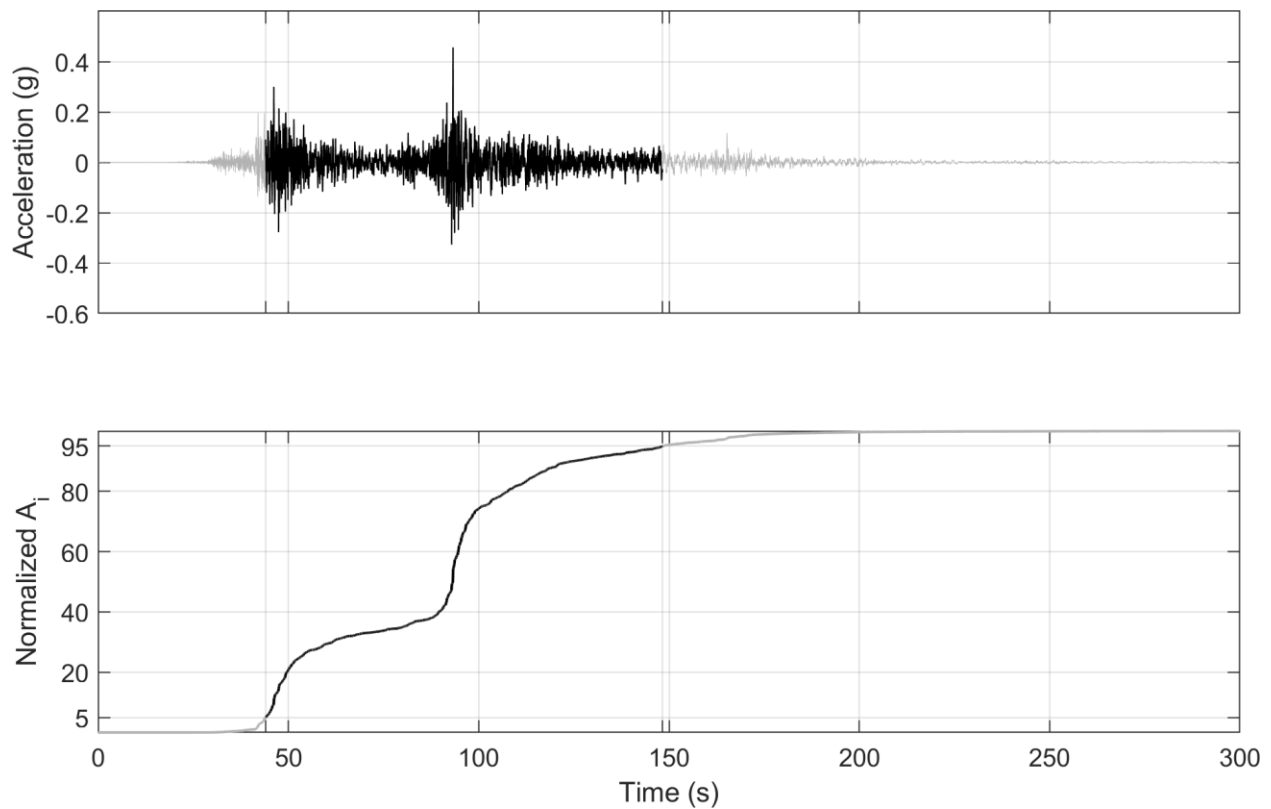


Figure 3.6 Illustration of significant duration (d_{5-95}) for Tohoku, 2011; station: MYG009-NS; $M_w = 9.1$; distance = 111 km; $d_{5-95} = 104.3$ s.

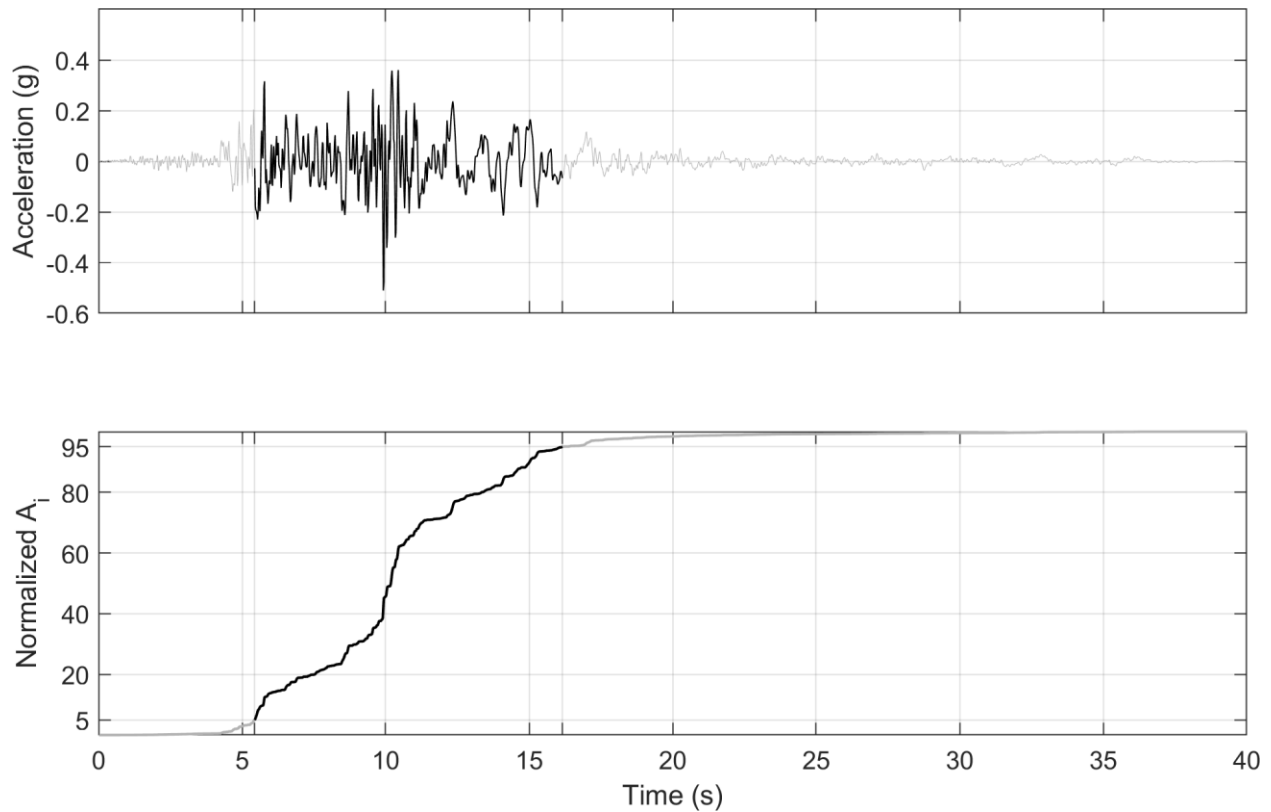


Figure 3.7 Illustration of significant duration (d_{5-95}) for Northridge, 1994; station: STM-360; $M_w = 6.7$; distance = 26 km; $d_{5-95} = 10.7$ s.

Other researchers have also compared different duration metrics. Chandramohan et al. (2013) compared bracketed duration, significant duration, Arias Intensity, cumulative absolute velocity (CAV), and a dimensionless metric proposed by Cosenza and Manfredi (1997) related to the peak ground acceleration (PGA), peak ground velocity (PGV) and energy ($\int a^2 dt$) of a record (I_D). They concluded that the most appropriate metric was significant duration (specifically 5-75% significant duration) as it was not strongly correlated with common intensity measures (such as spectral accelerations), is unaffected by linear scaling (thus does not need to be recomputed anytime a record is scaled), and does not bias spectral shape.

Bommer and Martinez-Pereira (1999) provide a thorough review different ground motion duration metrics. They classify common metrics into three main types: “bracketed durations”,

“uniform durations”, and “significant durations”. Bracketed durations are based on the time between first and last crossings of a specified threshold (usually acceleration). Uniform durations are defined by the amount of time shaking is above a specified threshold (e.g. length of time that $a^2 > a_{threshold}^2$). Both of these are highly sensitive to the threshold level selected and change as a record is linearly scaled, and thus were not considered in the work presented in this chapter. The authors later go on to define and recommend the effective strong motion duration (e.g. d_{5-95} ; as previously discussed).

3.3 Intensity Metric Study

A study was carried out to assess ground motion duration metrics using SDOF systems and a large suite of ground motion records. The objective was to find a metric that strongly correlated with structural instability of the model. The selected metric is intended be used in later work to quantify ground motion duration.

3.3.1 Ground Motion Database

The first step in this study was to select a ground motion database from which to select time history records. Time histories from the two major earthquake types: shallow crustal and subduction zone; should be selected to get a large range of shaking characteristics and motion durations.

Shallow crustal earthquakes comprise the major of most widely available ground motion databases. The most comprehensive and up-to-date database of shallow crustal events is the PEER Next Generation Attenuation (NGA) West-2 database (Ancheta et al., 2013). This database includes a large number of records from worldwide events and provides thorough event metadata such as distances, spectral values, and soil conditions. The PEER NGA West-2 database was used to search for and obtain crustal records.

At the time of writing, there is not such a comprehensive database exists for subduction zone (interface and intraslab) events. Thus, a database of subduction zone events was compiled including time histories and event metadata. Various databases and providers were queried for appropriate records, which included records from large subduction interface events and well recorded intraslab events. The most well recorded active subduction zones are Japan and Chile, and thus records from these networks provided the majority of the database.

Japanese records were obtained from the K-Net and Kik-Net databases, which provide records from the Japanese National research Institute for Earth Science and Disaster Prevention (NIED) network (<https://www.kyoshin.bosai.go.jp/>). The K-Net/Kik-Net databases also provide thorough metadata for each record including soil profiles and distance metrics (Kinoshita, 1998).

Chilean records were downloaded from the Center for Engineering Strong Motion Data (CESMD; <https://strongmotioncenter.org/>) which is a collaboration between the United States Geological Survey (USGS), California Geotechnical Survey (CGS) and the Advanced National Seismic System (ANSS). The CESMD provides raw and corrected time histories from worldwide earthquake events recorded by many different networks. The two major Chilean seismograph networks are the Geurrero Accelerograph Network, owned and operated by the University of Reno Nevada, and the Red de Cobertura Nacional de Acelerografos (RENADIC) network, which is owned and operated by the University of Chile. Both of these networks have recorded many events, however not all station information, particularity site classification or soil information, is known.

Several other events, including those from the Pacific Northwest, Indonesia, and Central America, were identified. Recordings from these events were obtained from the CESMD. Ultimately, over 2000 tri-directional records from 18 unique subduction zone events were compiled from various networks and databases. These events, including the number of records

from each event, are summarized in Table 3.1. Table 3.2 provides the owners, networks, and providers for these records.

Type	Event	Magnitude (M_w)	Year	# of Records
Interface	Hokkaido, Japan	8.0	2003	358
	Tohoku, Japan	9.1	2011	701
	El Maule, Chile	8.8	2010	28
	Michoacán, Chile	8.1	1985	13
	Iquique, Chile	8.2	2014	10
	S. Sumatra, Indonesia	8.4	2007	1
	Coquimbo, Chile	8.3	2015	9
	Valparaiso, Chile	7.8	1985	23
	Valparaiso, Chile	6.4	2014	5
	Tarapaca, Chile	7.9	2005	14
Intraslab	Geiyo, Japan	6.8	2001	316
	Guerrero, Mexico	6.6	1994	13
	Michoacán, Mexico	7.1	1997	14
	El Salvador	7.6	2001	14
	Miyagi-Oki, Japan	7.2	2005	456
	Puget Sound, Washington	6.7	1965	2
	Olympia, Washington	7.1	1949	2
	Nisqually, Washington	6.8	2001	37

Table 3.1 Subduction zone database event summary.

Event(s)	Owner	Network	Provider
All Japan	NIED ¹	K-Net/Kik-Net	NIED ¹
Guerrero, Michoacán 1997, Michoacán 1985	University of Nevada Reno	Geurrero Accelerograph Network	CESMD ²
El Salvador	Universidad Centro Americana		CESMD ²
El Salvador	Centro de Investigaciones Geotechnicas		CESMD ²
All Washington	USGS		CESMD ²
Nisqually	University of Washington	Pacific Northwest Seismic Network	CESMD ²
El Maule	University of Chile	RENADIC	CESMD ²
Iquique	University of Chile	RENADIC	CESMD ²
Iquique	IRIS – Global Seismographic Network		CESMD ²
S. Sumatra	Caltech		CESMD ²

¹National research Institute for Earth Science and Disaster Prevention (<https://www.kyoshin.bosai.go.jp/>)

²Center for Engineering Strong Motion Data (<https://strongmotioncenter.org/>)

Table 3.2 Subduction zone database event owners and providers.

For large subduction interface events, the most appropriate distance metric is the closest distance, which is the closest distance from the rupture plane of an event to the recording station. For these large-magnitude events, the rupture plane is very large, and thus, the closest distance is a better distance metric than others such as hypocentral or epicentral distances, which assume a point source rupture and may be more appropriate for smaller magnitude events with small rupture areas. Neither K-Net/Kik-Net nor the CESMD provide the closest distance for their recordings, and thus it was computed using one of two methods:

- 1) Estimated – the rupture area was estimated using relationships proposed by Strasser et al. (2010). The rupture area was assumed to be circular and placed at the depth of the event. The closest distance from the station to this rupture area was then calculated.

- 2) GSI – The finite fault model of the event from GSI (Geospatial Information Authority of Japan) was adopted. The closest distance to the model rupture was calculated based on the fault model and its distance to the recording stations.

The second method was only possible for the 2011 Tohoku and 2003 Hokkaido subduction interface events for which finite fault information was available; for the other events, the first, more approximate, method had to be used.

All records in the database were corrected through baseline correction and filtering. Most records provided by the CESMD were corrected and filtered by their respective owners, and thus did not require further processing; however, those that were not were baseline corrected with a linear function and filtered using a 4th order band-pass Butterworth filter with cut-off frequencies of 0.10 and 25 Hz (cut-off periods of 10 and 0.04 s). Most records did not require any additional processing.

3.3.2 Ground Motion Selection and Scaling

A suite of 200 motions of various event types were selected from the complete database (crustal and subduction) and scaled to the 2015 Victoria, Site Class C, 2% in 50 year uniform hazard spectrum (UHS). This record suite was prepared for a different study; however, since only the relative differences in scaling are of interest, the specific locality (Victoria) is not important in this investigation. The records and scale factors were chosen to minimize the mean squared error (MSE) between the suite geomean and target spectrum using the algorithm developed by Baker and Jayaram (2011). The suite spectra and geomean are illustrated in Figure 3.8. A complete list of records is tabulated in Appendix A. Note that in this table, that the distance reported for subduction interface (Sd) events is the closest distance while the distance reported for crustal (Cr) and subduction intraslab (Scr) events is the hypocentral distance, as this distance is more

commonly available and a suitable surrogate for these smaller magnitude events. Some of the events do not list a V_{s30} if this was not known for the record at that time. The names listed in Appendix A refer to the ID given to the record in the database and includes the event name, station code, and direction information. In total, the suite comprised 150 shallow crustal records, 46 subduction interface records, and 4 subduction intraslab records.

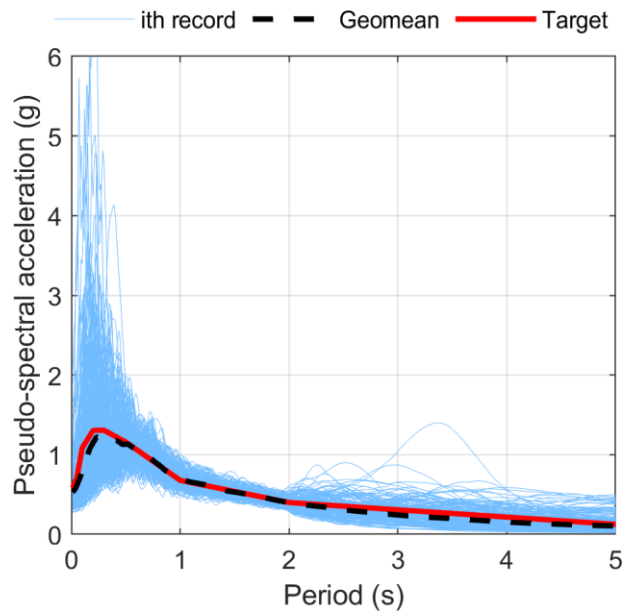


Figure 3.8 Suite of 200 motions linearly scaled to the 2% in 50 year Victoria Site Class CUHS.

3.3.3 SDOF Model

A nonlinear SDOF model was developed in the OpenSees framework (McKenna et al., 2000). The model features a column with a mass on its top and a single nonlinear shear spring at its midpoint. The rest of the column is rigid and fixed at its base. The column is connected through hinges to a “leaning” or P-Delta column, on which the gravity load is applied. The P-Delta column is used to model second-order P-Delta effects.

The backbone curve (force vs. shear deformation) of the hinge is a degrading bilinear model with no strain hardening as illustrated in Figure 3.9. The yield displacement is fixed at 1% of the model's height. The yield force is fixed at 9.5% of the weight of the model. The length of the plateau from yielding to the onset of in-cycle strength loss (μ) characterizes the ductility capacity and as set to 8% for this study. Collapse of the model is defined when the drift reaches 0.5% past the onset of strength loss. This simple model is used for the general study of collapse capacity with respect to ground motion duration and is not intended to represent a specific type of structural system or component.

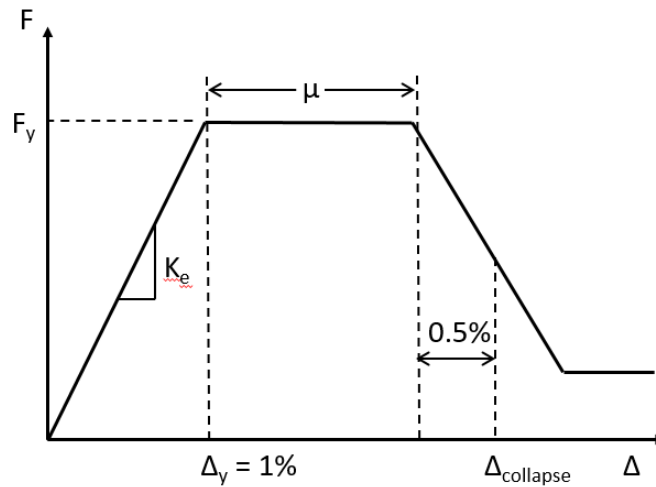


Figure 3.9 Degrading bilinear backbone curve used in the SDOF model.

3.3.4 Analysis and Results

Incremental dynamic analysis (IDA; Vamvatsikos and Cornell, 2002) was performed using the suite of 200 ground motions summarized in Figure 3.8 and Appendix A. The ground motions were scaled from 10% of their initial scaling in 10% increments until collapse was observed. As previously mentioned, collapse was defined as a drift level the exceeded 0.5% past the onset of in-

cycle strength loss. This “collapse scaling level”, expressed as a percentage of the initial scaling, was recorded for each motion.

The collapse scaling level was compared to the Arias Intensity, number of cycles, Housner intensity, RMS acceleration, specific energy density, and 5-95% significant duration of the initially scaled records (see Section 3.2 for a discussion of these metrics). No bracketed or uniform durations were considered since these would change based as the records were increasingly scaled during the IDA. Either a linear or second order exponential curve was fit to the collapse scaling level vs. duration metric result. The R^2 value of the fit, which explains how much the collapse scaling level is dependent on the duration metric, was then computed.

Three different hysteretic models were considered: a bilinear model, a peak-orientated model, and a pinching model (see Figure 3.4). The Ibarra-Medina-Krawinkler implementations of these models were used (*Bilin*, *Clough*, and *ModIMKPinching* material models in OpenSees). Cyclic strength and stiffness degradation were modelled using a lambda of 35 (Ibarra et al., 2005). The results for these three models are presented in Figure 3.10, Figure 3.11, and Figure 3.12, respectively.

For each hysteretic model, the Housner intensity and RMS acceleration do a poor job of predicting the collapse scaling level. This makes sense since these metrics are computed from the spectral velocity and acceleration spectral density curves, respectively, not integration over the record time histories.

The Arias Intensity and number of cycles provide a better correlation between collapse and duration, however their R^2 values are quite low (always less than 0.5). The best metrics for the three hysteretic models were the specific energy density and 5-95% significant duration, both of which involve integration of the record’s time history. The significant duration had a higher R^2 for

the bilinear and peak-orientated models, while the specific energy density had a higher value for the pinching model results.

From this study it can be concluded that duration metrics obtained from integration of the length of a time history are most correlated with the collapse of the SDOF model. This holds true independent on the hysteretic model considered, as long as cyclic degradation is included in the numerical model.

Chandramohan et al. (2013) identified three additional benefits to significant duration as a duration metric: 1) it is not strongly correlated to common intensity measures (such as spectral accelerations); 2) it is unaffected by linear scaling; and, 3) does not bias spectral shape. Due to the results of this study and these additional benefits, significant duration (specifically 5-95% significant duration) will be the main ground motion duration metric for further work.

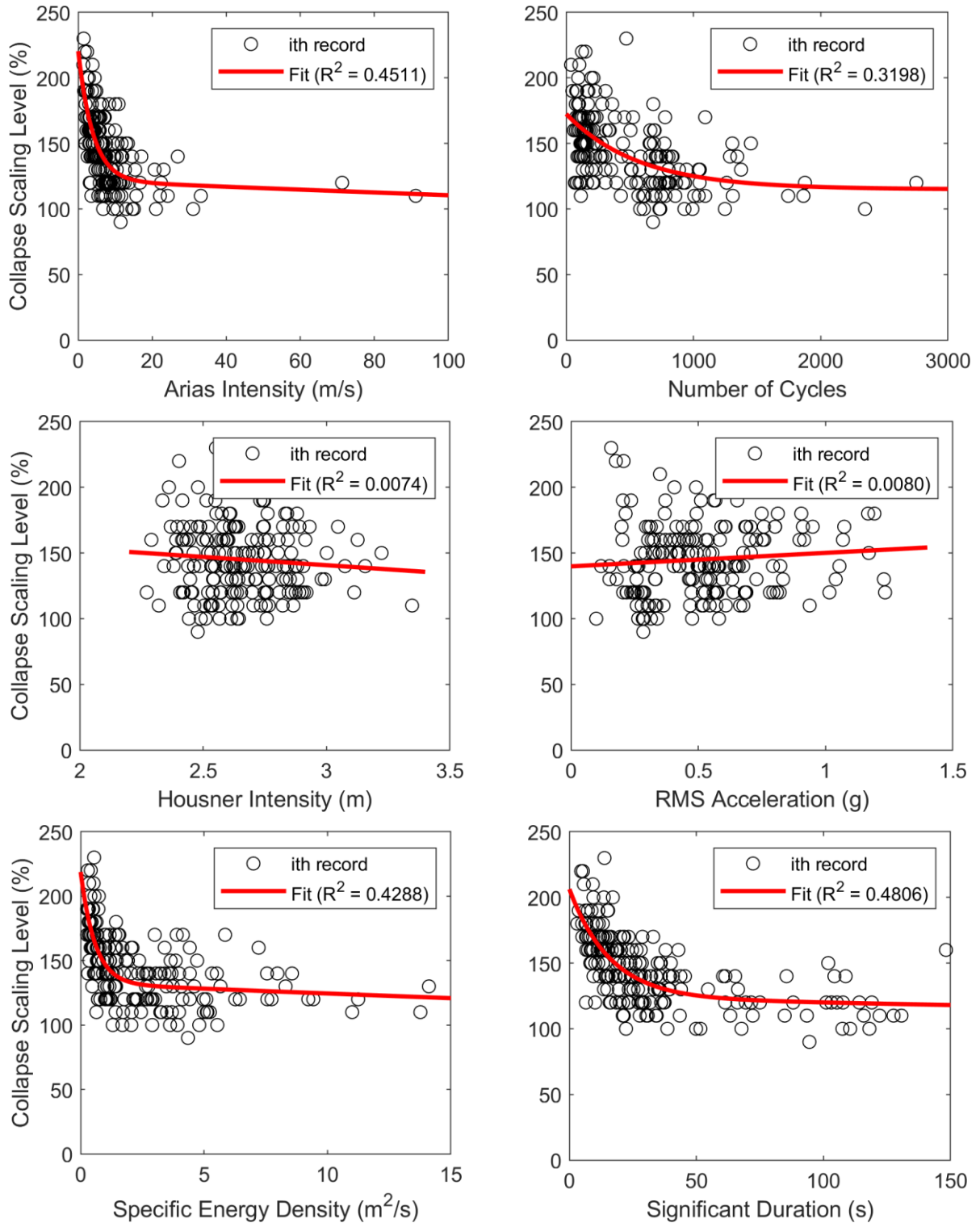


Figure 3.10 Collapse scaling level for bilinear degrading system with different duration metrics ; from top left to bottom right: Arias intensity, number of cycles, Housner intensity, RMS acceleration, specific energy density, and 5-95% significant duration

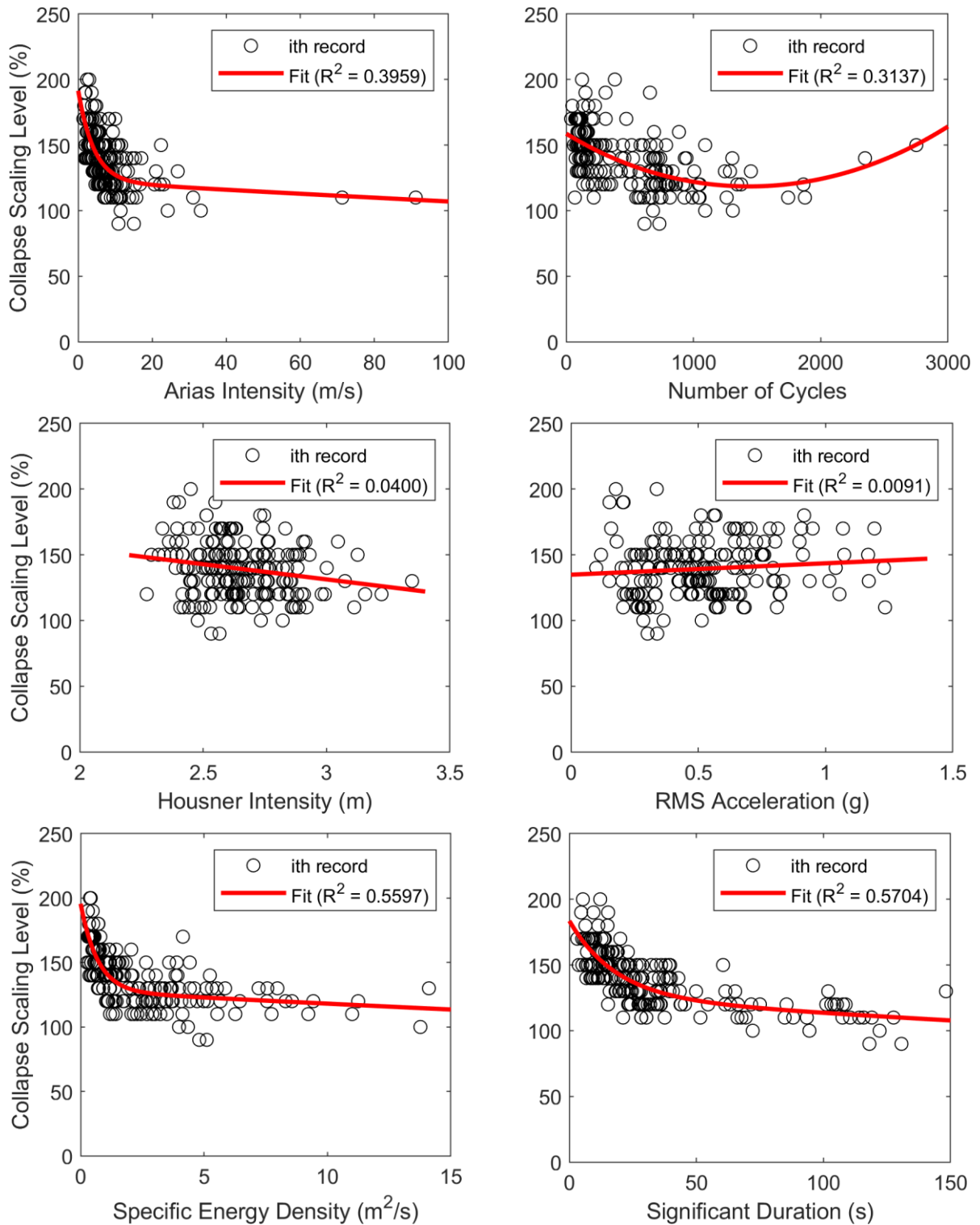


Figure 3.11 Collapse scaling level for peak-orientated degrading system with different duration metrics; from top left to bottom right: Arias intensity, number of cycles, Housner intensity, RMS acceleration, specific energy density, and 5-95% significant duration

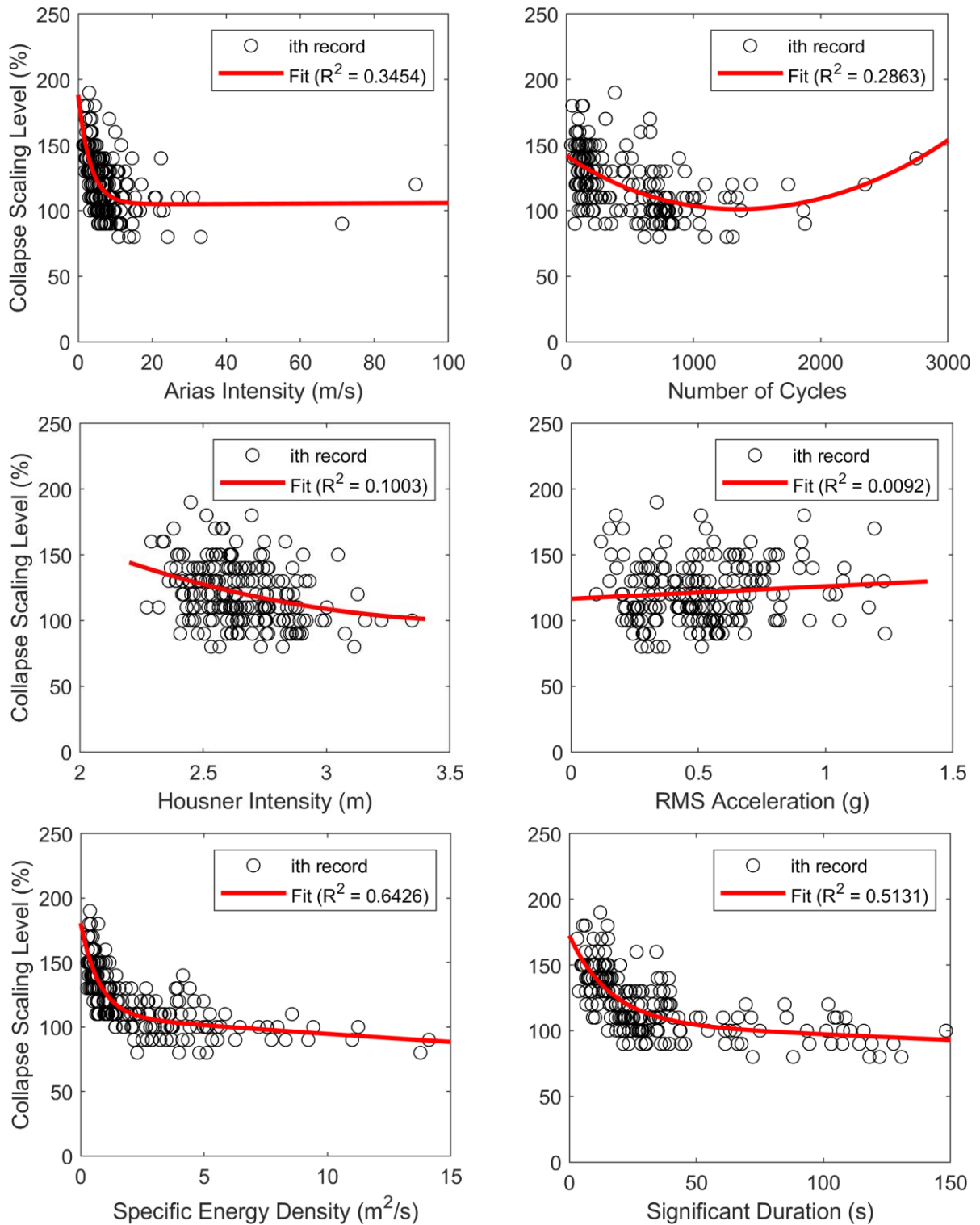


Figure 3.12 Collapse scaling level for pinching degrading system with different duration metrics; from top left to bottom right: Arias intensity, number of cycles, Housner intensity, RMS acceleration, specific energy density, and 5-95% significant duration

3.4 Effect of Ductility

The interplay of system ductility capacity (ability to deform past yielding) and ground motion duration was also investigated. Raghunandan and Liel (2013) identified that as a system's ductility demand (amount of deformation past yielding imposed by a load) increases, the larger effect ground motion duration has on the collapse risk of the system. This makes intuitive sense: a brittle (low or no ductility capacity) system will collapse suddenly during a ground motion if the motion is sufficiently intense. However, a very ductile system will withstand the many pulses of a long duration record, accumulating damage throughout the entire shaking time. The collapse of the ductile system will be strongly related to how much damage is accumulated through cyclic degradation.

The study presented in this chapter aims to further the understanding between the relationship between ground motion duration, system ductility, and system collapse.

3.4.1 Ground Motion Selection and Scaling

Two suites of 20 motions was selected and linearly scaled to the 2015 Victoria, Site Class C, 2% in 50 year UHS. One suite comprised shallow crustal motions, while the other comprised large-magnitude subduction interface records. These two suites are illustrated in Figure 3.13 with metadata, including significant duration, summarized in Table 3.3 and Table 3.4, respectively.

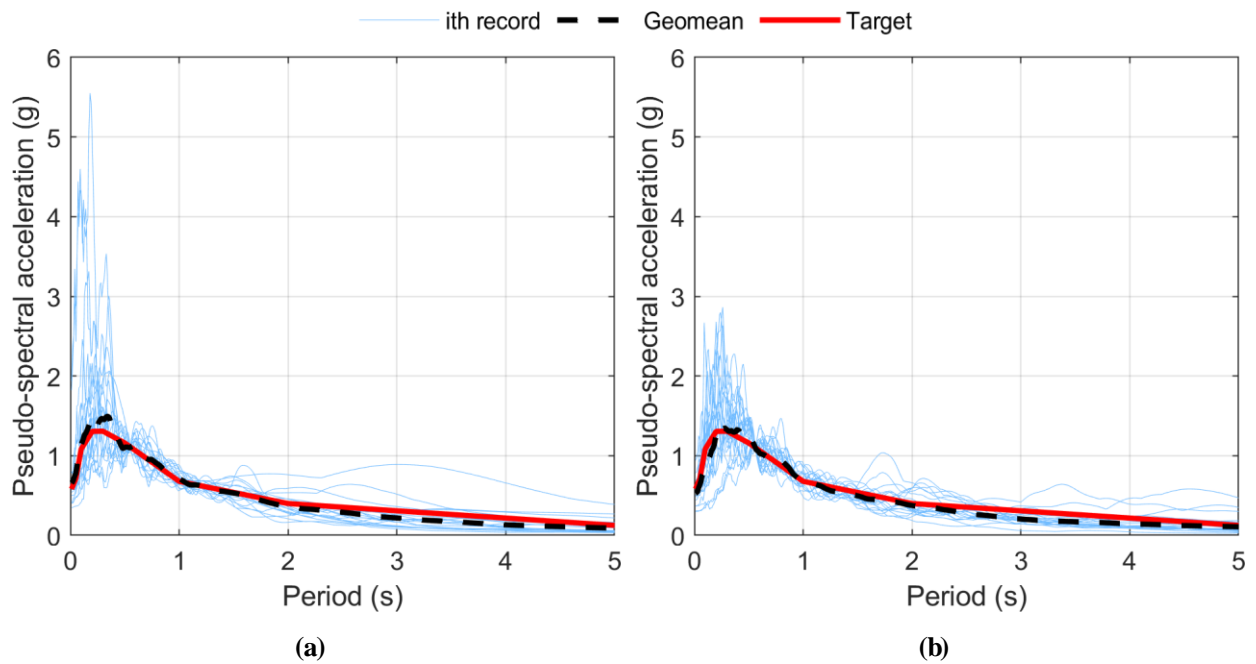


Figure 3.13 Two suites of 20 linearly scaled motions; a) crustal suite; and b) subduction suite.

Name	Scale Factor	Magnitude (M_w)	Distance (km)	V_{s30} (m/s)	d_{5-95} (s)
BAJA_CPE161	1.41	5.50	7.0	660	3.1
PALMSPR_DSP000	2.36	6.06	15.1	345	6.6
IMPVALL_H-E03140	2.16	6.53	30.3	163	11.9
KOBE_TAZ000	0.78	6.90	42.6	312	4.6
CAPEMEND_RIO270	1.49	7.01	24.6	312	15.3
IMPVALL_H-BRA315	2.26	6.53	44.3	209	14.0
NORTHR_STC180	0.87	6.69	17.8	281	10.6
CHICHI_TCU089-E	1.97	7.62	10.7	553	24.1
NORTHR_JEN022	1.29	6.69	21.8	373	6.9
NORTHR_0655-022	1.29	6.69	21.8	526	6.9
ERZIKAN_ERZ-EW	1.21	6.69	12.7	275	7.4
CHICHI_TCU067-N	1.23	7.62	29.8	434	23.0
IMPVALL_H-E08230	1.73	6.53	29.8	206	5.8
NAHANNI_SI010	1.77	6.76	10.5	660	7.9
NORTHR_CCN090	2.41	6.69	26.7	278	13.2
CHICHI_TCU101-E	2.08	7.62	45.8	273	19.0
NORTHR_SYL360	0.74	6.69	24.2	441	5.3
ITALY_B-CTR270	2.12	6.20	13.9	600	20.0
IMPVALL_H-E06230	1.79	6.53	29.2	203	8.5
IMPVALL_H-DLT352	1.83	6.53	35.2	275	50.3

Table 3.3 Crustal suite metadata.

Name	Scale Factor	Magnitude (M_w)	Distance (km)	V_{s30} (m/s)	d_{5-95} (s)
Hokkaido_HKD0750309260450-NS	1.68	8.00	110.2	422	14.9
Tohoku_MYG0091103111446-EW	1.67	9.10	111.3	954	101.9
Tohoku_TCG0071103111446-NS	3.94	9.10	117.5	765	63.8
Hokkaido_HKD0790309260450-NS	3.45	8.00	116.2	245	79.4
Hokkaido_HKD0770309260450-NS	1.79	8.00	81.6	249	38.6
Tohoku_AKT0161103111446-NS	3.44	9.10	183.8	217	115.4
Michoacan_CALE8509_191_N00W	2.88	8.10	15.0	800	24.2
Tohoku_IBR0091103111446-EW	3.89	9.10	155.3	322	93.9
Maule_stgopenalolen1002271-EW	2.13	8.80	176.5	452	34.2
Tohoku_CHB0171103111446-EW	3.83	9.10	201.6	281	94.4
Tohoku_TKY0241103111446-NS	2.81	9.10	177.5	-	108.7
Tohoku_SIT0031103111446-EW	2.55	9.10	163.6	122	119.0
Tohoku_NIG0121103111446-NS	3.68	9.10	193.6	287	110.5
Tohoku_TKY0051103111446-NS	3.59	9.10	218.6	352	67.8
Tohoku_GNM0081103111446-NS	3.92	9.10	186.3	410	61.3
Hokkaido_HKD1080309260450-EW	3.69	8.00	80.8	320	38.9
Tohoku_CHB0281103111446-NS	3.01	9.10	168.9	-	66.4
Tohoku_TKY0051103111446-EW	3.94	9.10	218.6	352	74.0
Tohoku_CHB0101103111446-EW	2.95	9.10	139.1	282	58.3
Tohoku_YMT0071103111446-EW	3.92	9.10	148.9	371	108.7

Table 3.4 Subduction interface suite metadata.

3.4.2 SDOF Model

The same SDOF model described in Section 3.3.3 was used for this study. The only difference is that the ductility parameter (μ in Figure 3.9) was varied from 2 to 8. For all analyses, the yield drift was fixed at 1%, and the yield shear force was fixed at 9.5% of the model weight. Collapse was defined as a drift past 0.5% of the strength loss drift (i.e. 1% yielding + μ + 0.5%).

3.4.3 Analysis and Results

For each ductility value, an IDA was performed using the two suites of motions illustrated in Figure 3.14 for a bilinear degrading system with a ductility capacity of 8. The median collapse scaling level and its standard deviation was recorded for each suite; these values were used to compute a lognormal collapse probability cumulative distribution function (CDF; see Figure 3.15).

The lognormal CDF curves for the basic bilinear model ($\lambda = 35$ for a moderate amount of cyclic degradation) for ductilities of 3-8 are presented in Figure 3.16. The median collapse scaling levels for each ductility capacity level are summarized in Figure 3.17. From this figure it can be seen that at lower ductility levels, the median collapse scaling level is similar between the two suites. This indicates that the ground motion duration is not significantly affecting the collapse of the model. However, at higher ductilities, the difference between the two becomes more apparent: the crustal suite requires significantly higher scaling to reach the same probability of collapse. This means that the longer subduction records are causing more damage, and thus, earlier collapse compared to the shorter crustal records. Figure 3.21 presents the probability of collapse at the 100% scaling level for each suite. Once again, the difference between the suites increases with the system ductility, with the crustal suite producing lower probabilities. These figures show that the longer duration subduction records are more damaging and likely to induce collapse at any given shaking level and produce at higher collapse risk when aggregating multiple shaking levels.

This analysis was repeated for a bilinear system with increased rate of cyclic degradation ($\lambda = 20$; bilin20) in Figure 3.19, Figure 3.20, and Figure 3.21; for a bilinear system with decreased rate of cyclic degradation ($\lambda = 50$; bilin50) in Figure 3.22, Figure 3.23, and Figure 3.24; and a bilinear system with no degradation ($\lambda = \text{infinity}$) in Figure 3.25, Figure 3.26, and Figure 3.27. As the amount of degradation decreases; from $\lambda = 20, 35, 50$ to infinity; the changes between the two suites tend to decrease. That is: with more degradation the ground motion duration tends to have a larger impact on the collapse probabilities of the system. This effect is further amplified as the ductility capacity of the system increases. When there is no degradation, the duration of the suite has almost no effect on the collapse probability no matter what system ductility is considered.

Figure 3.28 illustrates a simple cyclic pushover curve for each of the four bilinear models with different rates of cyclic degradation ($\lambda = \text{infinity}, 50, 35, \text{ and } 20$). The model had a yielding shear force equal to 9.5% of its weight (%W), a yield drift of 1.0%, and a ductility (μ) of 6. The cyclic loading comprised three cycles at each of six drift levels: 0.5, 1.0, 1.5, 2.0, 3.0, and 4.0% (Figure 3.28e).

Figure 3.29, Figure 3.30, and Figure 3.31 present the results for degrading peak-orientated system with moderate cyclic degradation ($\lambda = 35$); Figure 3.32, Figure 3.33, and Figure 3.34 present results for a pinching system ($\lambda = 35$). These results tend to agree with those presented for the bilinear degrading system, indicating that these observations hold true independent of cyclic behavior as long as degradation is considered. Figure 3.35 illustrates the cyclic pushover curves for the peak-orientated and pinching models ($\lambda = 35$, yielding force = 9.5%W, yield drift = 1.0%, and $\mu = 6$).

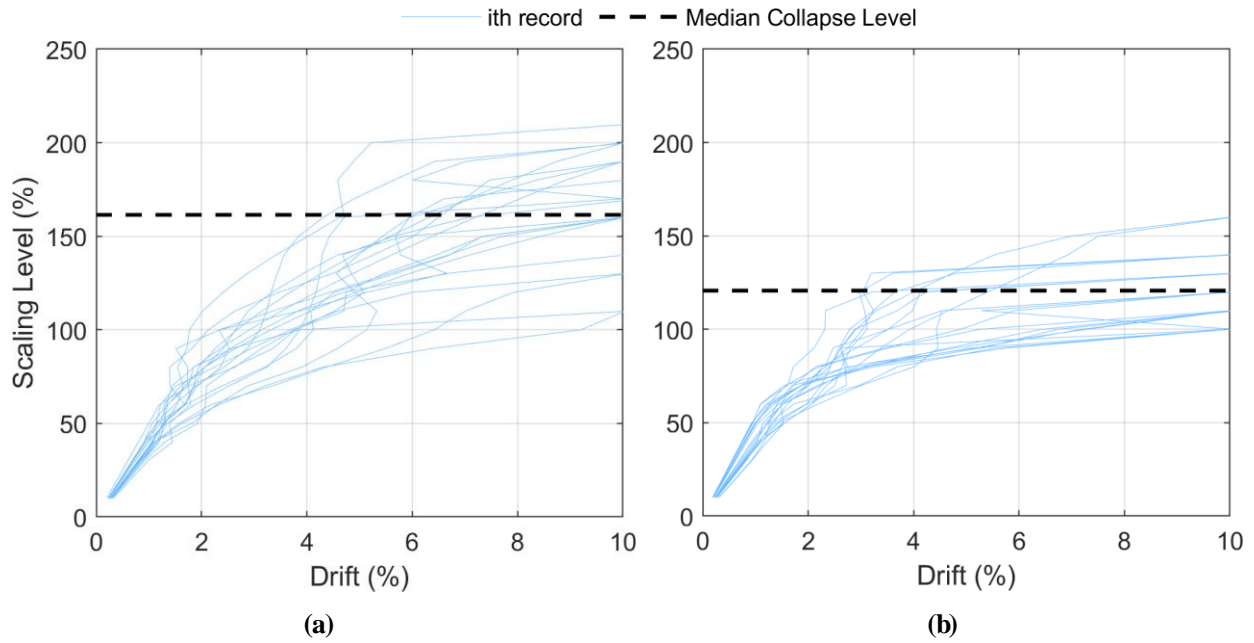


Figure 3.14 IDA curves for bilinear degrading system with ductility = 8: a) crustal suite; and b) subduction suite results.

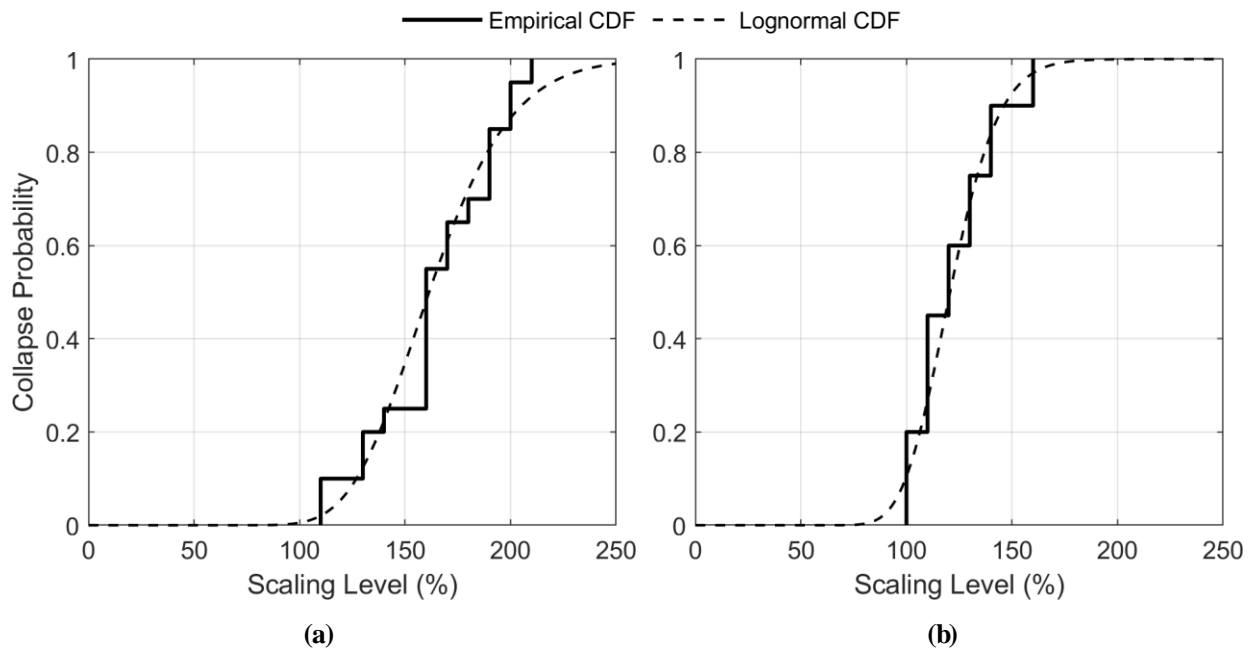


Figure 3.15 Empirical and lognormal cumulative distribution functions for bilinear degrading system with ductility = 8: a) crustal suite; and b) subduction suite results.

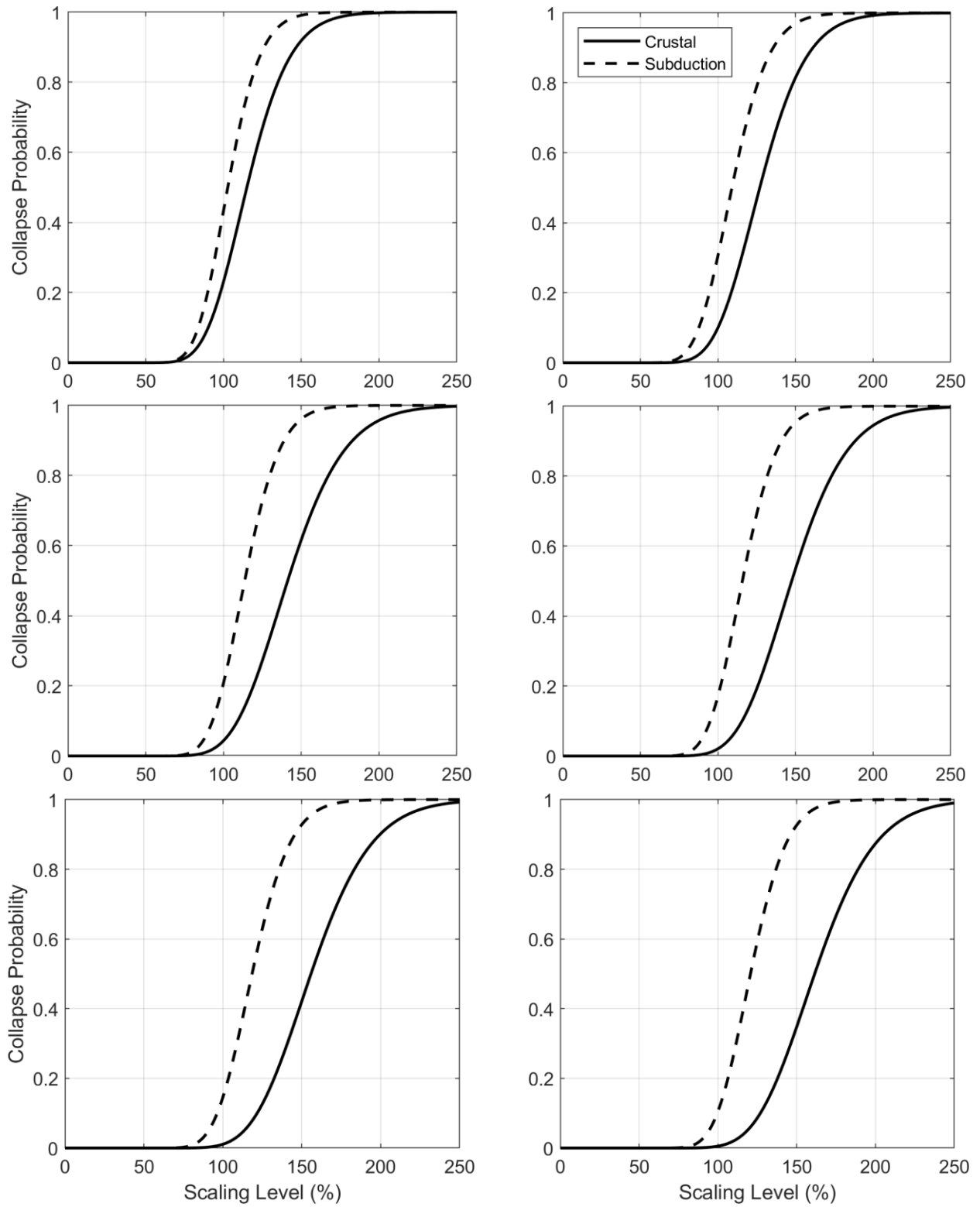


Figure 3.16 Collapse CDF for bilinear degrading system with (from top left to bottom right) ductility = 3, 4, 5, 6, 7, 8.

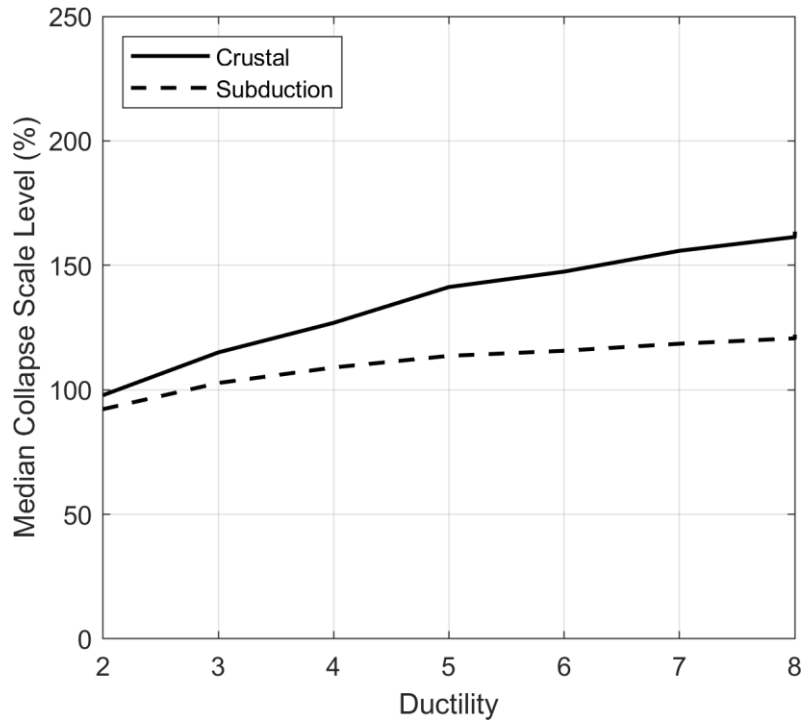


Figure 3.17 Mean collapse scale level for bilinear degrading system vs. level of ductility.

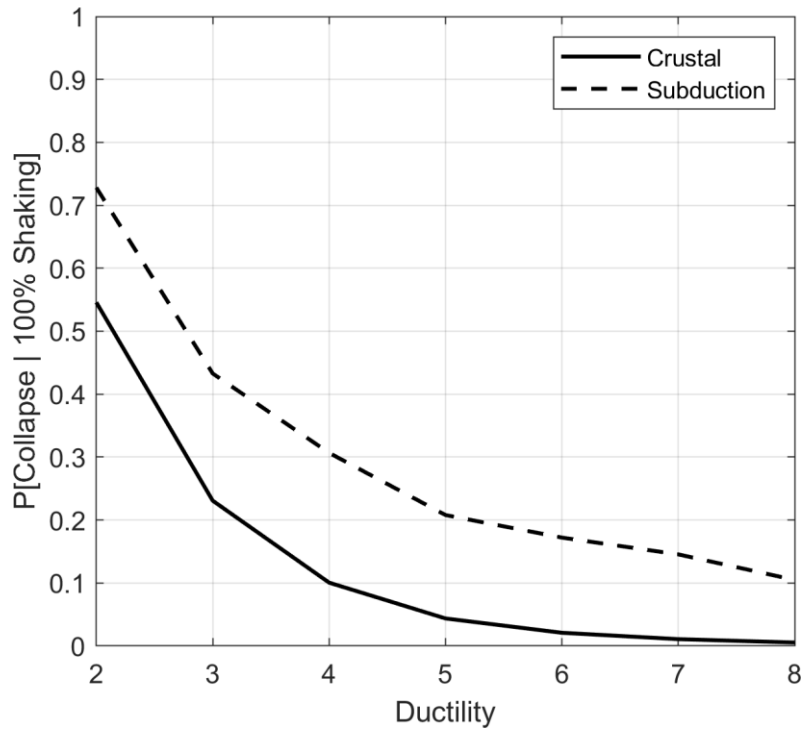


Figure 3.18 100% shaking level probability of collapse for bilinear degrading system vs. level of ductility.

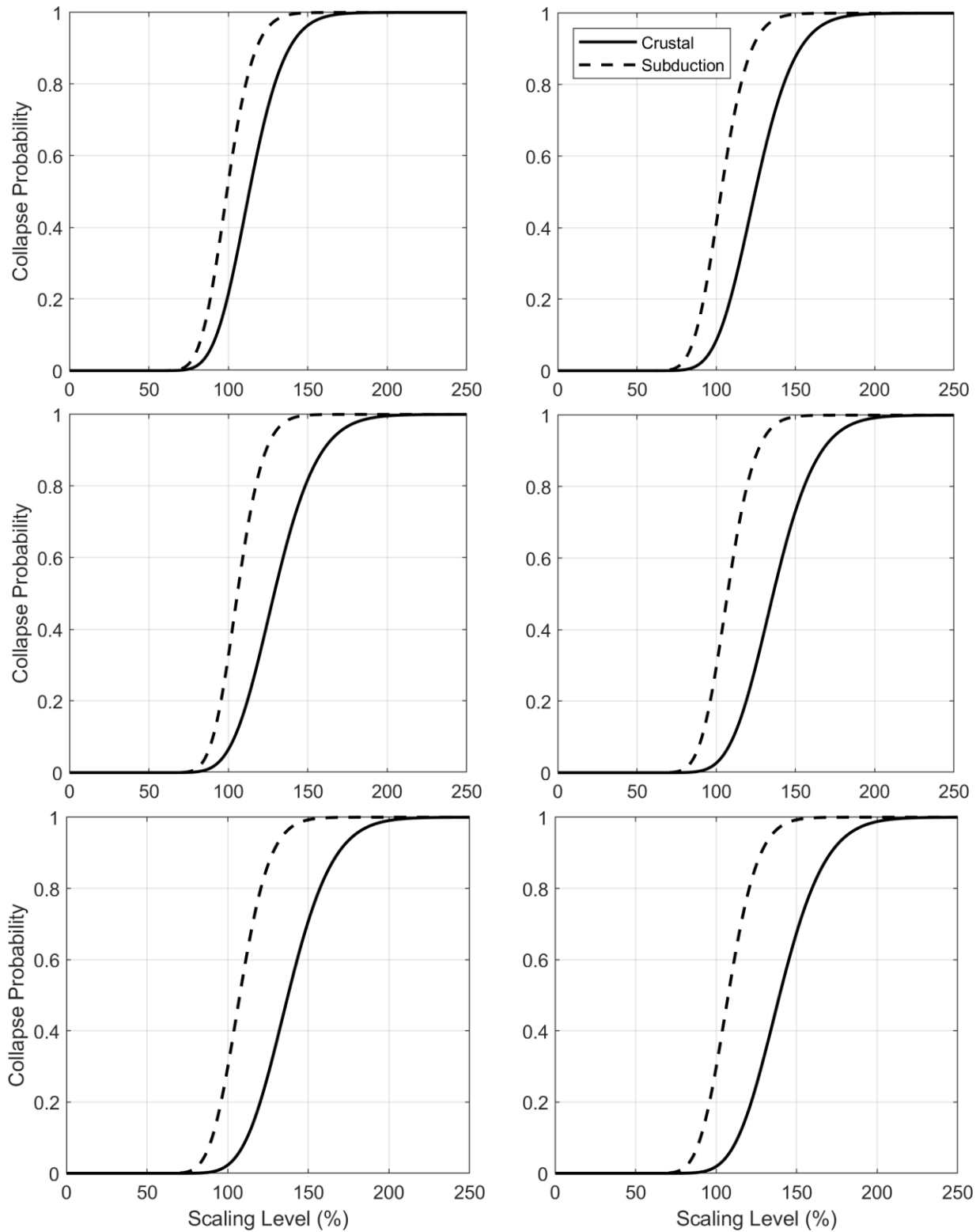


Figure 3.19 Collapse CDF for bilinear20 degrading system with (from top left to bottom right) ductility = 3, 4, 5, 6, 7, 8.

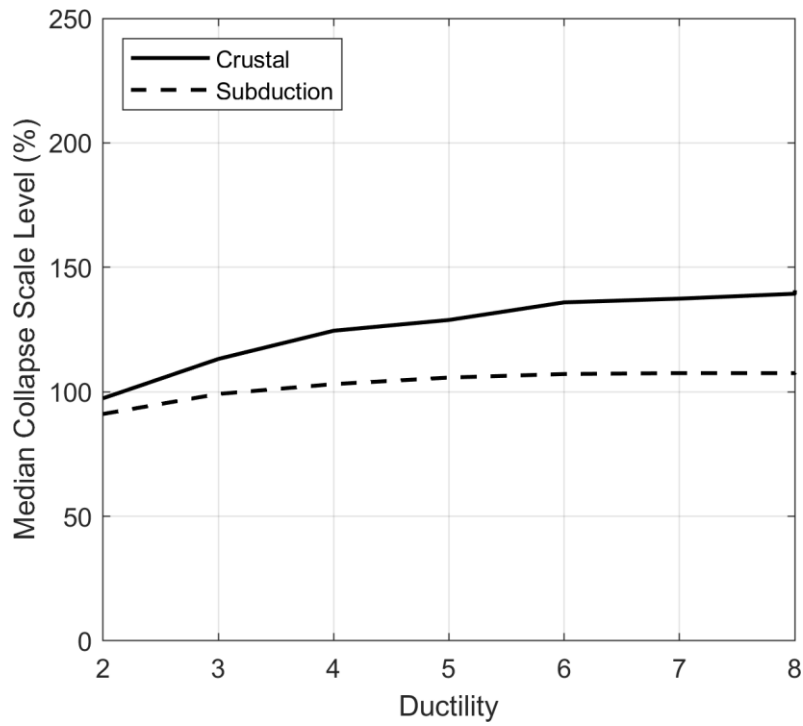


Figure 3.20 Median collapse scale level for bilinear20 degrading system vs. level of ductility.

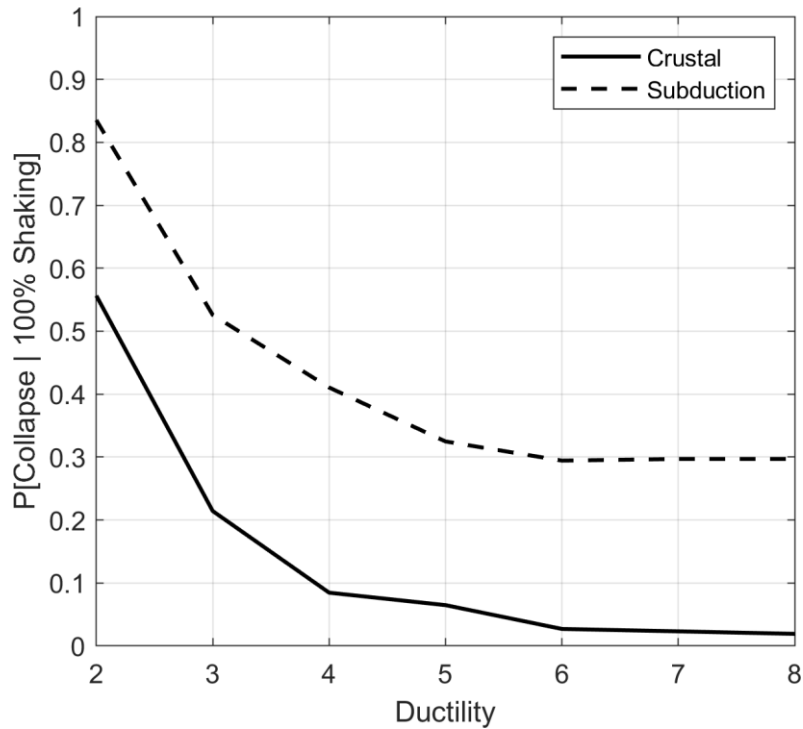


Figure 3.21 100% shaking level probability of collapse for bilinear20 degrading system vs. level of ductility.

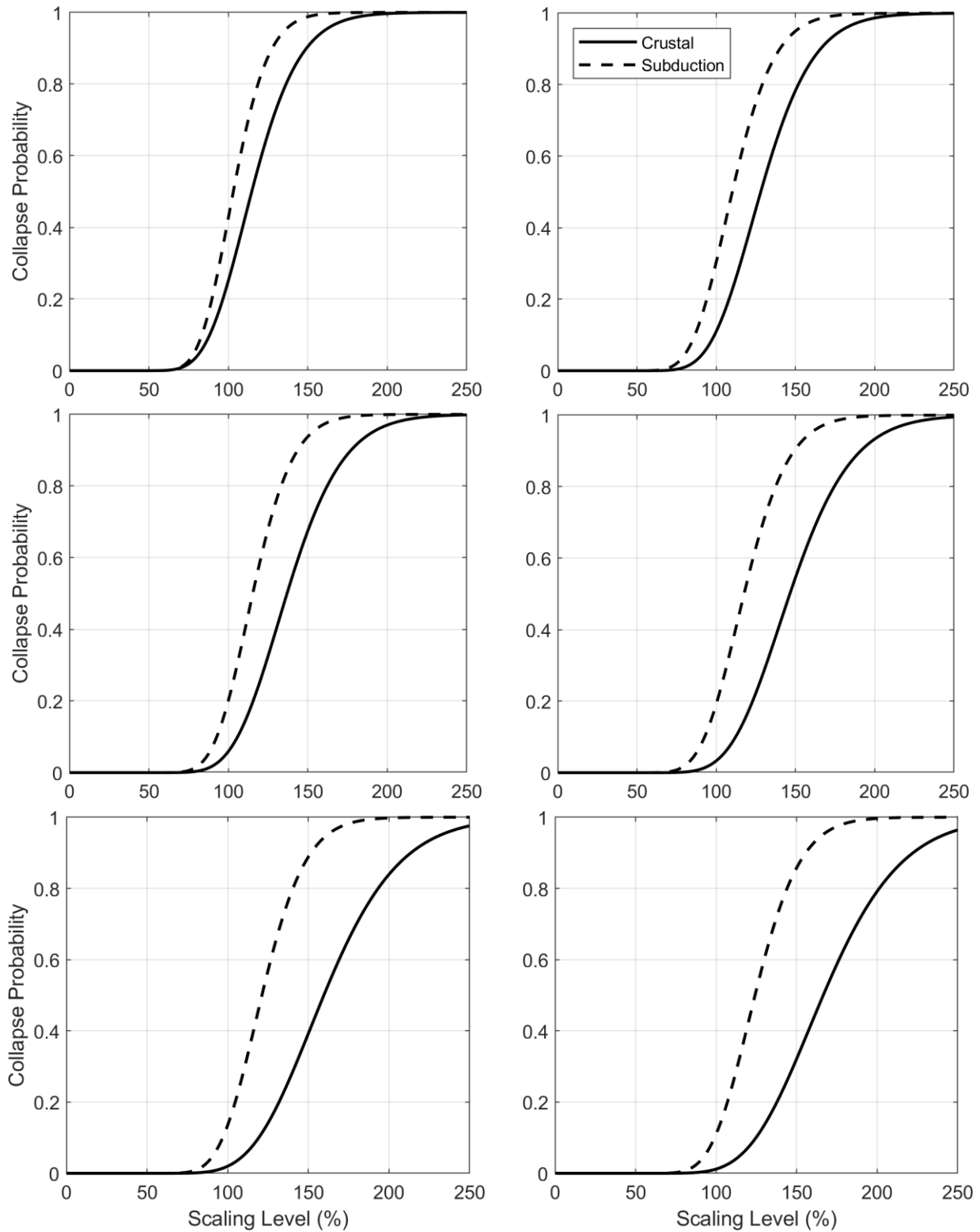


Figure 3.22 Collapse CDF for bilinear50 degrading system with (from top left to bottom right) ductility = 3, 4, 5, 6, 7, 8.

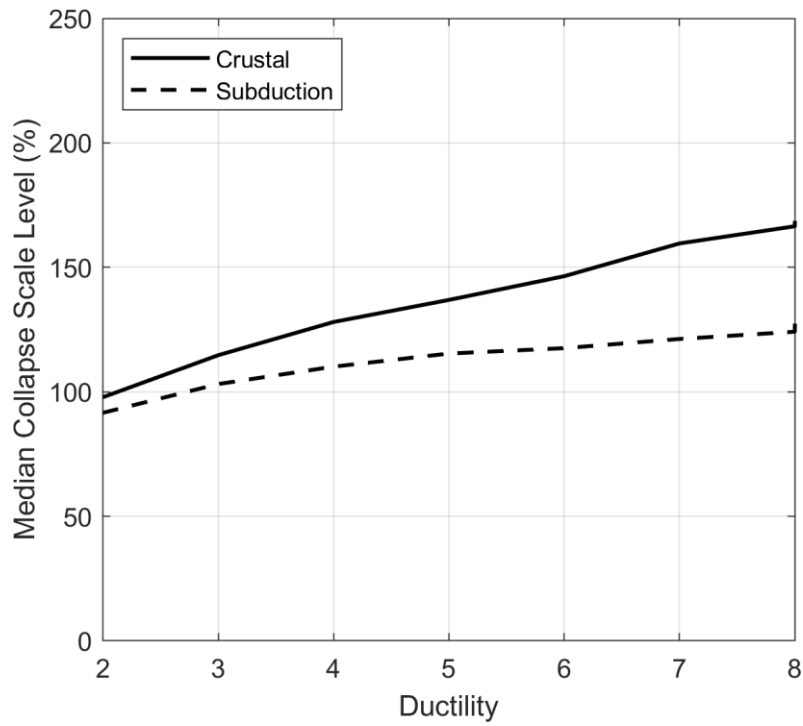


Figure 3.23 Median collapse scale level for bilinear50 degrading system vs. level of ductility.

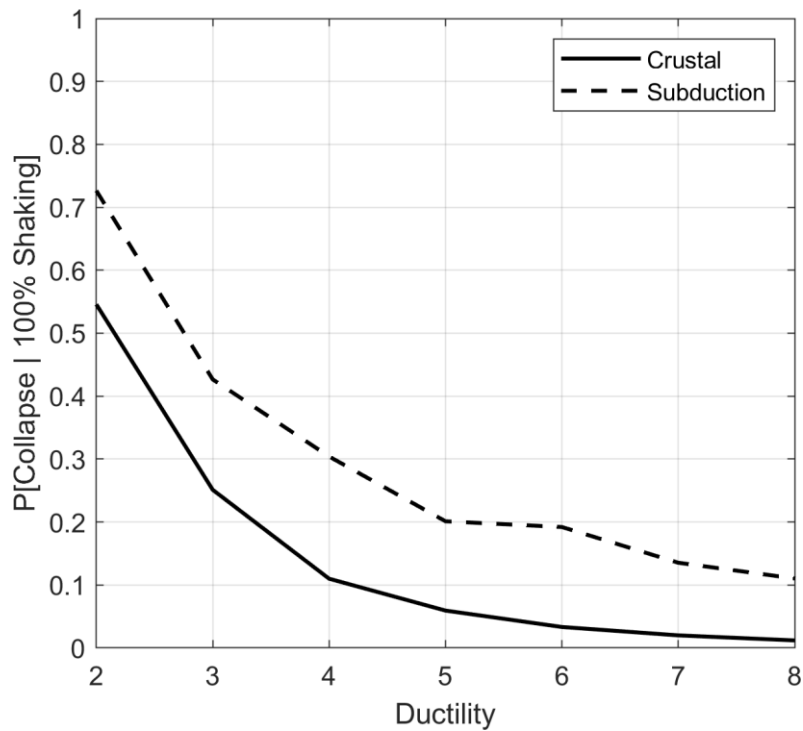


Figure 3.24 100% shaking level probability of collapse for bilinear50 degrading system vs. level of ductility.

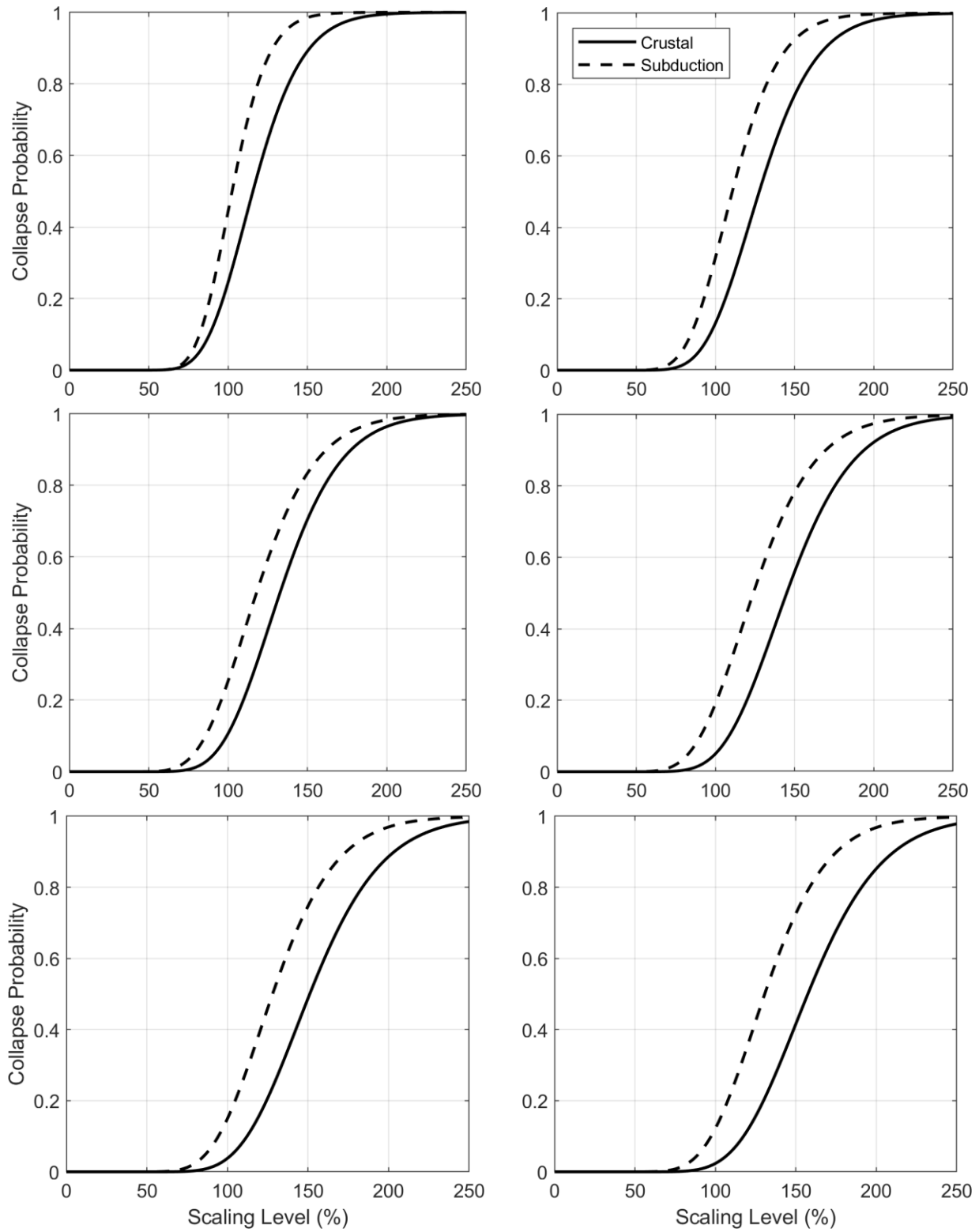


Figure 3.25 Collapse CDF for bilinear non-degrading system with (from top left to bottom right) ductility = 3, 4, 5, 6, 7, 8.

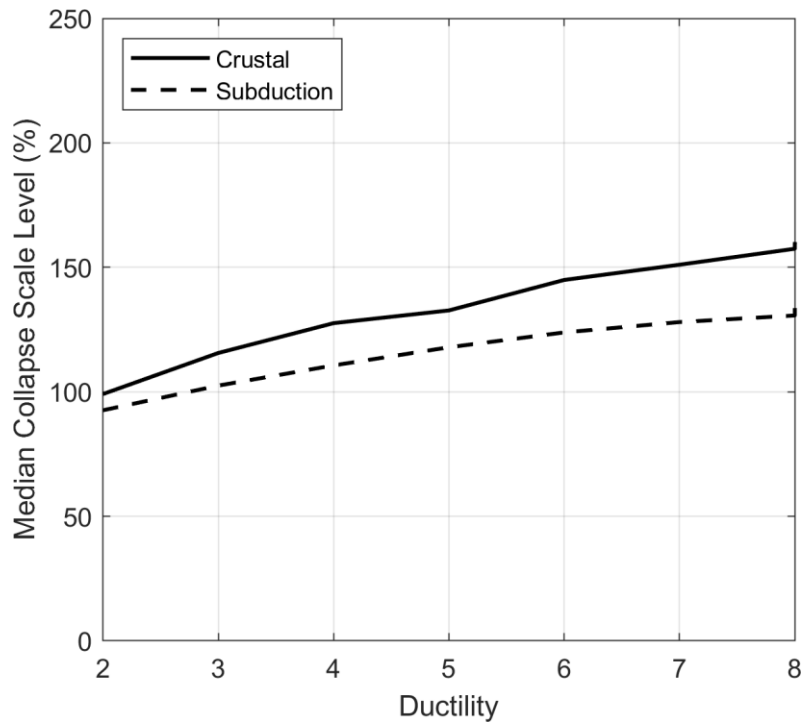


Figure 3.26 Median collapse scale level for bilinear non-degrading system vs. level of ductility.

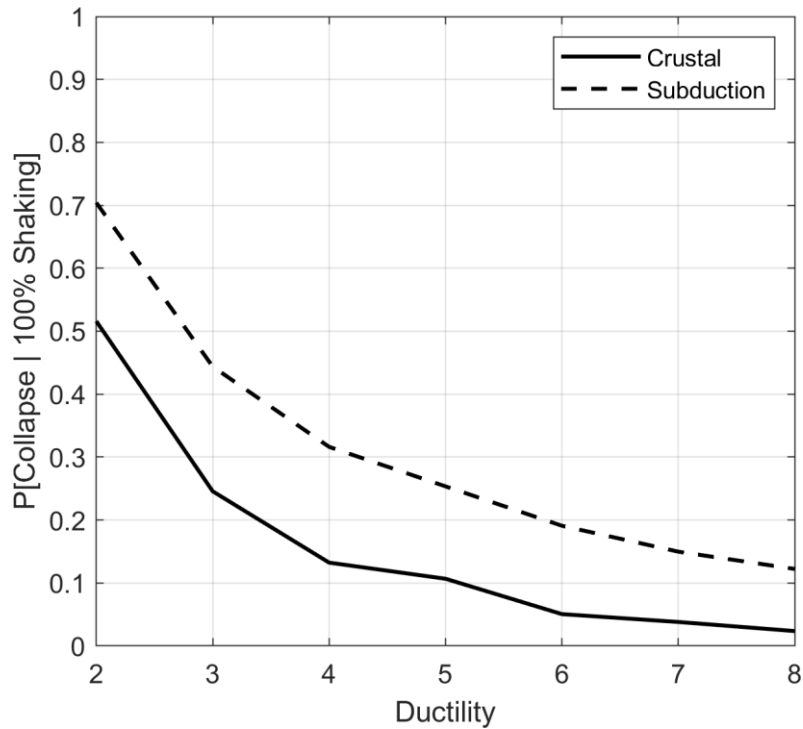


Figure 3.27 100% shaking level probability of collapse for bilinear non-degrading system vs. level of ductility.

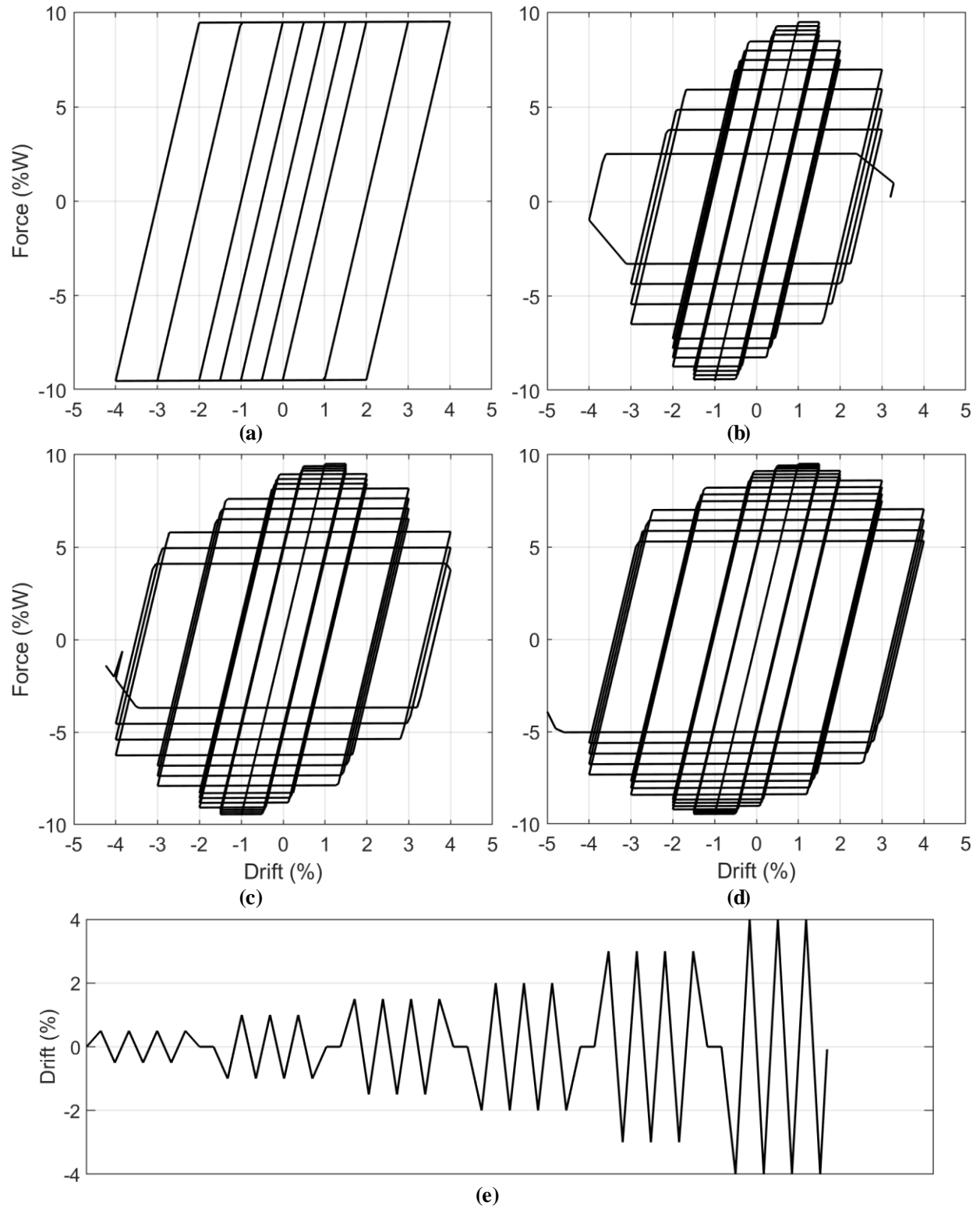


Figure 3.28 Cyclic pushover curves for bilinear systems with $\lambda =$ a) infinity, b) 20, c) 35, and d) 50, and e) cyclic loading protocol.

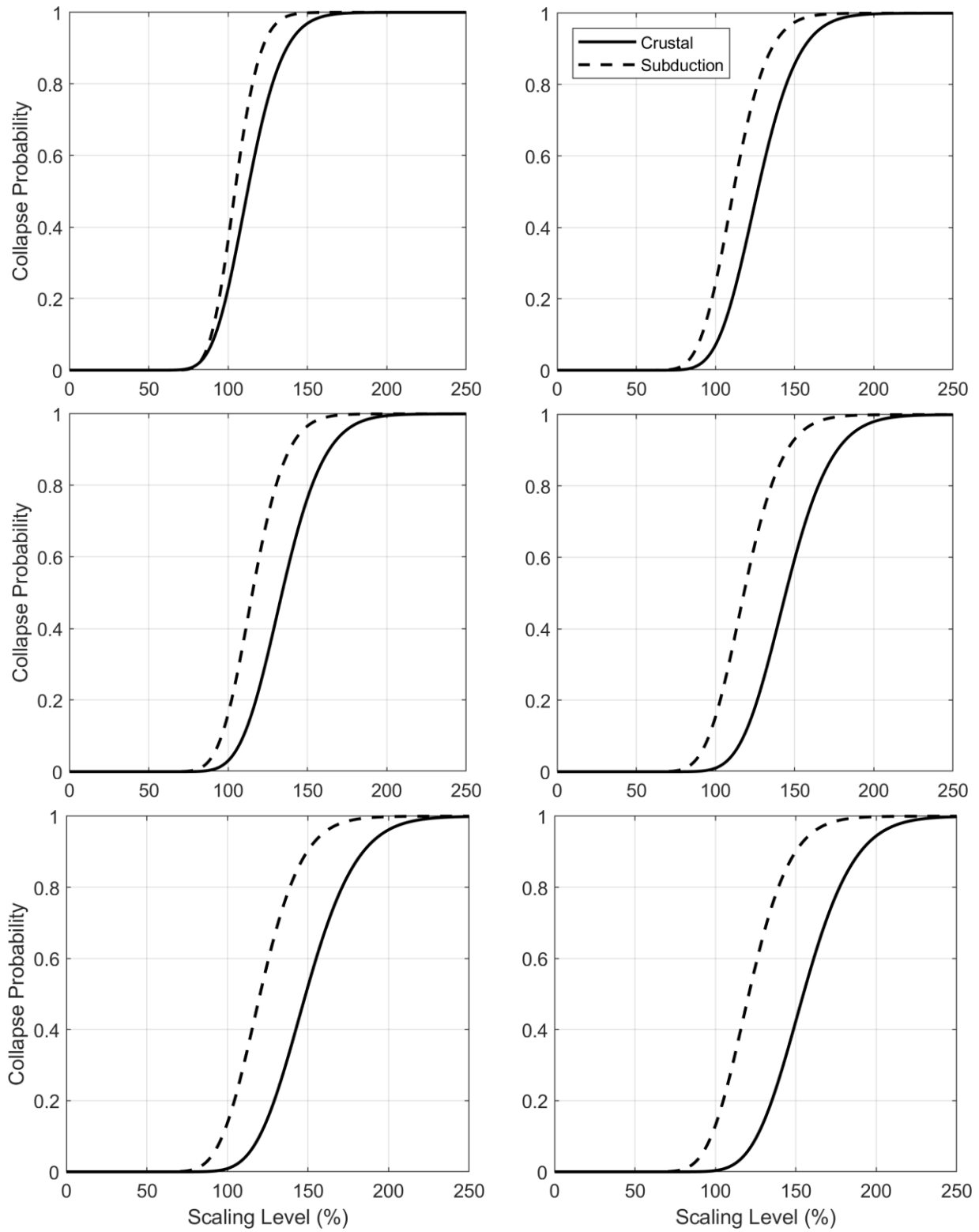


Figure 3.29 Collapse CDF for peak-orientated degrading system with (from top left to bottom right) ductility = 3, 4, 5, 6, 7, 8.

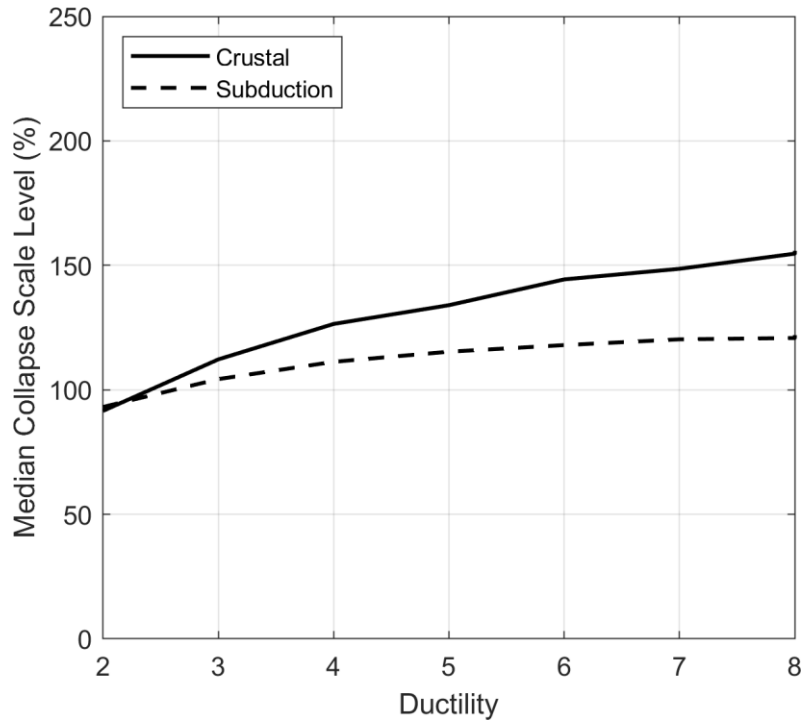


Figure 3.30 Median collapse scale level for peak-orientated degrading system vs. level of ductility.

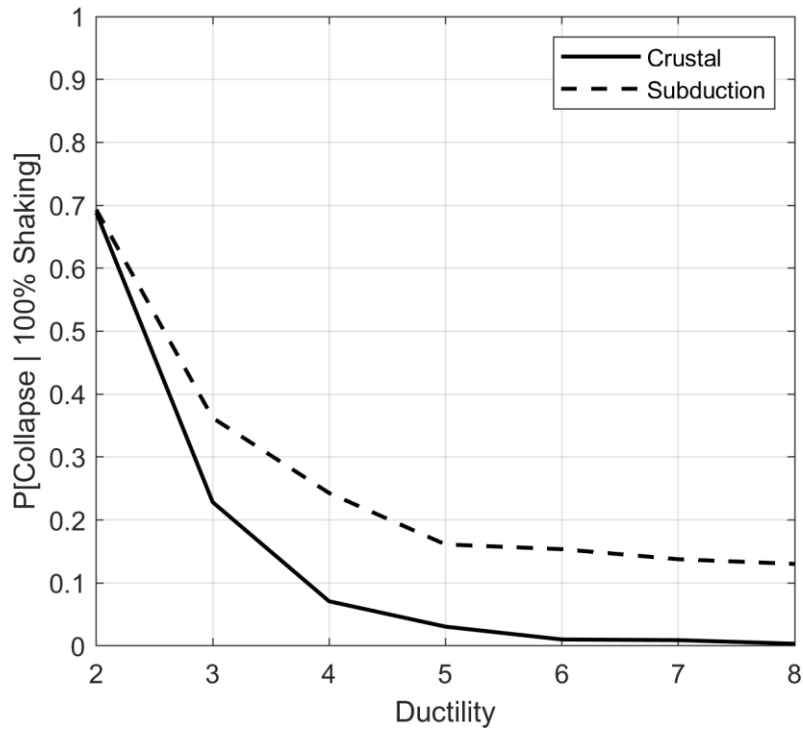


Figure 3.31 100% shaking level probability of collapse for peak-orientated degrading system vs. level of ductility.

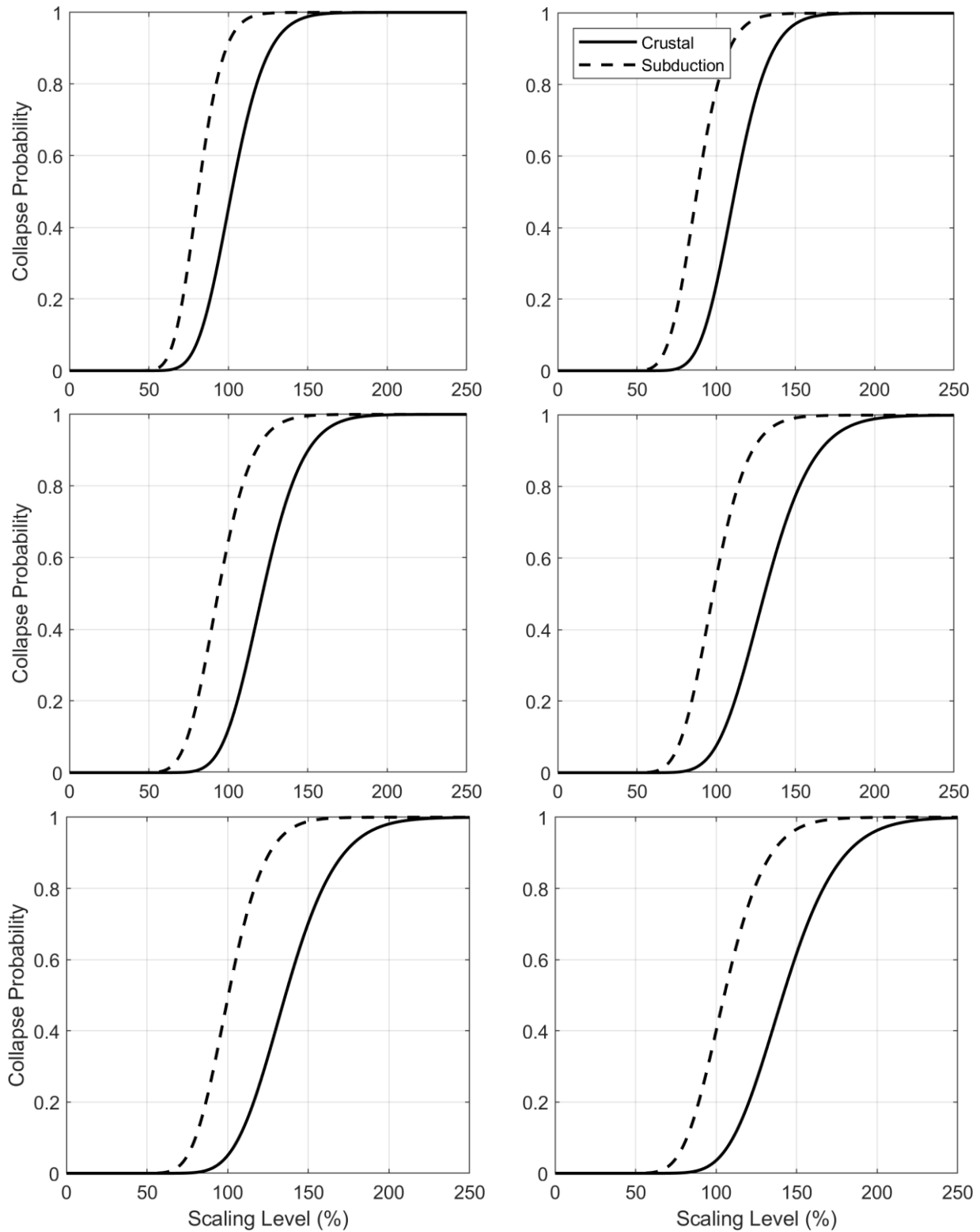


Figure 3.32 Collapse CDF for pinching degrading system with (from top left to bottom right) ductility = 3, 4, 5, 6, 7, 8.

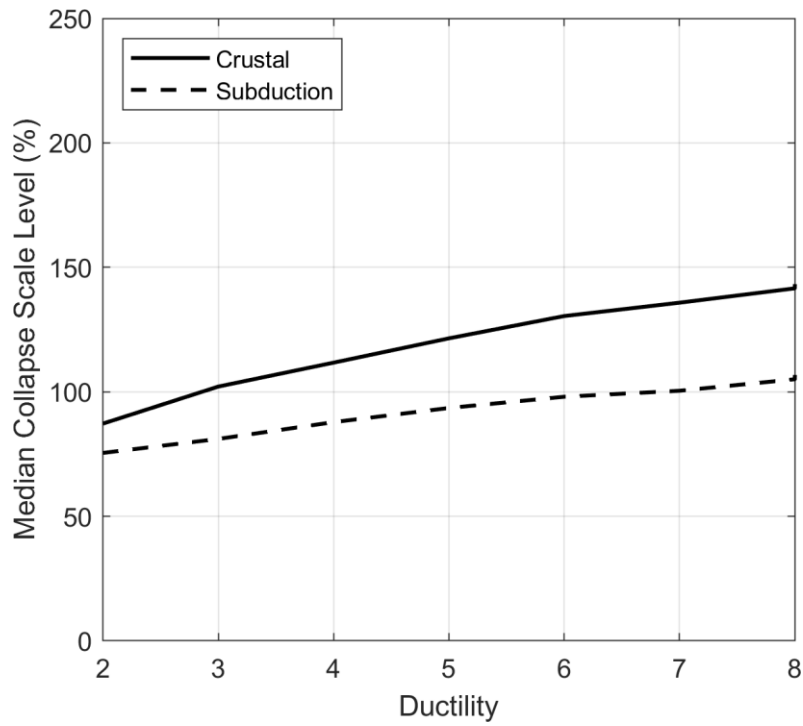


Figure 3.33 Median collapse scale level for pinching degrading system vs. level of ductility.

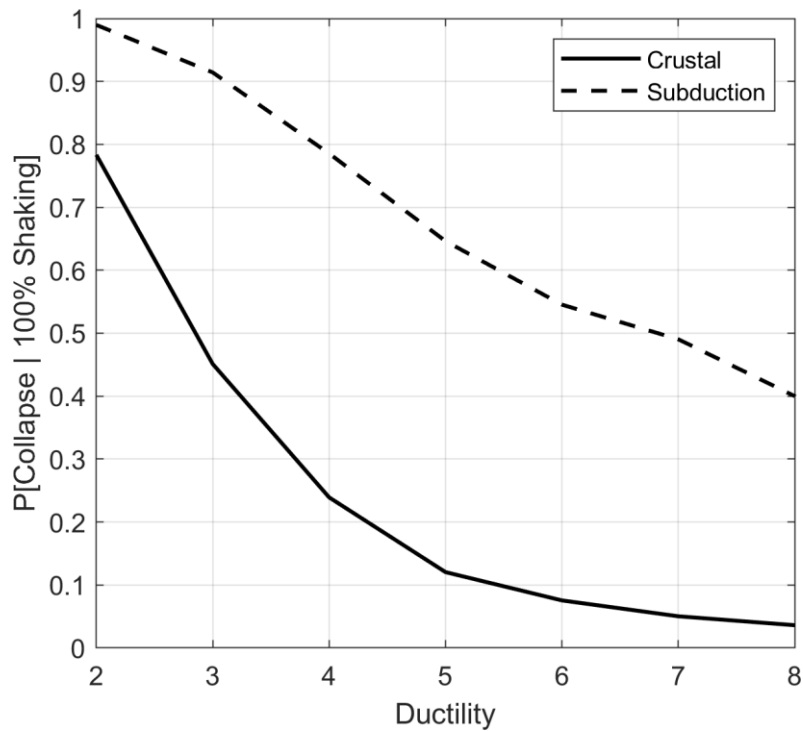


Figure 3.34 100% shaking level probability of collapse for pinching degrading system vs. level of ductility.

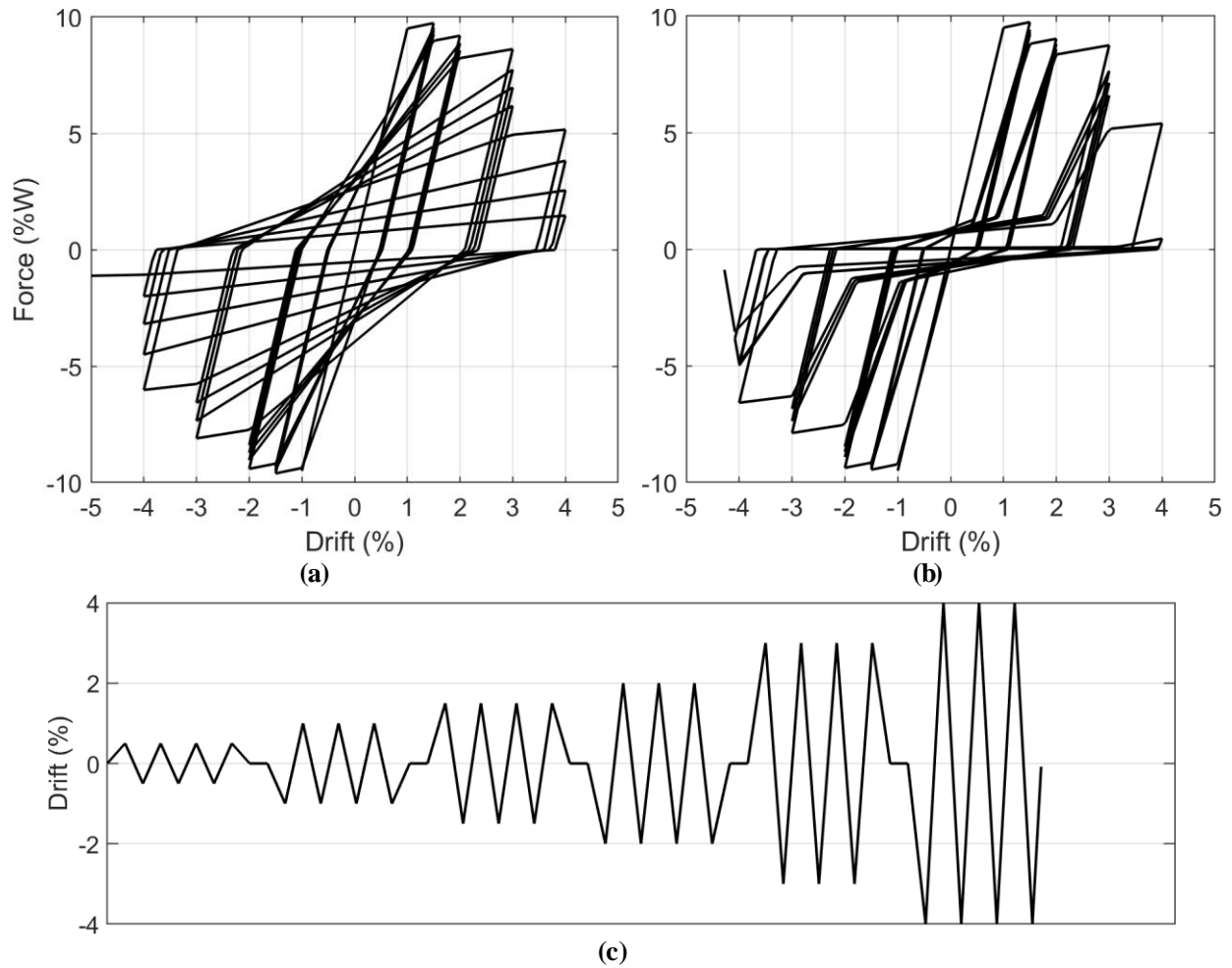


Figure 3.35 Cyclic pushover curves for a) peak-orientated model with $\lambda = 35$; b) pinching model with $\lambda = 35$; and c) cyclic loading protocol.

3.5 Conclusions

This chapter introduced the concepts of cyclic and in-cycle degradation as well as several commonly used hysteretic models that can incorporate these parameters. In-cycle degradation refers to the strength loss that occurs within a single loading cycle; while cyclic degradation refers to strength or stiffness loss that occurs between loading cycles due to damage incurred during the previous load cycle. Two main causes of cyclic degradation were identified: hysteretic cyclic degradation and ratcheting.

It was hypothesized that a longer ground motion would impose more loading cycles on a system, and thus, would cause the system to accumulate more damage earlier and potentially collapse, or become unstable, sooner than a similarly intense, but shorter, motion. However, the “duration” of a ground motion can be quantified using many metrics (the record length is not a suitable metric as it depends on the start and end triggers of the recording instrument). It was found that the significant duration of a motion was highly correlated with the collapse capacity of a simple SDOF degrading model. Significant duration also has some unique benefits compared to other duration metrics as identified in previous research (Chandramohan et al., 2013; Bommer and Martinez-Pereira, 1999), and thus, was selected as the main duration metric to be used in further studies.

The effect of ground motion duration on the collapse risk of systems with varying ductility capacities was also investigated. It was found that ground motion duration had a larger influence on the collapse probabilities of nonlinear models with larger ductilities. This means that when studying the effect of ground motion duration, particularly on the collapse risk of structures, that it is essential to account for the proper ductility capacity of the system, and that results may not be generalized to systems with different ductility levels.

Next, the effect of ground motion duration on the performance of RC shearwall buildings should be investigated to see if the conclusions made from this chapter hold true for more sophisticated numerical models. A suite of building models should be investigated in order to gain insight into the general behavior of this type of structural system. This is the goal of the next chapter.

Chapter 4: Effect of Ground Motion Duration on RC Shearwall Buildings

In this chapter, the effect of ground motion duration on concrete shearwall buildings is investigated using simplified 2D nonlinear models. These types of models are efficient for performing a large amount of sensitivity analyses, which was the purpose of the section.

Five archetype coupled concrete shearwall buildings from 6 to 30 stories are considered. Cyclic and in-cycle degradation is accounted for in the coupling beam models as well as the material models used in fiber sections of the shearwalls. Two suites of spectrally equivalent records are run at various levels of shaking, from code design level all the way to collapse level. The code level motions are run to see if ground motion duration can impact the typical code design of this type of building, while collapse level motions are ran to determine if the collapse risk of the structure is influenced by ground motion duration. Conventionally constructed designs were considered in this chapter since the minimally reinforced header beams used for this construction are expected to exhibit significant degradation compared to more detailed, ductile beams, emphasizing the effect of ground motion duration.

The work presented in this chapter has been published in *Earthquake Spectra*; see:

Fairhurst, M., Bebamzadeh, A., & Ventura, C. E. (2019). Effect of ground motion duration on reinforced concrete shear wall buildings. *Earthquake Spectra*, 35(1), 311-331.

4.1 Archetype Buildings

The archetype buildings considered in this study are RC coupled shearwall buildings typical of existing residential buildings constructed in Vancouver, BC (a large city with a dense urban population in close proximity to the Cascadia Subduction Zone). Buildings with 6, 12, 18, 24, and 30 stories are considered. The lateral load resisting system of the buildings includes three interior reinforced concrete shearwalls which comprise the elevator and stair core of the buildings.

The floor layout of the buildings is illustrated in Figure 4.1. The floor area is about 5200 ft² (480 m²) per story and the weight was calculated as 0.21 kips/ft² (approximately 10 kN/m²). The archetype building layouts were based off designs by a report prepared by Green and Karsh (2012).

The buildings were designed using the Equivalent Lateral Force Procedure (ELFP) for a base shear calculated in accordance with the 2010 National Building Code of Canada (NBCC; NRCC, 2010) for Vancouver, BC based on conventionally constructed coupled walls. The seismic force reduction factor ($R_d R_o$) of this system is 1.95. Conventionally constructed walls were used in this study to represent existing concrete shearwall buildings in Vancouver, BC, many of which were constructed from 1960-1980 (Yathon et al., 2017). Conventionally constructed walls include headers conventional stirrups instead cross-tied steel cage reinforcement. Although this type of header is less ductile, test results show that they are more susceptible to damage due to cyclic degradation than more ductile headers (Galano and Vignoli, 2000), which is why they were chosen for this study. Only the coupled NS direction (see Figure 4.1) was considered for analysis.

Three sets of core walls were designed: one for the 6 and 12 story buildings (Figure 4.2), one for the 18 story building (Figure 4.3), and one for the 24 and 30 story buildings (Figure 4.4). The walls are connected by 20" by 24" (508 by 610 mm) deep header beams (Figure 4.5) which are reinforced by transverse 15M stirrups spaced at 4" (100 mm). All concrete had a specified compressive strength $f'_c = 5.08$ ksi (35 MPa) and effective strength of $f'_{ce} = 1.3f'_c = 6.6$ ksi (45.5 MPa; LATBSDC, 2017); steel was specified as A615 Grade 60 with an effective yield strength $f_{ye} = 70$ ksi (483 MPa), and effective ultimate strength $f_{ue} = 106$ ksi (730 MPa). The gravity resisting system of the buildings comprises 24" (600 mm) diameter circular perimeter and interior columns and 8" (200 mm) slabs at each story.

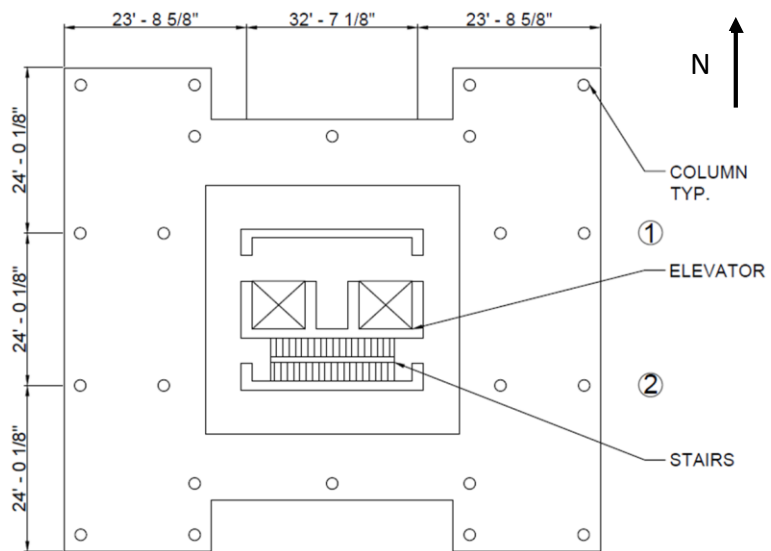


Figure 4.1 Archetype building floor plan.

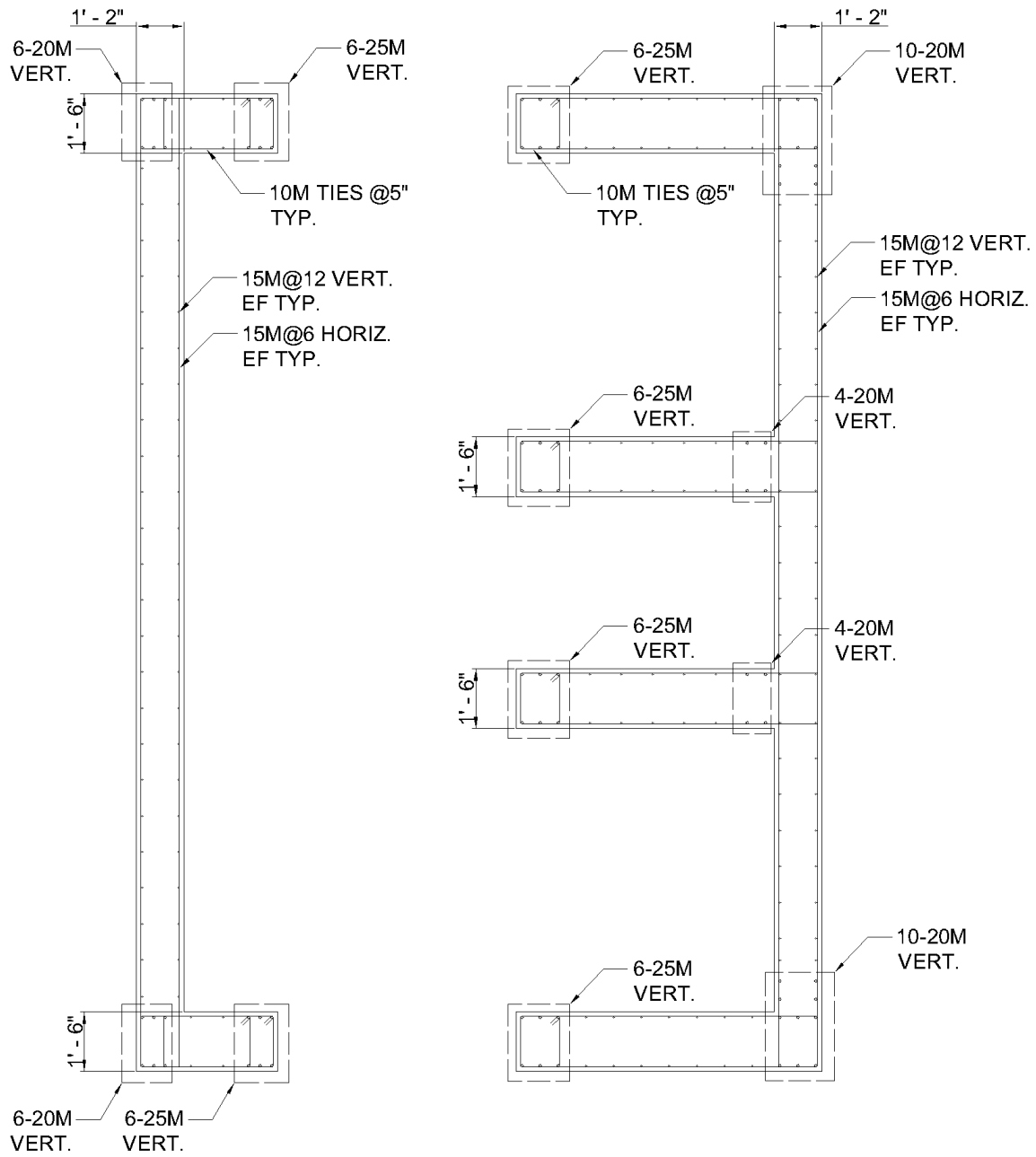


Figure 4.2 Reinforcement details of 6 and 12 story shearwall buildings.

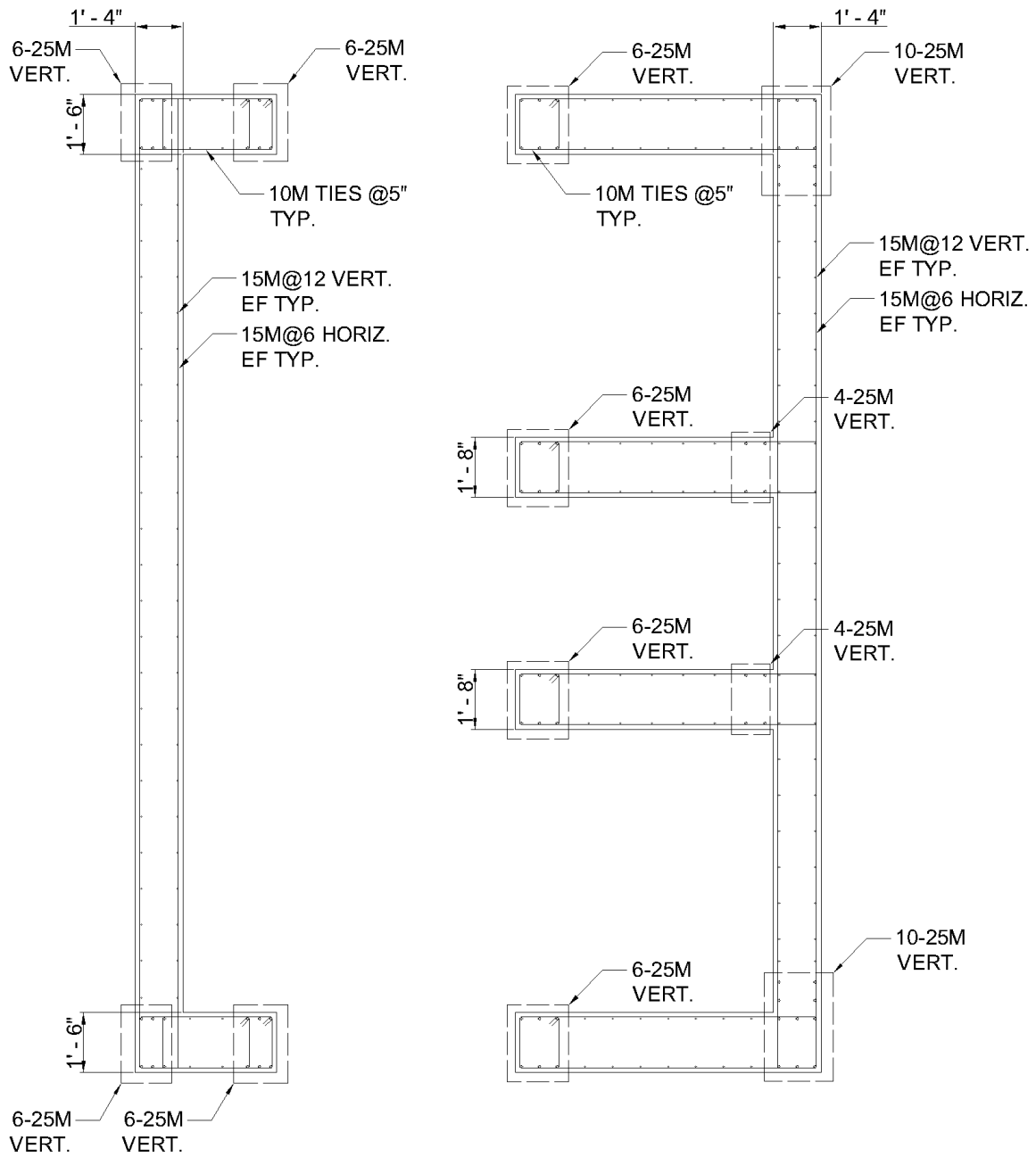


Figure 4.3 Reinforcement details of 18 story shearwall building.

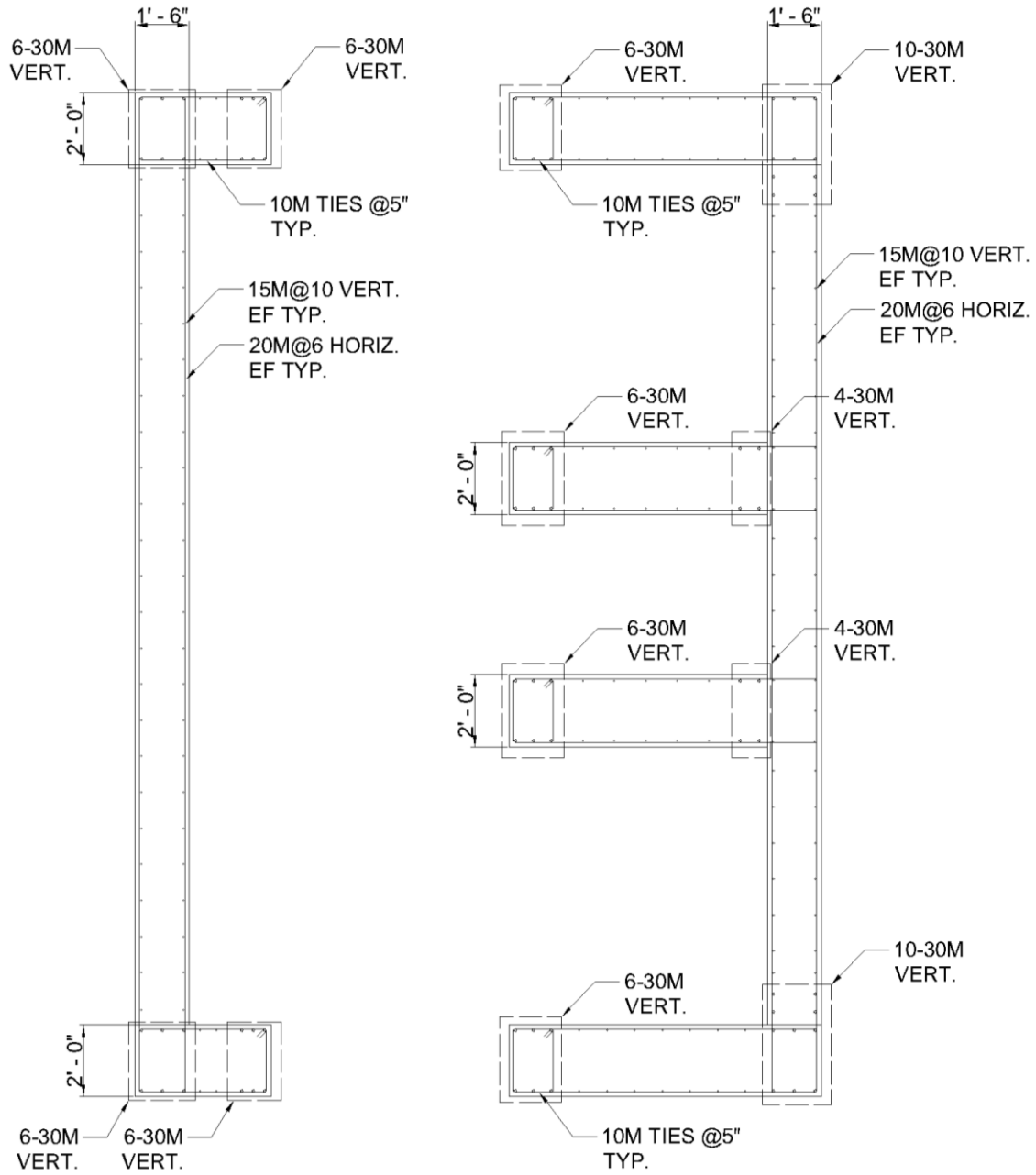


Figure 4.4 Reinforcement details of 24 and 30 story shearwall buildings.

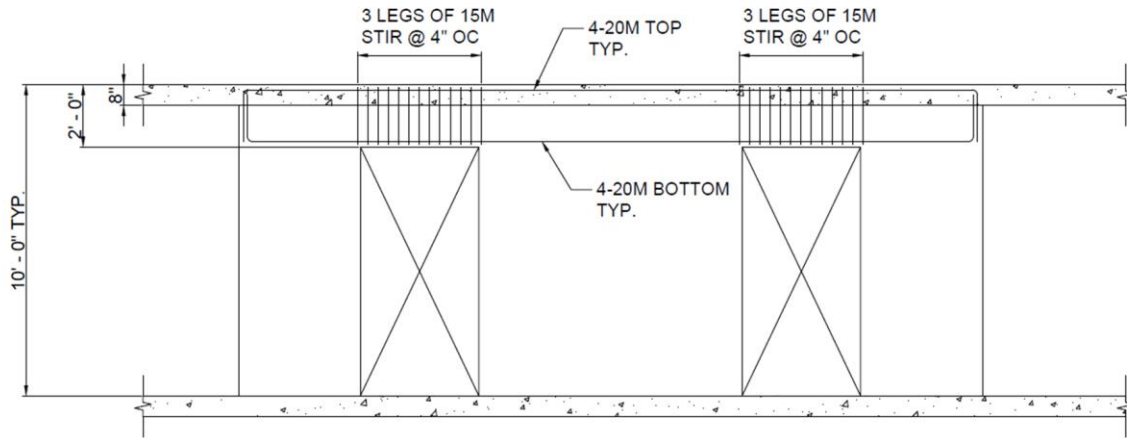


Figure 4.5 Elevation view of slabs and header beams.

4.2 Numerical Modelling

The OpenSees framework (McKenna et al., 2000) was used to develop a numerical model for each archetype building. The following sections provide details about the models used for the different elements considered, including:

- shearwall modelling;
- header beam modelling and calibration;
- P-Delta effects, and;
- damping.

Note that only the lateral force resisting system (walls interconnected with header beams) were modelled; the gravity resisting system (columns and slabs) were not considered.

4.2.1 Shearwall Model

The interior shearwalls were modeled using fiber elements with a displacement-based formulation. Elastic shear deformations were captured by including a linear shear hinge at the midpoint of the walls at each story. The shear hinges were modeled with stiffness equal to the

cracked shear area multiplied by the shear modulus divided by the story height. To account for the loss of area due to cracking, the gross area was multiplied by 0.1 based on the recommendations by Pugh (2012).

The use of fiber sections is generally considered acceptable for approximating the response of slender RC shearwalls and has been used to successfully simulate the response of such walls (ATC, 2010; Orakal and Wallace, 2006). However, fiber section models with uncoupled shear springs may underestimate compression strains at boundary regions (Orakal and Wallace, 2006) and may overestimate the lateral capacity of moderate aspect ratio shearwalls (Kolozviri et al., 2018; Kolozviri and Wallace, 2016). In Appendix C, one of the fiber element models developed in this section was compared to an equivalent wall model which used a sophisticated shear-flexure interaction (SFI) model developed by Kolozviri et al. (2018). The results showed that the fiber element model was generally able to predict deformations similar to the SFI, which was the main metric used for evaluating performance in this section.

4.2.1.1 Material Models

Concrete was modeled with a linear tension softening concrete material model (*Concrete02*; Yassin, 1994) which includes unloading stiffness degradation. This concrete model is able to capture degradation through both crushing and spalling. Confinement was accounted for using the Mander et al. (1998) relationship - the ratio of confined to unconfined concrete compression strength was 1.3. The confined material model was used in the end zones of the walls; the unconfined model was used elsewhere. The hysteretic response of the confined and unconfined material models are illustrated in Figure 4.6a and b, respectively. This figure shows the larger (1.3x) compressive strength in the confined model as well as the significantly increased ductility capacity due to confinement.

Reinforcing steel was modeled using the *ReinforcingSteel* material model which accounts for cyclic fatigue in the steel bars according to Brown and Kunnath (2000). Buckling and fracture of the reinforcement was captured through the OpenSees *MinMax* material. This material returns zero strength and stiffness once a predetermined strain (i.e. the fracture strain of steel) is surpassed. To account for buckling, the negative limit of the *MinMax* material was set to the concrete crushing strain, assuming steel buckling will occur immediately after the surrounding concrete crushes. Bar slip, which could be another source of degradation, was not modeled. The hysteretic response of the steel material model is illustrated in Figure 4.6c.

4.2.2 Header Beam Model

The header beams were modeled using elastic beam elements with nonlinear shear hinges. The elastic beam elements were modeled considering a cracked section modulus ($I_{\text{cracked}} = 0.35I_{\text{gross}}$) to account for bending deformations. Between the header beam elements and wall elements, rigid beam elements were modeled to account for the physical width of the walls. A shear hinge was modeled at the midpoint of each header beam to account for the shear yielding and nonlinearity in the elements.

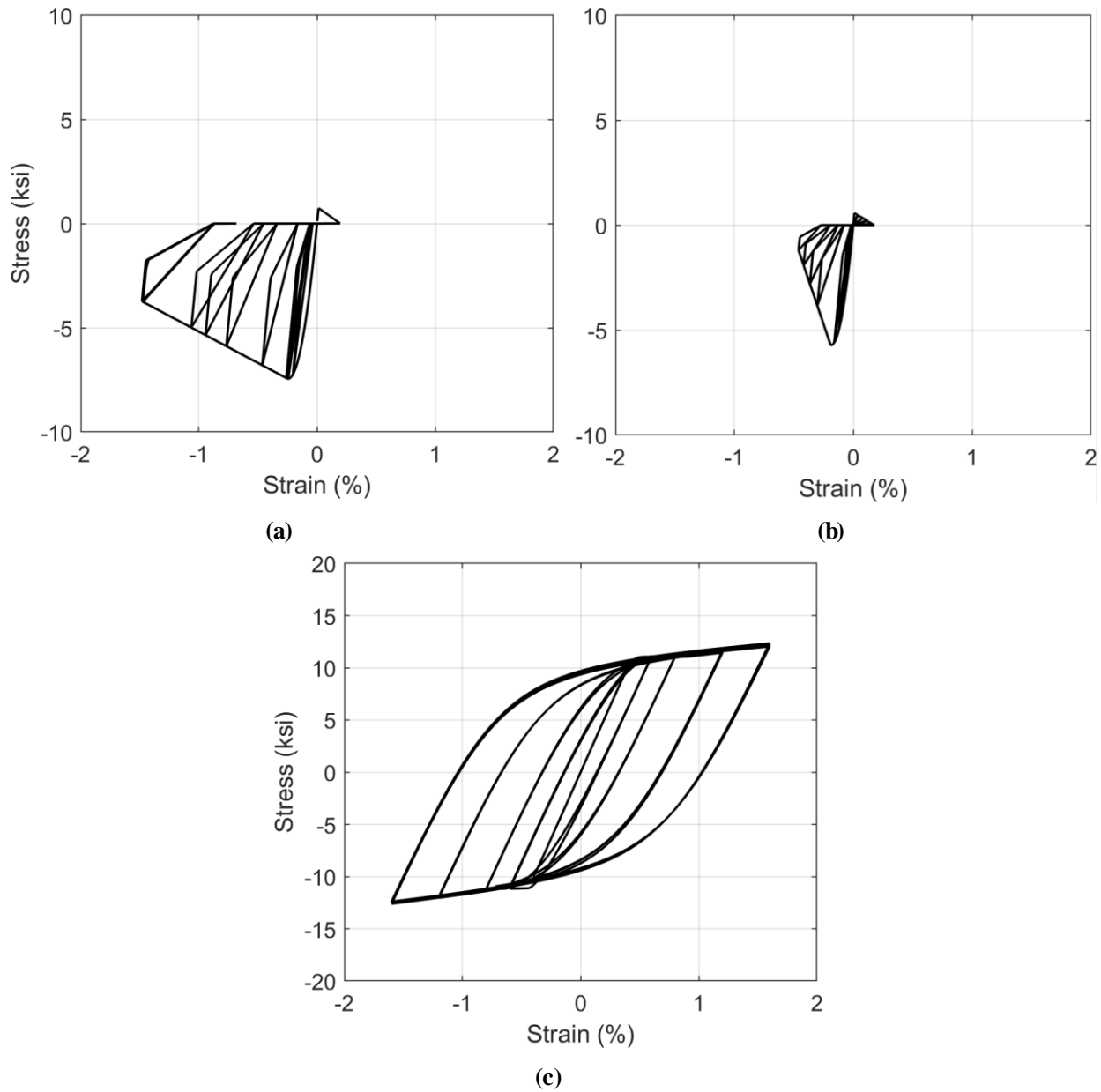


Figure 4.6 Material models: 1) confined concrete (*Concrete02*); b) unconfined concrete (*Concrete02*); c) steel (*ReinforcingSteel*).

4.2.2.1 Calibration

The nonlinear shear hinge properties were calibrated to a reverse-cyclic test on a header beam performed by Galano and Vignoli (2000): specimen P02 (Figure 4.7). This specimen had

transverse #8 bars every 10" (250 mm) with transverse reinforcement ratio (ρ_v) of 0.84. It had an aspect ratio (length/width) of 2.5, which is similar to that found in residential RC buildings (Naish, 2010).

The *Pinching4* material model (Lowe et al., 2004) was employed to capture pinching, in-cycle degradation, and cyclic stiffness and strength degradation in the nonlinear shear hinges. A comparison of the test results to the nonlinear shear material is presented in Figure 4.8 including the monotonic backbone curve assumed.

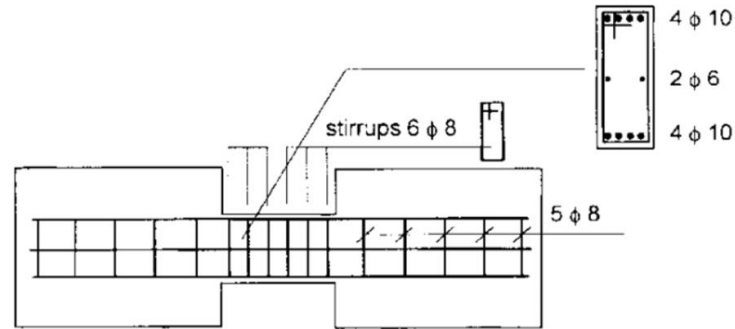


Figure 4.7 Specimen P2 elevation and cross section (Galano and Vignoli, 2000).

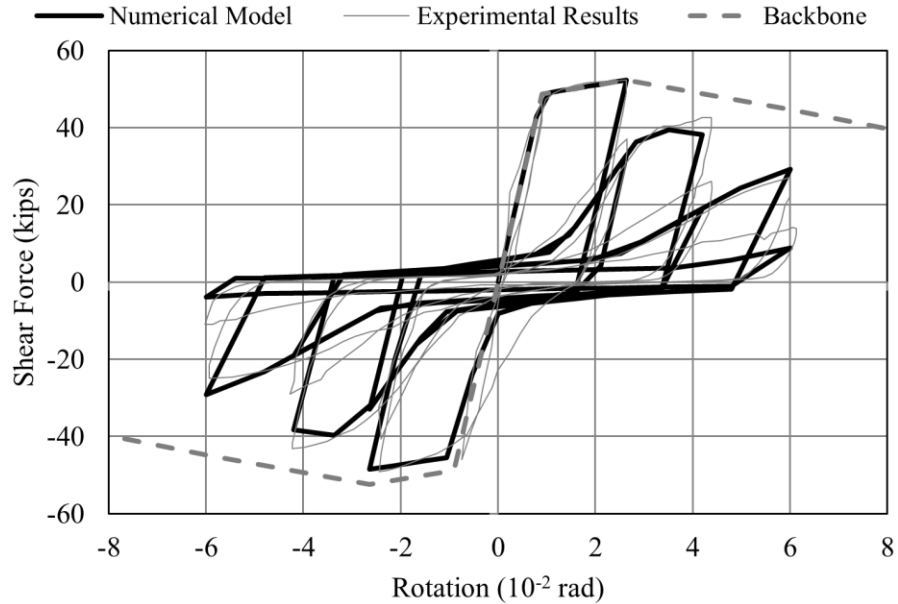


Figure 4.8 Nonlinear shear hinge model for header beams vs experimental results (Galano and Vignoli, 2000).

4.2.3 P-Delta Effects

The weight based on the tributary area of the core walls was applied directly on the wall elements. The gravity system was not explicitly modeled; however, to account for the second order effects of the weight carried by the gravity system a leaning (or P-Delta) column was included in the model. The weight of the structure not applied directly on the shearwalls was applied on the leaning column, which was pinned at the base and constrained to the walls at each story level. Rigid diaphragm constraints were applied at each level. An illustration of the OpenSees model is presented in Figure 4.9.

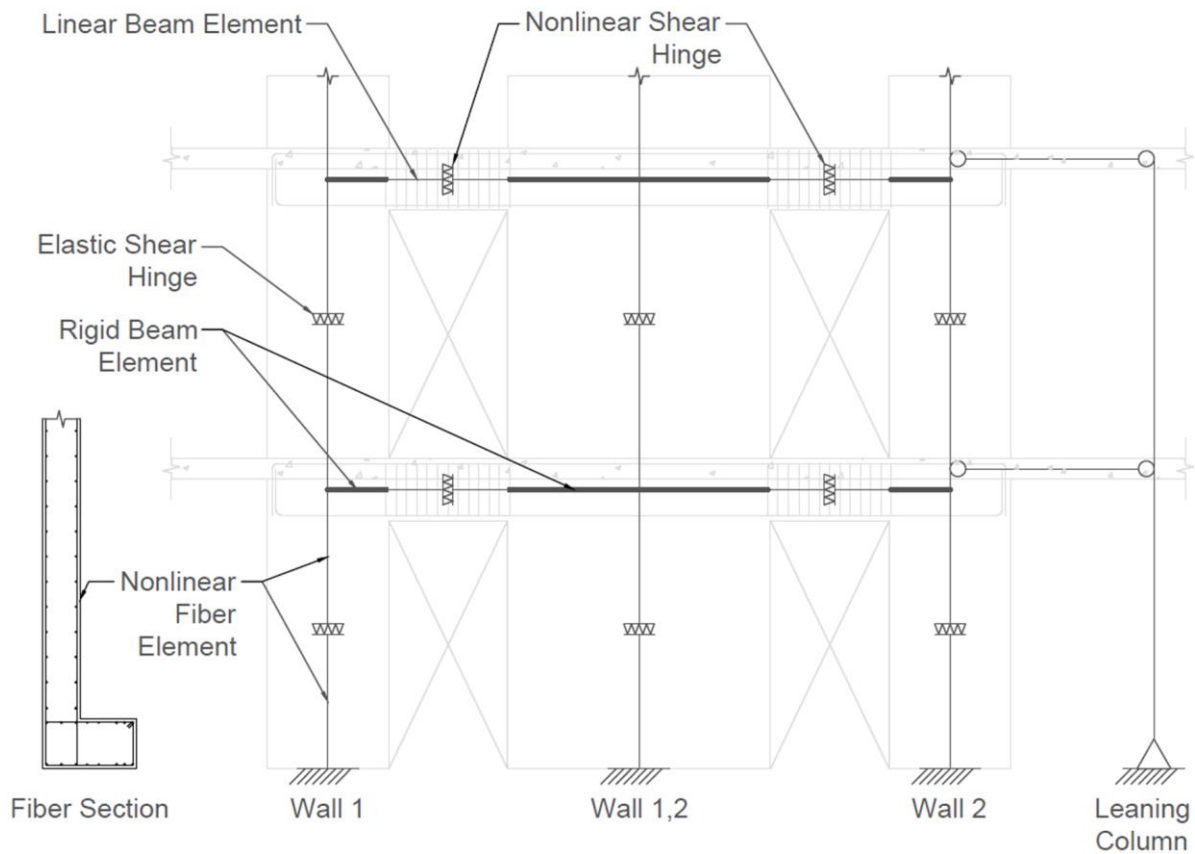


Figure 4.9 Illustration of a typical story of the 2D OpenSees numerical models.

4.2.4 Damping

An equivalent viscous damping of 2.5% was applied to all models following the recommendations of LATBSDC (2017) for MCE_R level analysis (~2% in 50 year shaking level). Damping was applied as Rayleigh damping in the first and third modes. Rayleigh damping was chosen because it will dampen the effects of high local modes of vibration which may cause numerical problems if not accounted for. Rayleigh damping also extends damping into the lower frequencies so that once the models yield and their effective periods increase, the damping will still be effective. This follows the recommendations for NTHA from ASCE 7-16 (ASCE/SEI, 2016).

The total amount damping of the models will be higher due to the additional hysteretic damping from the nonlinear elements. The total amount of hysteretic damping will vary based on the amount of nonlinear behavior. Typical hysteretic damping will provide ~1-4% of critical (ASCE/SEI, 2016).

The first three elastic periods of the models are summarized in Table 4.1.

Number of Stories	T1 (s)	T2 (s)	T3 (s)
6	0.44	0.14	0.083
12	1.05	0.32	0.17
18	1.74	0.51	0.26
24	2.56	0.70	0.25
30	3.73	0.85	0.46

Table 4.1 First three elastic periods of the 5 RC shearwall archetype building numerical models.

4.3 Ground Motion Suites

Two suites of 30 ground motion records were selected in order to investigate the effect of ground motion duration on the archetype building models. Records were selected from the PEER NGA-West 2 database (crustal events) and the subduction zone database described in Section 3.3.1. The first suite of motions contained long duration records, while the second comprised spectrally equivalent short duration records. The 5-95% significant duration (d_{5-95}) was adopted to quantify record duration based on the conclusions from Section 3.3.

First, 30 long duration records ($d_{5-95} > 35$ s) were selected and linearly scaled to the Vancouver 2% in 50 year spectrum. The Kempton and Stewart (2006) and Bommer et al. (2009) GMMs predict 5-95% significant durations of ~100 and ~20 s, respectively, for a magnitude 9.0 earthquake in Vancouver (distance of ~135 km on 760 m/s soil). This magnitude and distance were

the mean results from a probabilistic seismic hazard analysis of subduction sources affecting Vancouver, BC. Although these GMMs are only valid to magnitudes of 7.5 and 8, respectively, there are currently no GMMs proposed for larger magnitude earthquakes. The 20 second lower bound from Bommer et al. (2009) was considered quite low and too close to the short duration limit, so adding one standard deviation to the median prediction gave the lower bound limit of 35 sec for long duration records. The Afshari and Stewart (2016) significant duration GMM was also considered; however, it did not extrapolate well past magnitude 7.9 (see the sharp increase in significant duration prediction past magnitude 7.5 in Figure 2.7).

Most of the events are from large magnitude subduction interface and crustal events. For this study, spectral shape and significant duration were the most important aspects of the records, thus, no selection constraints, other than limiting initial scale factors to the design spectrum to 4.0, were employed in order to maximize the number of records available. This limit was applied to both record suites. The long duration events and records selected are summarized in Table 4.2. Although, all the records were considered to have a long duration, they came from both crustal and subduction interface events. The results of this study may differ if only subduction events were chosen. Since the subduction interface records tend to be longer than the long duration crustal motions that were identified, the differences between the two record suites would likely be further emphasized if only subduction interface records were chosen.

The methodology employed in the Chandramohan (2016b) study was then used to select spectrally equivalent short duration motions. This methodology removes the influence of spectral shape so that the effect of duration can more easily be isolated. Accordingly, a short duration ($d_{0.95} < 20$ s) record was selected to best match the spectrum of each of the 30 long duration records. The best match was obtained by minimizing the mean squared error (MSE) between the spectra of

the two records. The short duration upper limit of 20 s was the average of the Kempton and Stewart (2006), Bommer et al. (2009), and Afshari and Stewart (2016) GMMs for a magnitude 7.2 earthquake at a distance of 20 km. This magnitude and distance were the mean results from a probabilistic seismic hazard analysis of shallow crustal sources effecting Vancouver, BC (see Section 2.2.2.2).

Event	Type	Magnitude (M _w)	Year	Number of Stations	Station Code(s)
Chi-Chi, Taiwan	Crustal	7.6	1999	7	CHY004, CHY032, CHY055, CHY076, CHY100, CHY116
Hokkaido, Japan	Subduction	8.0	2003	2	HKD125, HKD127
Kobe, Japan	Crustal	6.9	1995	2	ABN, SKI
Kocaeli, Turkey	Crustal	7.6	1999	1	BUR
Landers, Ca.	Crustal	7.3	1992	1	MCF
Michoacán, Mexico	Subduction	8.0	1985	1	VILE
Tohoku, Japan	Subduction	9.0	2011	16	CHB009, CHB010, CHB024, CHB029, FKS022, IBR009, KNG006, KNG201, KNG205, NIG012, SIT009, TKY005, TKY016, TKY017, TKY024, TKY025
Chi-Chi, Taiwan	Crustal	7.6	1999	7	CHY004, CHY032, CHY055, CHY076, CHY100, CHY116
Hokkaido, Japan	Subduction	8.0	2003	2	HKD125, HKD127
Kobe, Japan	Crustal	6.9	1995	2	ABN, SKI
Kocaeli, Turkey	Crustal	7.6	1999	1	BUR

Table 4.2 Long duration suite summary.

Figure 4.10 illustrates an example of a long record and spectrally equivalent short duration record. Scaling factors and MSE was computed between 0.07-5.6 s, which is equal to 0.15 times the 6 story model's period to 1.5 times the 30 story model's period. Table 4.3 summarizes the

selected short duration events and records. The short duration records were obtained exclusively from worldwide shallow crustal events.

Figure 4.11 presents the spectra of the two suites compared to the Vancouver 2015 design spectrum. Figure 4.12 compares the significant duration of the two suites. The short duration suite comprised records with a 5-95% significant durations of 5 to 15 s with a mean of 11 s. The long duration suite had a range of 40 to 150 s and a mean of 80 s.

Event	Type	Magnitude (M_w)	Year	Number of Stations	Station Code(s)
Chi-Chi, Taiwan (3)	Crustal	6.2	1999	1	CHY028
Chi-Chi, Taiwan (4)	Crustal	6.2	1999	1	TCU116
Chi-Chi, Taiwan (6)	Crustal	6.3	1999	2	CHY028, CHY035
Duzce, Turkey	Crustal	7.2	1999	1	DZC
Greece	Crustal	6.2	1999	1	KAL
Imperial Valley, Ca.	Crustal	6.5	1979	6	E01, E05, E05, E07, ECC, HVP
Kocaeli, Turkey.	Crustal	7.6	1999	2	GBZ, IZT
Loma Prieta, Ca.	Crustal	6.9	1989	6	A01, ADL, CH12, HAD, SLC, SLC
Northridge, Ca.	Crustal	6.7	1994	5	CCN, LDM, SCE, STM, SYL
San Salvador	Crustal	5.8	1986	1	NGI
Superstition Hills, Ca.	Crustal	6.5	1987	4	BRA, KRN, POE, PTS

Table 4.3 Short duration suite summary.

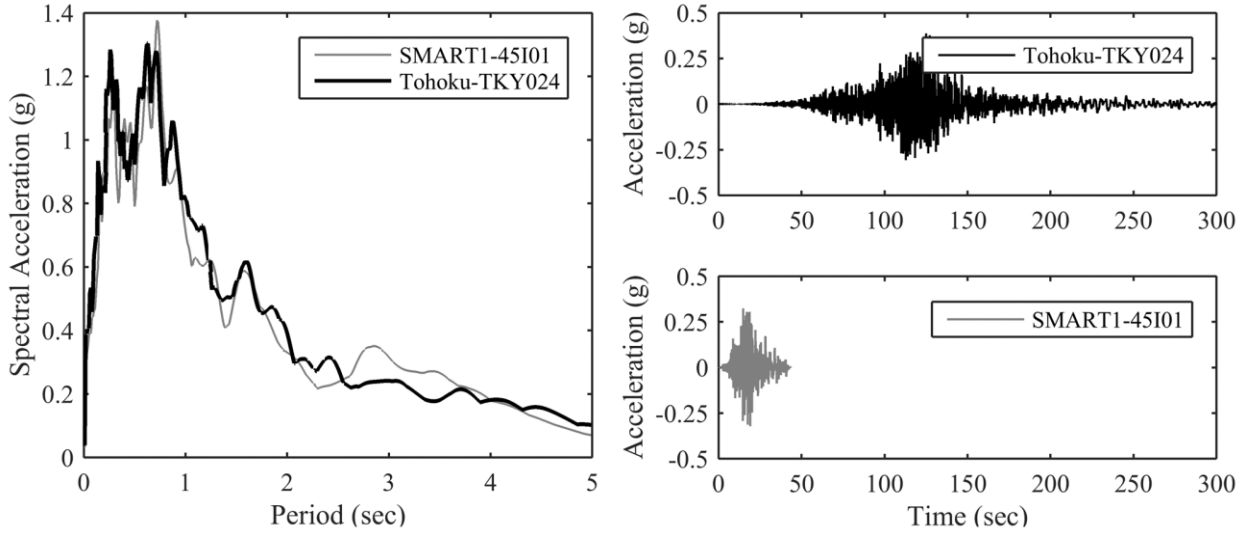


Figure 4.10 Example of spectrally equivalent record acceleration response spectra and time histories.

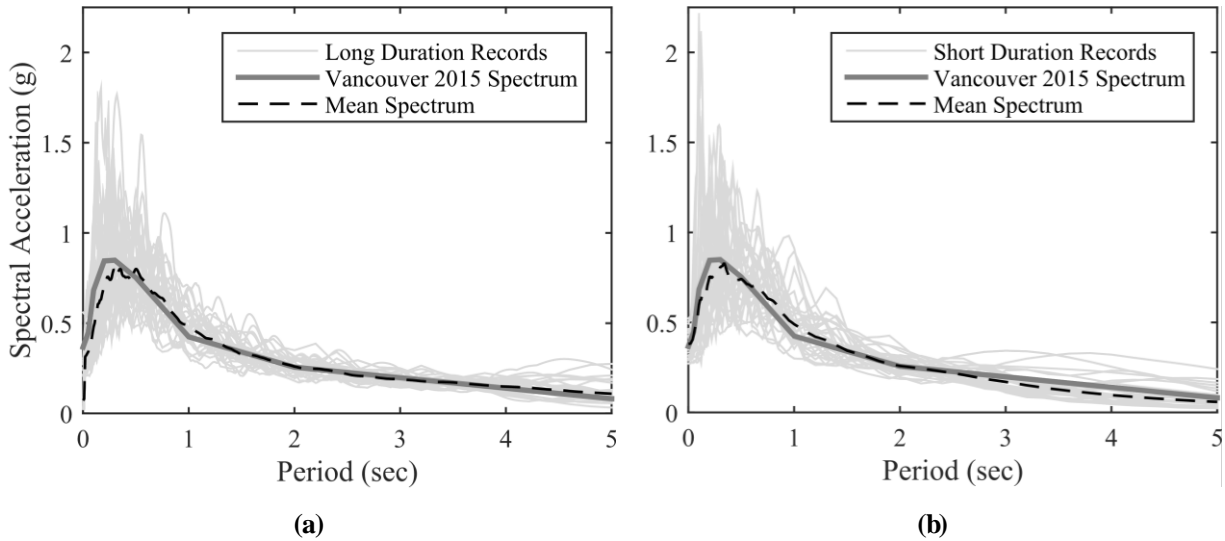


Figure 4.11 Spectra of (a) the long duration suite and (b) the short duration suite compared to the Vancouver 2% in 50 year design spectrum.

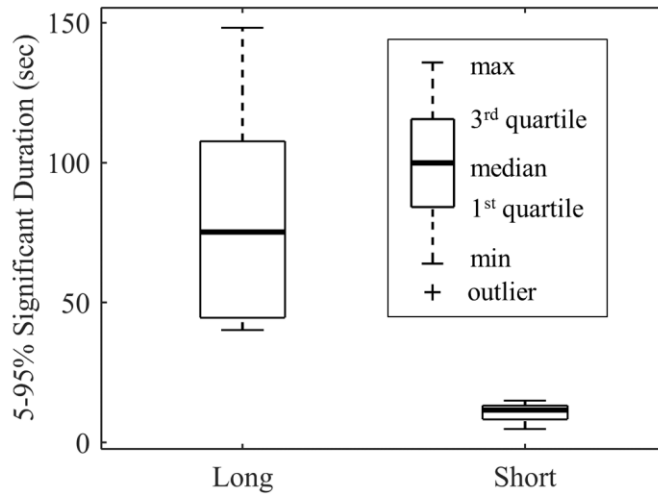


Figure 4.12 Long and short duration suite significant duration (d_{5-95}) comparison.

4.4 Code Level Analysis

The NBCC specifies a ground motion shaking level with a 2% in 50 year probability of exceedance for code-level design and analysis of Canadian buildings. Accordingly, the two suites of ground motions were first scaled to the Vancouver NBCC 2015 (NRCC, 2015) design spectrum (see Figure 4.11) and used to analyze the models using nonlinear time history analysis.

The resulting maximum interstory drifts for the models are illustrated in Figure 4.13 to Figure 4.17 and summarized in Table 4.4. The NBCC uses interstory drifts as a surrogate for structural damage, and limits regular buildings to a mean maximum interstory drift of 2.5% of the story height when using a suite of records to conduct time history analysis. For the collapse prevention evaluation used in performance-based design, mean and maximum interstory drifts are limited to 3.0% and 4.5%, respectively (LATBSDC, 2017). As seen in Table 4.4 and the accompanying figures, neither suite surpasses these limits, nor the conservative NBCC limit of 2.5%, for any building height.

The suite by suite results are very similar for the two shortest models (6 and 12 stories). This may be because the overall damage (interstory drift levels) is quite low at this level of shaking (maximum interstory drift of ~1% for the two suites). At these lower levels of damage, the amount of degradation in the walls and header beams is low, which will largely nullify the effect of the ground motion duration. However, the intra-suite differences in drift demands are larger for the three taller models (18, 24, and 30 stories). This may be due to larger displacements in the taller models which stimulate more damage and degradation.

The coupling beam rotations and shear force and moment demands for the models are presented in Appendix D. The shear force and overturning moment demands for these two suites of ground motions are similar, as these are governed by the strengths of the walls. The coupling beam rotations follow similar trend to the drift results present here.

Number of Stories	Mean of Maximum Drifts (%)	
	Long Duration Suite	Short Duration Suite
6	0.8	0.7
12	1.2	1.1
18	1.6	1.3
24	1.5	1.2
30	1.3	1.1

Table 4.4 Mean of maximum interstory drifts summary for all archetype models at the 2% in 50 year shaking level.

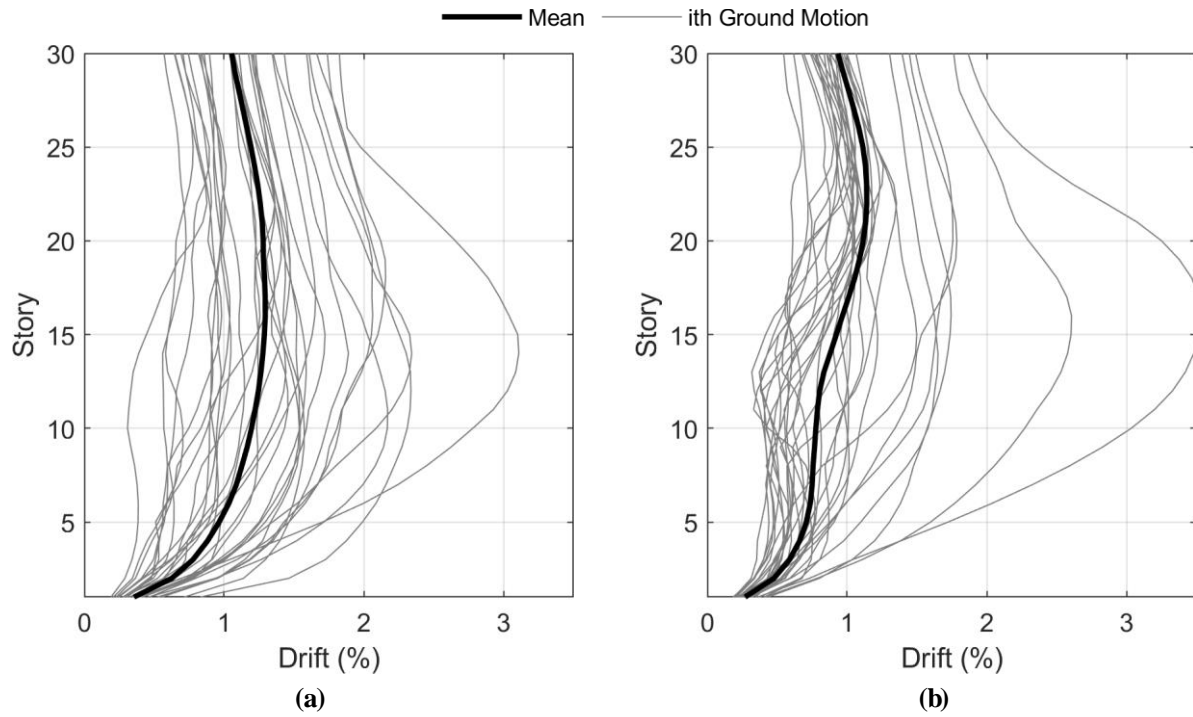


Figure 4.13 Interstory drift results for the 30 story model at the code shaking level for (a) the long duration suite and (b) the short duration suite.

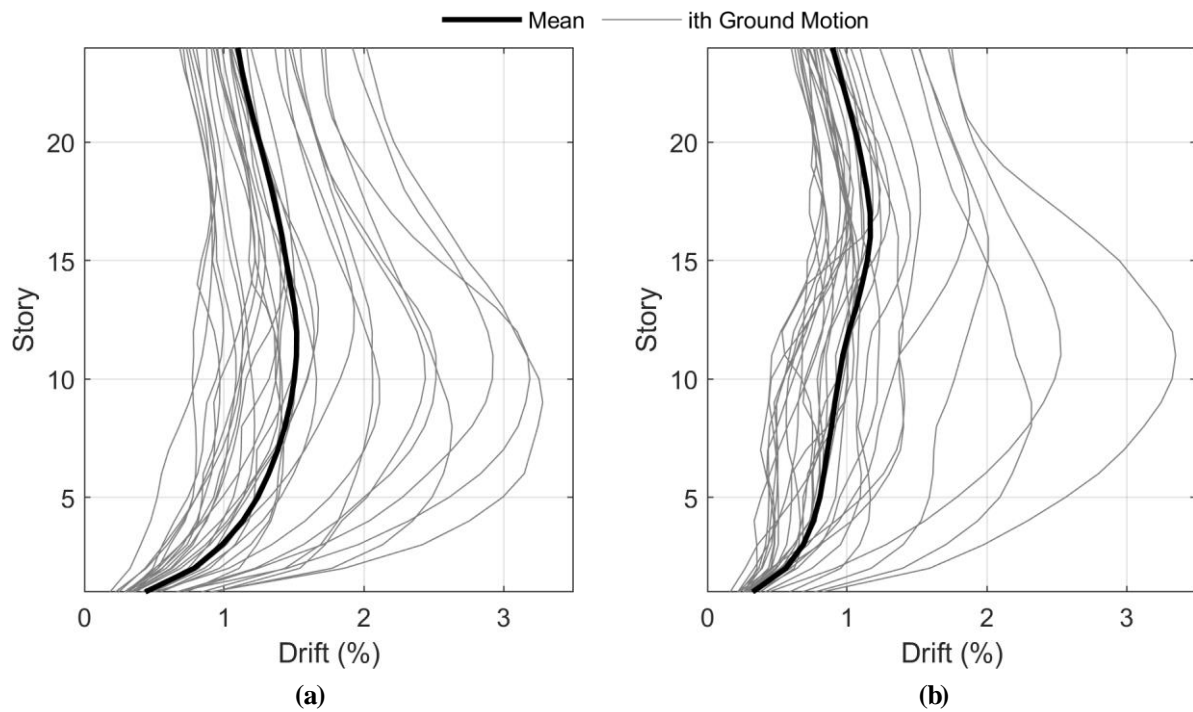


Figure 4.14 Interstory drift results for the 24 story model at the code shaking level for (a) the long duration suite and (b) the short duration suite.

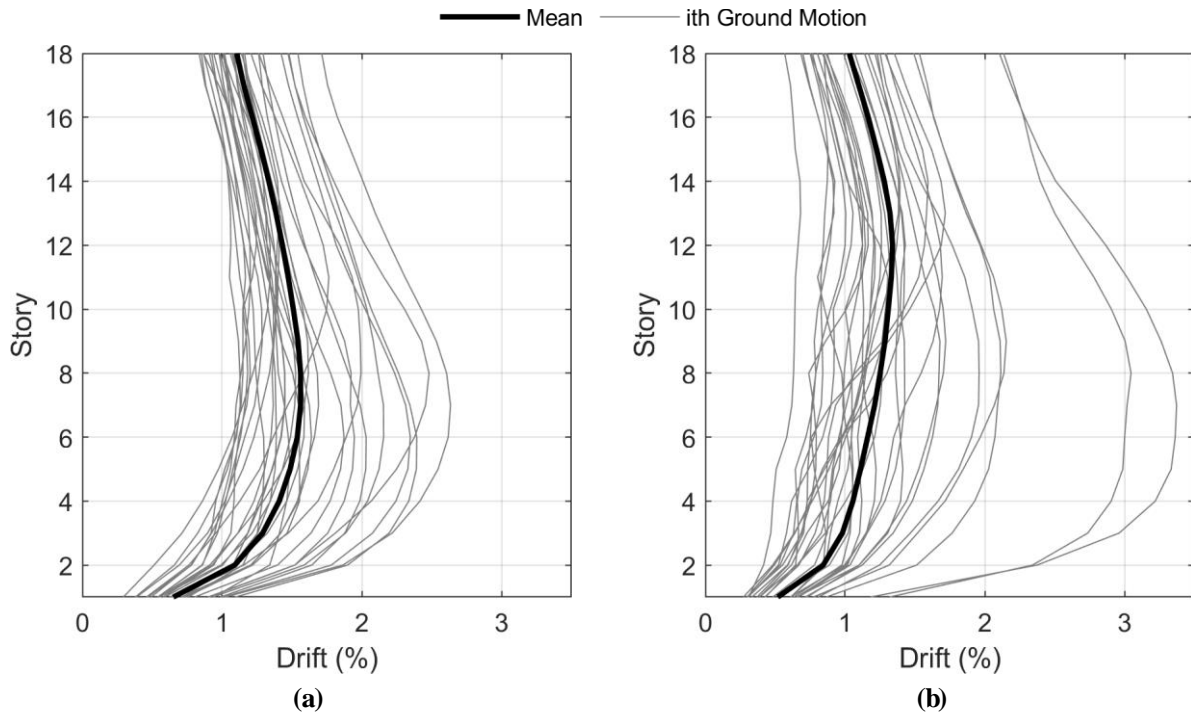


Figure 4.15 Interstory drift results for the 18 story model at the code shaking level for (a) the long duration suite and (b) the short duration suite.

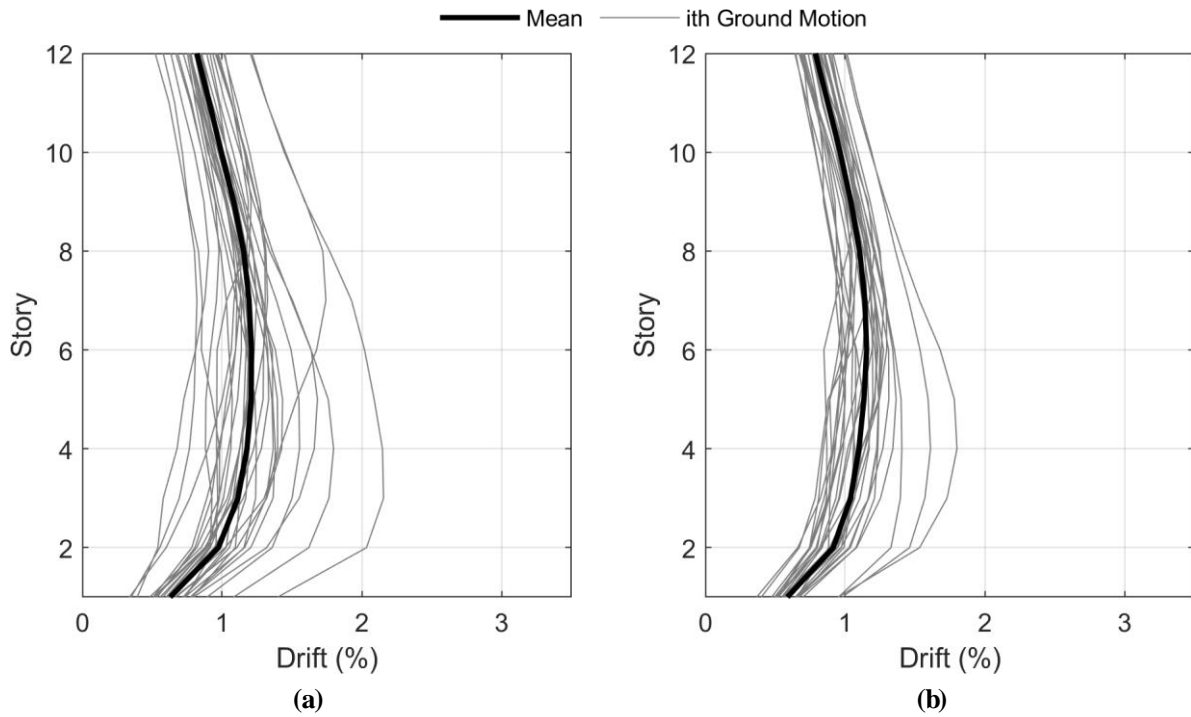


Figure 4.16 Interstory drift results for the 12 story model at the code shaking level for (a) the long duration suite and (b) the short duration suite.

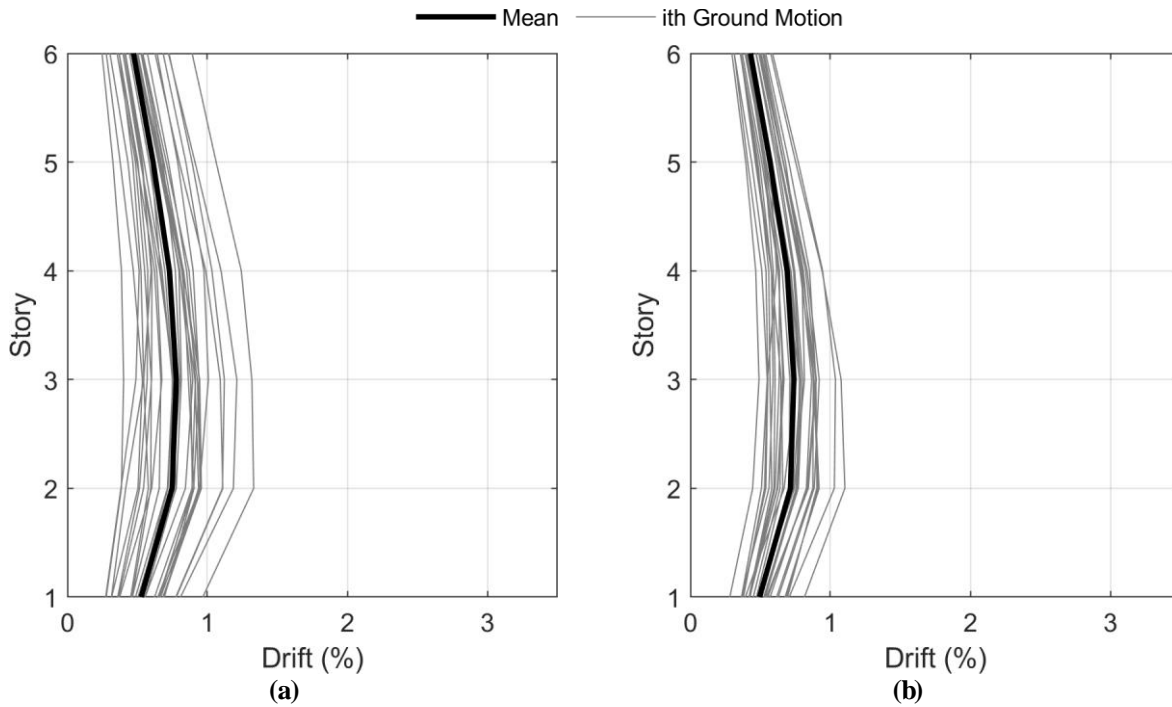


Figure 4.17 Interstory drift results for the 6 story model at the code shaking level for (a) the long duration suite and (b) the short duration suite.

The energy demands of the 30 story structure were also computed during the time history analysis by considering the energy dissipated through both yielding of the walls and header beams. The force-displacement response of the header beams and moment-rotation results of the wall elements were recorded throughout the analyses. The areas under these curves were used to compute energy. Figure 4.18 compares the energy response calculated in the structure at this level of shaking for the two motion suites. Despite producing comparable peak displacement and force results, the long duration suite has much higher energy demands, due to the large number of cycles the longer motions subject the structure to. This may lead to more structural and nonstructural damage in the building (Bertero et al., 1978).

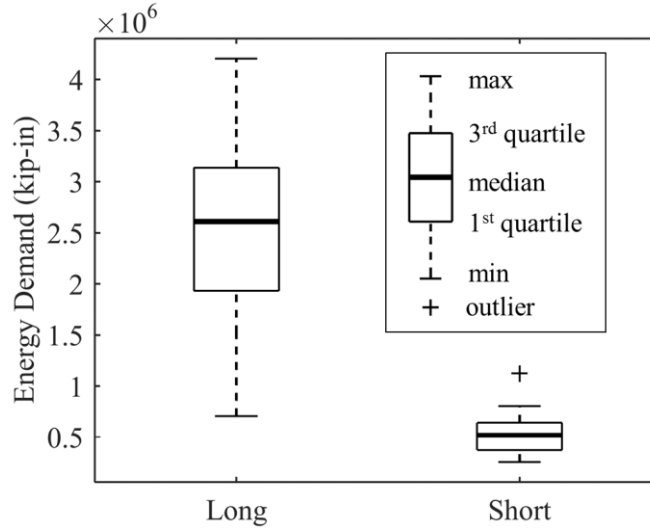


Figure 4.18 Energy demand statistics for the 30 story model at the code shaking level.

4.5 Collapse Level Analysis

Next, in order to determine if long duration ground motions increase the collapse risk of reinforced concrete shearwall structures at higher shaking levels, the two suites of ground motions were incrementally scaled up until collapse was reached. Collapse is defined in this study as excessive interstory drifts (>5%). This drift limit was chosen because the gravity system; which was not explicitly modeled but idealized as a single leaning column; is not expected perform past 5% drift. This is also slightly over the allowable maximum drift limit from LATBSDC of 4.5% (LATBSDC, 2017). This limit is also past the point where the models become unstable and the incremental dynamic analysis (IDA) curves became flat. Other forms of non-simulated collapse, including shear demands in the walls were checked, but did not govern.

As described by Chandramohan (2016), using non-convergence as a failure criterion will tend to bias the results towards the short duration motions, as the longer motions will have a larger chance of terminating due to non-convergence. Accordingly, if either of the records in a pair

initiated failure due to non-convergence the cumulative distribution function (CDF) was modified as follows: 1) first, the median collapse scaling level was computed without considering any non-converged records; 2) then, if the record was below this median collapse scaling level when non-convergence occurred, it was completely removed, since there is no way to know if that record could have gone on to increase the median level. If convergence failure occurred at a level above the median collapse scaling level, it was used to re-compute the median collapse scaling level once all non-converged records were accounted for. Since it cannot be known how much further the non-converged records could have been scaled, they were not used to compute the standard deviation of the function.

Figure 4.19a presents the empirical and lognormal fragility curves derived for the 6 story building model for the two ground motion suites. In this figure the 100% scaling level refers to the 2% in 50 year shaking level (the code design level according to the NBCC). Note that the 2% in 50 year shaking level is computed with contributions from both crustal and subduction ground motions. The same reference level was considered for both suites (as opposed to using a 2% in 50 year shaking level computed for each individual source) because the object of this study was to compare the effect of short and long duration motions – not crustal vs. subduction ground motions.

For the 6 story model, the median collapse levels for the long and short suites are 146% and 190% of the design scaling level, respectively. The median collapse scaling levels for the other archetype models are summarized in Table 4.5. The short duration suite consistently requires scaling levels ~20-30% higher than those required for the long duration suite to induce collapse. The minimum required increase in collapse scaling level is 16% for the 24 and 30 story models, while the maximum is 30% for the 6 story model. This makes sense considering the 6 story model has a much lower period compared to the 24 and 30 story models, meaning it will undergo more

cycles during the motions and will accumulate more inelastic damage, increasing the difference between the two record suites.

Number of Stories	Median Collapse Scaling Level (% of 2% in 50 year level)		
	Long Duration Suite	Short Duration Suite	Short/Long
6	146	190	1.30
12	136	166	1.22
18	146	189	1.29
24	174	201	1.16
30	185	214	1.16
Average	157	192	1.22

Table 4.5 Median collapse scaling level for all archetype models.

The CDFs in Figure 4.19a only show record-to-record (RTR) variability which arises from disparities between the ground motion records selected. According to FEMA P695 (FEMA, 2009), there are other sources of uncertainty that should be accounted for when assessing the safety of building types including design-requirement, test-data, and modeling related uncertainties. Because the design, testing, and modeling of reinforced concrete shearwalls is well established, it was assumed that each of these uncertainties is very low (the lowest beta values recommended by FEMA P695 of 0.1 were selected for each.) In Figure 4.19b, the CDFs for the 6 story model were recalculated considering the contributions of these sources of uncertainty along with the RTR variability (denoted “total variability”). In Figure 4.19b the area below a 10% probability of collapse is highlighted to emphasize that the probability of collapse at the 2% in 50 year shaking level must be less than 10% according to FEMA P695. Figure 4.20 present the CDFs for the other four model heights derived considering both RTR variability and total variability.

The two major requirements for safe design according to FEMA P695 are: 1) a low probability of collapse ($P[\text{Collapse}]$) for 2% in 50 year level ground motions (2% probability of exceedance in 50 years); and 2) an acceptable margin of safety against collapse. In order to satisfy requirement (1), there are two basic collapse prevention objectives at the 2% in 50 year shaking level: (i) probability of collapse less than 10% across the group of archetype models; and (ii) probability of collapse less than 20% for each individual model. In order to ensure a sufficient margin of safety against collapse, FEMA P695 uses the collapse margin ratio (CMR), which is the ratio between the median collapse shaking level and the 2% in 50 year shaking level, of each archetype. Both (i) the average CMR of the group, and (ii) each individual CMR, must exceed a minimum acceptable value as proposed in FEMA P695, depending on the total system collapse uncertainty ($\text{CMR}_{10\%}$ for the group and $\text{CMR}_{20\%}$ for each individual model). Table 4.6 summarizes both the collapse probabilities at the 2% in 50 year shaking level and CMRs, along with the FEMA P695 acceptable CMRs (in parentheses), for each model. Note that this study does not attempt to strictly follow the FEMA P695 methodology to assess the safety of reinforced concrete shearwall buildings - these FEMA P695 metrics have simply been adopted as convenient means to compare the relative safety of the structures computed when subjected to the two suites of motions.

According to these objectives, if this building type were being assessed using either record suite, it would pass both (1) and (2). However, the long duration suite was much closer to the limit for all criteria: the 8.0% average probability of collapse at the 2% in 50 year shaking level is very close to the 10% limit, and the average CMR of 1.57 was only just above the limit of 1.52.

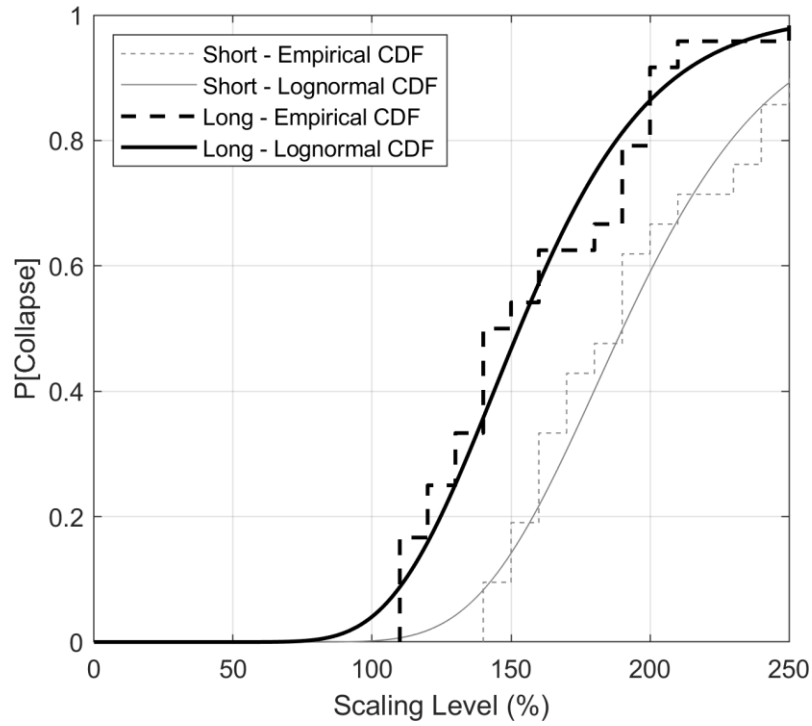
These results show that ground motion duration can significantly affect the collapse risk and margin of safety (quantified by the CMR) of this type of reinforced concrete structure. The

long duration suite caused both an increase in the probability of collapse at the 2% in 50 year shaking level and a decreased CMR across the entire suite of archetype models.

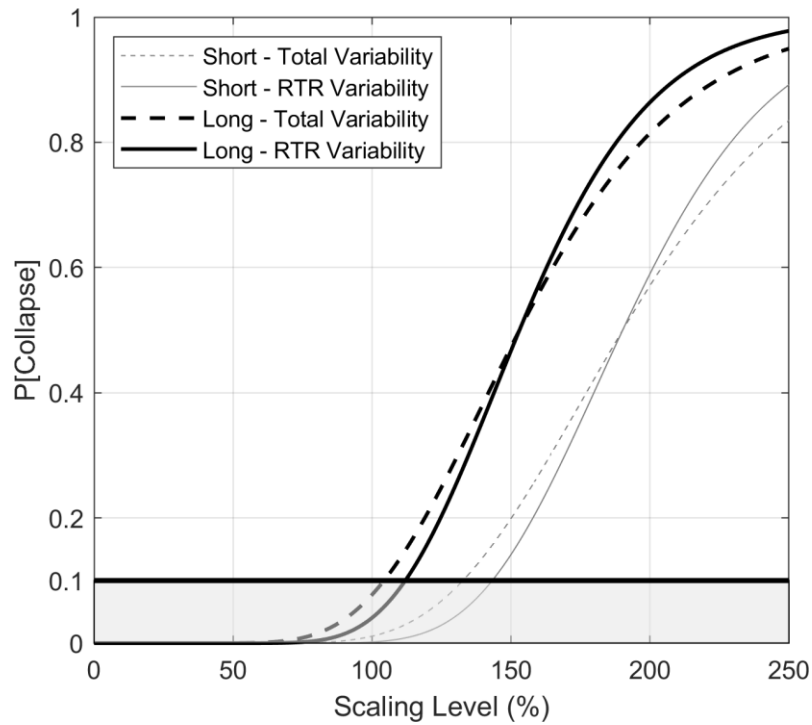
Since the spectral shapes of the anticipated motions was not accounted for, only the relative safety between the system subjected to short and long motion suites can be commented on. The absolute safety of the system should not be implied from these results.

Number of Stories	P[Collapse] at 2% in 50 year shaking level (%)		Collapse Margin Ratio (Acceptable CMR)	
	Long Duration Suite	Short Duration Suite	Long Duration Suite	Short Duration Suite
6	7.3	1.0	1.46 (1.32)	1.90 (1.26)
12	13.7	3.6	1.36 (1.28)	1.66 (1.27)
18	10.2	2.0	1.46 (1.30)	1.89 (1.30)
24	6.9	1.7	1.74 (1.37)	2.01 (1.32)
30	1.8	0.4	1.85 (1.29)	2.14 (1.28)
Average	8.0	1.7	1.57 (1.52)	1.92 (1.47)
Maximum	13.7	3.6	-	-

Table 4.6 Collapse probability at the 2% in 50 year shaking level and CMRs for all archetype models.



(a)



(b)

Figure 4.19 CDF results for the long and short duration suites for the 6 story model including (a) RTR variability only, and (b) total variability.

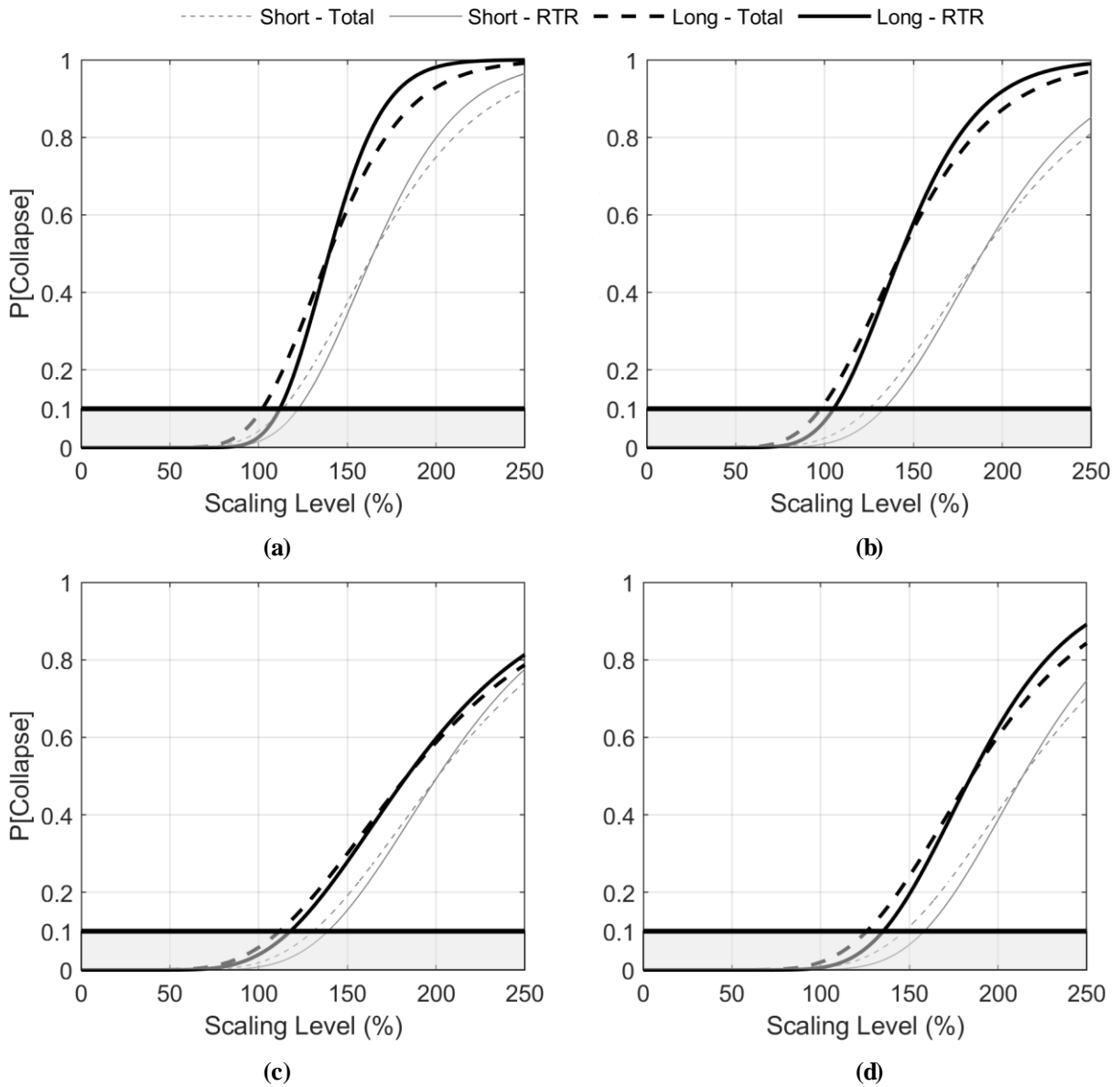


Figure 4.20 CDF results, including total variability, for the long and short duration suites for: (a) the 12 story; (b) the 18 story model; (c) the 24 story model; and (d) the 30 story model.

4.6 Conclusions

This chapter investigated the general effect of ground motion duration on the performance of RC shearwall buildings. A sensitivity study was conducted wherein a variety of building heights, from 6 to 30 stories, were subjected to two suites of spectrally equivalent records with

different duration characteristics. At code specified shaking levels, the results were not significantly different between the two motion types. This is because little damage and degradation was induced at this level of shaking. However, the longer duration motions imposed greater displacement and energy demands at higher shaking levels, where more component degradation was observed, resulting in lower collapse scaling levels when conducting IDA. This was consistent across the range of heights and scaling levels considered.

This study only considered existing, conventionally constructed, coupled RC shearwall buildings and used simplified 2D numerical models. The purpose of this study was to examine the differences between the two types of motions – not to make general conclusions about the safety of the system with respect to motion type.

In order to properly investigate the effect of ground motion duration on the safety building systems, it is important to first select proper, hazard-consistent, record suites to isolate the effect of duration. The development of appropriate subduction interface and crustal ground motion record suites will be the focus of the next chapter.

Chapter 5: An Algorithm to Match a Target Mean Spectrum and Variation

The aim of this chapter is to provide a methodology for developing ground motion suites that can be used for two purposes:

1. Comparing the difference in structural response between two suites (e.g. long vs. short duration suites).
2. Providing results from nonlinear time history analysis (NTHA) that can be used in seismic risk assessment.

In both of these goals, mean structural response, as well as variation in response, is required to be captured. Thus, the algorithm should provide ground motion suites that match both expected earthquake geophysical parameters (e.g. magnitude and distance) as well as a target spectrum mean and standard variation. It is essential to capture the variability (i.e. target spectrum standard deviation), as record-to-record spectral variability will affect the variability in structural response, which then can greatly influence the total seismic risk.

5.1 Background

In traditional time history analysis, representative time histories are typically selected and scaled to match the mean hazard, with no consideration of variation. If drawing records from a well-populated database, such as the PEER NGA-West2 database (Ancheta et al., 2013) or using spectral matching to match seed record spectra to a target mean spectrum, record-to-record variation in the response of a nonlinear model may be underestimated. Such suites may be capable of reliably predicting mean structural responses; however, may prevent the analyst from observing extreme, yet statistically relevant, responses. If higher percentile estimations of responses are required (e.g. mean plus one standard deviation demands), such records suites would not be appropriate.

On the other hand, if selecting records from a limited database, it may be possible to find a suite of records with a mean that matches a target; however, due to a mismatch of spectral shape, the spectral variation might be very large at many or all periods. Such suites might contain one or more records that induce uncharacteristically large responses in a nonlinear structural model. In both cases, it would be useful to control the spectral variation, along with the mean, of the suite of records to be used in subsequent time history analyses.

5.1.1 Variable Target Spectra

The variable target spectrum (VTS) method for spectral matching a suite of records can be used to develop a suite of motions to tightly match a mean target spectrum (Seifried, 2013; Carballo and Cornell, 1998). In the VTS method, a period dependent factoring function ($FF(T)$) is computed as the ratio of the target spectrum to the unmodified geometric mean (geomean) of the input, or “seed”, record suite. The seed records are typically first linearly scaled to the target spectrum over a certain period range of interest if their spectral amplitudes generally mismatch the target. Then, each seed record spectrum is multiplied by $FF(T)$; these are referred to as the record’s variable target spectra, as the VTS varies for each seed record. Each seed record is then spectrally matched to its VTS in the period range of interest. The result is a suite of modified records whose geomean matches the target spectrum in the period range of interest, while maintaining the spectral variability of the seed suite. The records also typically require less modification than tight spectral matching, since each record’s VTS will be closer to the original spectrum than the (typically) smooth target spectrum (uniform hazard spectrum, UHS, or otherwise).

With the VTS method, the natural spectral peaks and troughs of each record’s spectrum will also be maintained. It has been argued that removal of these spectral characteristics due to tight spectral matching to a smooth target may reduce the demand imposed by the record during

nonlinear time history analysis (e.g. Carballo and Cornell, 2000; Bazzurro and Luco, 2006; and Seifried, 2013). Although it should be noted that this conclusion has not been consistently reported (e.g. Hancock et al., 2008; and Heo et al., 2010).

Figure 5.1 illustrates the complete VTS method. A suite of 22 sample records was first linearly scaled to a conditional mean spectrum (CMS) target (Figure 5.1a) between 0.3 to 3.0 s (unshaded region). The FF(T) (Figure 5.1b) was then computed and used to define 22 unique VTS (Figure 5.1c). RSPMatch05 (Hancock et al., 2006) was then used to spectrally match each seed record to its target VTS from 0.3-3.0 s (Figure 5.1d). Note that the small mismatches between the seed suite geomean and target (Figure 5.1a) have essentially been removed (Figure 5.1d) in the matching range. Outside of this period range, there has been no modification to the seed spectral values.

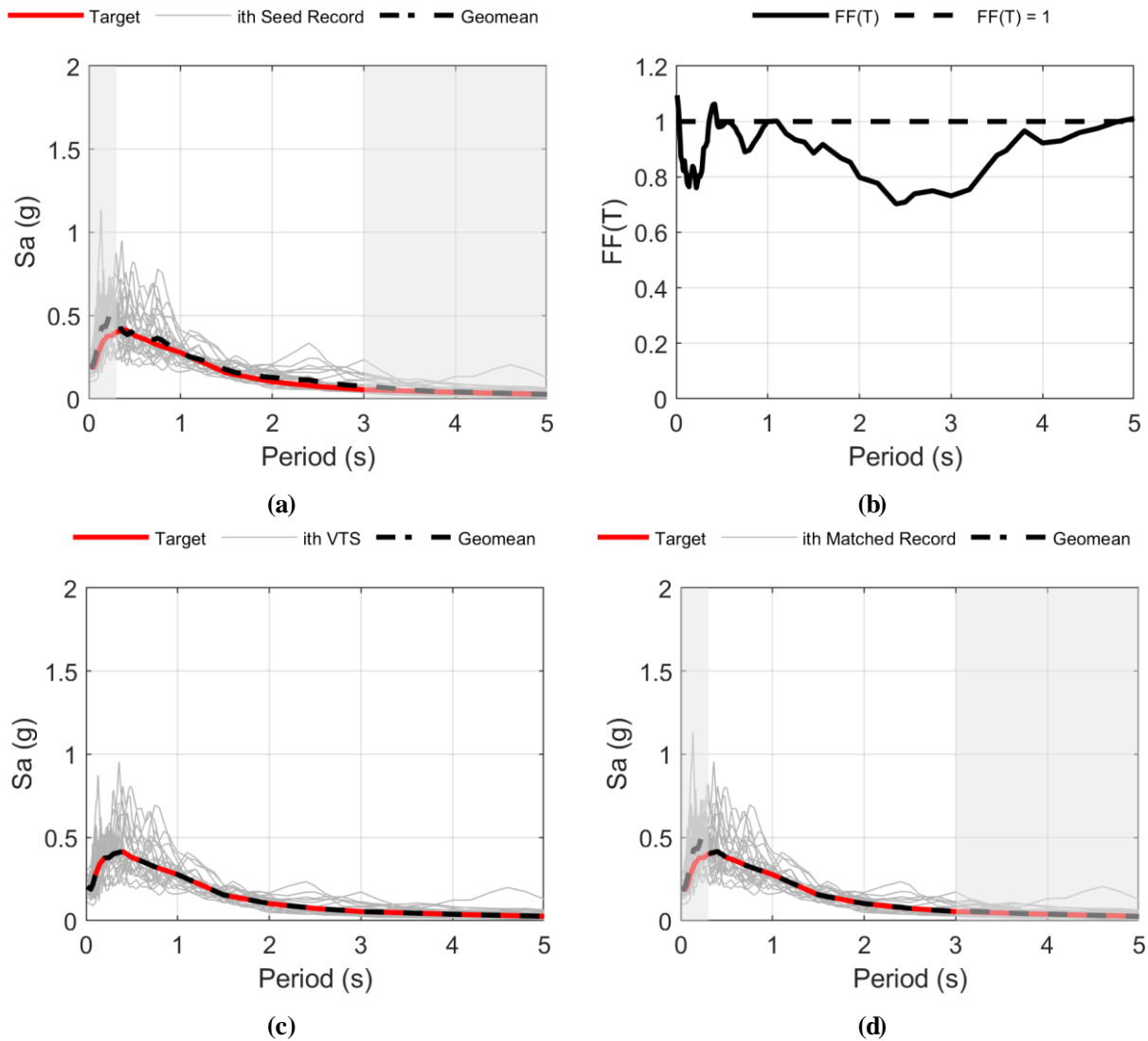


Figure 5.1 VTS method illustration: a) sample seed suite linearly scaled to a target CMS from 0.3-3.0 s, b) resulting $FF(T)$, c) suite of VTS, and d) suite of records matched to their individual VTS targets (matched from 0.3-3.0 s).

5.1.2 Conditional Spectrum

The conditional spectrum (CS; Lin et al., 2013) is a scenario- and period-dependent response spectrum and is computed using seismic hazard deaggregation information obtained from traditional probabilistic seismic hazard analysis (PSHA). A CS is recommended for risk-based

assessments and collapse analysis as it properly targets both the mean and the variation of the spectrum (NEHRP Consultants Joint Venture, 2011). Because the variation (uncertainty) in the target spectrum is explicitly accounted for, a suite of records selected to match a CS should provide time history analysis results that accurately represent the appropriate record-to-record variability when performing response history analysis.

From Lin et al. (2013), the mean of a CS, conditioned at period T_c , for each period, T_i : $\mu_{\ln SA|\ln SA(T_c)}(T_i)$; is computed as:

$$\mu_{\ln SA|\ln SA(T_c)}(T_i) = \mu_{\ln SA}(M, R, \theta, T_i) + \rho(T_i, T_c) \cdot \varepsilon(T_c) \cdot \sigma_{\ln SA}(M, R, \theta, T_i) \quad (5-1)$$

where $\mu_{\ln SA}(M, R, \theta, T_i)$ is the mean logarithmic spectral acceleration predicted by an appropriate ground motion model (GMM) for T_i based on a scenario-specific magnitude, M ; distance metric, R ; and any other number of parameters, θ ; $\rho(T_i, T_c)$, is the epsilon correlation coefficient between T_i and T_c ; $\sigma_{\ln SA}(M, R, \theta, T_i)$ is the lognormal standard deviation from the GMM for the specified scenario; and $\varepsilon(T_c)$ is the epsilon value at the T_c , for the specified hazard level, computed as:

$$\varepsilon(T_c) = \frac{\ln(SA(T_c)) - \mu_{\ln SA}(M, R, \theta, T_i)}{\sigma_{\ln SA}(M, R, \theta, T_i)} \quad (5-2)$$

where $SA(T_c)$ is the spectral acceleration required at the conditioning period for the specific hazard level, and all other terms have previously been defined. For example, $SA(T_c)$ may be the spectral acceleration with an annual exceedance frequency (AEF) of 1/2475 at T_c . M , R , and θ would come from a seismic hazard deaggregation for this spectral value at T_c .

Then, the logarithmic standard deviation at each period, $\sigma_{\ln SA|\ln SA(T_c)}(T_i)$, of the CS is computed as:

$$\sigma_{\ln SA|\ln SA(T_c)}(T_i) = \sigma_{\ln SA}(M, R, \theta, T_i) \cdot \sqrt{1 - \rho^2(T_i, T_c)} \quad (5-3)$$

Once a target mean and lognormal standard deviation have been defined, algorithms for developing suites of motions to match a CS can be employed if a sufficiently large record database is available (Jayaram et al., 2011).

Equations 5-1 and 5-3 depend on the epsilon correlation coefficients ($\rho(T_i, T_c)$) between each period, T_i , and the conditioning period, T_c . These essentially define, for each T_i , how correlated the epsilon value at T_i is to that at T_c . When $T_i = T_c$, the correlation is 1.0; as T_i moves away from T_c the correlation would be expected to drop, as further spaced periods would tend to be less correlated. For example, if a ground motion record had a very high epsilon at a very short period (i.e. very rare level of shaking at that period), one would expect other short periods to also have high epsilons (produce large spectral values compared to those predicted by an appropriate GMM); however, one would not necessarily assume that very high period spectral values are equally as rare. Thus, these high periods would be expected to have much lower epsilon values (since high epsilon values are, by definition, rare), and therefore, would have low epsilon correlations to the short periods.

Baker and Jayaram (2008) developed a set of equations to compute $\rho(T_i, T_c)$ using ground motions from the PEER NGA-West2 database and the PEER NGA-West2 GMMs to compute ε . These equations are commonly employed to compute CS – however their application to subduction zone earthquake is not clear. The application of the Baker and Jayaram (2008) epsilon correlations is further explored in Section 5.4.1 using records from the subduction ground motion database developed in Section 3.3.1.

5.1.3 Subduction Interface Records

Algorithms for developing suites of motions to match a CS have been developed (Jayaram et al., 2011); however, these depend on large databases of motions, such as the PEER NGA-West2

database (Ancheta et al., 2013). Due to the limited number of megathrust subduction earthquake recordings, it is difficult to find suitable subduction recordings to match a target spectrum, especially when constrained by parameters such as site class, distance, and magnitude. Due to this, the proposed methodology is particularly useful for developing suites of subduction records that match both the target conditional mean spectrum and a target standard deviation required when using a CS.

The Center for Engineering Strong Motion Data (CESMD) provide data for only six subduction events larger than magnitude 8.0, of which only two are above 8.5 (Table 5.1). The majority of these events were poorly recorded, with few recordings available, many from recording stations too far away to be useful or without site class information. For large magnitude megathrust subduction record selection, only two of these events are particularly useful (have records with appropriate distance ranges and site information): Maule, Chile and Tohoku, Japan. Since there are no large magnitude subduction event recordings from the Cascadia region (which is capable of producing up to magnitude 9.0 events), records from these two events are generally used in this region. Accordingly, it can be difficult to select and scale ground motion records to reasonably match a target subduction UHS or conditional mean spectrum (CMS), and much more so to match a CS.

Event Location	Date	Magnitude	Number of Recordings
South Sumatra, Indonesia	Sept 12, 2007	8.4	1
Samoa Islands Region	Sept 29, 2009	8.0	1
Maule, Chile	Feb 27, 2010	8.8	35
Tohoku, Japan	Mar 11, 2011	9.1	1226
Iquique, Chile	Apr 01, 2014	8.2	1
Coquimbo, Chile	Sept 16, 2015	8.3	8

Table 5.1 Subduction earthquake events greater than magnitude 8.0 with time history data available by the CESMD (<https://www.strongmotioncenter.org/>, accessed 07/18) and K-Net/KiK-Net (Kinoshita, 1998) databases.

5.2 Methodology

Once a target mean spectrum and standard deviation have been defined, the following steps are taken to simultaneously match a seed suite to both targets.

First, the geometric mean (geomean) of the seed suite spectra, $SA_{geo}(T_i)$, is computed as:

$$SA_{geo}(T_i) = \sqrt[n]{SA_1(T_i) \cdot SA_2(T_i) \cdot \dots \cdot SA_n(T_i)} \quad (5-4)$$

where n is the number of records in the suite and $SA_n(T_i)$ is the spectral acceleration value of the n th seed record at period T_i .

Next, a period-dependent factor function, $FF(T_i)$, is computed as the ratio between the target mean spectrum: $SA_{target}(T_i)$, and $SA_{geo}(T_i)$. This is similar to that explored by Seifried (2013) and Carballo and Cornell (1998):

$$FF(T_i) = \frac{SA_{target}(T_i)}{SA_{geo}(T_i)} \quad (5-5)$$

Then, the VTS for each seed record, j , is computed by multiplying the record's seed spectrum, $SA_j(T_i)$, by the factor function at each period, T_i :

$$VTS_j(T_i) = FF(T_i) \cdot SA_j(T_i) \quad (5-6)$$

The suite of VTS_j will match the target geomean spectral accelerations for all (T_i) ; however, the target spectra must still be modified to match the target standard deviation. This can be done by applying two simple observations:

- 1) If a series of data points is linearly scaled by a factor, the standard deviation and mean of the series will also scale by the same factor, and;
- 2) if a factor is added to each data point in a series, the mean will be increased by the factor, while the standard deviation will remain unchanged.

From the first statement, it follows that each data point, in this case: $VTS_j(T_i)$; can be modified by a single linear function in log-space to adjust the standard deviation of the suite at each period T_i :

$$\ln(VTS'_j(T_i)) = \ln(VTS_j(T_i)) \cdot \frac{\sigma_{target}(T_i)}{\sigma_{VTS}(T_i)} \quad (5-7)$$

where $VTS'_j(T_i)$ is the modified VTS for record j , $\sigma_{target}(T_i)$ is the target lognormal standard deviation, and $\sigma_{VTS}(T_i)$ is the lognormal standard deviation of the suite of $VTS_j(T_i)$ before modification.

However, according to (1), this has also changed the mean of the suite of $VTS'_j(T_i)$, which previously matched the target. Thus, (2) is employed to set the mean of $VTS'_j(T_i)$ back to the target:

$$\ln(VTS^*_j(T_i)) = \ln(VTS'_j(T_i)) - \mu_{VTS}(T_i) \cdot \frac{\sigma_{target}(T_i)}{\sigma_{VTS}(T_i)} + \mu_{target}(T_i) \quad (5-8)$$

where $VTS_j^*(T_i)$ is the correctly modified VTS for record j , $\mu_{\text{target}}(T_i)$ is the target lognormal mean spectrum, $\sigma_{\text{target}}(T_i)$ is the target lognormal standard deviation, $\sigma_{VTS}(T_i)$ is the lognormal standard deviation of the suite of $VTS_j(T_i)$ before modification; and $\mu_{VTS}(T_i)$ is the lognormal mean of the suite before modification. Combining Equations 5-7 and 5-8, yields a complete equation to compute $VTS_j^*(T_i)$ for each seed record:

$$\ln(VTS_j^*(T_i)) = \ln(VTS_j(T_i)) \cdot \frac{\sigma_{\text{target}}(T_i)}{\sigma_{VTS}(T_i)} - \mu_{VTS}(T_i) \cdot \frac{\sigma_{\text{target}}(T_i)}{\sigma_{VTS}(T_i)} + \mu_{\text{target}}(T_i) \quad (5-9)$$

The suite of $VTS_j^*(T_i)$ will have the correct lognormal standard deviation, however the mean has been unchanged and will still match the mean of $VTS_j(T_i) = \mu_{\text{target}}(T_i)$.

Finally, each seed record is spectrally matched to its target $VTS_j^*(T_i)$ in the period range of interest. This can be done using existing spectral matching techniques (e.g.: Al Atik and Abrahamson, 2010; Hancock et al., 2006). The resulting suite of matched records will match both the target mean spectrum and target standard deviation in the period range of interest.

For multiple degree of freedom (MDOF) systems, which may be governed by the response at several periods; and inelastic systems, which may yield and undergo period elongation; multiple CS are recommended in order to capture the response at all periods that significantly affect the behavior of the system (NEHRP Consultants Joint Venture, 2011; ASCE/SEI, 2016). Due to this, it is recommended to initially select and scale a suite of motions to a UHS, rather than CMS, so that the same seed suite can be used to match multiple CS. The seed suite should be selected from a database filtered by geophysical parameters such as site class, event magnitude, and distance, which can be obtained from seismic hazard deaggregation at the conditioning period of interest.

5.2.1 Application to CS

To apply the methodology from the previous section to a CS target, the target spectrum required in Equation 5-5 is set to the CMS as:

$$SA_{target}(T_i) = e^{\mu_{\ln SA|\ln SA(T_c)}(T_i)} \quad (5-10)$$

The target lognormal mean spectrum and standard deviation required in Equation 5-9 are simply defined as the CS targets:

$$\mu_{target}(T_i) = \mu_{\ln SA|\ln SA(T_c)}(T_i) \quad (5-11a)$$

$$\sigma_{target}(T_i) = \sigma_{\ln SA|\ln SA(T_c)}(T_i) \quad (5-11b)$$

The entire algorithm to match a target CS summarized in Figure 5.2.

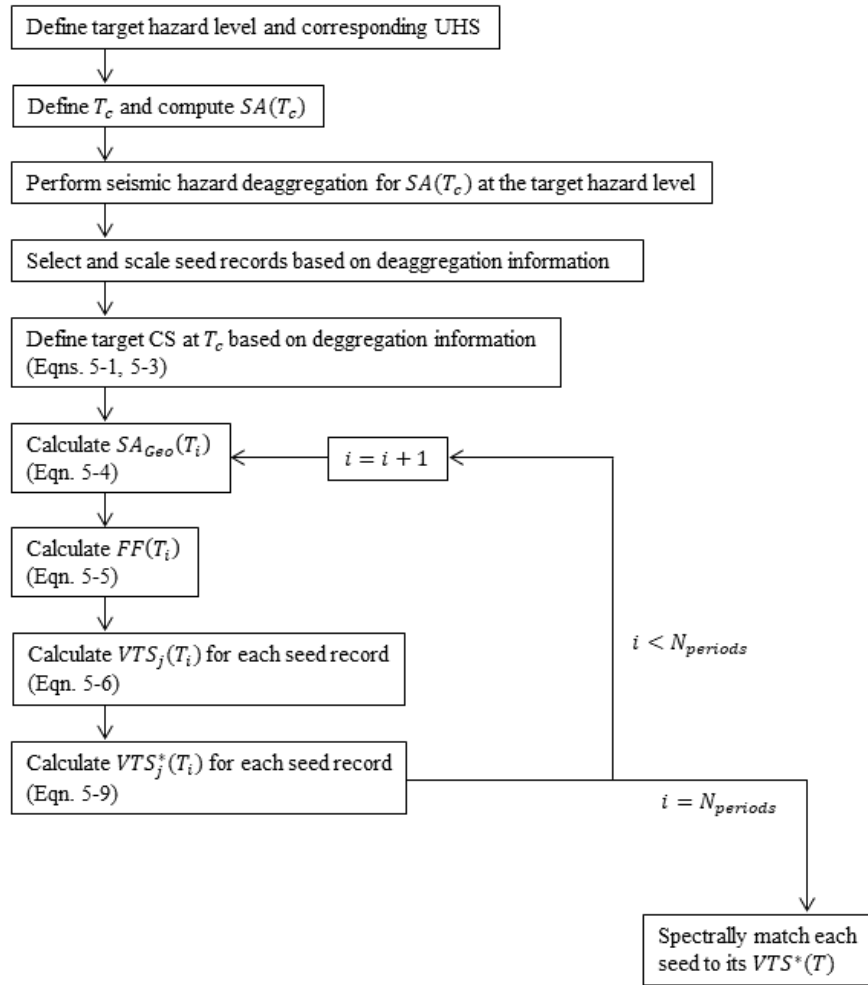


Figure 5.2 Algorithm for developing a suite of records matched to a target conditional mean spectrum and standard deviation.

5.2.2 Modification of Outliers

When computing $VTS_j^*(T_i)$ for each seed record at period i , Equation 5-9 essentially expands or constricts the $VTS_j(T_i)$ spectral values for the suite at period i to increase or decrease the spectral variation. If the target variation is higher than the natural variation in the suite of $VTS_j(T_i)$, then all $VTS_j^*(T_i)$ above the mean will be increased, while all $VTS_j^*(T_i)$ below the mean

will be reduced (vice versa when reducing the variation). If the target lognormal standard deviation is much different than the lognormal standard deviation of the suite of $VTS_j(T_i)$, then the changes to some of the $VTS_j(T_i)$ may be very large. This, after the subsequent spectral matching, could produce records with very high spectral values at certain periods.

When performing nonlinear time history analysis of buildings or other structures, a single particularly demanding record may cause an unexpectedly large response, which could significantly affect the statistics of the suite analyses. Thus, another step can be introduced into the algorithm in order to reduce outlying records by a modification to $VTS_j^*(T_i)$ before spectral matching.

To do this, first, a parameter, $\varepsilon_{s_j}(T_i)$, is defined for each $VTS_j^*(T_i)$ as the number of lognormal standard deviations the spectral value is above the mean of the suite of $VTS_j^*(T_i)$ at T_i :

$$\varepsilon_{s_j}(T_i) = \frac{\ln(VTS_j^*(T_i)) - \mu_{VTS}(T_i)}{\sigma_{VTS}(T_i)} \quad (5-12)$$

where, as before, $\mu_{VTS}(T_i)$ and $\sigma_{VTS}(T_i)$ are the lognormal mean and standard deviation of the suite of $VTS_j^*(T_i)$.

An outlying spectral value is defined as any $\varepsilon_{s_j}(T_i)$ that exceeds a specified limit: ε_{lim} . ε_{lim} could be defined at each period ($\varepsilon_{lim}(T_i)$), but for simplicity it can be set constant for all T_i . Outliers are determined and modified on a period-by-period basis.

At any period, i , if $\varepsilon_{s_j}(T_i) > \varepsilon_{lim}$, then $VTS_j^*(T_i)$ can be modified by rearranging Equation 5-12:

$$\ln(VTS_j^*(T_i)) = \varepsilon_{lim} \cdot \sigma_{VTS}(T_i) + \mu_{VTS}(T_i) \quad (5-13a)$$

Similarly, if $\varepsilon_{s_j}(T_i) < -\varepsilon_{lim}$:

$$\ln(VTS_j^*(T_i)) = -\varepsilon_{lim} \cdot \sigma_{VTS}(T_i) + \mu_{VTS}(T_i) \quad (5-13b)$$

This is done for all $VTS_j^*(T_i)$ with $\text{abs}(\varepsilon_{s_j}(T_i)) > \varepsilon_{lim}$.

This process, however, will modify both $\mu_{VTS}(T_i)$ and $\sigma_{VTS}(T_i)$; and thus, after any modification $VTS_j^*(T_i)$ must be re-derived for all j using Equation 5-9. Accordingly, Equations 5-9, 5-12, and 5-13 should be solved in a loop until all $\text{abs}(\varepsilon_{s_j}(T_i)) \leq \varepsilon_{lim}$ and $\mu_{VTS}(T_i) = \mu_{target}(T_i)$ and $\sigma_{VTS}(T_i) = \sigma_{target}(T_i)$.

This process is repeated for at each period of interest for matching. Once a $VTS_j^*(T_i)$ has been defined for all periods, each seed record is then spectrally matched to its target VTS^* . The complete methodology (with or without outlier modification) is presented in Figure 5.3.

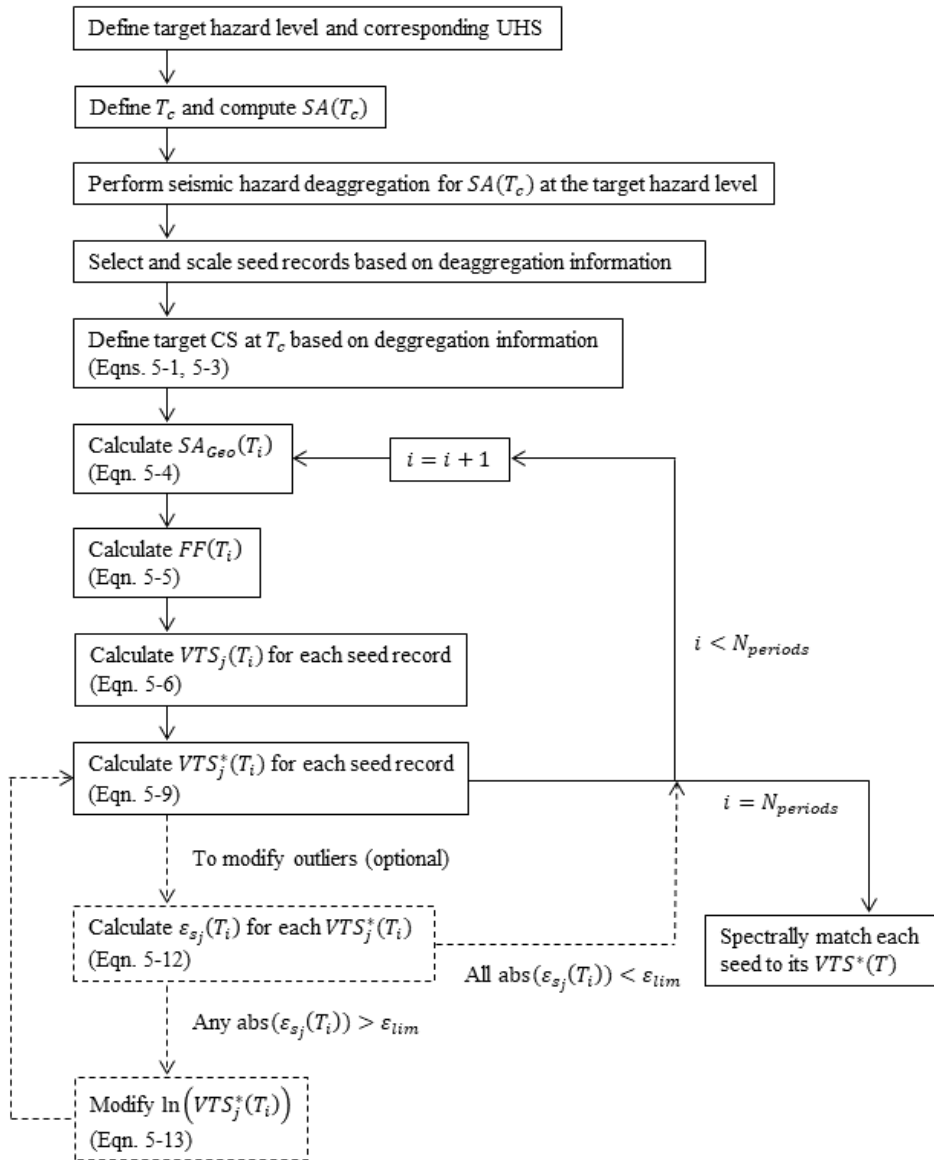


Figure 5.3 Algorithm for developing a suite of records matched to a target conditional mean spectrum and standard deviation (with outlier modification).

5.3 Example Suite Development

In this section, a subduction interface ground motion suite is developed in order to exemplify the proposed methodology. First, a set of seed records is scaled to the 2015 Vancouver 2% in 50 year subduction interface source-specific UHS. The proposed methodology is then used to match the suite to a target CS, including mean and variation, developed for Vancouver, BC. This suite is compared to one spectrally matched to the target using traditional strict spectral matching.

5.3.1 Target Conditional Spectra

The target CS is computed using the subduction source GMM developed by Abrahamson et al. (2016) and the Baker and Jayaram (2008) epsilon correlation coefficients, which have been observed to be suitable for both crustal and subduction events (Bebamzadeh et al., 2017; Carlton and Abrahamson, 2014; Jayaram et al., 2011). The CS is conditioned at $T_c = 1.0$ s to the 1/2475 spectral acceleration ($SA(T_c = 1.0) = 0.277$ g) for Vancouver, BC, Site Class C, obtained using the 2015 GSC seismic hazard model run with subduction sources only (Halchuk et al., 2014). The subduction source-specific UHS and target CMS are presented in Figure 5.4a; the seismic hazard deaggregation of magnitude and distance for $SA(T_c = 1.0) = 0.277$ g is presented in Figure 5.4b. The mean magnitude (M_w) at the hazard level is 8.82, and the mean closest distance (R_{CD}) is 137.5 km. The reason the CMS peaks above the UHS at periods < 1.0 s is because the CMS was developed using only the Abrahamson et al. (2016) GMM, while the seismic hazard model used to generate the subduction UHS uses a weighted logic tree with four distinct subduction-source GMMs (one of which is the Abrahamson et al., 2016 model; Halchuk et al., 2014; Table 2.1).

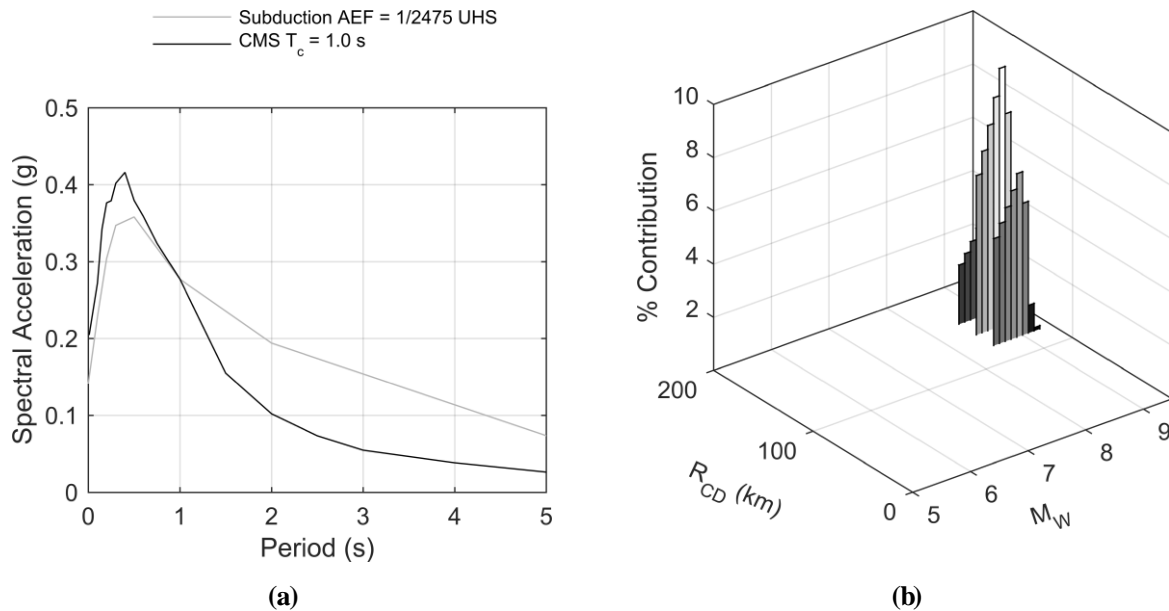


Figure 5.4 (a) Source-specific subduction UHS with $AEF = 1/2475$ and CMS with $T_c = 1.0$ s; and (b) Vancouver subduction hazard magnitude and distance deaggregation for $SA(T_c = 1.0) = 0.277$ g (mean magnitude, $M_w = 8.82$; mean distance, $R_{CD} = 137.5$ km).

Eleven seed records (with two horizontal components each, for a total of 22 components) were selected from the 2010 Maule, Chile ($M_w = 8.8$) and 2011 Tohoku, Japan ($M_w = 9.1$) earthquakes. NEHRP Site Class C ($V_{s30} = 360$ - 760 m/s) records from $R_{CD} = 75$ - 150 km were preferred. The records were selected based on their fit to the source-specific UHS¹ and then linearly scaled to the target CMS (Figure 5.4a). The records were scaled to minimize the mean squared error (MSE) between the target CMS and geomean of the horizontal record components. The metadata of the seed records is summarized in Table 5.2. Figure 5.5a and b illustrate the seed record spectra and suite geomean spectrum compared to the target CMS, and the seed record lognormal standard deviation compared to the target lognormal standard deviation, respectively.

¹ The source-specific UHS is obtained by conventional PSHA, except that only a specific type of source is included in the model

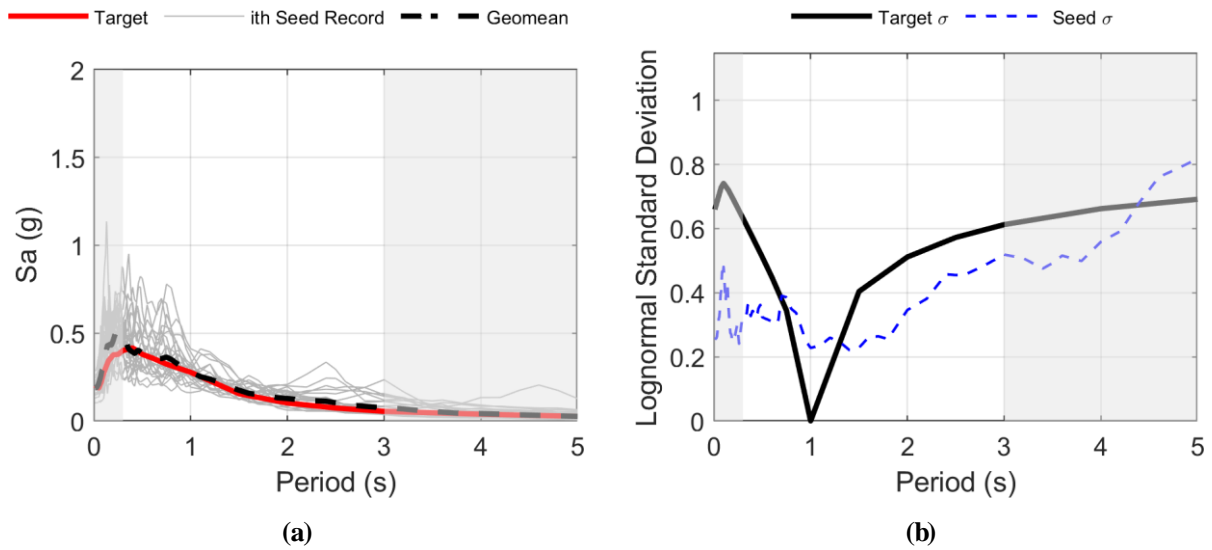


Figure 5.5 Seedrecord suite: (a) acceleration spectra vs. target CMS (conditioned to $SA(T_c = 1.0) = 0.277g$); and, (b) lognormal standard deviation vs. target conditional standard deviation.

Event	Station	R_{CD} (km)	V_{s30} (m/s)	Scale Factor
Maule	Hualane	35	528	0.61
Maule	Matanzas	79	370	0.54
Maule	SJCH	177	495	0.54
Maule	Stgo La Florida	174	685	1.30
Maule	Stgo Penalolen	177	452	0.77
Tohoku	AKT006	194	404	2.49
Tohoku	CHB013	178	374	1.40
Tohoku	FKS021	161	453	2.28
Tohoku	MYG016	114	580	0.54
Tohoku	SIT001	188	360	1.74
Tohoku	SIT002	180	351	1.47

Table 5.2 Subduction seedrecord metadata.

In order to apply the proposed methodology, first the $FF(T)$ function and VTS for the suite were computed. Figure 5.6a presents the $FF(T)$ function, obtained by Equation 5-5; and Figure 5.6b illustrates the unmodified VTS for the suite obtained by multiplying $FF(T)$ by the original spectra for each seed record (Equation 5-9).

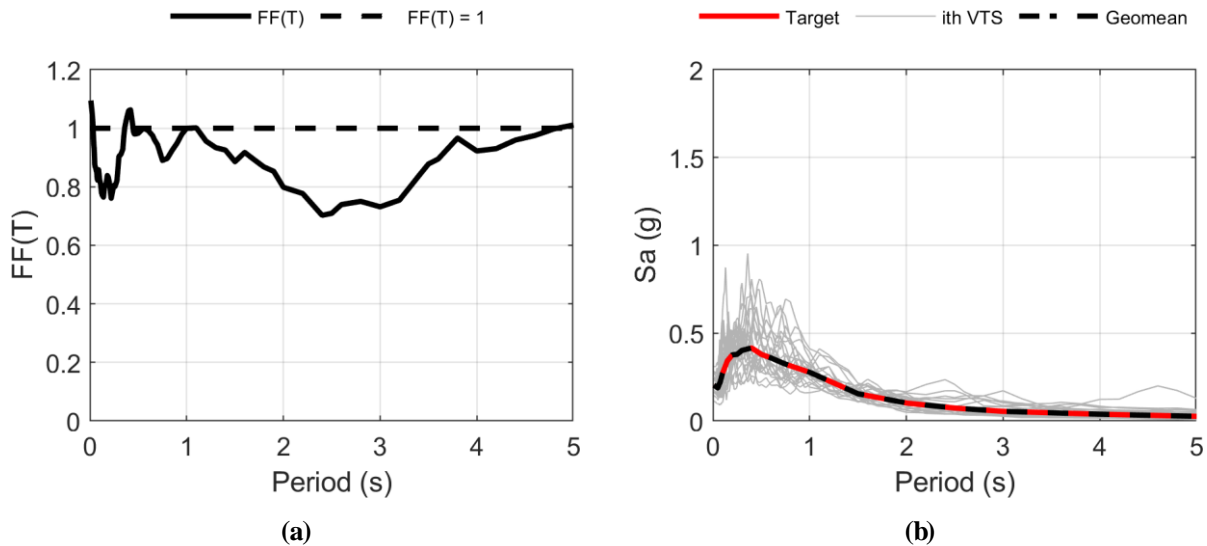


Figure 5.6 Seed records suite: (a) $FF(T)$; and, (b) target VTS.

Each seed record was then spectrally matched to its target VTS from 0.3-3.0s using RSMATCH05 (Hancock et al., 2006). The default matching parameters were used with a 5% matching tolerance. The resulting spectra are illustrated in Figure 5.7a; note that the geomean of the matched suite nearly perfectly matches the target CMS in the matched period range. Figure 5.7b shows the lognormal standard deviation of the seed suite compared to the conditional target standard deviation. Because the traditional VTS matching method does not consider standard deviation, the suite does not match the target standard deviation; the standard deviation depends entirely on the seed records selected. The selection of a different suite of seed records would result in a completely different variation; this is not ideal if the records were to be used for a risk-based assessment, which strongly depends on record-to-record variation from time history analysis.

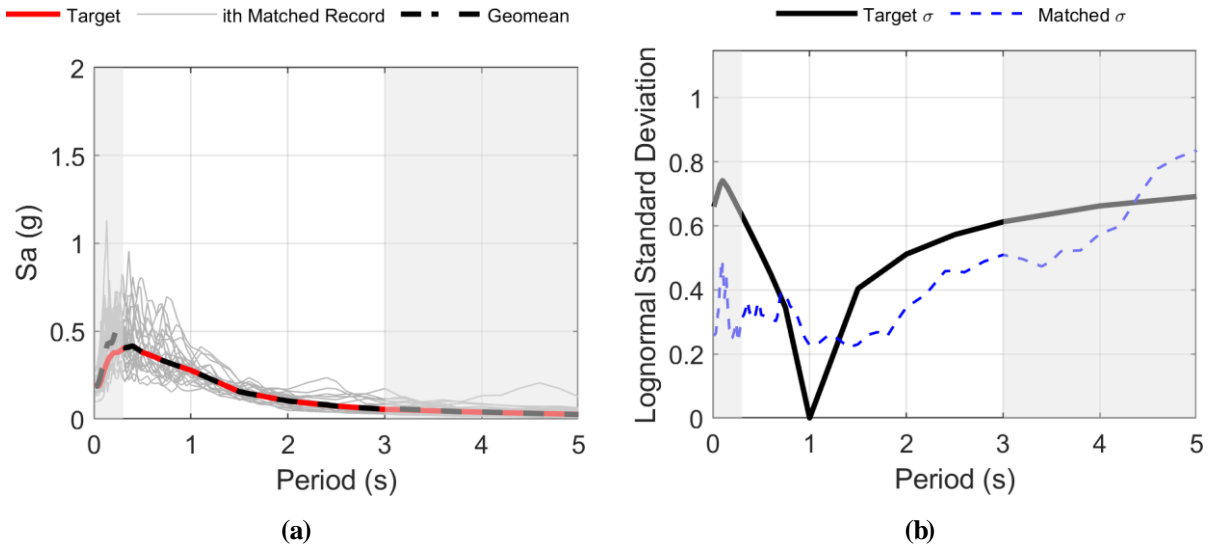


Figure 5.7 Matched (to VTS from 0.3-3.0s) recordsuite: (a) acceleration spectra vs. target CMS (conditioned to $SA(T_c = 1.0) = 0.277g$); and, (b) lognormal standard deviation vs. target conditional standard deviation.

Next, target VTS* are developed following the algorithm outlined in Figure 5.2. The individual VTS* and the geomean of the suite are presented in Figure 5.8a; the lognormal standard deviation of the suite of VTS* is presented in Figure 5.8b. Note that the geomean of the suite matches the target CMS and the lognormal standard deviation of the suite perfectly matches the target conditional standard deviation. Figure 5.9a and b show the resulting suite of records spectrally matched to the target VTS* from 0.3-3.0s. It can be observed that many of the spectral values, especially around 0.3-0.5s, have been significantly amplified in order to meet the target standard deviation. To remedy this effect, the optional outlier modification method should be employed.

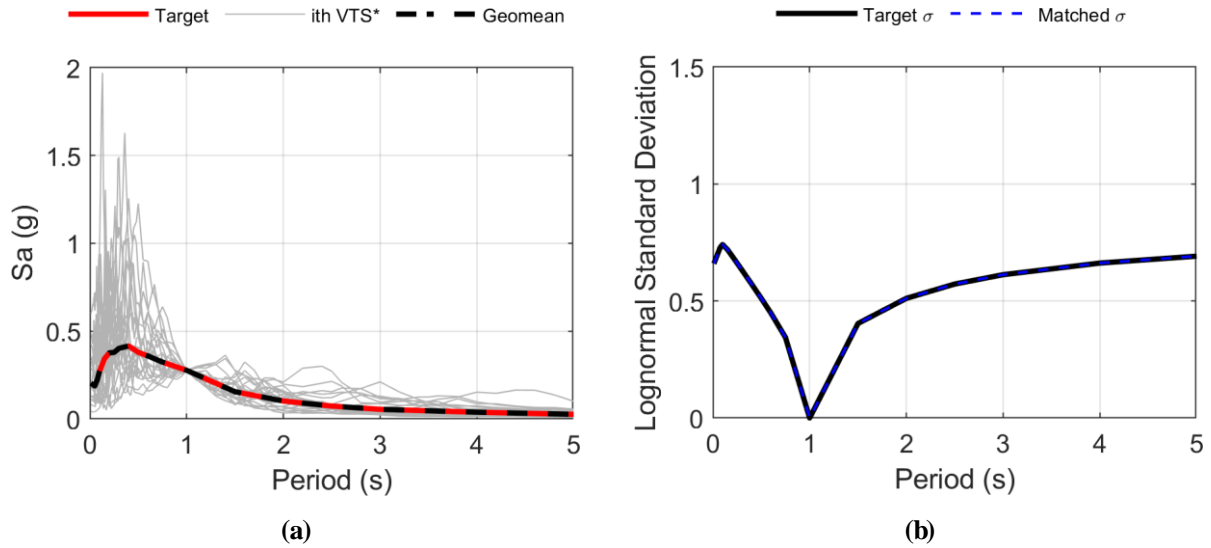


Figure 5.8 Target VTS* suite: (a) acceleration spectra vs. target CMS (conditioned to $SA(T_c = 1.0) = 0.277g$); and, (b) lognormal standard deviation vs. target conditional standard deviation.

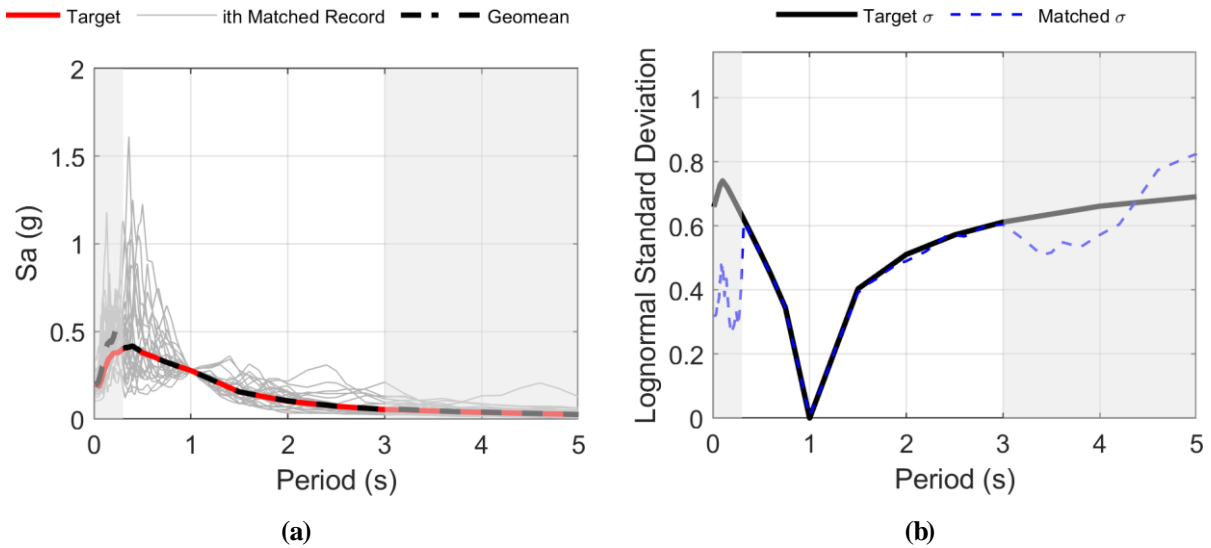


Figure 5.9 Matched (to VTS* from 0.3-3.0s) records suite: (a) acceleration spectra vs. target CMS (conditioned to $SA(T_c = 1.0) = 0.277g$); and, (b) lognormal standard deviation vs. target conditional standard deviation.

Accordingly, the VTS* were then re-derived using the full algorithm from Figure 5.3 (including outlier modification). The ϵ_{lim} was set to a 2.0 in this example. Figure 5.10a and b present the results of the matched suite – the matched suite geomean and lognormal standard deviation still match the targets in the 0.3-3.0s matching range – however, comparing Figure 5.9a and Figure 5.10a shows that the large spectral ordinates in the matched suite around ~0.3-0.5 s and ~2.0 s have been reduced. Figure 5.11a and b illustrate the ϵ_s of the suite matched without and with the outlier modification, respectively. Figure 5.11b illustrates how, within the matching period range of 0.3-3.0s, all ϵ_s values have been limited to 2.0; whereas before modification there were several periods where records exceeded this value. Results from time history analysis using this suite of records would be expected to predict the correct mean and record-to-record variation without any unexpected bias from potential outlying records.

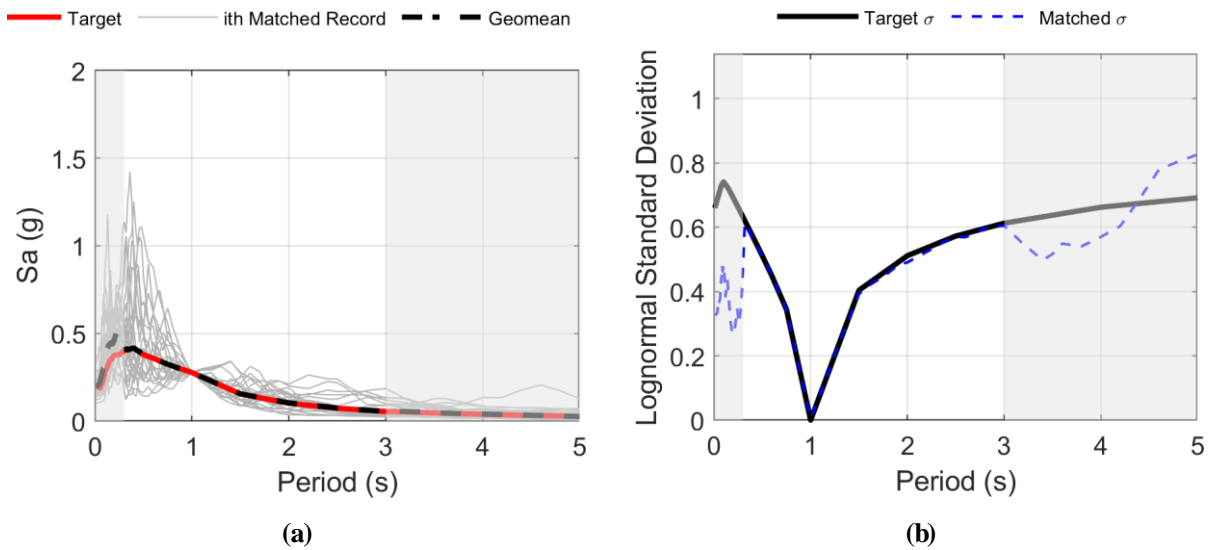


Figure 5.10 Matched (to VTS* from 0.3-3.0s, with outliers modified) record suite: (a) acceleration spectra vs. target CMS (conditioned to $SA(T_c = 1.0) = 0.277g$); and, (b) lognormal standard deviation vs. target conditional standard deviation.

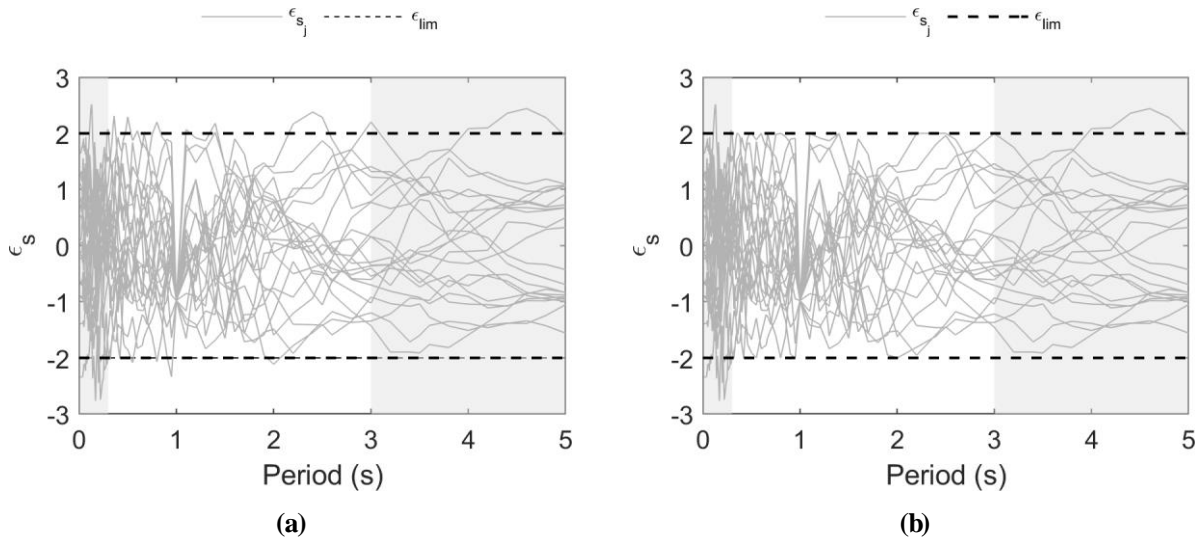


Figure 5.11 $\epsilon_{s_j}(T)$ for record suite matched to VTS* from 0.3-3.0s (a) without outlier modification; and, (b) with outlier modification ($\epsilon_{lim} = 2.0$).

5.3.2 Comparison to Traditional Spectral Matching

For comparison, each seed record was also spectrally matched to the target UHS from 0.3-3.0 s using traditional spectral matching. Using this approach, each record is tightly matched to the target (target CMS in this case) using spectral matching. The resulting spectra and lognormal standard deviation of the suite are presented in Figure 5.12a and b, respectively. This case is used as an example show how traditional spectral matching removes all variability in the matched suite in the matching range.

Figure 5.13a and b present the spectra of an example record: Tohoku MYG016, matched to the target UHS and to its specific VTS*, respectively. To ensure that spectrally matched records are realistic and acceptable, various time series of the seed and matched records are typically compared: including acceleration, velocity, displacement, and Arias Intensity. Preferably, the spectral matching process would not induce and large changes in any of these time series that may cause the record to be considered unrealistic (Al Atik and Abrahamson, 2010). Accordingly,

Figure 5.14 and Figure 5.15 present the time histories of this record before and after matching to the target UHS and target VTS*, respectively. It is observed in Figure 5.13 that less change to the spectra of the record is required when matching to the VTS*, as it is closer to the seed record spectrum than the smooth target UHS. Due to this, there is less change in the time histories when matching this record to its VTS* (Figure 5.15) compared to the UHS (Figure 5.14). This is typical of all the matched records and is another benefit that can be realized when using the proposed methodology.

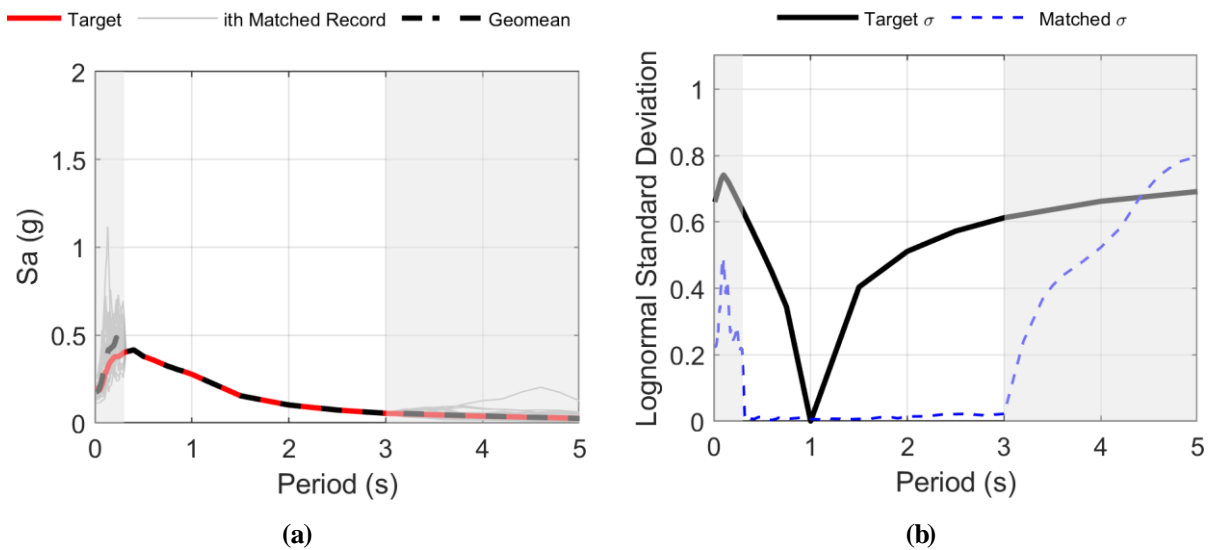
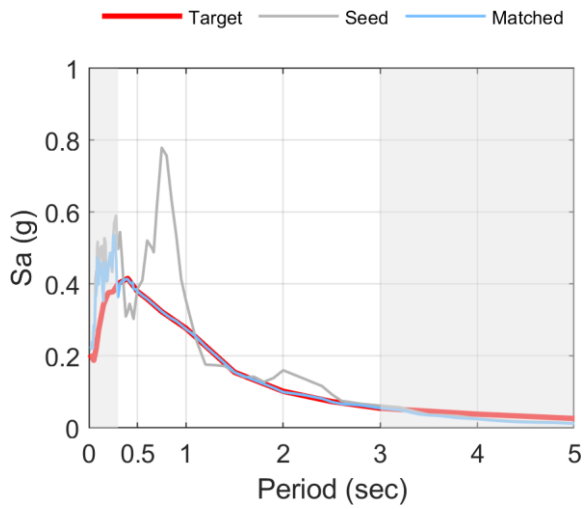
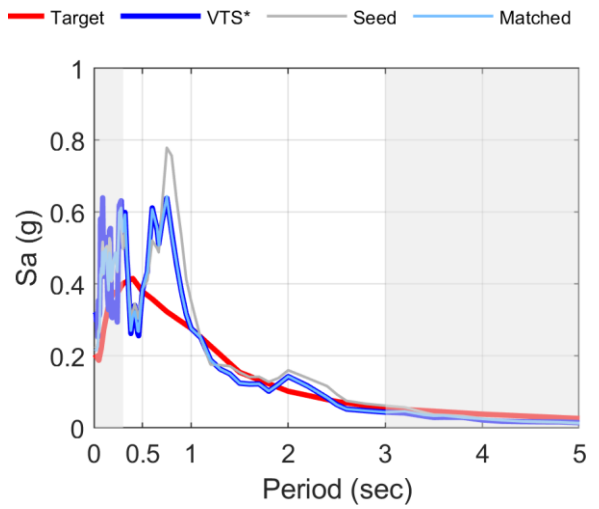


Figure 5.12 Matched (using traditional spectral matching from 0.3-3.0s) records suite: (a) acceleration spectra vs. target subduction source-specific UHS (1/2475 annual exceedance frequency); and, (b) lognormal standard deviation vs. target conditional standard deviation.



(a)



(b)

Figure 5.13 Example Tohoku, Japan record matched (from 0.3-3.0s) to: (a) the target CMS; and, (b) its target VTS*.

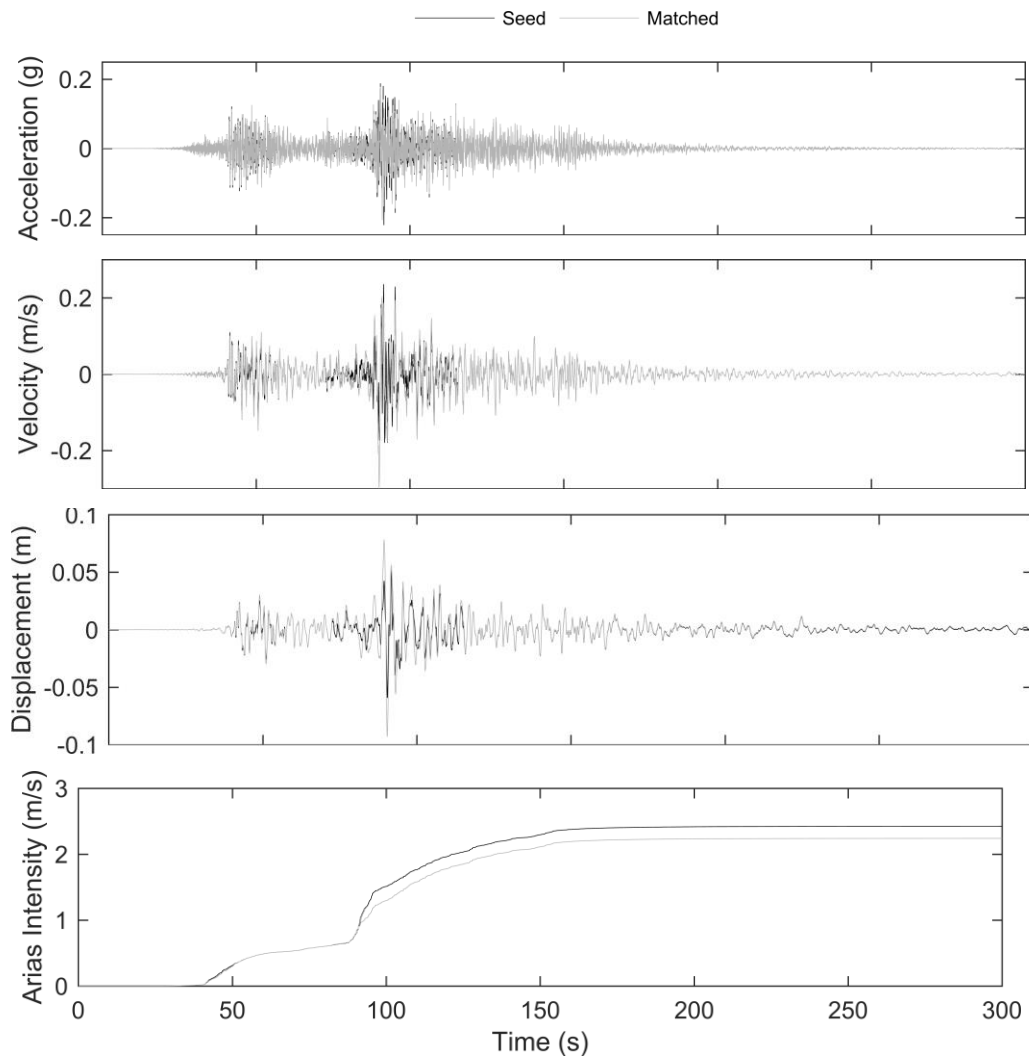


Figure 5.14 Example Tohoku, Japan seed and matched record (from 0.3-3.0s) to the target UHS, from top to bottom: acceleration; velocity; displacement; and, Arias intensity time histories.

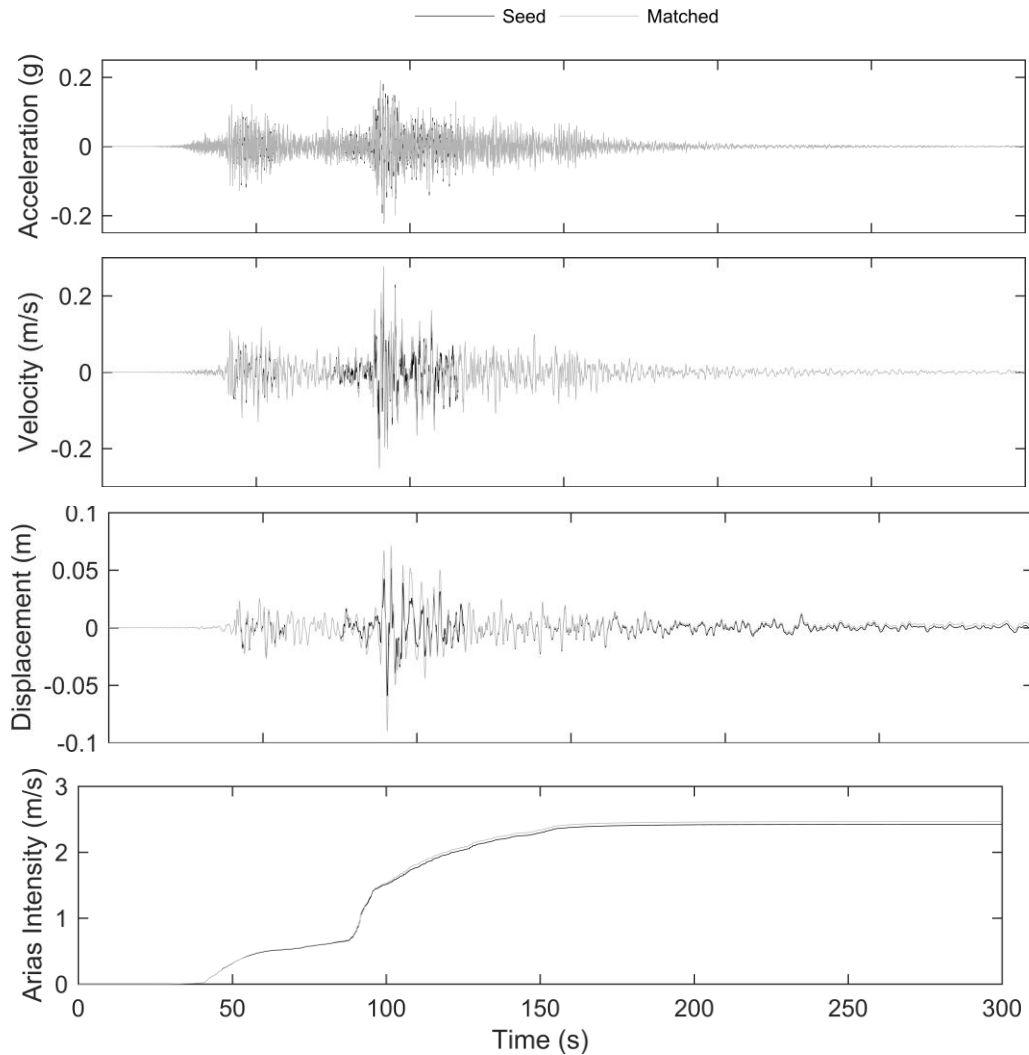


Figure 5.15 Example Tohoku, Japan seed and matched record (from 0.3-3.0s) to its target VTS*, from top to bottom: acceleration; velocity; displacement; and, Arias intensity time histories.

5.4 Other Considerations

This section explores two other topics related to the application of the proposed methodology to match subduction zone earthquakes to a target CS. First, the correlation of spectral values in subduction earthquake events is explored. Typically, the Baker and Jayaram (2008) epsilon correlation model is used when developing CS. For convenience, it would be beneficial to use this same model for subduction earthquake events – however this has not been sufficiently

studied using large magnitude subduction interface event records. In Section 5.4.1 epsilon correlation coefficients are computed for a database of subduction zone events and compared to those from the Baker and Jayaram (2008) model.

Next, the period range of interest for matching a target spectrum is investigated in Section 5.4.2. It is important to have a well-defined period range when performing any type of ground motion record scaling or matching. The period range should include all periods that significantly contribute to the response of the structure, including both higher mode and period elongation effects, so that the ground motions are truly representative of the hazard level for the structure. The period range for RC shearwall buildings is studied using three numerical models and three different types of ground motion records in order to give recommendations for appropriate period ranges for ground motion modification for this type of structure.

5.4.1 Correlation of Spectral Values in Subduction Earthquake Events

Ground motion models (GMMs) have been developed to predict the mean and standard deviation of the logarithm of spectral acceleration for a wide variety of earthquake types and locations. Examples include the PEER NGA-West1 and West2 GMMs, which were developed for shallow, crustal events typical of locations such as California (Bozorgnia et al, 2014). Many researchers have extended these models by determining the correlation between response spectral values at different periods (Baker and Cornell, 2006; Baker and Jayram, 2008). These results can be used to develop CS and CMS (Baker and Cornell, 2006), which are becoming more commonly used for ground motion selection and scaling (NEHRP Consultants Joint Venture, 2011). Currently, the correlation coefficients developed by Baker and Jayram (2008) are commonly used to develop CS and CMS, however these were developed considering only shallow, crustal events from the NGA-West2 database. Whether or not these correlations and corresponding equations are

valid for other tectonic regimes, such as subduction zones, is currently unknown. One study by Jayram et al. (2011) investigated the correlation of response spectral values in Japanese ground motions and compared them to the Baker and Jayram (2008) correlation coefficients. It was concluded that the spectral correlations in the Japanese motions were similar to those developed by Baker and Jayram (2008), and these spectral correlations could be used as a viable surrogate for Japanese motions. The database in this study comprised of crustal and subduction zone (interface and intraslab) events; however, the largest earthquake in the database was the 2003 $M_w = 8.0$ Hokkaido earthquake.

In this section, the response correlation values from a large database of worldwide subduction zone earthquakes, including the 2011 $M_w = 9.1$ Tohoku earthquake is evaluated. The database used is that developed in Section 3.3.1, which comprises 2000 processed records from 18 earthquake events (1162 records from 10 interface events; 854 records from 8 intraslab events). The results are then compared to the correlations observed by Baker and Jayram (2008) for shallow, crustal events. These results can be used to develop CS and CMS in worldwide subduction tectonic zones, such as those found in South and Central America, Japan, and the Pacific Northwest of North America.

5.4.1.1 Spectral Correlation Calculations

A GMM typically predicts the spectral acceleration, $Sa(T)$, as a function of period, with following form:

$$\ln Sa(T) = \mu_{\ln Sa}(M, R, \theta, T) + \sigma_{\ln Sa}(M, R, \theta, T) * \varepsilon(T) \quad (5-14)$$

where $\mu_{\ln Sa}(M, R, \theta, T)$ and $\sigma_{\ln Sa}(M, R, \theta, T)$ are the mean and standard deviation of the natural log of spectral acceleration (Sa) predicted by the GMM for T . The predictions, $\mu_{\ln Sa}$ and $\sigma_{\ln Sa}$ depend on the magnitude of the event: M , some type of distance metric: R , the period of interest:

T , and any number of other parameters: θ . These parameters may include local site conditions (i.e. site class or Vs30), event type (i.e. interface or intraslab), location, etc. The term $\varepsilon(T)$ defines the number of standard deviations by which $\ln Sa$ deviates from the predicted mean: $\mu_{\ln Sa}$. For an observed ground motion with known $Sa(T)$, M , R and θ , $\varepsilon(T)$ is determined simply by calculating the number of standard deviations that the observed $Sa(T)$ varies from the mean predicted $\mu_{\ln Sa}$ from a specific GMM. This is shown mathematically by rearranging Equation 5-14 to get:

$$\varepsilon(T) = \frac{\ln Sa(T) - \mu_{\ln Sa}(M, R, \theta, T)}{\sigma_{\ln Sa}(M, R, \theta, T)} \quad (5-15)$$

For this study, the $\varepsilon(T)$ for a variety of periods is calculated for each ground motion in the database, using a variety of GMMs to determine $\mu_{\ln Sa}$ and $\sigma_{\ln Sa}$. Then, the spectral correlations between different periods are calculated using the Pearson product-moment correlation coefficient (Kutner et al., 2004) as follows:

$$\rho_{\varepsilon(T_1), \varepsilon(T_2)} = \frac{\sum_{i=1}^n (\varepsilon_i(T_1) - \overline{\varepsilon(T_1)}) (\varepsilon_i(T_2) - \overline{\varepsilon(T_2)})}{\sqrt{\sum_{i=1}^n (\varepsilon_i(T_1) - \overline{\varepsilon(T_1)})^2 \sum_{i=1}^n (\varepsilon_i(T_2) - \overline{\varepsilon(T_2)})^2}} \quad (5-16)$$

where $\varepsilon_i(T_1)$ and $\varepsilon_i(T_2)$ are the i th observations of $\varepsilon(T_1)$ and $\varepsilon(T_2)$, $\overline{\varepsilon(T_1)}$ and $\overline{\varepsilon(T_2)}$ are the means of the sample of ground motions, and n is the number of considered ground motions.

5.4.1.2 Results

Figure 5.16a presents the epsilon correlation coefficients calculated for the entire database of records calculated using Equation 5-16. Each plot in Figure 5.16 represents a different value of T_2 . The x-axis represents values of T_1 , while the y-axis represents the epsilon correlation coefficient, $\rho_{\varepsilon(T_1), \varepsilon(T_2)}$, between T_2 and T_1 . The GMM developed by Zhou et al. (2006) was used to predict geometric mean (geomean) spectral accelerations and standard deviations for the ground motions at different periods for use in Equation 5-14 and Equation 5-15. Zhao et al. (2006) provide

an empirical GMM for both interface and intraslab subduction events based on Japanese earthquake data. It was considered here initially because it can be used for both interface and intraslab events, and because the considered database is dominated by Japanese events. Figure 5.16b illustrates the epsilon correlation coefficients predicted using the Baker and Jayram (2008) model, which is based on shallow crustal events primarily from North America. Similar trends can be observed when comparing Figure 5.16a and b, although differences can be observed when T_1 is small (<0.5 s) and T_2 is large.

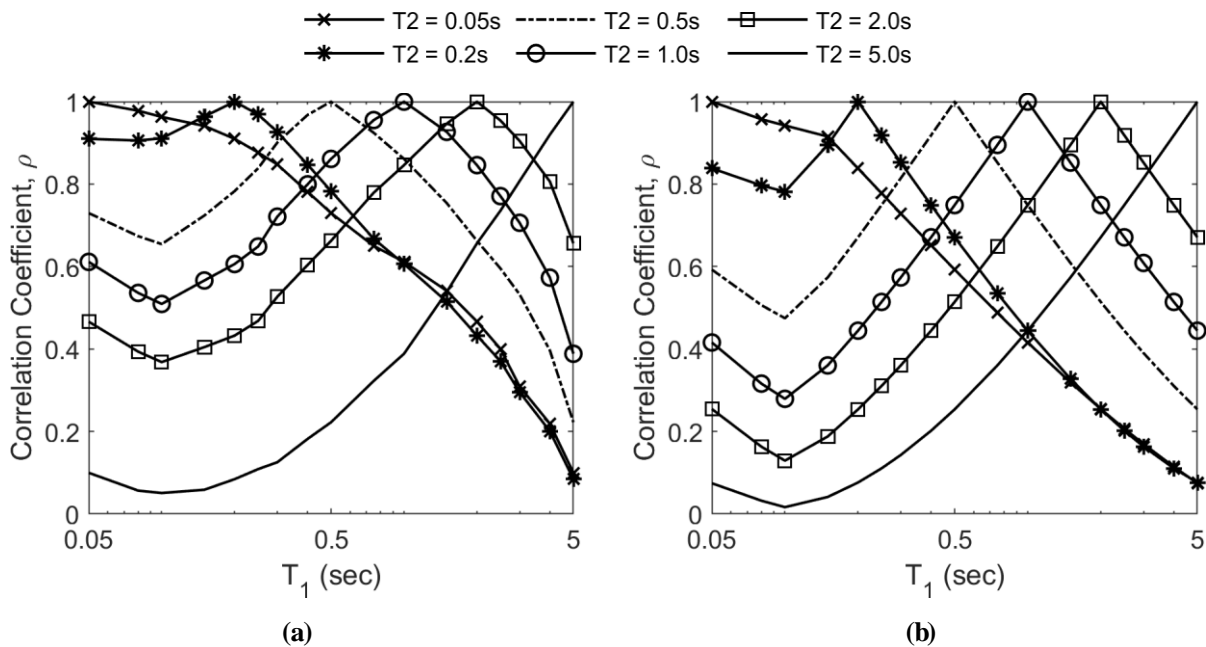


Figure 5.16 Plots of epsilon correlation coefficients, $\rho_{\varepsilon(T_1),\varepsilon(T_2)}$, between T_2 and T_1 estimated using residuals of the Zhao et al. (2006) GMM for (a) the entire record database and (b) predicted by the Baker and Jayram (2008) correlation model.

Similarly, Figure 5.17a and b present the epsilon correlation coefficient plots for the separated interface and intraslab events, respectively. These results are similar to those observed in Figure 5.16. The major difference between the two record subsets appears to be stronger

correlations between T_2 and T_1 for the subduction interface records when the two periods are far apart.

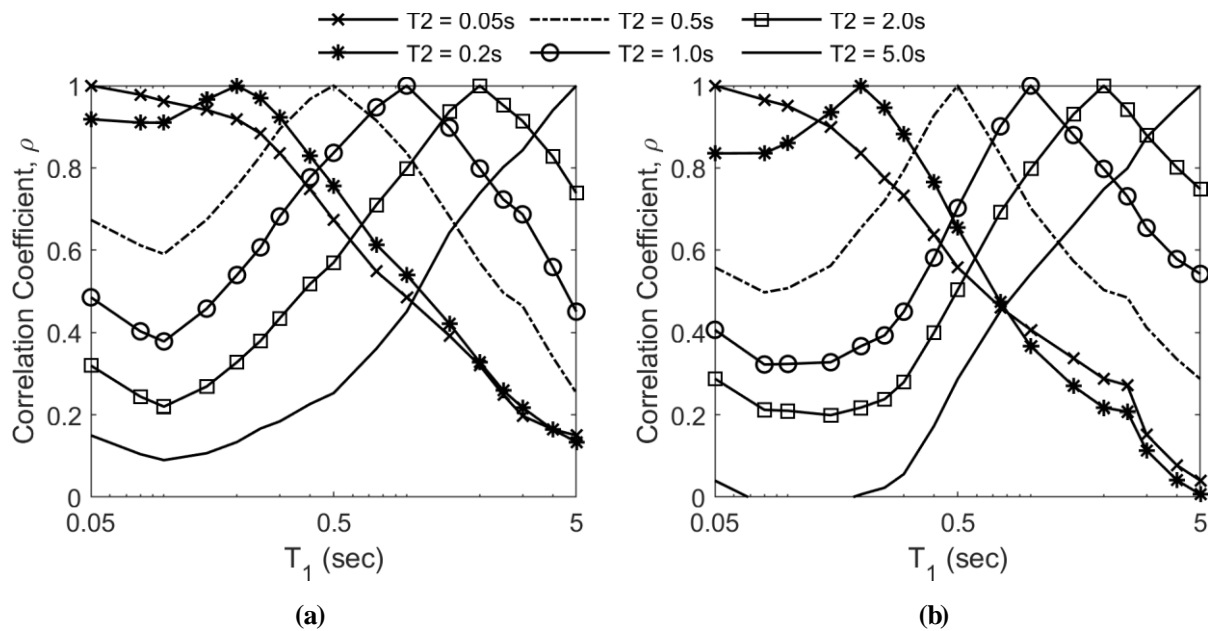


Figure 5.17 Plots of epsilon correlation coefficients, $\rho_{\varepsilon(T_1), \varepsilon(T_2)}$, between T_2 and T_1 estimated using residuals of the Zhao et al. (2006) GMM for (a) the interface records and (b) the intraslab records.

To further compare the epsilon correlation coefficients observed between the record subsets and the Baker and Jayram (2008) correlation model, an “acceptance region” was constructed around each line in Figure 5.17. These acceptance regions express the uncertainty in the correlation estimates due to the limited number of ground motion records. The uncertainty is inversely proportional to the number of records; i.e., fewer records produces less certain results. The acceptance regions are developed around one set of observations (i.e. epsilon correlation coefficients observed for the interface records) so that if the second set of observations (i.e. epsilon correlation coefficients predicted using the Baker and Jayram (2008) model) falls outside the region, then there is less than a 5% chance that the difference is due solely to the limited number of records. In other words, the acceptance region provides a 95% confidence interval (CI) around

the first set of observations. If the second set of observations falls within this interval, then the differences in the two sets of correlations are insignificant at the 95% significance level.

Figure 5.18 presents the subduction interface database results, including the acceptance region, for $T_2 = 0.05, 0.5, 2.0,$ and 5.0 s, compared to the Baker and Jayram (2008) predictions. Similarly, Figure 5.19 presents results derived using the intraslab database. Figure 5.19 shows a high degree of conformity between the observed epsilon correlation coefficients for the intraslab database and the Baker and Jayram (2008) predictions, meaning that the Baker and Jayram (2008) model is a suitable surrogate for predicting epsilon correlations for worldwide subduction intraslab events. Figure 5.18 shows a less good match when considering the subduction interface database – however, the results indicate that the Baker and Jayram (2008) model, while less accurate, still provides reasonably close results to those observed while using the interface database.

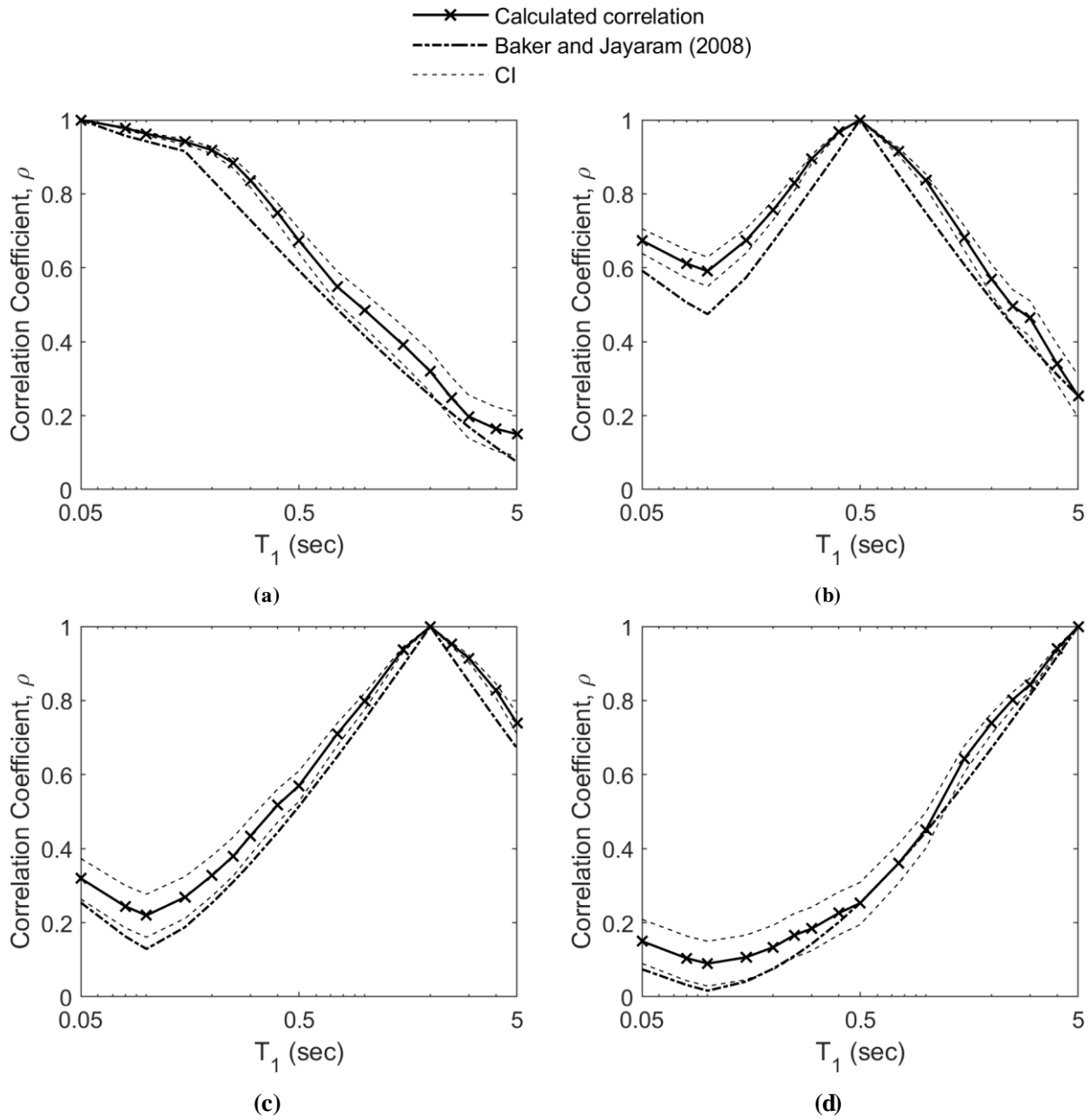


Figure 5.18 Plots of epsilon correlation coefficients, $\rho_{\varepsilon(T_1), \varepsilon(T_2)}$, between T_2 and T_1 estimated using residuals of the Zhao et al. (2006) GMM for the subduction interface database compared to the Baker and Jayaram (2008) predictions for (a) $T_2 = 0.05$ s, (b) $T_2 = 0.5$ s, (c) $T_2 = 2.0$ s, and (d) $T_2 = 5.0$ s. Also included is the 95% confidence interval (CI).

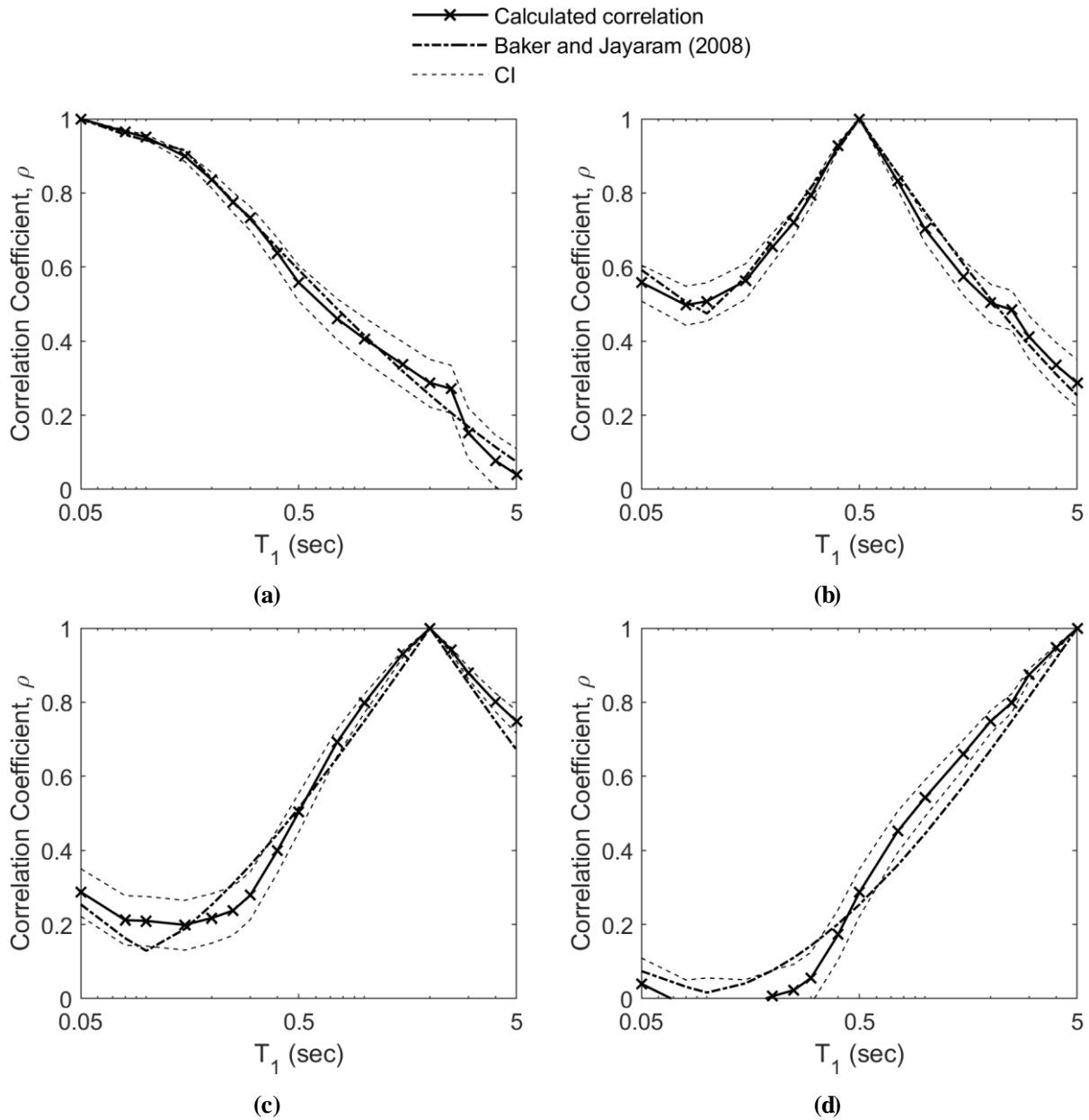


Figure 5.19 Plots of epsilon correlation coefficients, $\rho_{\varepsilon(T_1), \varepsilon(T_2)}$ between T_2 and T_1 estimated using residuals of the Zhao et al. (2006) GMM for the subduction intraslab database compared to the Baker and Jayaram (2008) predictions for (a) $T_2 = 0.05$ s, (b) $T_2 = 0.5$ s, (c) $T_2 = 2.0$ s, and (d) $T_2 = 5.0$ s. Also included is the 95% confidence interval (CI).

Also, of interest is the effect on the epsilon correlation coefficients when considering other GMMs. There are a large number of subduction zone GMMs that have been developed by researchers using different suites of motions and different parameters. In this study, five modern subduction zone GMMs are considered as summarized in Table 5.3.

Authors	Year	Source Type
Zhao et al.	2006	Interface/Intraslab
Atkinson and Macias	2009	Interface
Ghofrani and Atkinson	2014	Interface
Abrahamson et al. (BC Hydro Model)	2016	Interface/Intraslab
Atkinson and Boore global model	2003	Interface/Intraslab

Table 5.3 Summary of modern subduction zone GMMs considered.

The results derived using the Zhao et al. (2006) GMM were presented in Figure 5.16 and Figure 5.17. Figure 5.20 illustrates the results observed from the other four GMMs.

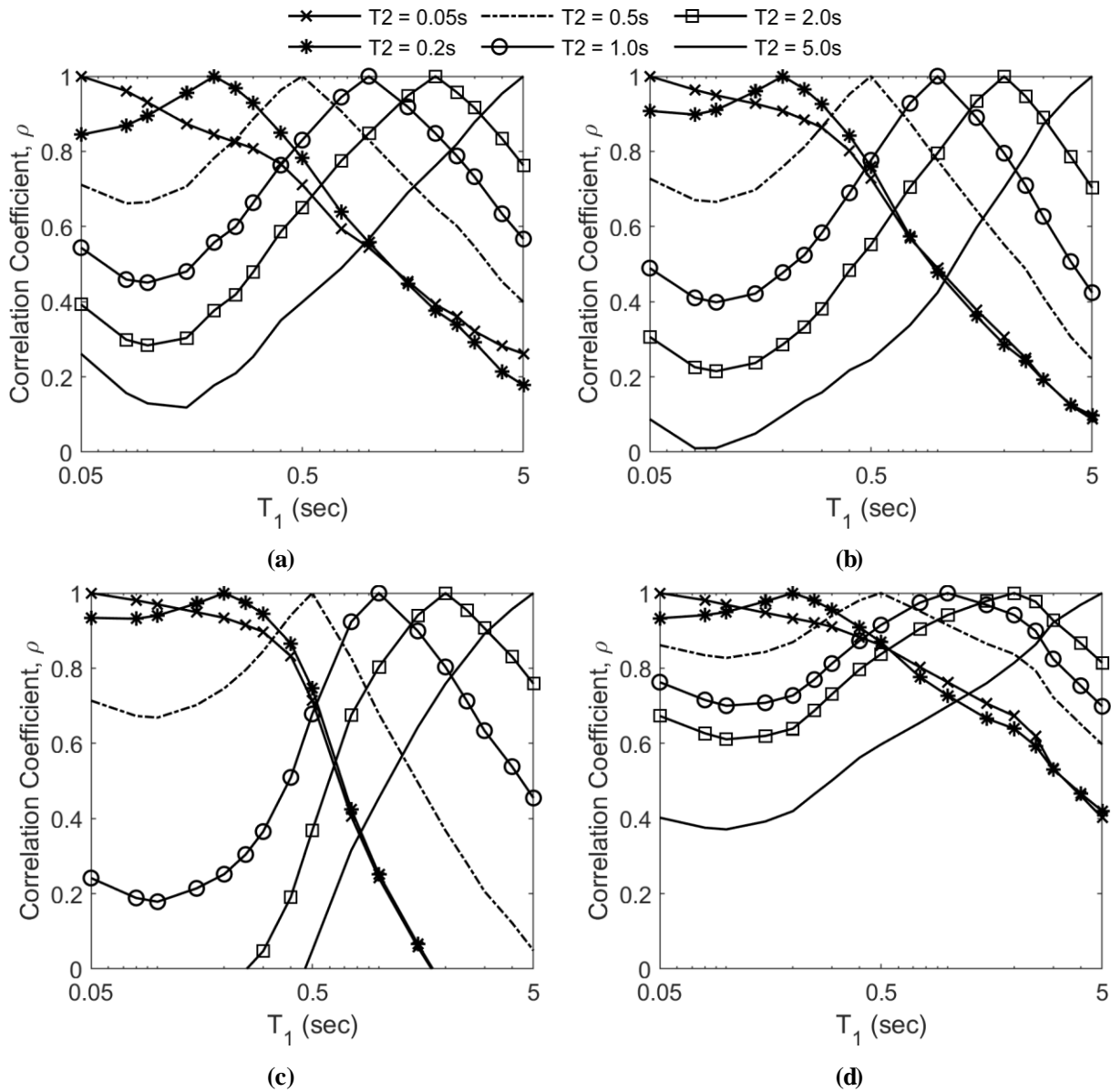


Figure 5.20 Plots of epsilon correlation coefficients, $\rho_{\varepsilon(T_1), \varepsilon(T_2)}$, between T_2 and T_1 estimated using residuals of the (a) Atkinson and Macias (2009), (b) Ghofrani and Atkinson (2014), (c) Abrahamson et al. (BC Hydo, 2016), and (d) Atkinson and Boore global GMM (2003).

5.4.1.3 Combining GMMs

Typically, PSHA models multiple applicable GMMs will be weighted and combined for ground motion prediction. This is done in order to better account for the epistemic uncertainty involved in the estimation of ground motion attenuation from source to site.

Both the Geological Survey of Canada (GSC) and the United States Geological Survey (USGS) have used this method in their PSHA models. Table 5.4 and Table 5.5 summarize the considered GMMs and their respective weights for the GSC 2015 (Halchuk et al., 2014) and USGS 2014 (Rezaeian et al., 2014) intraslab and interface ground motion prediction models, respectively. These GMMs were used in the development of the 2015 and 2014 national seismic hazard maps in Canada and the United States, respectively.

GMM	GSC 2015	USGS 2014
Zhao et al. (2006)	1	0.33
Abrahamson et al. (BC Hydro Model; 2012)	0	0.33
Atkinson and Boore global model (2003)	0	0.167
Atkinson and Boore Cascadia model (2003)	0	0.167

Table 5.4 Summary of GSC (2015) and USGS (2014) subduction intraslab GMM weights.

GMM	GSC 2015	USGS 2014
Zhao et al. (2006)	0.1	0.3
Abrahamson et al. (BC Hydro Model; 2012)	0.2	0.3
Atkinson and Macias (2009)	0.5	0.3
Ghofrani and Atkinson (2014)	0.2	0
Atkinson and Boore global model (2003)	0	0.1

Table 5.5 Summary of GSC (2015) and USGS (2014) subduction interface GMM weights.

The epsilon correlation coefficients computed using these two combined GMMs are summarized in Figure 5.21 and Figure 5.22 for the intraslab and interface events, respectively.

Figure 5.21 and Figure 5.22 show similar trends between the two combined GMMs. Figure 5.23 compares the results in Figure 5.21 for intraslab events to the Baker and Jayaram (2008) correlation coefficients (Figure 5.16b) for $T_2 = 0.2$ and 2.0 s. This reveals a relatively good match when using the GSC 2015 intraslab GMM. However, when using the USGS 2014 intraslab GMM, the observed epsilon correlations are lower, on average, than the Baker and Jayaram (2008) coefficients.

A similar comparison is made for the two combined interface GMMs in Figure 5.24. From this figure it can be seen that the Baker and Jayaram (2008) correlation coefficients are, on average, lower than the observed interface correlations and outside of the acceptance region.

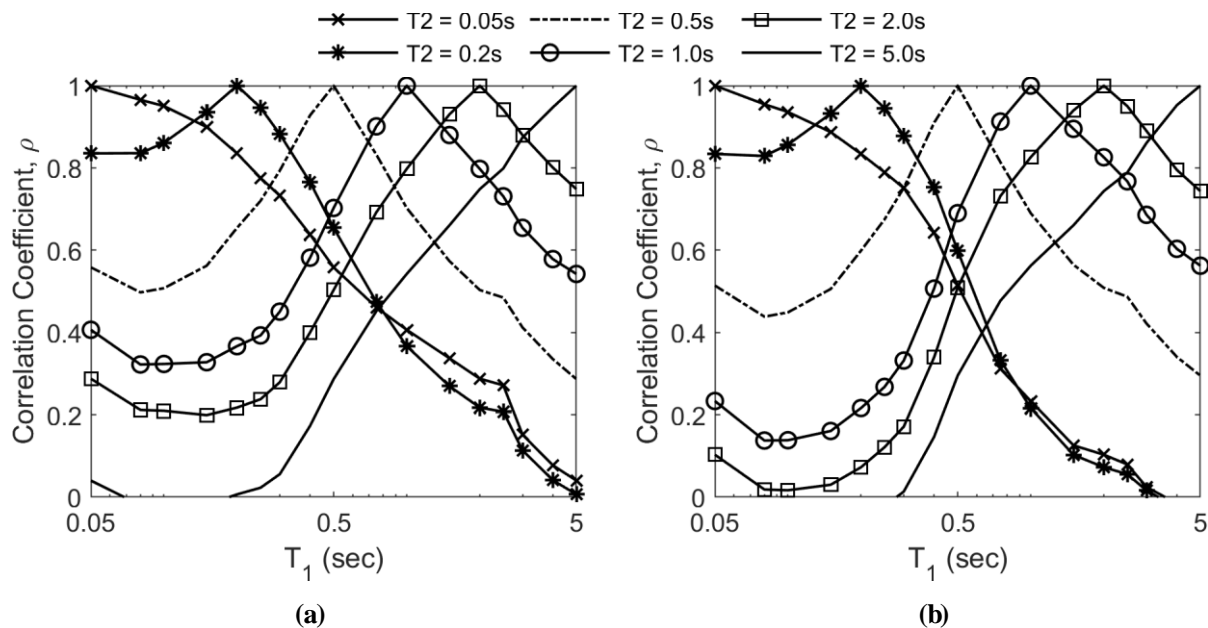


Figure 5.21 Epsilon correlation coefficient, $\rho_{a(T_1),a(T_2)}$, plots between T_2 and T_1 calculated using residuals of the (a) GSC 2015 intraslab GMM and (b) USGS 2014 intraslab GMM.

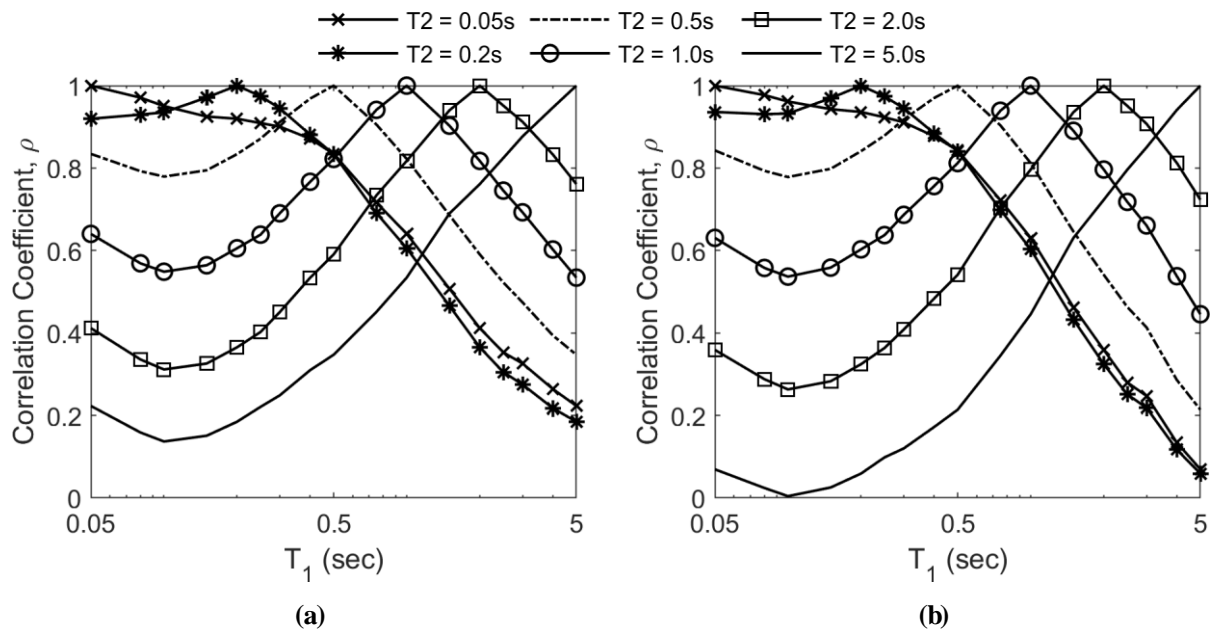


Figure 5.22 Epsilon correlation coefficient, $\rho_{\alpha(T_1),\alpha(T_2)}$, plots between T_2 and T_1 calculated using residuals of the (a) GSC 2015 interface GMM and (b) USGS 2014 interface GMM.

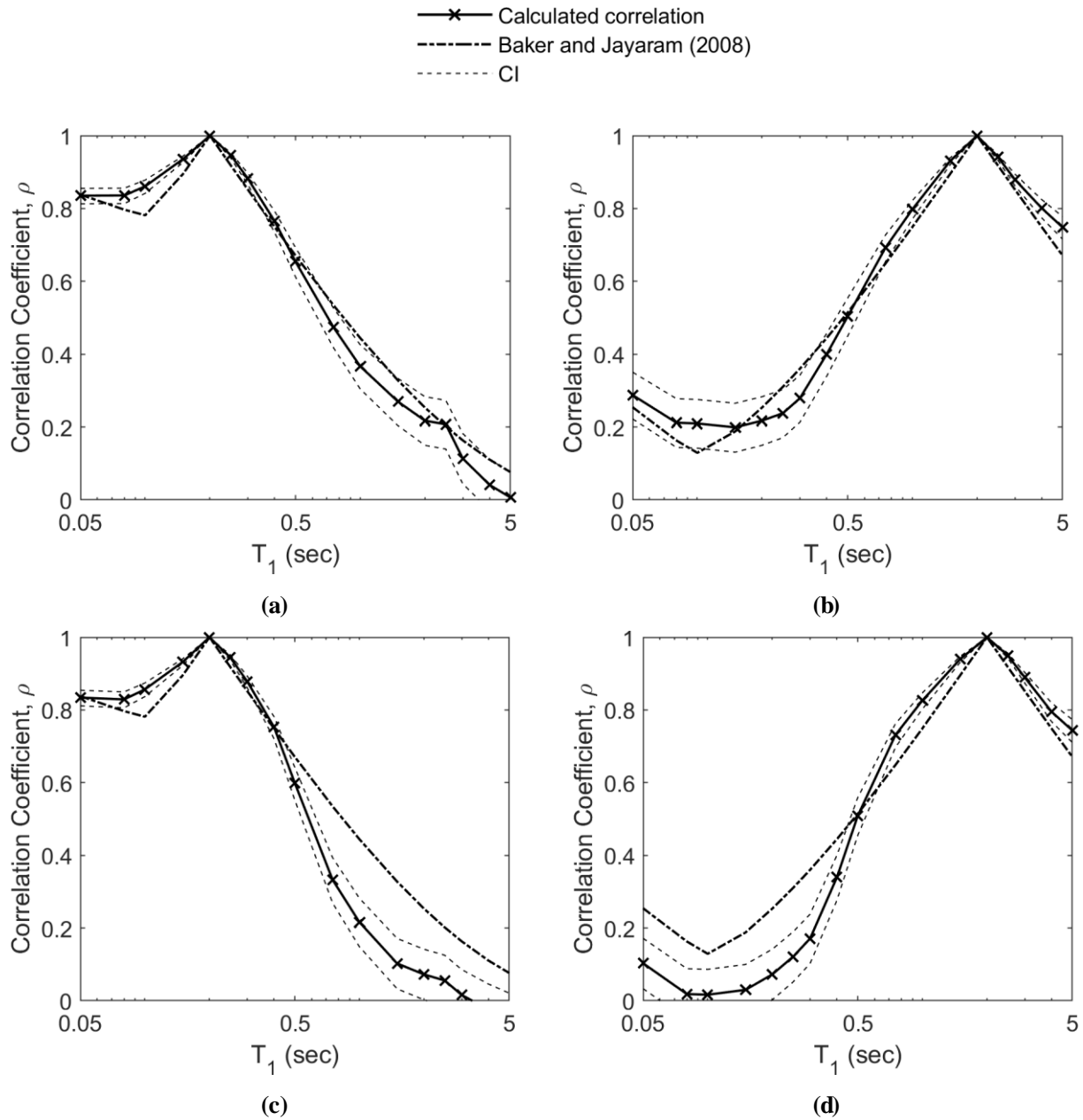


Figure 5.23 Epsilon correlation coefficient, $\rho_{\varepsilon(T_1),\varepsilon(T_2)}$, plots between T_2 and T_1 calculated using the Baker and Jayaram (2008) predictions for compared to (a) GSC 2015 GMM for the intraslab database at $T_2 = 0.2$ s, and (b) $T_2 = 2.0$ s; (c) USGS 2014 GMM for the intraslab database at $T_2 = 0.2$ s, and (d) $T_2 = 2.0$ s. Also included is the 95% confidence interval (CI).

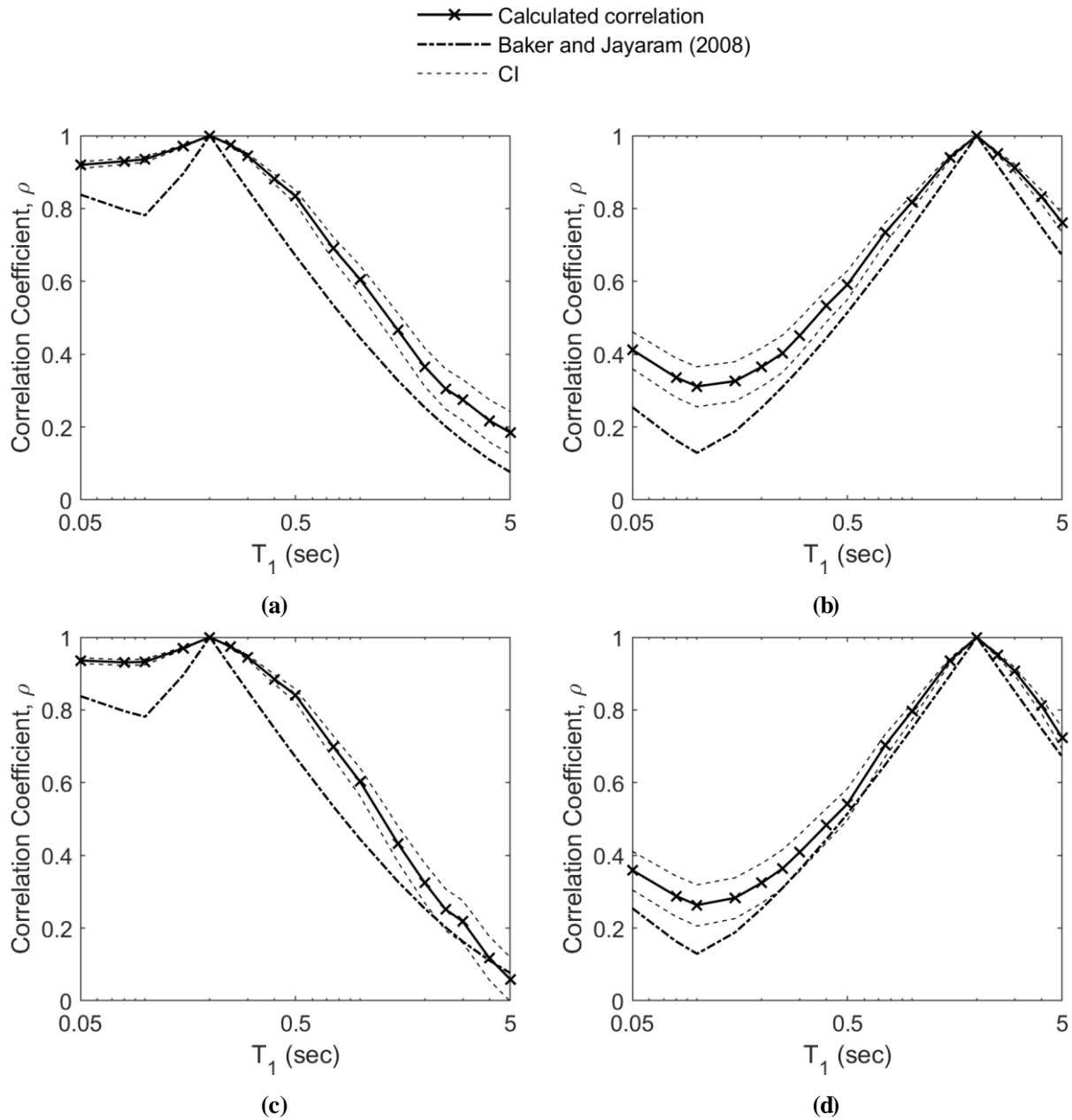


Figure 5.24 Epsilon correlation coefficient, $\rho_{\varepsilon(T_1),\varepsilon(T_2)}$, plots between T_2 and T_1 calculated using the Baker and Jayaram (2008) predictions for compared to (a) GSC 2015 GMM for the interface database at $T_2 = 0.2$ s, and (b) $T_2 = 2.0$ s; (c) USGS 2014 GMM for the interface database at $T_2 = 0.2$ s, and (d) $T_2 = 2.0$ s. Also included is the 95% confidence interval (CI).

5.4.1.4 Observations

In the previous sections, a database of worldwide subduction zone (both interface and intraslab) events was studied to determine their epsilon correlation coefficients. The database comprised several large magnitude events including the 2010 $M_w = 9.1$ Tohoku, Japan earthquake.

The observed correlations were compared to the Baker and Jayaram (2008) epsilon correlations, which are commonly used to develop CS and CMS. Using the Zhao et al. (2006) GMM to calculate epsilon values, it was noted that the Baker and Jayaram correlation coefficients matched well with the observed values. This means that the Baker and Jayaram coefficient equations would be a suitable surrogate for these types of events. Several other modern subduction zone GMMs were also used to calculate epsilon values. Some produced similar results to those observed using Zhao et al. (2006) GMM, while others predicted much higher or lower correlations.

Next, the GSC 2015 and USGS 2014 subduction GMMs, which comprise a weighted average of several GMMs, were used to calculate epsilon values for the record database. For each record type (interface or intraslab) the two GMM combinations produced similar results, which were comparable to the Baker and Jayaram (2008) correlation values (although not strictly within the 95% confidence acceptance region). Due to these findings, it may be acceptable to use the Baker and Jayaram (2008) epsilon correlation coefficients when developing CS or CMS for subduction zone events in the Northwest Pacific United States and Southwestern Canada. However, for more accurate results, interface or intraslab specific correlation coefficients could be used.

5.4.2 Period Range of Interest

To define a period range of interest for matching or scaling input time histories, the complete response of the model should be considered. This includes higher modes effects as well

as effects from period elongation due to yielding. As a model begins to yield and soften, its period will typically elongate – thus records scaled to the initial elastic conditions may no longer impose the appropriate demands on this “new”, softened structure. Accordingly, input time histories are typically scaled over a broad range of periods.

The NBCC recommends, for concrete shearwall buildings, $0.2-2.0 \cdot T_1$ as a range for ground motion scaling, where T_1 is the fundamental period of the undamaged model (NRCC, 2015). The lower limit is imposed to capture effects from higher modes (aiming for a period with 90% modal mass contribution); the upper limit is an estimation of the magnitude of period elongation due to damage at the considered hazard level (earthquake with a 2% in 50 year probability of exceedance for code design).

To investigate the period range that defines the behavior of a model, three archetype RC shearwall buildings with 6, 18, and 30 stories were considered. These archetype buildings are all RC shearwall buildings typical of existing residential buildings constructed in Vancouver, BC. The buildings were modelled in OpenSees with nonlinear fiber sections for the wall elements and nonlinear shear hinges for the coupling beams. Cyclic and in-cycle degradation is accounted for in the coupling beam models as well as the material models used in fiber sections of the shearwalls. See Sections 4.1 and 4.2 for further details about the building design and modelling, respectively. The first three elastic periods (T_1 , T_2 , and T_3 , respectively) of the models are provided in Table 5.6.

Number of Stories	T1 (s)	T2 (s)	T3 (s)
6	0.44	0.14	0.083
18	1.74	0.51	0.26
30	3.73	0.85	0.46

Table 5.6 First three elastic periods of the three RC shearwall prototype buildings.

5.4.2.1 Analysis

Dynamic time history analyses were performed using three ground motions: one $M_w = 9.1$ Tohoku, 2011, record (very long subduction interface motion); one $M_w = 8.0$ Hokkaido, 2003, record (subduction interface motion); and one $M_w = 6.7$ Northridge, 1994, record (short, shallow crustal motion). These records were scaled to the Vancouver 2% in 50 year UHS over a large period range of 0.08-6.0 s; metadata for these scaled records can be found in Table 5.7. The three records were run at three levels of shaking (relative to the initial 2% in 50 year shaking level): 100%, 150%, and 200% to see if the higher shaking levels would affect the period elongation more than the design level (100%). If the higher shaking levels cause additional period elongation, then it might be necessary to increase the scaling period range when selecting time histories for collapse analysis or higher shaking analyses.

It should be noted that modern structures, under the 2% in 50 year design hazard level, are intended to yield in order to dissipate energy – this means that even at the design level, one would expect significant amounts of yielding and period elongation. Each record was run followed by 50 s of quiet time afterward to allow any remaining free vibration to dampen out.

During the analyses, every 10 timesteps, a modal analysis was performed, and the first three periods were computed and recorded.

Event	Station-Direction	Magnitude (M_w)	Distance (km)	Scale Factor
Tohoku, 2011	MYG009-NS	9.1	111	0.98
Hokkaido, 2003	HKD125-NS	8.0	134	2.60
Northridge, 1994	STM-360	6.7	26	1.38

Table 5.7 Metadata for the three input time series scaled to the 2015 Vancouver 2% in 50 year UHS.

5.4.2.2 Results

The period vs. time plots for the 18 story model subjected to the three earthquake records and three shaking levels is illustrated in Figure 5.25 to Figure 5.27. Also included is the roof drift response time history under the 200% shaking level. Using roof drift as a gross surrogate for total demand, this allows us to see if the maximum period elongation corresponds to the point in time where the displacement demand is maximized. Similar results are presented for the 6 and 30 story models in Appendix B.

In Figure 5.28a, the cumulative distribution function (CDF) of the period ratio (instantaneous period divided by the initial period: T_1 , T_2 , or T_3) is computed for the 18 story model during the 5-95% significant duration time interval for the Tohoku record scaled at 100%. From this plot it is observed that for ~90% of the significant shaking duration, the first mode period remained less than double the first mode elastic period: T_1 . In Figure 5.28b the power spectral density (PSD) of roof drift is plotted. Here we observe significant amount of energy density at $\sim 2 * T_1 = 3.5$ s. Figure 5.29 and Figure 5.30 present similar results for this model for the other two records scaled to 100%. In both figures we observe that the 90th percentile period ratio is around 2-2.5 (i.e. for 90% of the shaking duration, the initial period is less than 2-2.5x the initial period). Both figures also show a large amount of energy density around $2 * T_1$.

Similar figures for the other two models (6 and 30 stories) are included in Appendix B. These plots show trends similar to those observed in the 18 story model; however, slightly less period elongation was observed for all records and levels.

Table 5.8 summarizes the initial, end, and maximum observed fundamental period (T_1) of the 6 story model subjected to the three records and three scaling levels. At the 100% shaking level, the end period was approximately double the initial period; however, at the 200% level, the end period reached almost 2.5 times the initial period for all three records. The maximum periods were about 2.5 times the initial period at the 100% level, up to over 5.5 times the initial period during the Tohoku record scaled at 200%. However, it can be observed in Figure B.1 that this extreme value was only observed for a short time period ~ 100 s into the record and immediately reduced after this peak.

Table 5.9 presents similar results for the 18 story model. Once again, the end periods were $\sim 2x$ the initial at the 100% level, up to $\sim 2.5x$ the initial at the 200% level. Much larger maximum periods, again, were observed: up to $\sim 4x$ and $\sim 5.5x$ the initial period at the 100 and 200% levels, respectively.

Results for the 30 story model are summarized in Table 5.10. The end period reached only $\sim 1.1x$ the initial period at the 100% level, up to $2.2x$ at the 200% level. The maximum period reached $\sim 2.7x$ the initial period at the 100% level, and almost $4x$ the initial period at the 200% level.

From these results, it can be seen that a range up to $4x$ the initial period would be necessary to capture the complete period range of the models at the 100% shaking level. However, these extreme period values were only observed instantaneously and immediately fell back down. Since the structure would not even have time to complete one cycle of vibration at this period during the

time it was elongated, we should not worry about these peaks. Also, from the CDF plots, it was observed that for the majority of the strong shaking duration of the records, the period did not maintain at these peaks.

From Figure B.1, Figure 5.25, and Figure B.7, at the 100% shaking level, we would expect a maximum sustained period of approximately double the initial elastic period to be more appropriate. This is also confirmed by the CDF plots: for ~90% of the significant duration, the periods were less than or equal to double the initial periods, for all models, at the 100% shaking level for the records. The roof drift PSD plots show a significant amount of energy above the elastic first mode period; however, this drops off past ~2-2.5 times the initial period. These conclusions agree with the NBCC recommendations for period ranges up to two times the initial, elastic, first mode period. At the 200% shaking level, this range may be slightly extended to ~2.5x the initial period, due to the increased damage at this higher level of shaking.

Record	Level	T1 Initial (s)	T1 End (s)	T1 Max (s)
Tohoku-MYG009 NS Hokkaido-HKD125 NS Northridge-STM360	100%	0.44	0.86 0.95 0.66	1.00 1.10 1.08
Tohoku-MYG009 NS Hokkaido-HKD125 NS Northridge-STM360	150%	0.44	0.82 0.94 0.96	1.44 1.44 1.58
Tohoku-MYG009 NS Hokkaido-HKD125 NS Northridge-STM360	200%	0.44	0.91 1.07 1.11	2.51 1.92 2.35

Table 5.8 Periodelongation summary for the 6 story model subjected to three records at three scaling levels.

Record	Level	T1 Initial (s)	T1 End (s)	T1 Max (s)
Tohoku-MYG009 NS Hokkaido-HKD125 NS Northridge-STM360	100%	1.74	2.21 3.99 2.16	5.03 7.25 4.85
Tohoku-MYG009 NS Hokkaido-HKD125 NS Northridge-STM360	150%	1.74	3.75 3.57 2.85	7.59 9.13 5.79
Tohoku-MYG009 NS Hokkaido-HKD125 NS Northridge-STM360	200%	1.74	3.95 4.77 4.00	7.09 10.14 7.91

Table 5.9 Periodelongation summary for the 18 story model subjected to three records at three scaling levels.

Record	Level	T1 Initial (s)	T1 End (s)	T1 Max (s)
Tohoku-MYG009 NS Hokkaido-HKD125 NS Northridge-STM360	100%	3.73	3.94 4.14 4.03	9.09 10.00 9.26
Tohoku-MYG009 NS Hokkaido-HKD125 NS Northridge-STM360	150%	3.73	5.02 4.35 4.03	9.77 11.44 9.37
Tohoku-MYG009 NS Hokkaido-HKD125 NS Northridge-STM360	200%	3.73	4.97 6.06 5.25	14.09 14.71 11.66

Table 5.10 Periodelongation summary for the 30 story model subjected to three records at three scaling levels.

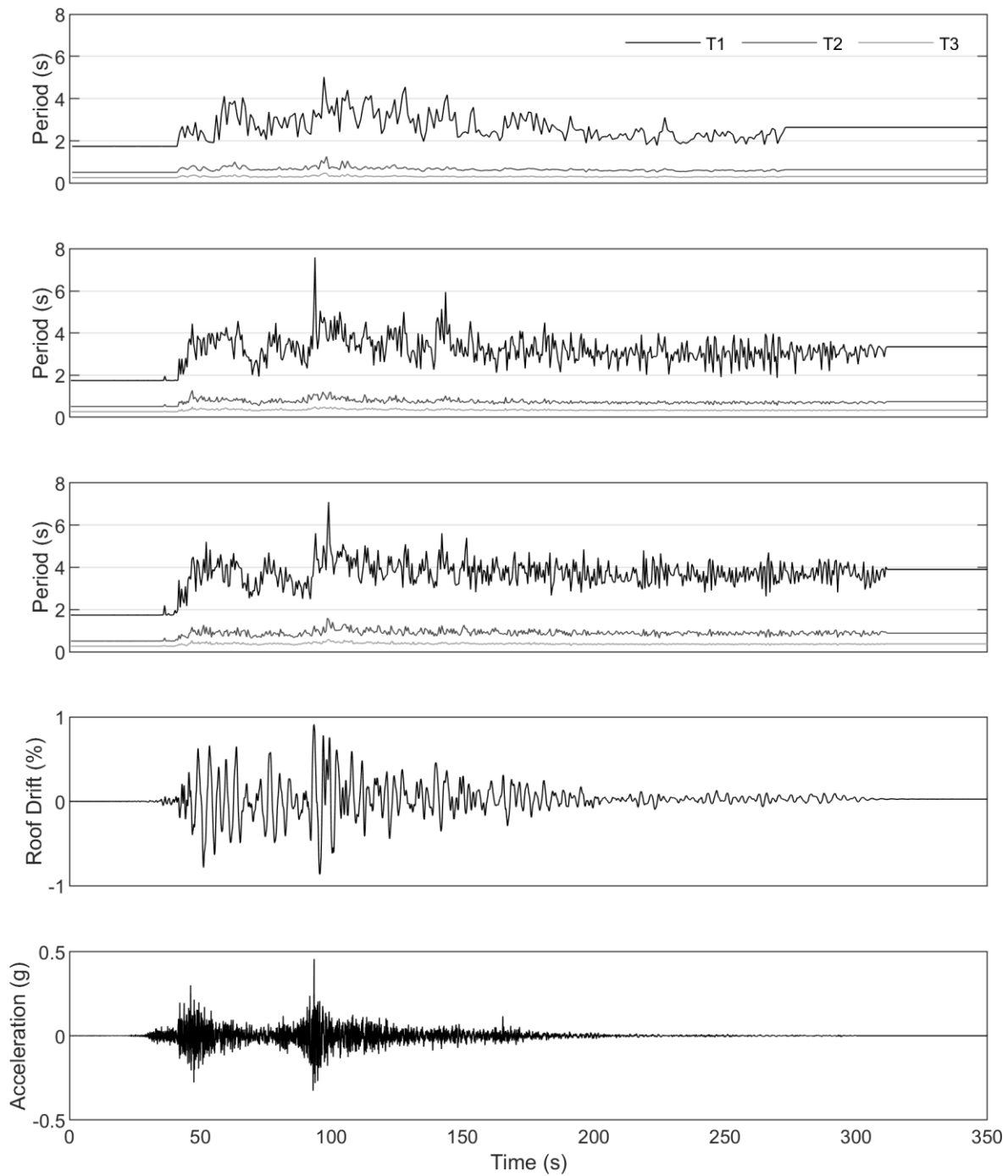


Figure 5.25 First three periods of 18 story RC shear wall model subjected to the Tohoku-MYG009 NS ground motion; from top to bottom: scaled to 100%, 150%, and 200%; roof drift time history response under the 200% shaking level; and input acceleration time history scaled to 100% Vancouver 2% in 50 year target UHS.

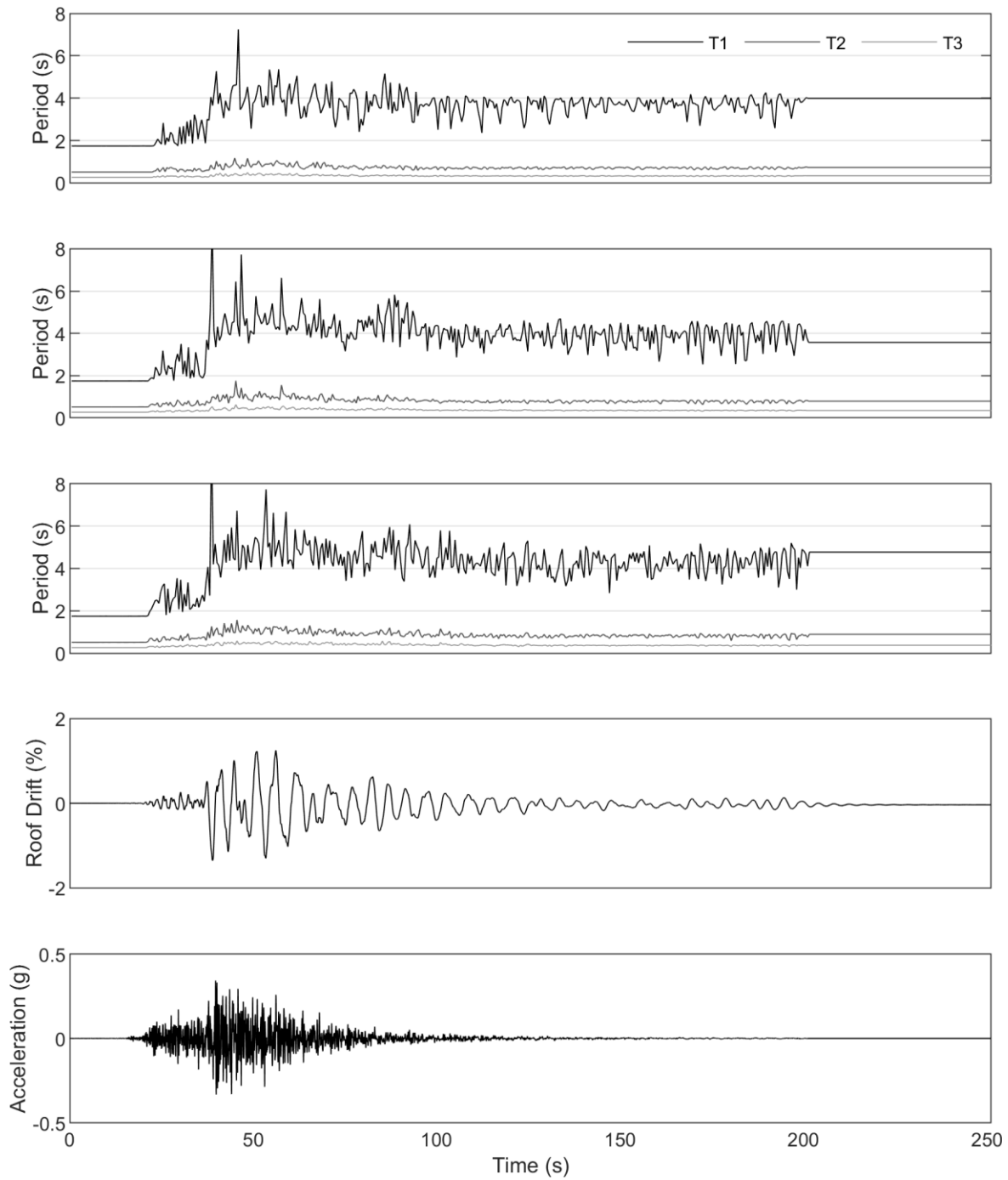


Figure 5.26 First three periods of 18 story RC shear wall model subjected to the Hokkaido-HKD125 NS ground motion; from top to bottom: scaled to 100%, 150%, and 200%; roof drift time history response under the 200% shaking level; and input acceleration time history scaled to 100% Vancouver 2% in 50 year target UHS.

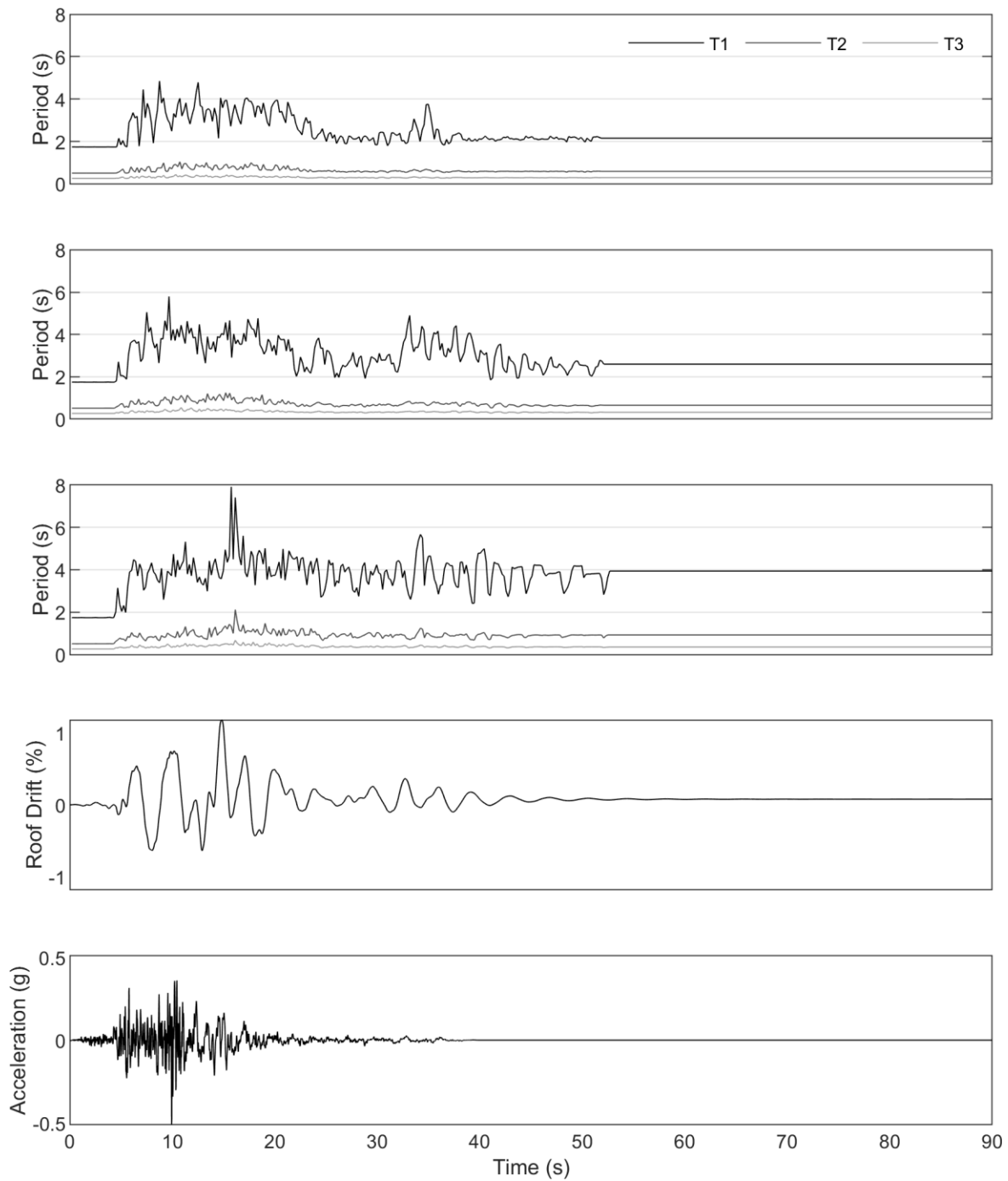


Figure 5.27 First three periods of 18 story RC shear wall model subjected to the Northridge-STM360 ground motion; from top to bottom: scaled to 100%, 150%, and 200%; roof drift time history response under the 200% shaking level; and input acceleration time history scaled to 100% Vancouver 2% in 50 year target UHS.

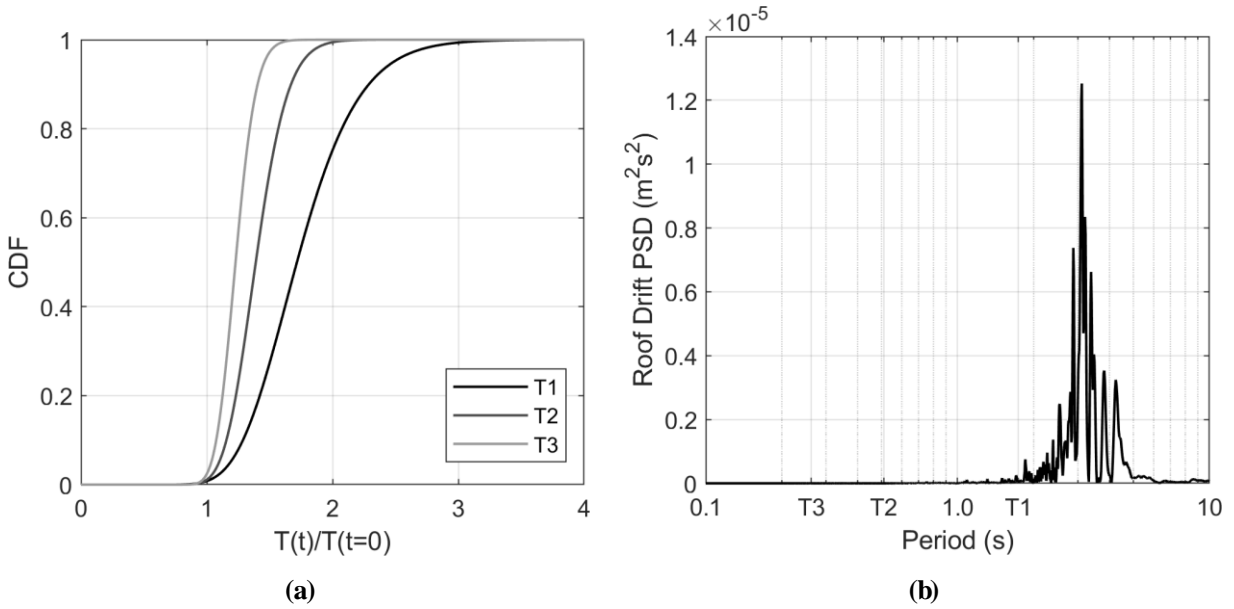


Figure 5.28 (a) First three period cumulative distribution function; and, (b) power spectral density of roof drift of 18 story RC shear wall model subjected to the Tohoku-MYG009 NS ground motion scaled to 100%.

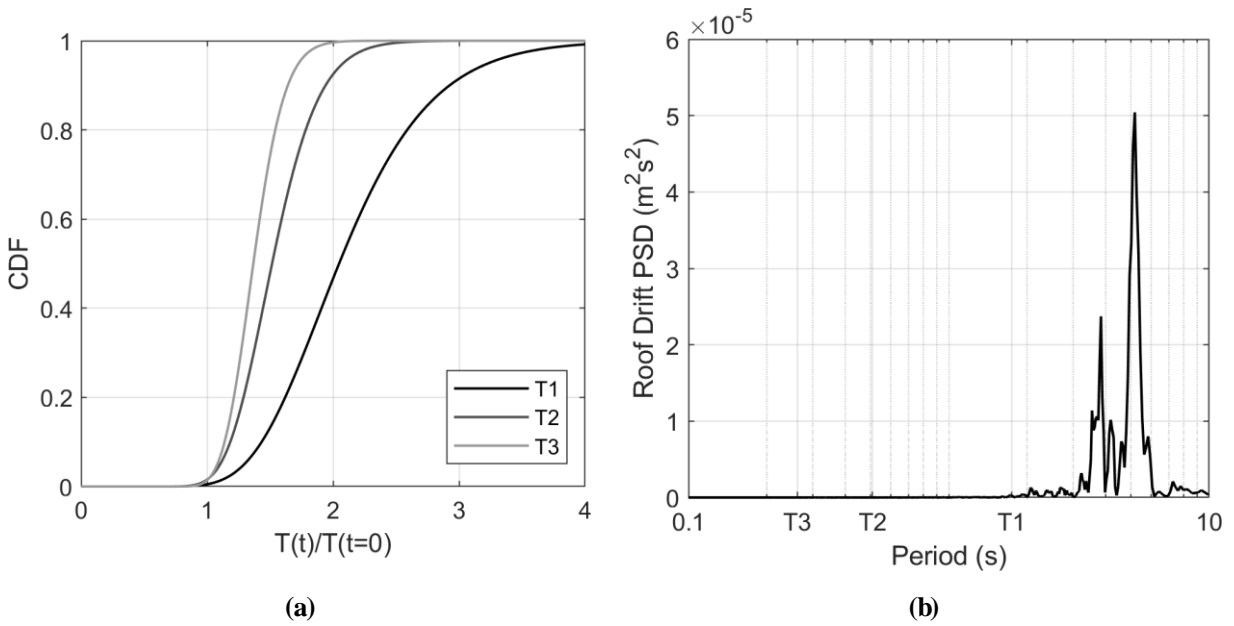


Figure 5.29 (a) First three period cumulative distribution function; and, (b) power spectral density of roof drift of 18 story RC shear wall model subjected to the Hokkaido-HKD125 NS ground motion scaled to 100%.

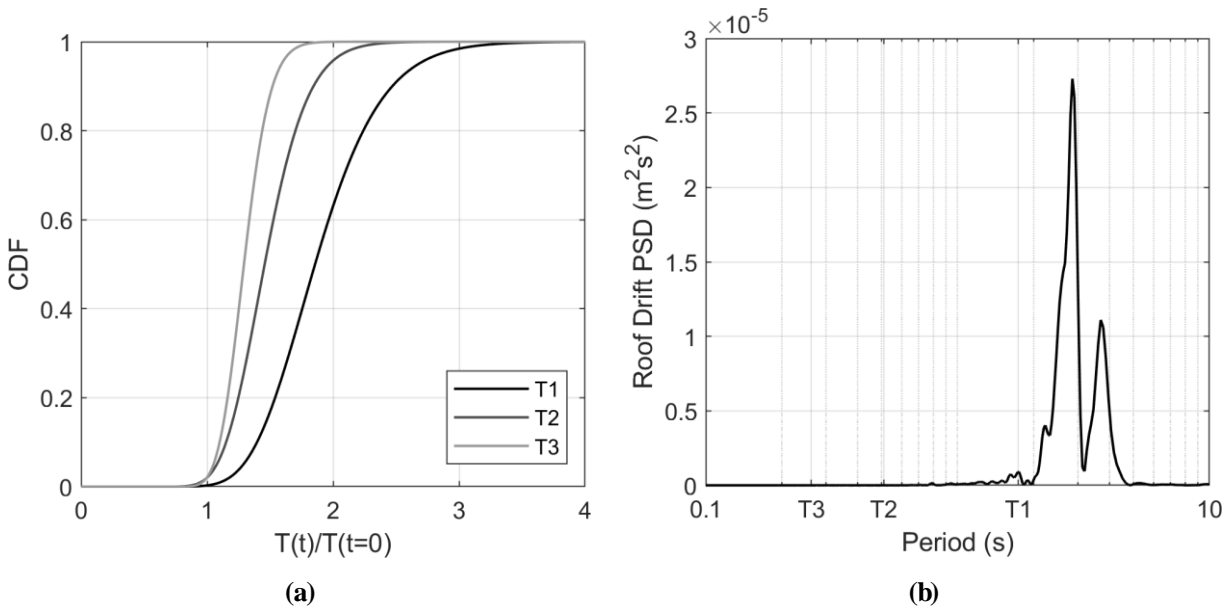


Figure 5.30 (a) First three period cumulative distribution function; and, (b) power spectral density of roof drift of 18 story RC shear wall model subjected to the Northridge-STM360 ground motion scaled to 100%.

5.5 Conclusions

This chapter introduced a novel algorithm, based on variable target spectra and spectral matching that can be used to develop a suite of records that represents both the mean and variation of a specified hazard. Results from time history analysis using record suites developed using this algorithm are expected to reliably estimate both mean structural demands (e.g. displacements or forces) and the record-to-record variability in these demands (e.g. mean plus one standard deviation results).

A modification was also introduced in order to limit outlying spectral values. When conducting nonlinear time history analysis of structures, a particularly demanding record may produce an unexpectedly large response, which could significantly affect the mean and variability from the subsequent analyses (the geomean would also be affected, but less so than the mean). If

the analyzer wants to limit exposure to a potential extreme record, they may opt to use the additional modification to reduce outlying spectral accelerations from the matched record suite.

Record suites developed using this algorithm will be appropriate for typical design-focused time history analyses where, typically, only mean results are used (ASCE/SEI, 2016; NRCC, 2015; LATBSDC, 2017; PEER, 2017). These standards also typically limit the number of records that cause outlying structural responses (e.g. non-convergence, excessive displacements, or non-simulated collapse modes); therefore, the method to reduce outlying spectral ordinates may be useful to limit the exposure to records that cause uncharacteristically large responses. For structural collapse assessment or risk-based analyses, such as those required to determine structural safety factors (FEMA, 2009), this algorithm is recommended when traditional CS record selection algorithms (Jayaram et al., 2011) cannot be performed due to record availability or other constraints.

This method can be used to produce spectrally similar record suites which can be used to fairly compare different motions type (e.g. long vs. short duration or shallow crustal vs. subduction interface). Since fragility curves resulting from incremental dynamic analysis depend on the record-to-record spectral variation of the input ground motion time histories, records suites produced using this methodology will be valid for risk-based comparisons. This is also an important consideration when assessing or developing code-based seismic reduction factors (FEMA, 2009). The methodology also mitigates the potential problem of subduction interface record suite development due to the limited number of recordings for this earthquake type. Thus, the methodology presented in this chapter can later be used for record suite comparison and for safety factor calibration/assessment. These topics are the foci of the studies in the final two chapters.

Chapter 6: RC Shearwall Model 3D Analysis

The goal of this chapter is to compare the performance of RC shearwall structures when subjected to long or short duration ground motion suites using sophisticated 3D models subjected to hazard-consistent (considering mean and variation in spectral values) ground motion suites. The analyses in this chapter will highlight the difference in behavior expected from these two motion types. The results will be useful for evaluating the safety of these buildings and for assessing the suitability of modern building code standards for the design of RC shearwall structures in subduction earthquake zones.

This chapter will expand the results of Chapter 4 to 3-dimensional models. 3D models are more comprehensive than 2D due to their ability to capture torsion and the coupling effects between the two directions. Torsion can impact demands in one direction, but also allows the overstrength of the stronger direction to sustain some of these increased demands. This is particularly important for taller buildings, which tend to have a more pronounced torsional response compared to shorter buildings. Thus, it is typically recommended to develop 3D models for the analysis and design of tall buildings (LATBSDC, 2017; PEER, 2017).

However, this comes at a cost, as 3D models, especially nonlinear models analyzed using time history analyses are much more computationally demanding. Thus, while Chapter 4 considered a range of archetype buildings from 6 to 30 stories, as well as two large ground motion suites, for the 3D analyses in this section, only two archetype 18 story buildings were considered.

6.1 Archetype Buildings

Two archetype buildings were considered: one designed as a ductile coupled RC shearwall building; and another similar design, based on conventional construction (non-ductile), as introduced in Chapter 4. In Chapter 4, all designs used conventional construction factors ($R_d R_o =$

1.95), and conventionally reinforced header beams with stirrups rather than cross ties and full section confinement. This was because these nonductile beams were expected to undergo more cyclic degradation and thus exhibit more of a response to ground motion duration, which was being studied. These designs are also more representative of existing concrete structures in the study area (Vancouver, BC), of which the majority were designed and constructed from 1960-1980 (Yathon et al., 2017).

However, modern tall RC buildings in Western Canada are typically designed with ductile header and wall detailing. These designs benefit from much higher seismic force modification factors ($R_d R_o = 6.8$), which allows for much lower design base shears. Accordingly, the headers and walls of the 18 story archetype building were redesigned with enhanced detailing and ductile seismic force modification factors.

6.1.1 Conventional Construction

The conventional construction (CC) designed building was previously discussed in Chapter 4. Its period and corresponding first mode design spectral acceleration (from NBCC, 2010) are 1.18 s and 0.30 g, respectively. Note that the change in period from 1.74 s reported for the 18 story model in Chapter 4 is due to the increased stiffness of the 3D model which includes the complete gravity system as discussed in the next section. With a conventional construction $R_d R_o$ of 1.95 and story weight of 1100 kips (4890 kN), the design base shear, V , can be estimated using the equivalent lateral force procedure (ELFP) from the NBCC as:

$$V = Sa(T = 1.18 \text{ s}) * \frac{W I_E M_V}{R_d R_o} = 0.3 \text{ g} * \frac{1100 \frac{\text{kips}}{\text{story}} * 18 \text{ stories}}{1.95} \approx 3050 \text{ kips (13570 kN)}$$

where W is the weight of the structure, I_E is the earthquake importance factor (taken as 1.0), and M_V is the higher mode effect factor (1.0 in this case). Its wall reinforcement was presented in Figure 4.3 and its header reinforcement was illustrated in Figure 4.5.

6.1.2 Ductile Design

The ductile archetype was designed according to the 2015 NBCC with a fundamental period of 1.18 s and $R_d R_o$ of 6.8; its design base shear is calculated as:

$$V = Sa(T = 1.18 \text{ s}) * \frac{W I_E M_V}{R_d R_o} = 0.39 g * \frac{1100 \frac{\text{kips}}{\text{story}} * 18 \text{ stories}}{6.8} \approx 1150 \text{ kips (5115 kN)}$$

Its wall reinforcement is presented in Figure 6.1 and its header reinforcement is illustrated in Figure 6.2.

The header shear capacity was computed using (ACI, 2008):

$$V_n = 2A_{vd}f_y \sin(\alpha)$$

where V_n is the nominal shear capacity, A_{vd} is the area of diagonal steel, f_y is the yield strength of the steel, and α is the angle of the diagonal steel. The shear requirements for the headers were obtained through ELFP. The headers in stories 1-6 used 8-35M bars ($A_{vd} = 12.4 \text{ in}^2$ [8000 mm²]; $V_n = 470 \text{ kips}$ [2090 kN]); stories 7-13 used 6-35M bars ($A_{vd} = 9.3 \text{ in}^2$ [6000 mm²]; $V_n = 352 \text{ kips}$ [1566 kN]); and stories 14-18 used 6-30M bars ($A_{vd} = 6.5 \text{ in}^2$ [4190 mm²]; $V_n = 247 \text{ kips}$ [1100 kN]).

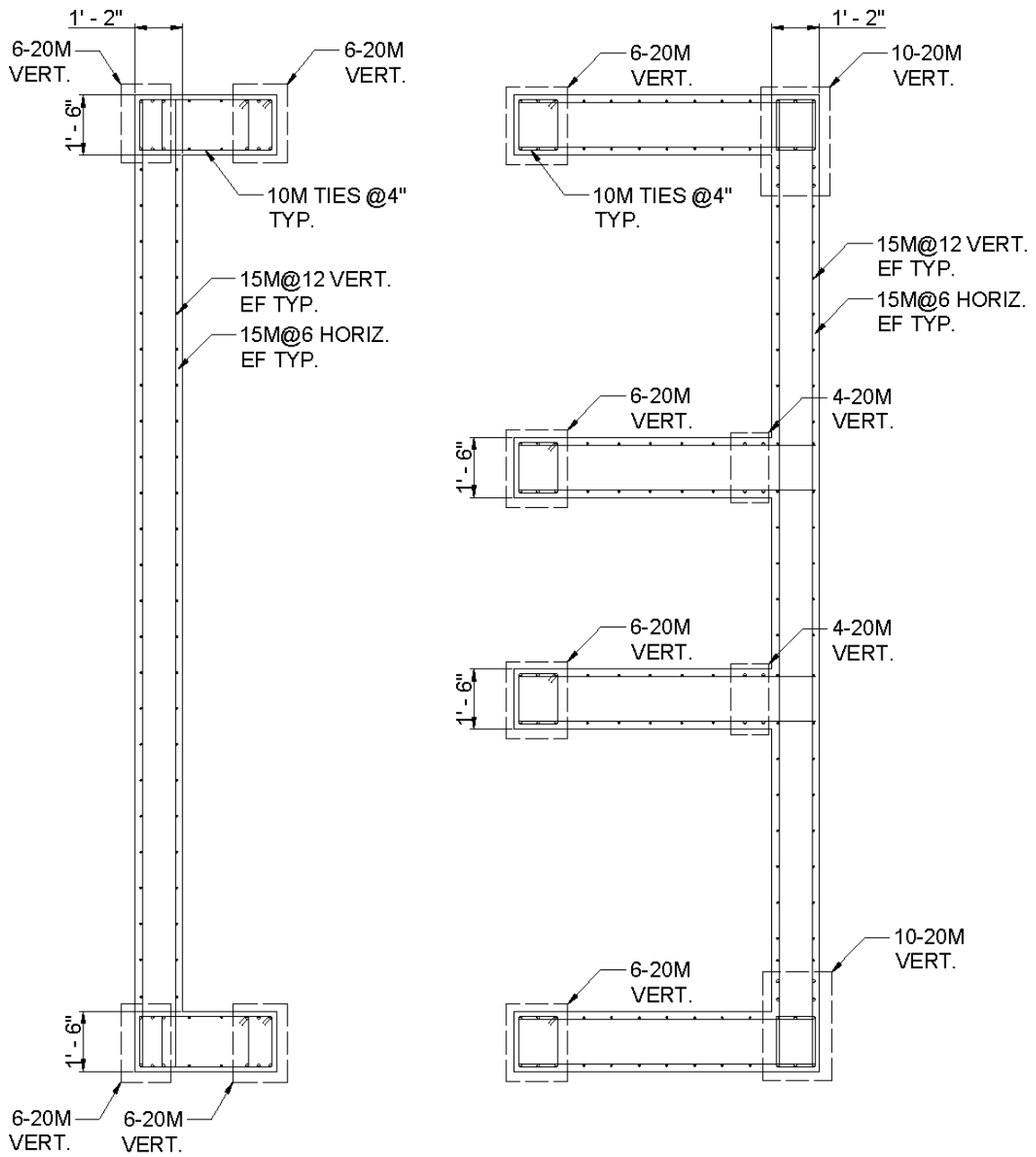


Figure 6.1 Reinforcement details of 18 story ductile shearwall building.

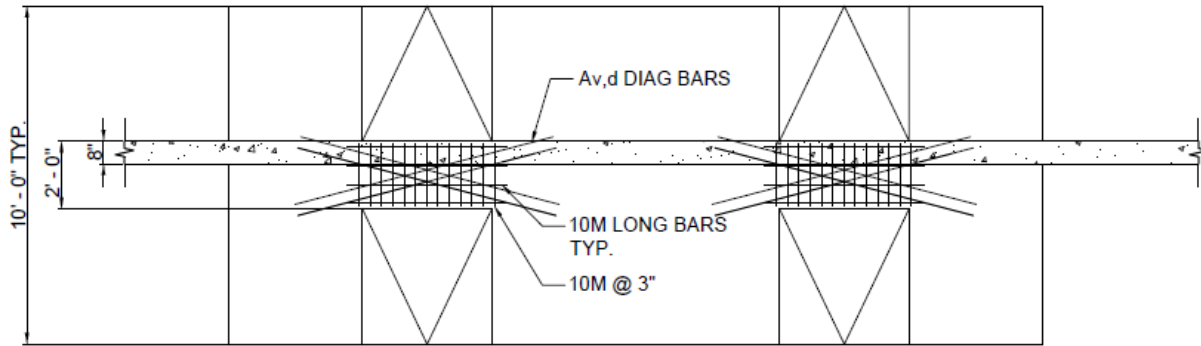


Figure 6.2 Ductile header beam detailing: stories 1-6 $A_{vd} = 8\text{-}35\text{M bars}$; stories 7-13 $A_{vd} = 6\text{-}35\text{M bars}$; and stories 14-18 $A_{vd} = 6\text{-}30\text{Mbars}$.

6.2 Numerical Modelling

The 3D numerical models were similar to the 2D models described in Chapter 4. The material models implemented remained the same (see: Figure 4.6) and the conventional header beam modelling was not changed (see: Section 4.2.2).

The gravity system (columns and slabs) were included in the 3D models, as well as a *zeroLength* fiber section at the base of each wall to account for reinforcement strain penetration into the foundation. The following sections describe these additions as well as the new, ductile header beam models.

6.2.1 Header Beam Shear Hinges

The header beams were modeled using elastic beam elements with nonlinear shear hinges. The elastic beam elements were modeled considering a cracked section modulus ($I_{\text{cracked}} = 0.35I_{\text{gross}}$) to account for bending deformations. Between the header beam elements and wall elements, rigid beam elements were modeled to account for the physical width of the walls. A shear hinge was modeled at the midpoint of each header beam to account for the shear yielding and nonlinearity in the elements.

6.2.1.1 Ductile Header Calibration

The material model for the ductile beam shear hinges were calibrated to a reverse-cyclic test performed by Naish (2010) on specimen CB24F-RC. CB24F-RC was a fully confined section with #3 transverse bars every 3" (150 mm) and included a RC slab cast into the beam. This specimen had an aspect ratio (length/width) of 2.4, which is typical for residential buildings, and is illustrated in Figure 6.3. Naish also tested diagonally confined specimens and noted similar strength, stiffness, and degradation characteristics; thus, the specimen type chosen for calibration should not affect the ultimate model behavior.

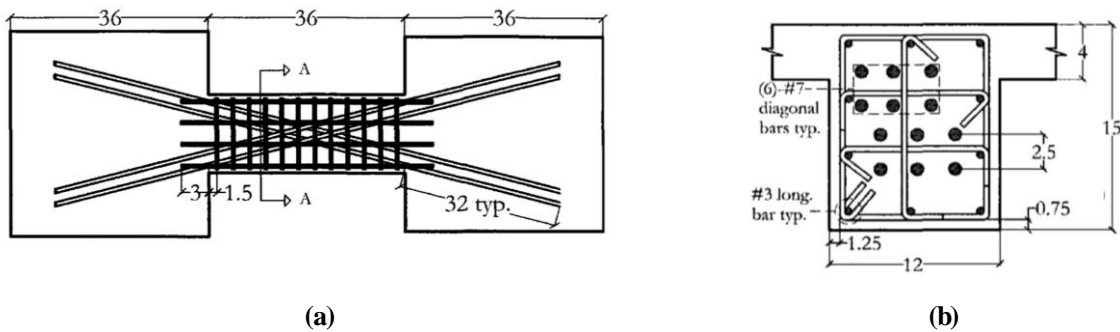


Figure 6.3 Specimen CB24F-RC: a) elevation; and b) cross section (from: Naish, 2010). All units are in inches.

The *Pinching4* material model (Lowe et al., 2004) was employed to capture pinching, in-cycle degradation, and cyclic stiffness and strength degradation in the nonlinear shear hinges. A comparison of the test results to the nonlinear shear material is presented in Figure 6.4 including the monotonic backbone curve assumed.

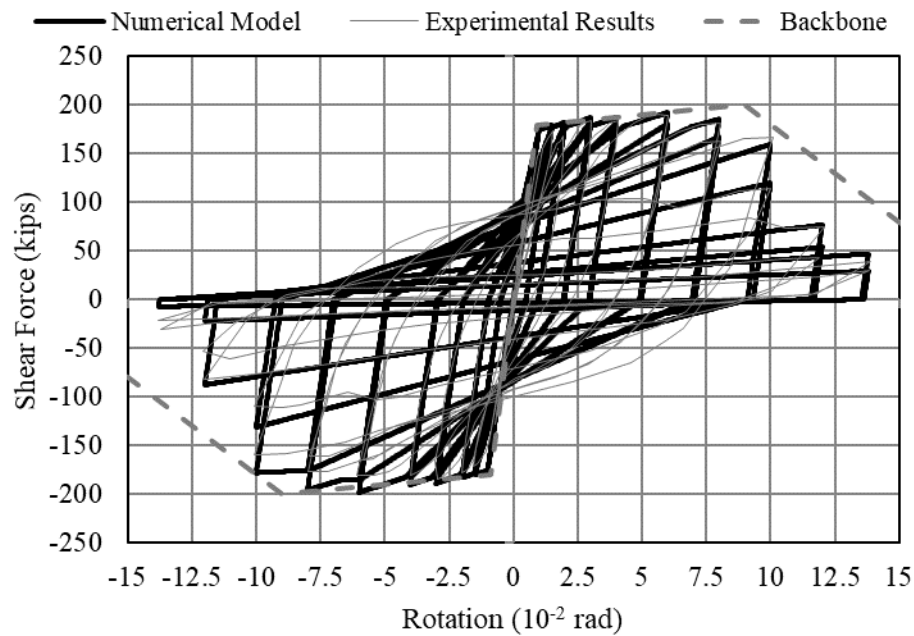


Figure 6.4 Nonlinear shear hinge model for ductile header beams vs experimental results (Naish, 2010).

6.2.2 Gravity System

Unlike in the 2D model from Chapter 4, the 3D models in this section include the entire gravity system including column and slabs. The circular columns have a 24" (610 mm) diameter over the entire height of the buildings and the slabs are 8" (200 mm) thick. The columns were modeled as elastic elements with a nonlinear rotation spring at each terminal end. The elastic element was modeled with the columns effective cracked section properties ($1.0A_g$ for axial resistance; $0.7I_g$ for flexure; $0.4A_g$ for shear; LATBSDC, 2017; A_g = gross cross-sectional area, and I_g = gross moment of inertia) to capture the elastic behavior of these elements. The nonlinear rotational springs at the terminal ends were modeled with a bilinear material with 0.25% strain hardening (Figure 6.5). The plateau length between yielding and strength loss ($\theta_c - \theta_y$) was taken

from ASCE-41 (ASCE/SEI, 2017) for columns with a shear reinforcement ratio (ρ) >0.006 and an axial load ratio ($P/A_g f'_C$) <0.1 , which resulted in a plateau length of 0.035 rad post-yielding.

The slabs were modelled as “slab-beams” – meaning that two beam elastic beam elements are used to capture the effective width and stiffness of the slabs. Two beam elements are required because the effective width depends on the width of the connecting vertical element; thus, the slabs have a greater effective width at the wall-end than at the column-end. These beams were used to connect to walls to the columns. The effective area of the beam elements was reduced to 25% for axial and moment resistance, and 10% for shear resistance to account for cracking (LATBSDC, 2017). At each end (wall-end and column-end) a nonlinear rotational spring with a generic bilinear backbone curve (Figure 6.5) was utilized to capture nonlinear behavior in the slab-wall and slab-column connections. The plateau length of these springs ($\theta_c - \theta_y$) was taken as 0.03 rad from ASCE-41 (ASCE/SEI, 2017). The yield moment was calculated based on the effective beam width and 0.25% strain hardening was modelled.

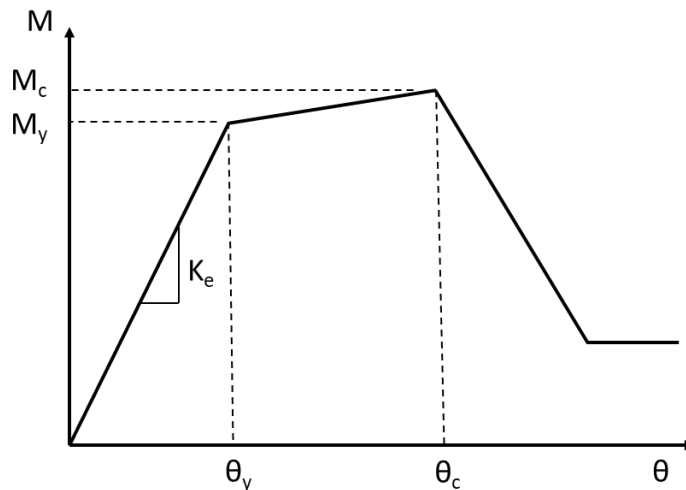


Figure 6.5 Generic bilinear moment-rotation (M- θ) spring with in-cycle strength loss.

6.2.3 Foundation Model

In order to capture the effect of rebar slip into the foundation, which could result in cyclic degradation due to ratcheting, an additional *zeroLengthSection* was modelled at the base of each wall. These sections were fiber sections with the same cross-section as the rest of the wall, however the steel was modeled with the *Bond-SPI* material model (Zhao and Sritharan, 2007). This material model can be used to model strain penetration at column-to-footing or wall-to-footing intersections and the resulting bond slip over the reinforcement anchorage length. The hysteretic behavior of the *Bond-SPI* material model used to model the steel reinforcement in the base zero-length section is illustrated in Figure 6.6c. Note that this assumes that the foundation of the structures is directly below grade, which may not be realistic, but is a common modelling simplification (LATBSDC, 2017).

Following the modelling recommendations from Zhao and Sritharan (2007), the concrete models in the base section were revised to exclude in-cycle strength loss greater than 80% of the peak strength. This is because the zero-length section along with the plane section requirement of a flexural member can impose unrealistically large compressive strains in the concrete fibers. These strains are only possible due to confinement effects from the adjoining wall member and fixed base and because of localized deformations at the member end and could far exceed the typical concrete strain capacity of confined concrete models. The concrete was otherwise modeled similarly to the wall section concrete model with the *Concrete02* uniaxial material model. The hysteretic models for the confined and unconfined concrete models used in the base zero-length section are illustrated in Figure 6.6a and b, respectively.

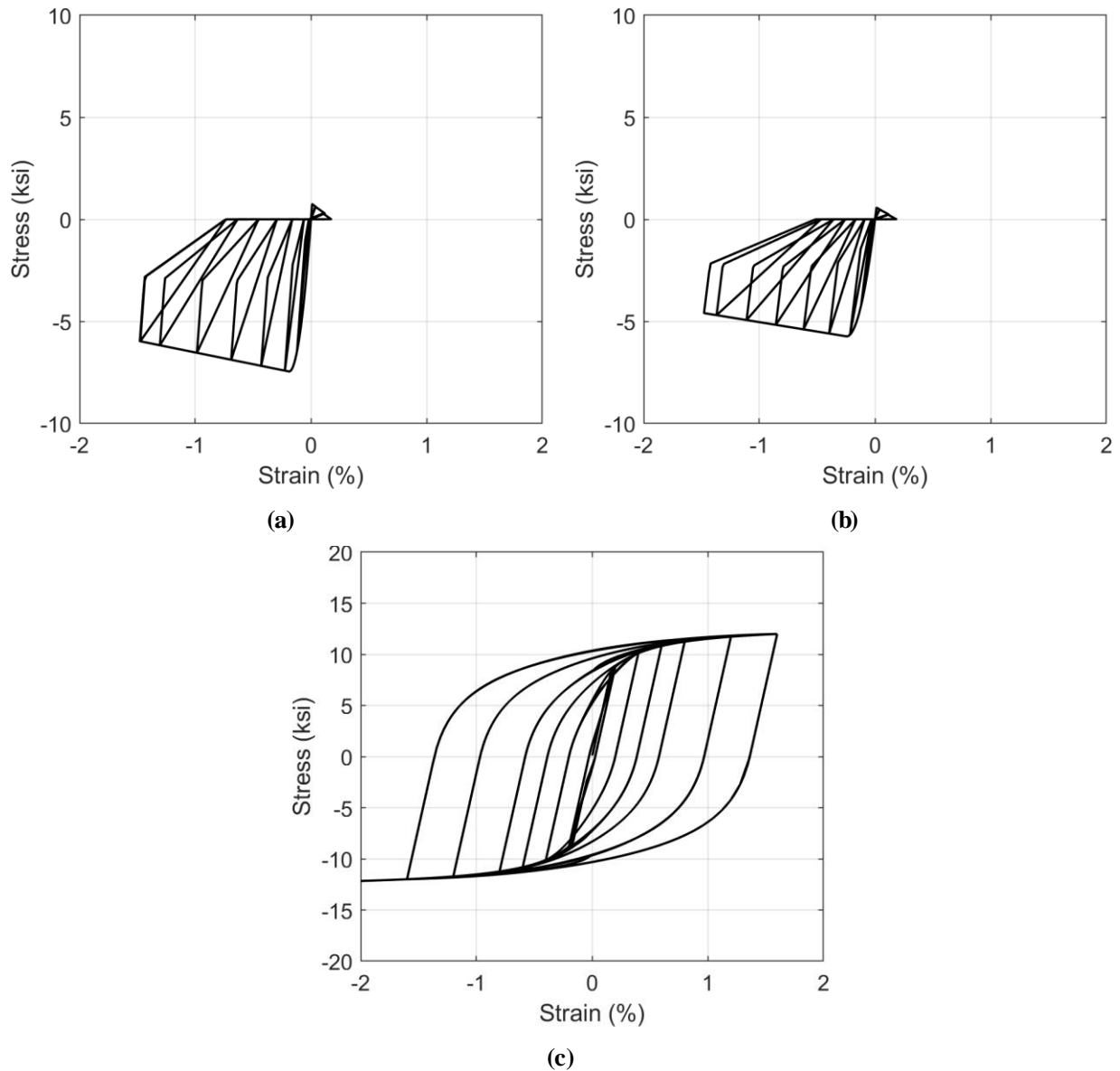


Figure 6.6 Material models for the zero-length base section: **1)** confined concrete (*Concrete02*); **b)** unconfined concrete (*Concrete02*); **c)** steel bond-slip material (*Bond-SPI*).

6.2.4 Model Summary

An illustration of the OpenSees model is illustrated in Figure 6.7. The first three elastic modes are presented in Table 6.1. Note that the NS direction is the coupled direction (see archetype building floor plan: Figure 4.1). The 3D models are slightly stiffer than the 18 story 2D model

from the Chapter 4 due to the additional of the gravity system (which was omitted in the 2D model).

A nonlinear static (pushover) analysis was performed on each model in the coupled-wall direction – these results (base shear vs. drift) are presented in Figure 6.8. Each model tends to yield at its design base shear level (3050 and 1150 kips [13570 and 5115 kN] for CC and ductile construction, respectively) and has a large amount of overstrength due to strain hardening. The CC model loses lateral stability at ~2.75% drift, which is to be expected for this non-ductile design; while the ductile model remains stable to ~5% drift. The CC model sees a peak lateral strength of ~3500 kips (15570 kN; ~15% higher than its design base shear), and the ductile model has a peak strength of ~2200 kips (9790 kN; ~90% higher than its design base shear).

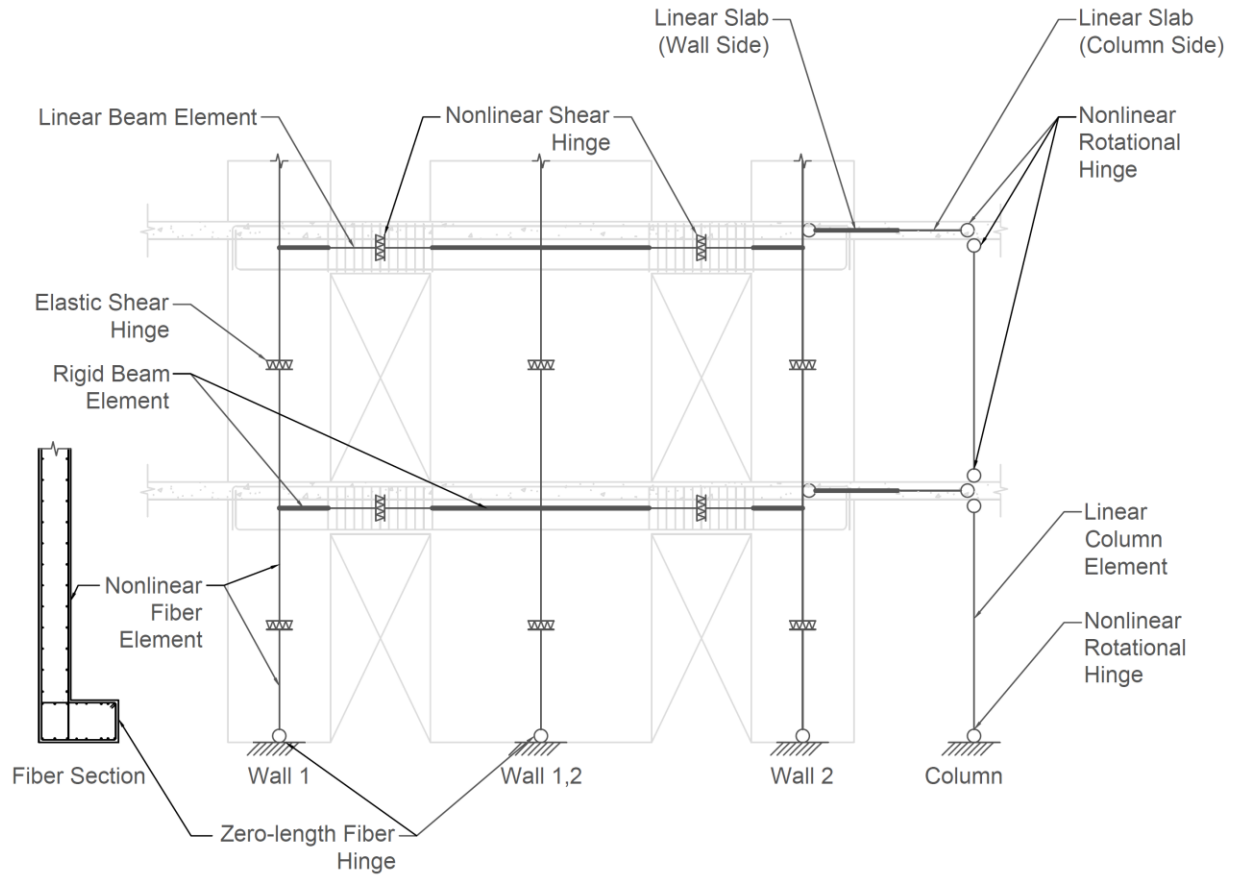


Figure 6.7 Illustration of a typical story of the 3D OpenSees numerical models.

Mode	Direction	CC (s)	Ductile (s)
T1	NS	1.177	1.182
T2	EW	1.110	1.117
T3	Torsional	0.582	0.585
T4	NS	0.268	0.269
T5	EW	0.192	0.193
T6	Torsional	0.181	0.183
T7	NS	0.123	0.123
T8	EW	0.107	0.108
T9	Torsional	0.077	0.078

Table 6.1 First nine elastic periods of the 18 story RC shearwall archetype building numerical models.

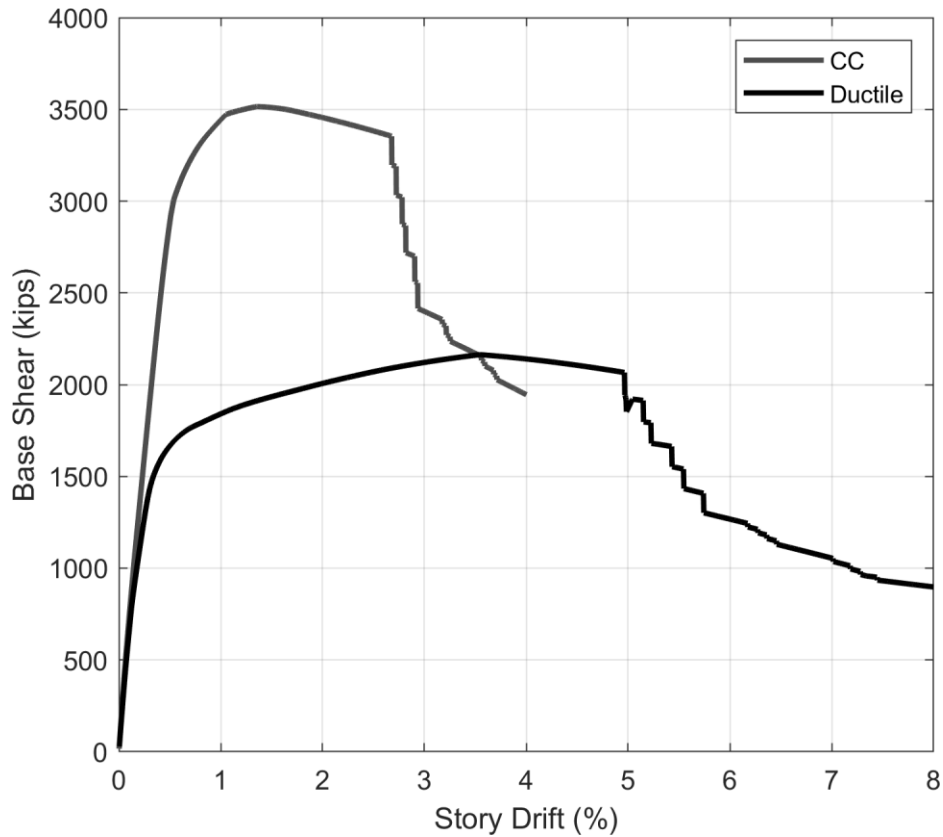


Figure 6.8 18 story ductile vs. conventional construction (CC) base shear vs story drift pushover curves.

6.3 Ground Motion Suites

For this chapter, the CS approach with two conditioning periods was implemented. From the previous sections, the periods of the 18 story 3D models were ~1.2 s. To capture the nonlinear model behavior (which is how the model is expected to behave for a majority of the shaking duration according to Section 5.4.2), 2.0 s was selected as one conditioning period (CS20). To capture more higher mode behavior, which is ultimately expected to govern force demands, a second conditioning period of 0.75 s was selected (CS075). Both of these periods were conditioned to the 2% in 50 year hazard level for Vancouver, BC, obtained from the 2015 GSC seismic hazard model (Halchuk et al, 2014).

First, seismic hazard deaggregation of the crustal and subduction interface sources was performed for periods of 0.75 and 2.0 s using the GSC model implementation in EZ-Frisk (Furgo, 2015). The governing scenarios (magnitudes and distances) were similar between both periods at the 2% in 50 year hazard level; results for the crustal and subduction interface sources at 0.75 s are illustrated in Figure 6.9a and b, respectively. The crustal contributions tend to come from sources ~0-50 km away with magnitudes of ~5-7.5; subduction interface contributions are governed by a magnitude ~9 event at 100-125 km (rupture of the Cascadia interface fault).

Next, the conditional mean spectra (CMS) and target lognormal standard deviations were developed using the Baker and Jayaram (2008) epsilon correlation coefficients and the GMMs used in the 2015 hazard model (Table 2.1) for the two conditioning periods (CS075 and CS20 for $T_C = 0.75$ and 2.0 s, respectively). These targets are illustrated in Figure 6.9c and d, compared to the Vancouver 2% in 50 year UHS for $V_{s30} = 450$ m/s.

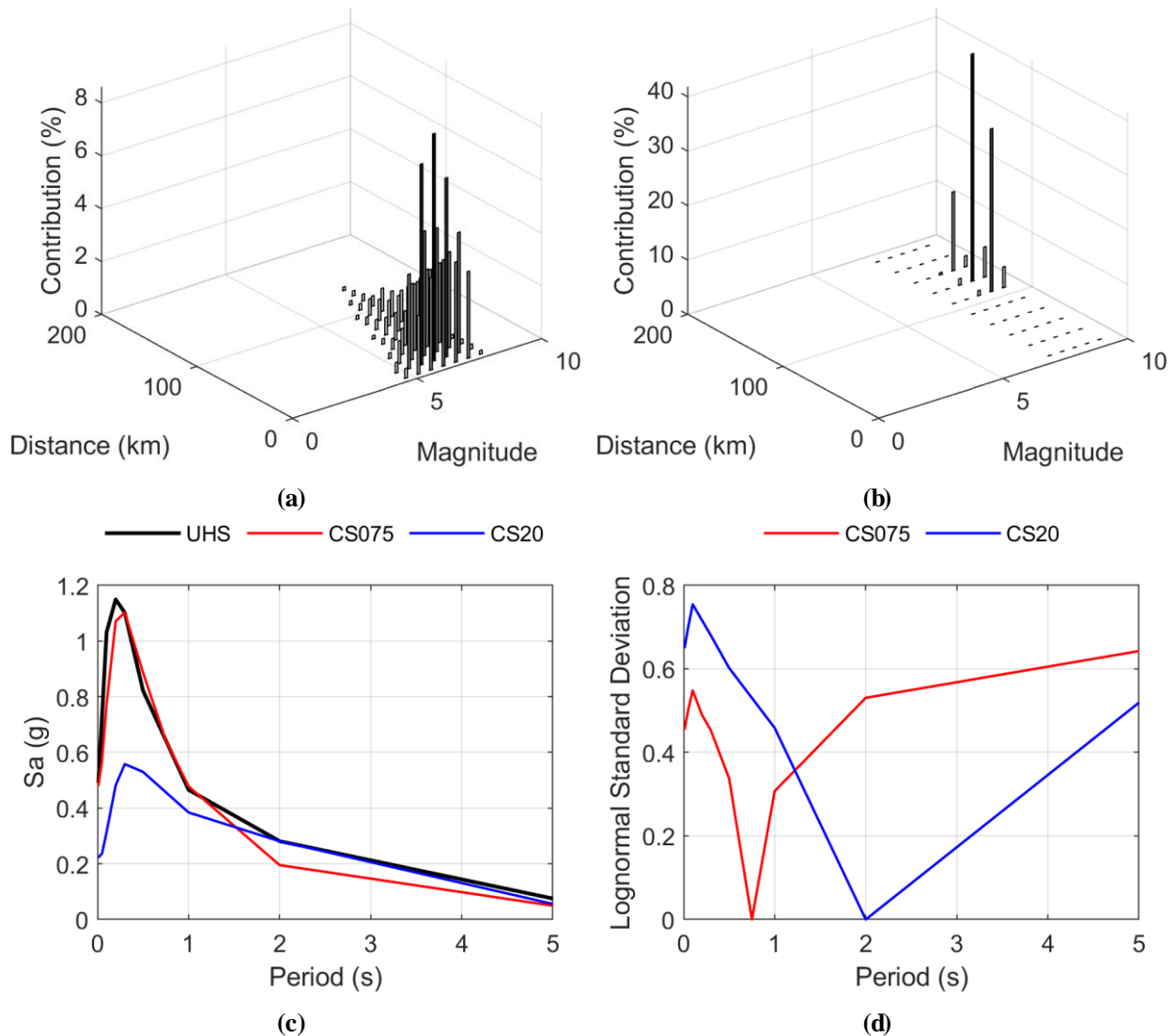


Figure 6.9 a) Crustal hazard deaggregation and, b) subduction interface deaggregation for 2% in 50 year hazard at $T = 0.75$ s for Vancouver, BC; c) 2% in 50 year UHS vs CMS targets; and, d) CS target lognormal standard deviations.

Two suites of bi-directional seed records were selected and scaled to the 2% in 50 year UHS: a crustal suite, and a subduction interface suite. The records were selected from the database developed in Section 3.3.1. The records were selected from the governing magnitudes and distances previously discussed; Site Class C stations ($V_{s30} = 360\text{-}760$ m/s) were preferred when possible. The metadata for the two suites is summarized in Table 6.2 and Table 6.3.

Using the methodology proposed in Section 5.2, each seed record geomean spectrum was matched to the target CS: CS075 and CS20. The targets (CMS and variance) were matched from 0.2-4.0 s, which is approximately $0.2 \cdot T_1$ to $2 \cdot T_1$ of the models. The seed records were spectrally matched to the target VTS* using RSPMatch05 (Hancock et al., 2006). The default matching parameters were used with a 5% matching tolerance and 5 matching passes. This produced four suites of CS matched motions: interface records matched to CS075: LONG075; interface record matched to CS20: LONG20; crustal records matched to CS075: SHORT 075; and crustal records matched to CS20: SHORT20. The seed and matched record pseudo-spectral acceleration values and lognormal standard deviations, compared to the targets, for these four suites are illustrated in Figure 6.10 to Figure 6.13. In these figures, the period range outside of the matching range is shaded in grey.

Event	Station	Magnitude (M_w)	Distance (km)	Vs30 (m/s)	d_{5.95} (s)
Cape Mendoza, 1992	FOR	7.01	20.0	660	18.7
Chi-Chi, 1999	CHY029	6.2	31.8	219	21.8
Chi-Chi, 1999	TCU070	6.2	46.4	219	21.2
Chi-Chi, 1999	TCU116	6.2	22.1	213	9.9
Chi-Chi, 1999	CHY034	6.2	28.5	219	20.2
Coalinga, 1983	COW	6.36	42.0	415	17.3
Duzce, Turkey, 1999	BOL	7.14	12.0	385	8.5
Landers, 1992	LCN	7.28	2.2	713	13.1
Landers, 1992	NPS	7.28	26.8	199	36.3
Loma Prieta, 1989	HSP	6.93	27.9	213	16.4
Mammoth, 1988	CVK	5.91	0.0	874	6.3
Northridge, 1994	5108	6.69	16.7	199	7.4
Northridge, 1994	FAI	6.69	44.8	199	20.9
Tabas, 1978	DAY	7.35	13.9	185	12.3
Tabas, 1978	TAB	7.35	2.1	257	16.5

Table 6.2 Crustal seed record metadata

Event	Station	Magnitude (M_w)	Distance (km)	Vs30 (m/s)	d_{5.95} (s)
Hokkaido, 2003	HKD039	8.0	161.3	727	59.1
Hokkaido, 2003	HKD105	8.0	124.9	257	29.2
Hokkaido, 2003	HKD129	8.0	163.5	384	90.4
Maule, 2010	SJCH	8.8	176.9	461	39.0
Maule, 2010	Hualane	8.8	35.0	823	61.7
Maule, 2010	Matanzas	8.8	79.3	217	34.0
Maule, 2010	Stgo La Florida	8.8	174.0	551	41.6
Maule, 2010	Stgo Penalolen	8.8	176.5	758	34.2
Michoacán, 1985	AZIH8509	8.1	93.4	535	19.8
Tohoku, 2011	AKT0061	9.1	193.9	212	105.1
Tohoku, 2011	AKT018	9.1	195.7	347	127.9
Tohoku, 2011	AOM021	9.1	196.4	1126	140.2
Tohoku, 2011	CHB013	9.1	178.1	452	110.1
Tohoku, 2011	MYG005	9.1	143.5	357	134.1
Tohoku, 2011	YMT002	9.1	170.0	590	138.9

Table 6.3 Subduction interface seed record metadata

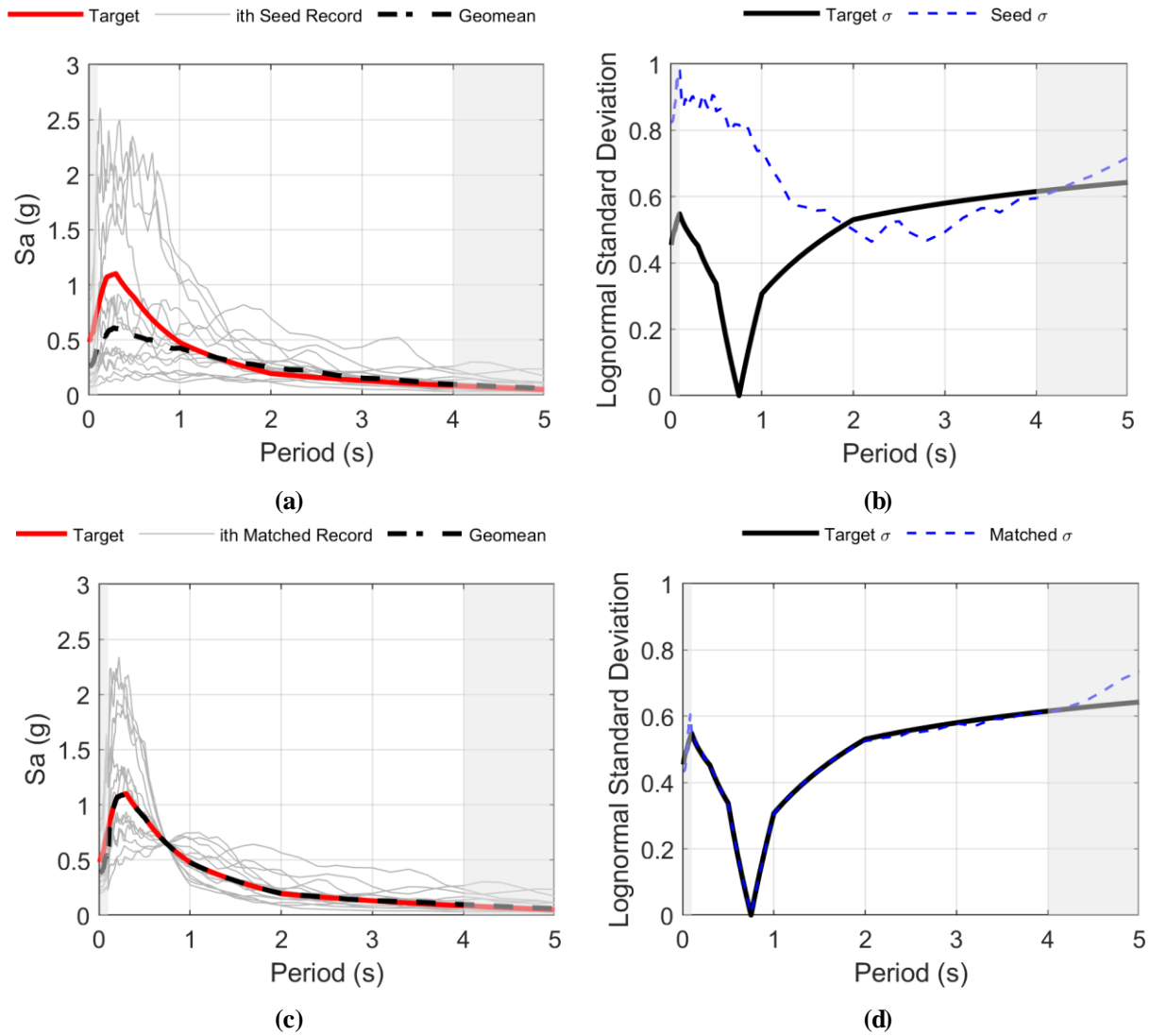


Figure 6.10 LONG075 suite: a) seed records suite spectra; b) seed records suite lognormal standard deviation; c) matched (from 0.2-4.0 s) records suite spectra; and, d) matched records suite lognormal standard deviation.

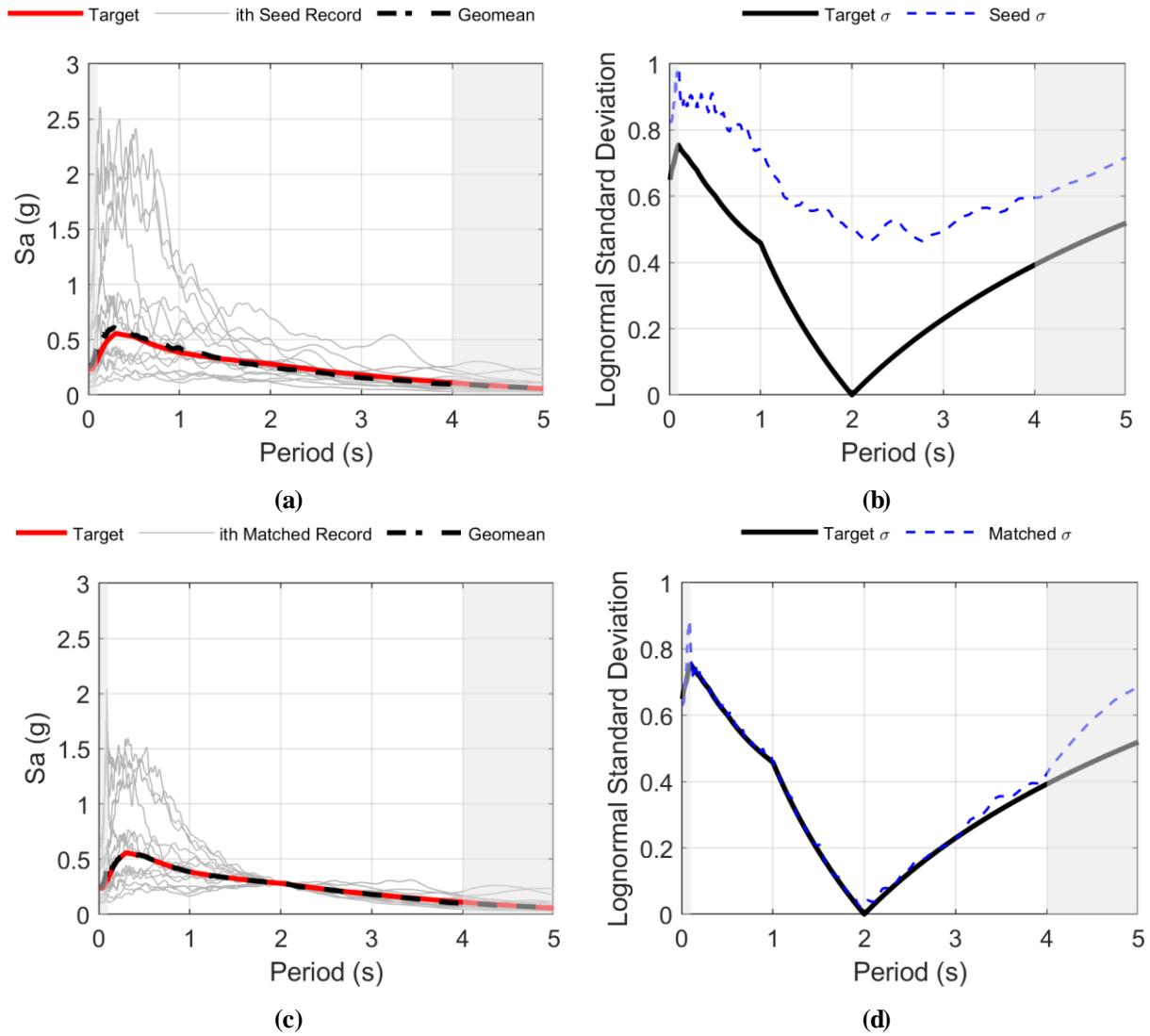


Figure 6.11 LONG20 suite: a) seed records suite spectra; b) seed record suite lognormal standard deviation; c) matched (from 0.2-4.0 s) records suite spectra; and, d) matched records suite lognormal standard deviation.

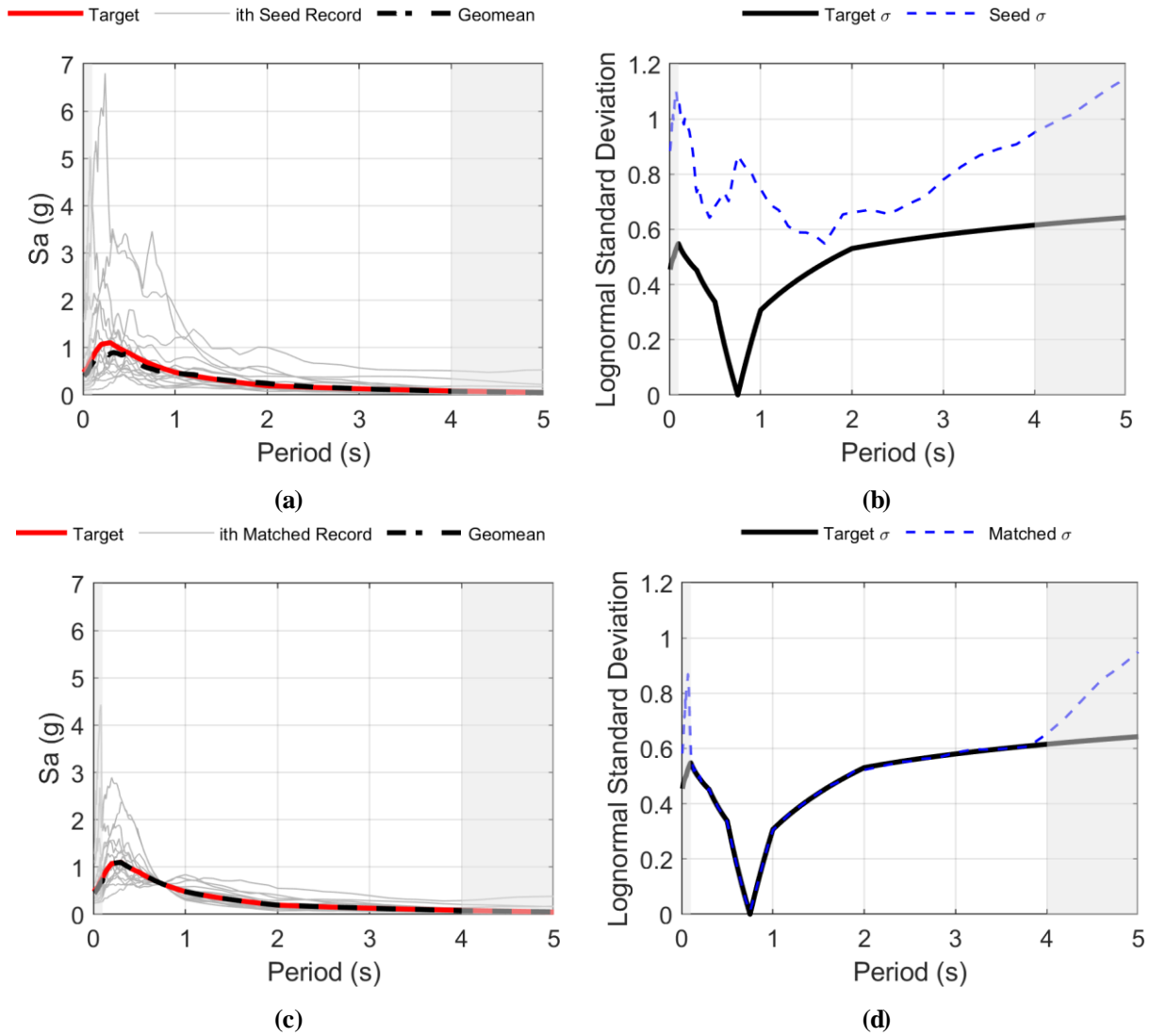


Figure 6.12 SHOR075 suite: a) seed records suite spectra; b) seed record suite lognormal standard deviation; c) matched (from 0.2-4.0 s) records suite spectra; and, d) matched records suite lognormal standard deviation.

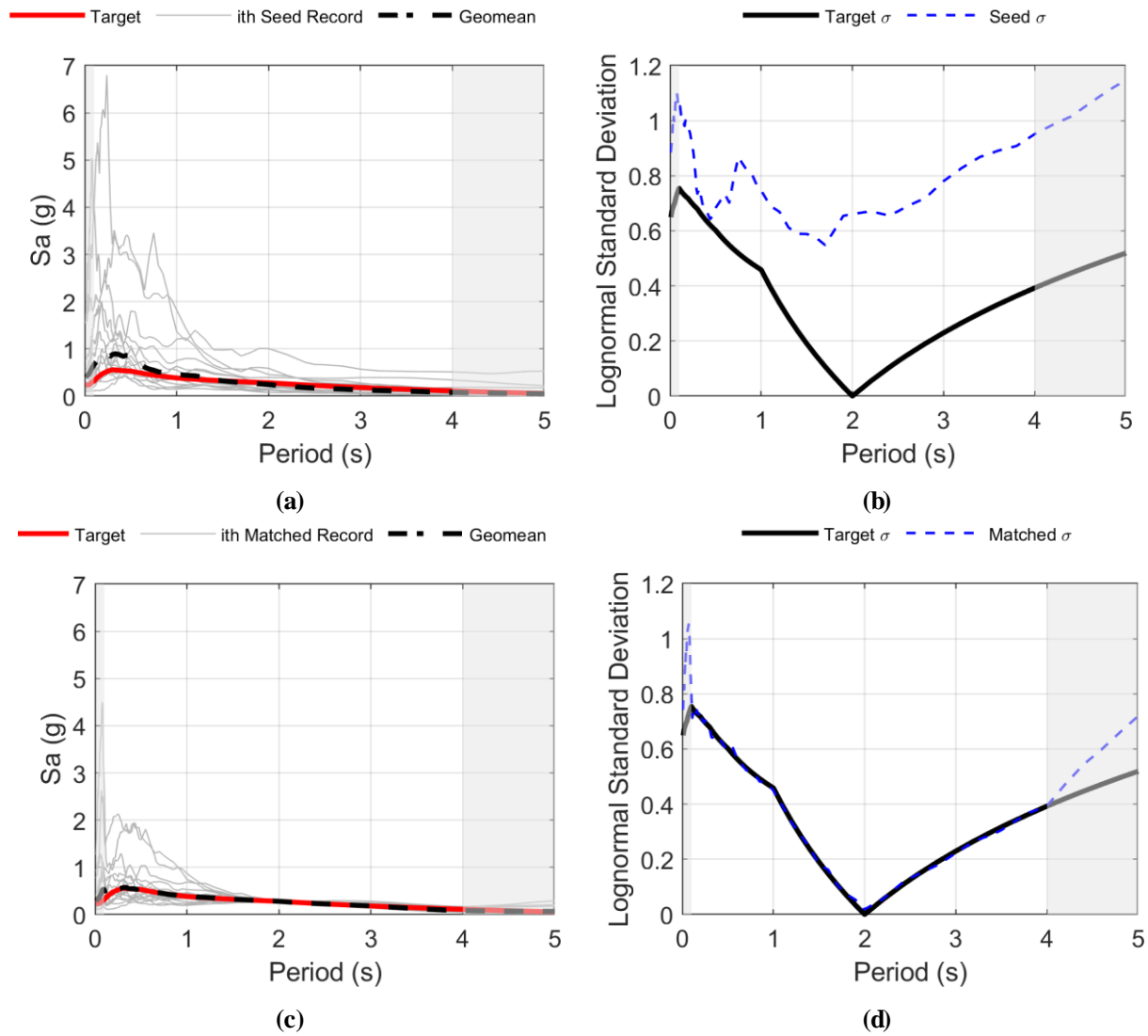


Figure 6.13 SHOR20 suite: a) seed record suite spectra; b) seed record suite lognormal standard deviation; c) matched (from 0.2-4.0 s) recordsuite spectra; and, d) matched recordsuite lognormal standard deviation.

6.4 Analysis Results

The code- and collapse-level analysis results for the two models and four ground motion suites are presented in the following sections. The code-level (ground motion shaking level with a 2% in 50 year probability of exceedance as per the NBCC) results are used to compare the results of the LONG and SHORT suites at a high, but not extreme, level of shaking.

The collapse-level results are obtained by running the models through IDA until collapse is observed. Collapse is defined as loss of lateral stability (i.e. model collapse/non-convergence) or reaching a non-simulated failure mode. The non-simulated failure modes include wall shear failure (one or more walls reaches its ultimate shear capacity), which is not captured in the nonlinear fiber models for the walls; or loss of the gravity system (axial column failure), which is not captured in the column models.

6.4.1 Ductile Design

6.4.1.1 Code Level Analysis

The analysis results are discretized into three sections:

- 1) **Lateral-force resisting system displacement results**: interstory drifts, header rotations, and wall strains.
- 2) **Lateral-force resisting system force demands**: story shear forces and overturning moments.
- 3) **Gravity system results**: column rotations.

Lateral-force resisting system displacement results

The resulting maximum interstory drifts for the models in the coupled and non-coupled directions are illustrated in Figure 6.14 and Figure 6.15, respectively, for the four ground motion suites. The NBCC uses interstory drifts as a surrogate for structural damage, and limits regular

buildings to a mean maximum interstory drift of 2.5% of the story height when using a suite of records to conduct time history analysis (dashed red line in Figure 6.14 and Figure 6.15). For the collapse prevention evaluation used in performance-based design, mean and maximum interstory drifts are limited to 3.0% (dashed blue line in Figure 6.14 and Figure 6.15), and 4.5%, respectively (LATBSDC, 2017). None of the suites surpasses these limits.

The LONG vs SHORT results are similar in both cases (CS075 and CS20 suites). This may be because the overall damage (interstory drift levels) is quite low at this level of shaking (maximum interstory drift of ~1% for the two suites). At these lower levels of damage, the amount of degradation in the walls and header beams is low, which will largely nullify the effect of the ground motion duration. This was also seen in the 2D model results (Section 4.4). The higher conditioning period of 2.0 s in the CS20 suite produced greater demands, indicating that the displacement (and therefore drift) results are governed by the nonlinear behavior of the models. Figure 6.16 presents the header rotation results over the height of the model. Once again, the SHORT and LONG suites produced similar rotation demands; in both cases the CS20 suites governed. From ASCE-41, for existing structures, the collapse prevention rotation for these well-confined headers would be 0.05 rad (dashed red line in Figure 6.16). For new structures with diagonally-reinforced header beams, LATBSDC (LATBSDC, 2017) recommends a total chord rotation limit of 0.06 rad (dashed blue line in Figure 6.16). The geometric mean results for all suites are well below these limits.

Finally, Figure 6.17 presents the wall strain results over the height of the model. Positive strains represent tension in the reinforcing steel, while negative strains represent concrete compression strains. The LATBSDC limits are shown as the dashed red lines.

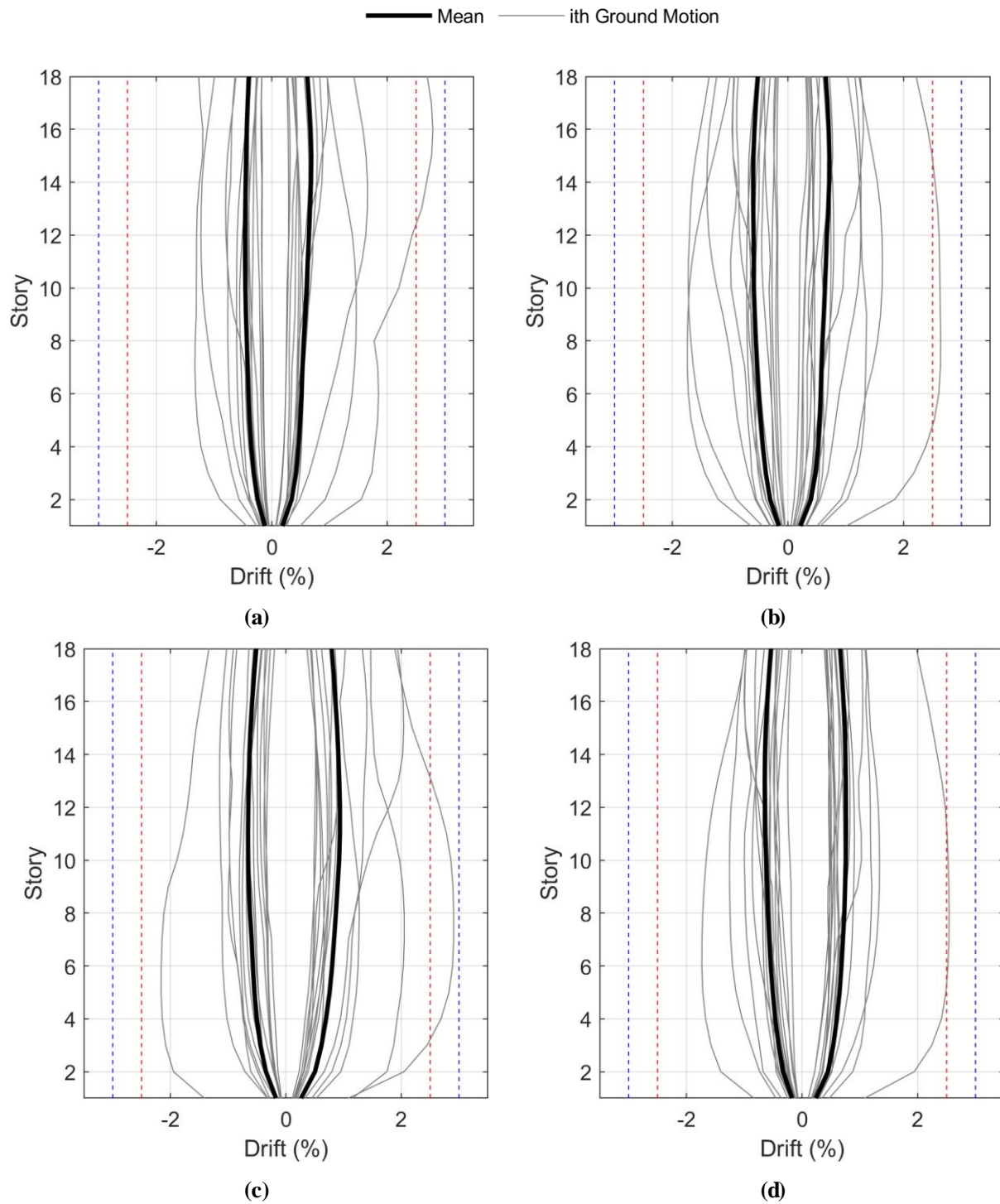


Figure 6.14 Coupled-direction interstory drift results for the ductile 18 story model at the code shaking level for: a) the SHORT075; b) LONG075; c) SHORT20; and, d) LONG20 ground motion suites.

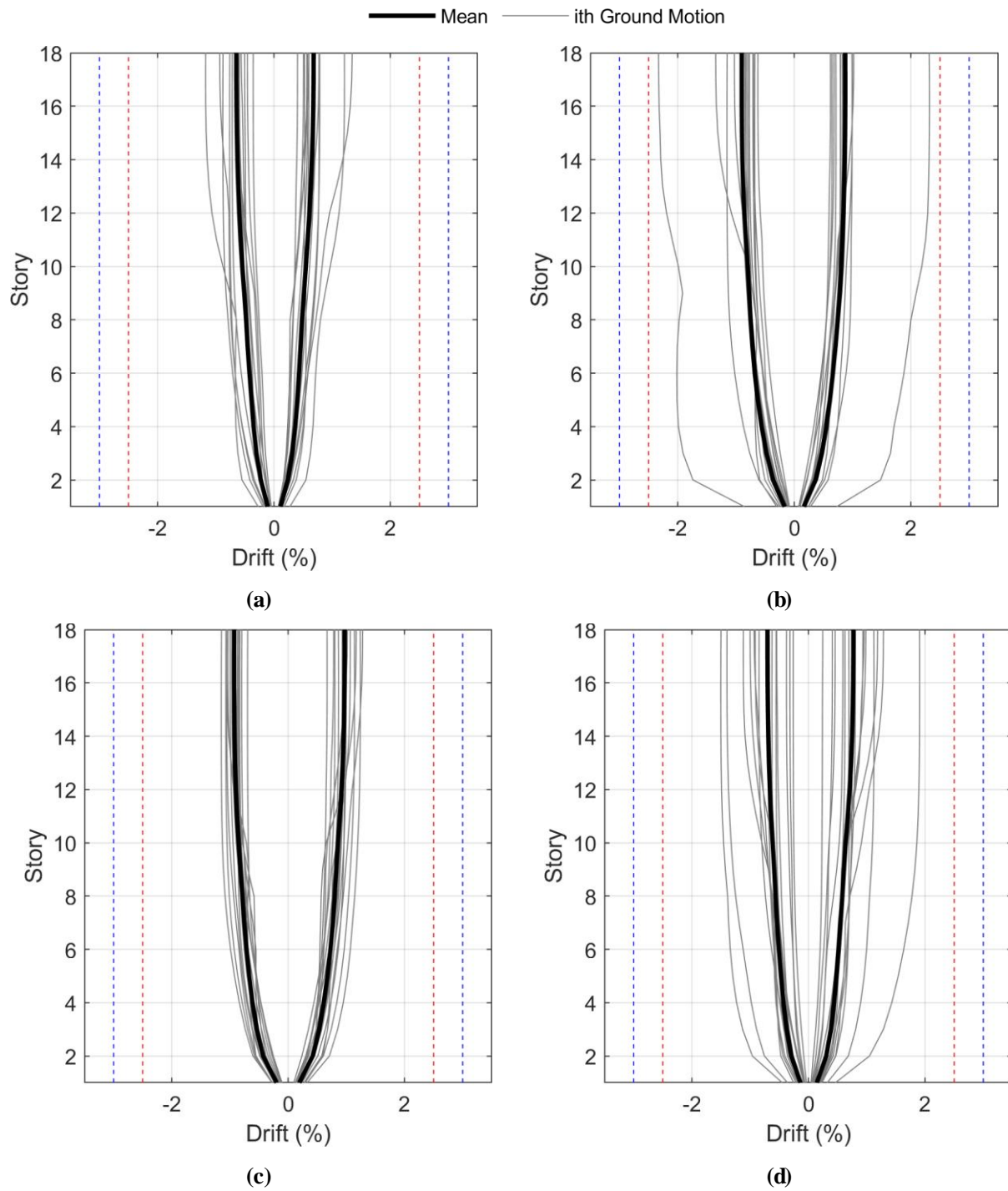


Figure 6.15 Wall direction interstory drift results for the ductile 18 story model at the code shaking level for: a) the SHORT075; b) LONG075; c) SHORT20; and, d) LONG20 ground motion suites.

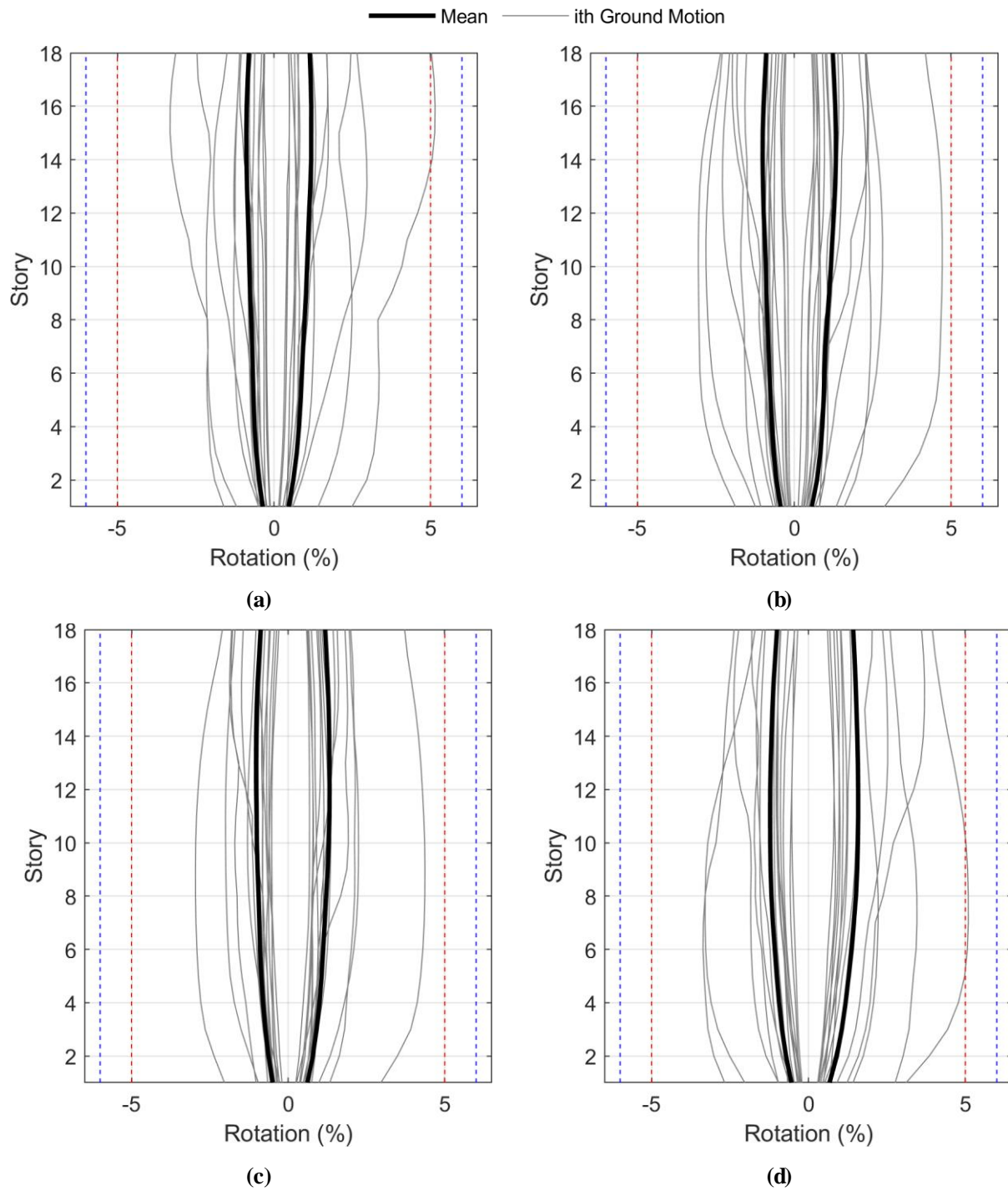


Figure 6.16 Header rotation results for the ductile 18 story model at the code shaking level for: a) the SHORT075; b) LONG075; c) SHORT20; and, d) LONG20 ground motion suites.

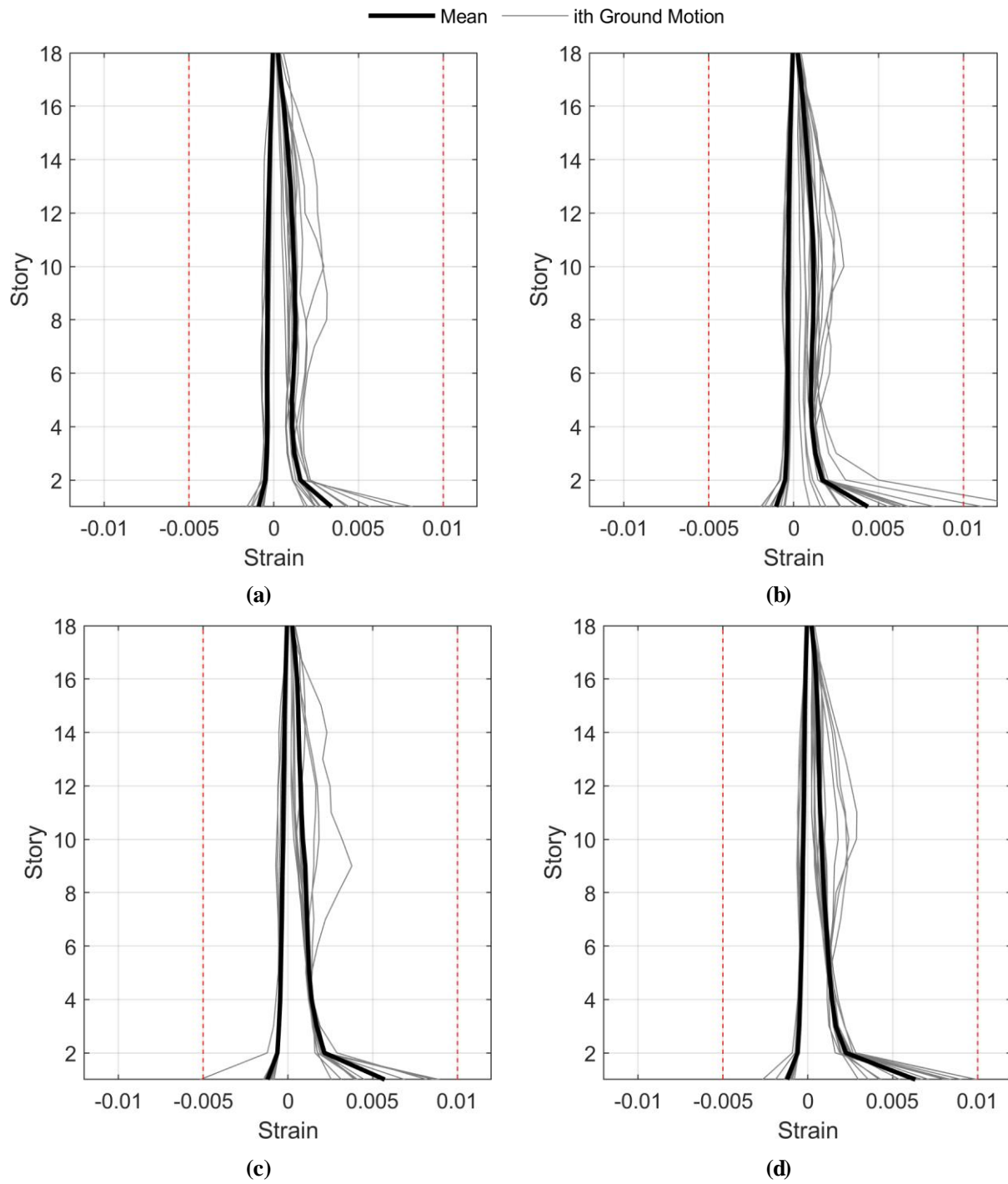


Figure 6.17 Reinforcement strain results for the ductile 18 story model at the code shaking level for: a) the SHORT075; b) LONG075; c) SHORT20; and, d) LONG20 ground motion suites.

Lateral-force resisting system force demands

The story force and moment demands are illustrated in Figure 6.18 and Figure 6.19, respectively. These results are presented as the governing results considering both directions of shaking. The overturning moment demands are similar for all four suites, as this is governed by the strength of the walls. The story shear forces were higher for the CS075 suites, but comparable between LONG075 and SHORT075. This indicates that the higher mode effects are increasing the story shear demands and exemplifies why these effect should not be ignored when developing ground motion suites for time history analysis (i.e. target spectra should be conditioned at periods both higher and lower than the elastic period when implementing a CMS or CS approach; scaling/matching ranges should be extended to lower periods when period-range scaling/matching ground motion suites.)

Following LATBSDC, the maximum allowable shear force (V_{allow}), based on the total wall shear area (sum of $A_{wi} = L_{wi}b_{wi}$ for each wall segment i) would be:

$$V_{allow} = \sum A_{wi} * \frac{8\sqrt{f'_c}}{1.5} \quad (6-1)$$

The total shear area of the three walls is 12750 in² (8.23 m²) in the NS direction and 12000 in² (7.64 m²) in the EW direction - this results in 5900 kips (26245 kN) in the NS direction and 5570 kips (24780 kN) in the EW direction using $f'_c = 5080$ psi (35 MPa). The mean shear force demands from Figure 6.18 are well below this limit. Additionally, each wall segment should have a shear force less than:

$$V_{allow,i} = A_{wi} * \frac{10\sqrt{f'_c}}{1.5} \quad (6-2)$$

This criterion is also not exceeded for any of the wall segments.

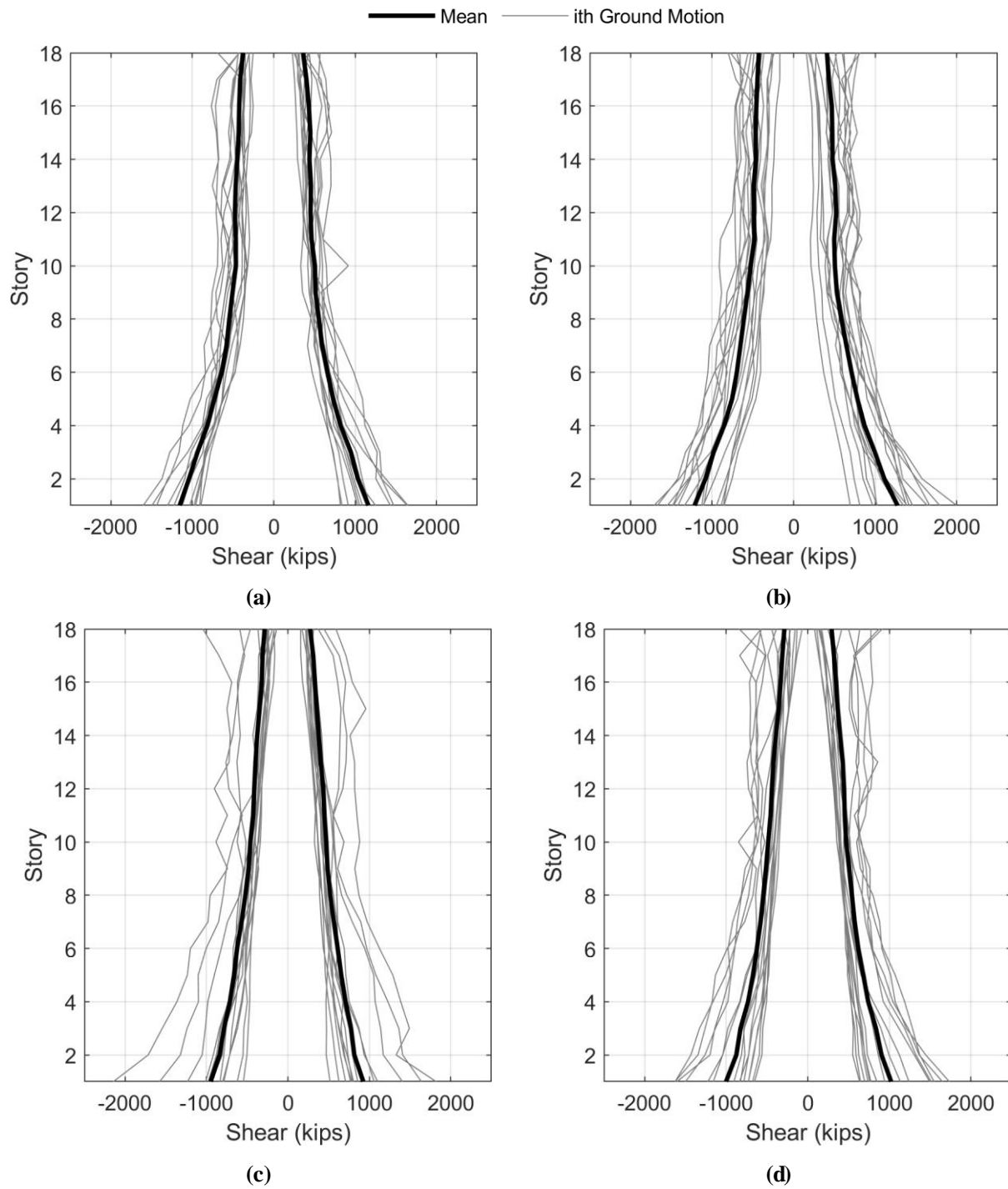


Figure 6.18 Story shear results for the ductile 18 story model at the code shaking level for: a) the SHORT075; b) LONG075; c) SHORT20; and, d) LONG20 ground motion suites.

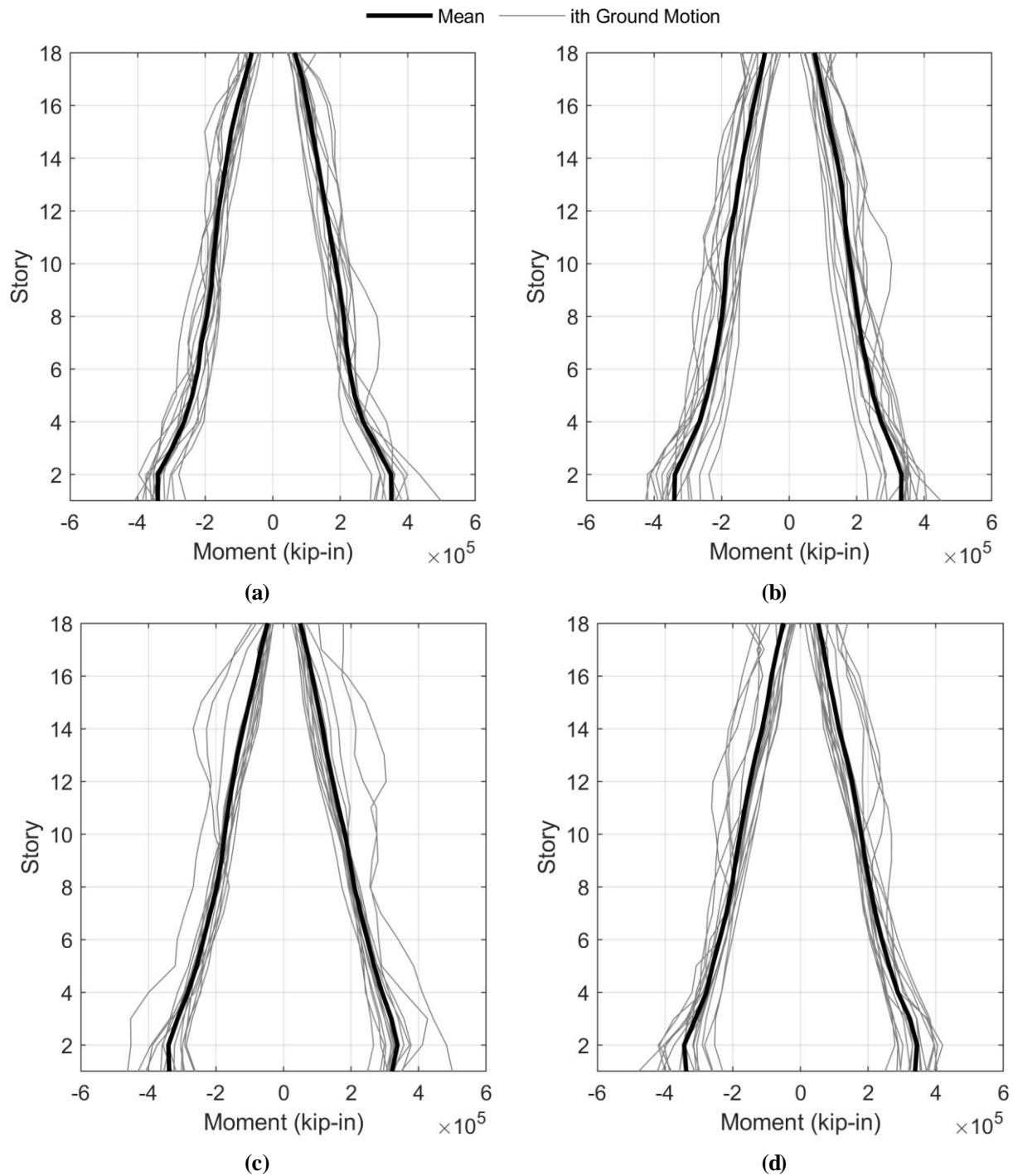


Figure 6.19 Story overturning moment results for the ductile 18 story model at the code shaking level for: a) the SHORT075; b) LONG075; c) SHORT20; and, d) LONG20 ground motion suites.

Gravity system results

Figure 6.20 presents the column hinge rotation results over the height of the model. The ASCE 41 collapse prevention rotation limit for this type of column ($\rho > 0.006$ and $P/A_g f'_c < 0.1$) is 6.0%. All resulting rotation demands are well below this limit.

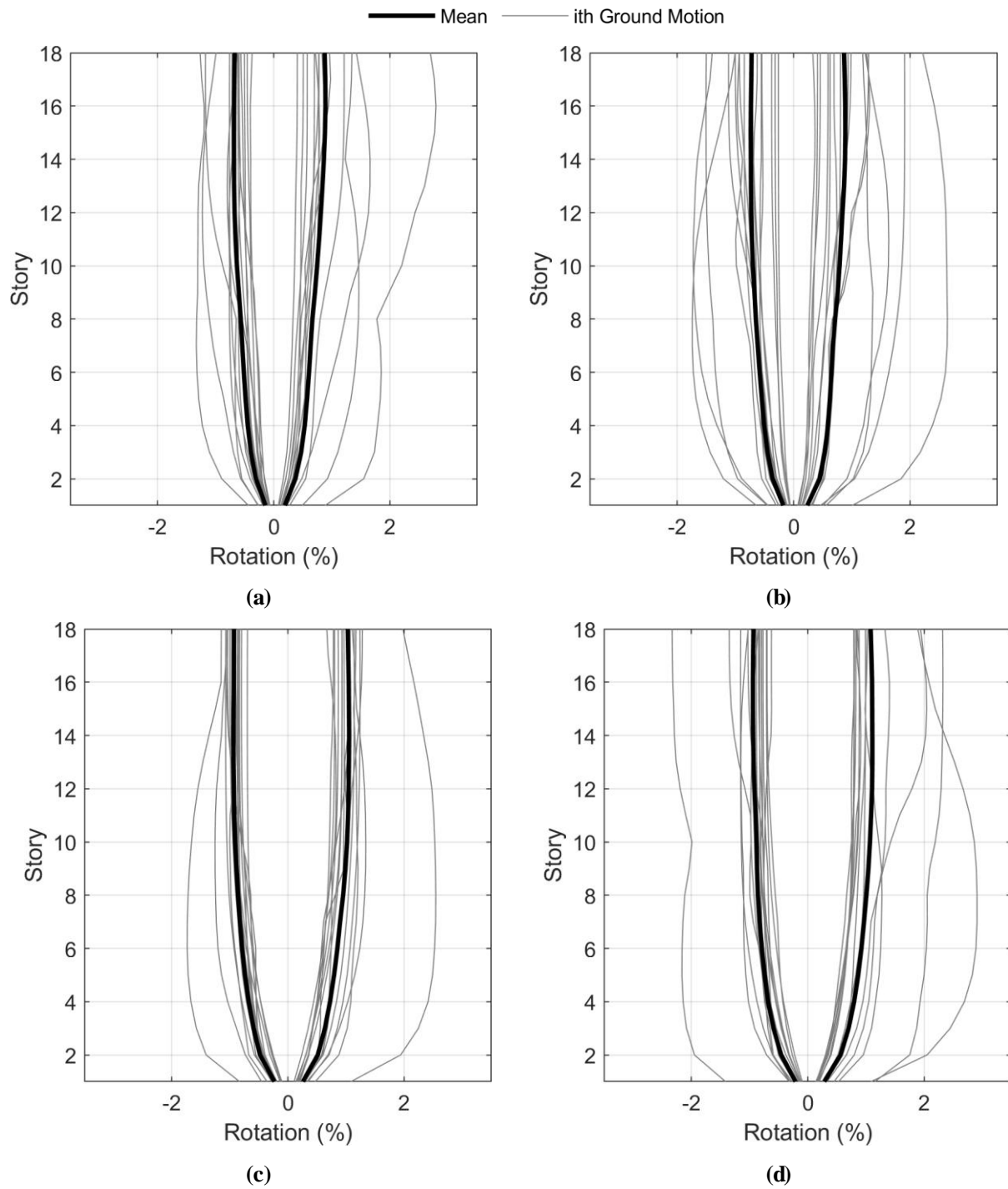


Figure 6.20 Column hinge results for the ductile 18 story model at the code shaking level for: a) the SHORT075; b) LONG075; c) SHORT20; and, d) LONG20 ground motion suites.

6.4.1.2 Collapse and Life Safety Analysis

For the ductile design, collapse is defined as interstory drift exceeding 5%, shear failure in any wall, or gravity system (column or slab) failure. Shear failure in the walls is defined using Equations 6-2 without the 1.5 factor. Column failure is defined as a rotation in one or more column springs that exceeds 0.06 rad post-yielding (collapse prevention rotation limit from ASCE-41 [ASCE/SEI, 2017] for columns with $\rho > 0.006$ and $P/A_g f'_C < 0.1$). At this plastic rotation level, the columns would be expected to lose their axial load capacity, resulting in local or global failure of the gravity system. Slab failure is defined as rotation in a slab spring that exceeds 0.05 rad post-yielding (collapse prevention rotation limit from ASCE-41 [ASCE/SEI, 2017] for slab-column connections reinforced connections). This is the level of damage where slabs would lose their shear resistance resulting in column punch-through, and ultimately, local gravity system failure.

The lognormal fitted CDF curves for the CS075 and CS20 motion suites are presented in Figure 6.21a and b, respectively. The resulting lognormal fitted curves are plotted with record-to-record (RTR) variability only (i.e. the variability observed solely from the difference in results from the different records) and the total variability (adjusted standard deviation using the FEMA P-695 factors; see Section 4.5). The median collapse scaling level (expressed as a percent of the 2% in 50 year hazard level) and collapse probability at the 2% in 50 year scaling level are summarized in Table 6.4.

The median collapse scaling levels for the LONG suites was ~20% lower than the comparable SHORT suites – the 2% in 50 year collapse probabilities were significantly lower for the SHORT075 and SHORT20 suites, respectively, compared to the corresponding LONG suites. The 2.0 s conditioned suites were more demanding than the 0.75 s suites (high collapse

probabilities at the 2% in 50 year level and lower median collapse scaling levels.) This indicates that the nonlinear model behavior, which governed displacements, ultimately lead to collapse, rather than the increased force demands from the higher modes. Note that collapse was defined as either model lateral stability due to excessive drifts or reaching a non-simulated failure mode (excessive shear demands in the walls or rotations in the columns).

Next, the life safety (LS) exceedance results were considered. LS refers to a level of damage where the safety of building occupants is not jeopardized and is the typical performance level desired for new construction (ASCE/SEI, 2017; ASCE/SEI, 2016; NRCC, 2015). LS acceptance criteria are stricter compared to collapse prevention criteria. Following ASCE-41, the header rotation was limited to 0.025 rad (for fully confined headers), the column rotation limit was reduced to 0.045 rad, and the column connection limit was reduced to 0.035 rad; the interstory drift limit was also reduced to 2.5% (NRCC, 2015). With these new criteria, the CDFs were rederived (Table 6.5 and Figure 6.22).

As expected, the median LS exceedance levels were lower than the collapse level and the probabilities of exceedance at 2% in 50 year shaking were increased. However, the same general trends remained: the LONG suites were more demanding than the SHORT, and the CS20 suites governed the results. The difference between SHORT20 and LONG20, however, was much smaller (only an 8% increase in median LS exceedance scaling). This is because less component degradation can occur before these stricter criteria are reached, reducing the effect of motion duration. This is similar to the conclusions made for the code-level analyses in Sections 4.4 and 6.4.1.1.

Suite	Median Collapse Scaling Level (% of 2% in 50 year level)		
	Long Duration Suite	Short Duration Suite	Short/Long
075	183	230	1.26
20	174	206	1.18
	P[Collapse] at 2% in 50 year shaking level (%)		
075	5.6	0.4	0.07
20	5.2	0.6	0.12

Table 6.4 Median collapse scaling level and probability of collapse at the 2% in 50 year shaking level for the 18 story ductile models.

Suite	Median LS Exceedance Scaling Level (% of 2% in 50 year level)		
	Long Duration Suite	Short Duration Suite	Short/Long
075	159	200	1.26
20	155	168	1.08
	P[LS] at 2% in 50 year shaking level (%)		
075	11.3	3.3	0.29
20	13.5	5.9	0.44

Table 6.5 Median life safety exceedance scaling level and probability of life safety exceedance at the 2% in 50 year shaking level for the 18 story ductile models.

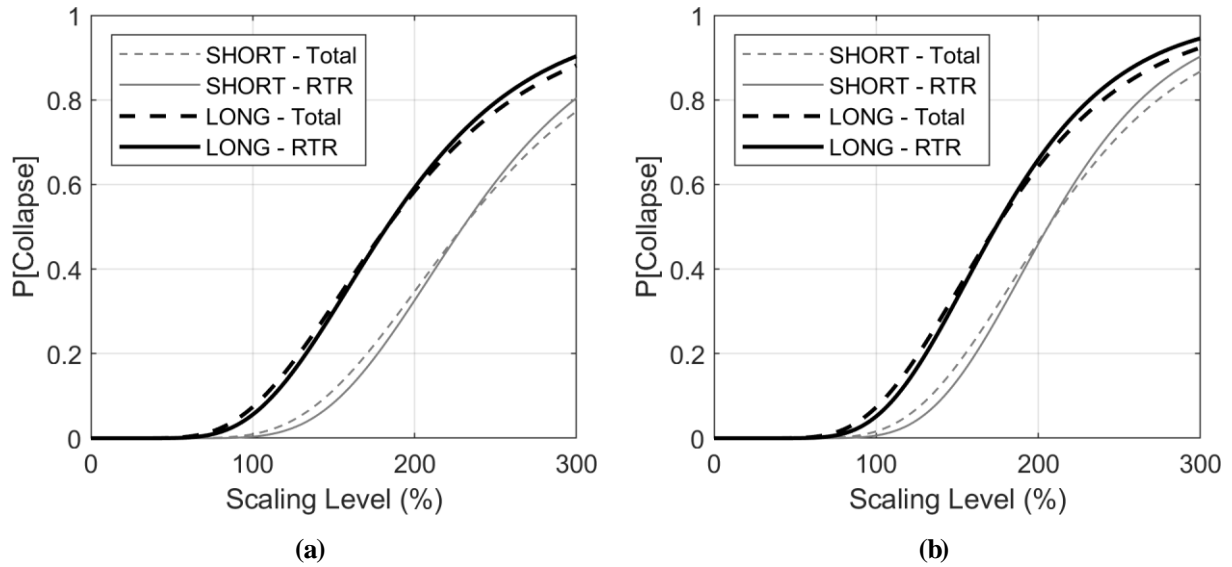


Figure 6.21 Collapse results for the ductile 18 story model: a) SHORT075 and LONG075 suites lognormal CDFs with total vs. RTR variability; and, b) SHORT20 and LONG20 suites lognormal CDFs with total vs. RTR variability.

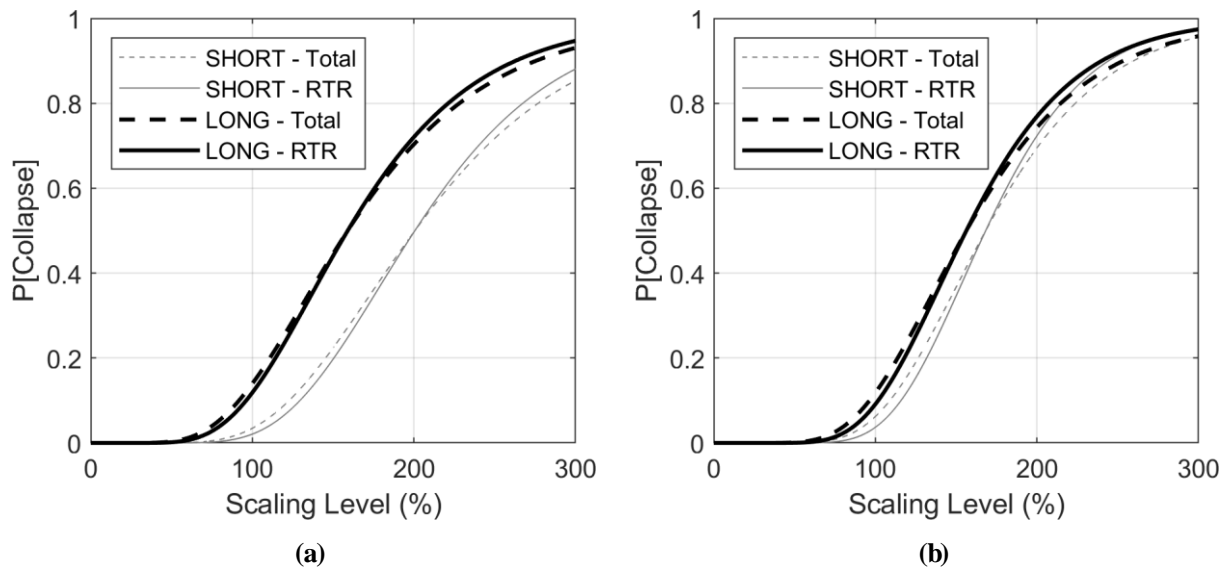


Figure 6.22 LS exceedance results for the ductile 18 story model: a) SHORT075 and LONG075 suites lognormal CDFs with total vs. RTR variability; and, b) SHORT20 and LONG20 suites lognormal CDFs with total vs. RTR variability.

6.4.2 Conventional Construction

6.4.2.1 Code Level Analysis

Lateral-force resisting system displacement results

The resulting maximum interstory drifts for the models in the coupled (NS) and non-coupled (EW) directions are illustrated in Figure 6.23 and Figure 6.24, respectively, for the four ground motion suites. None of these drifts exceed the NBCC drift limit (2.5%) or LATBSDC drift limits (3.0 and 4.5% for the suite mean and maximum, respectively). In both directions the LONG20 suite is the most demanding; however, the differences between the four suites are quite small.

Figure 6.25 presents the header rotation results over the height of the model. Once again, the SHORT and LONG suites produced similar rotation demands; in both cases the CS20 suites governed. From ASCE-41, the collapse prevention rotation for these unconfined headers would be 0.03 rad for existing structures (dashed red line in Figure 6.25). For new structures with conventionally-reinforced header beams, LATBSDC (LATBSDC, 2017) recommends a total chord rotation limit of 0.04 rad (dashed blue line in Figure 6.25). The geometric mean results for all suites are well below these limits.

Finally, Figure 6.26 presents the wall strain results over the height of the model. The LATBSDC limits are shown as the dashed red lines.

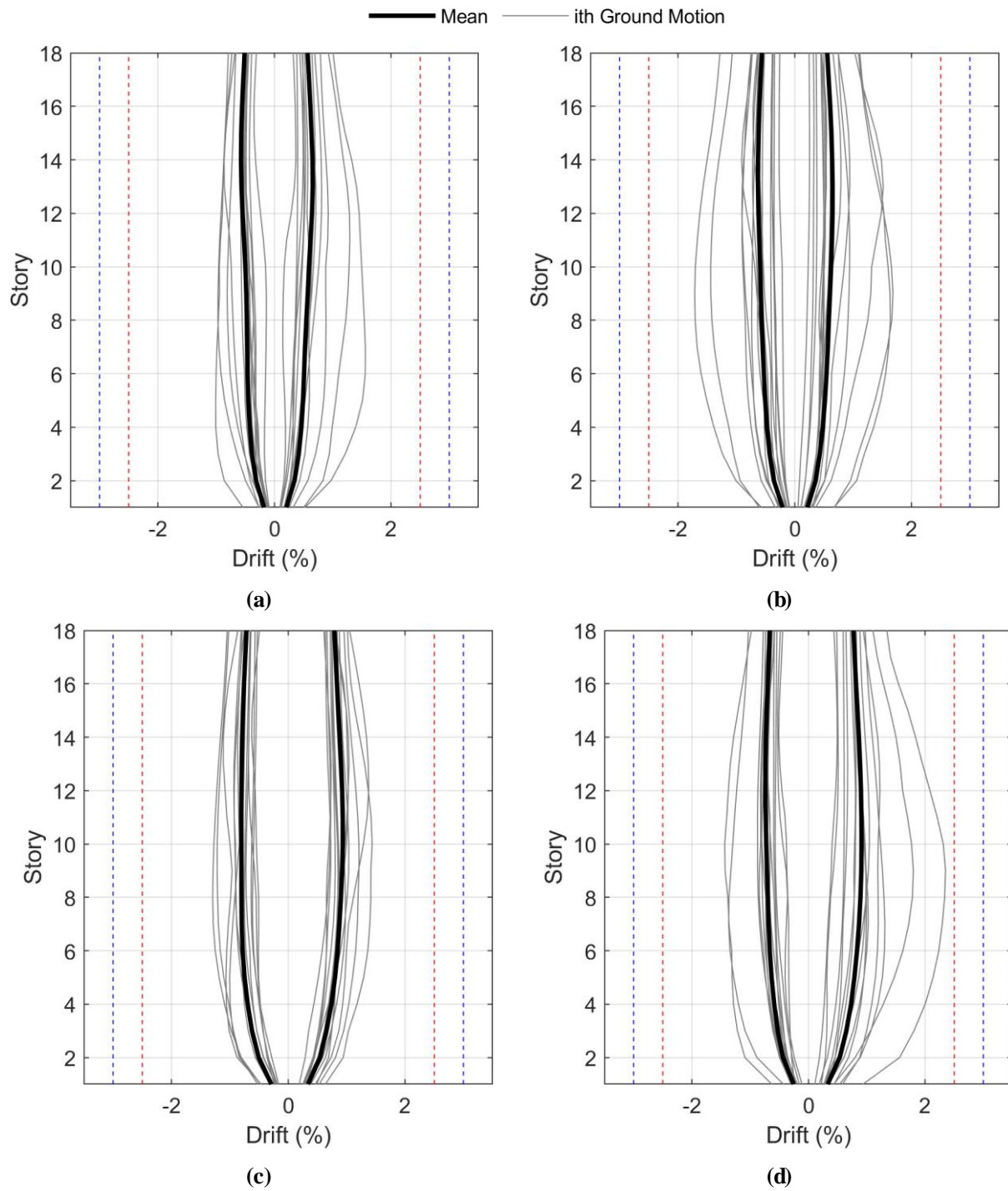


Figure 6.23 Coupled-direction interstory drift results for the CC 18 story model at the code shaking level for: a) the SHORT075; b) LONG075; c) SHORT20; and, d) LONG20 ground motion suites.

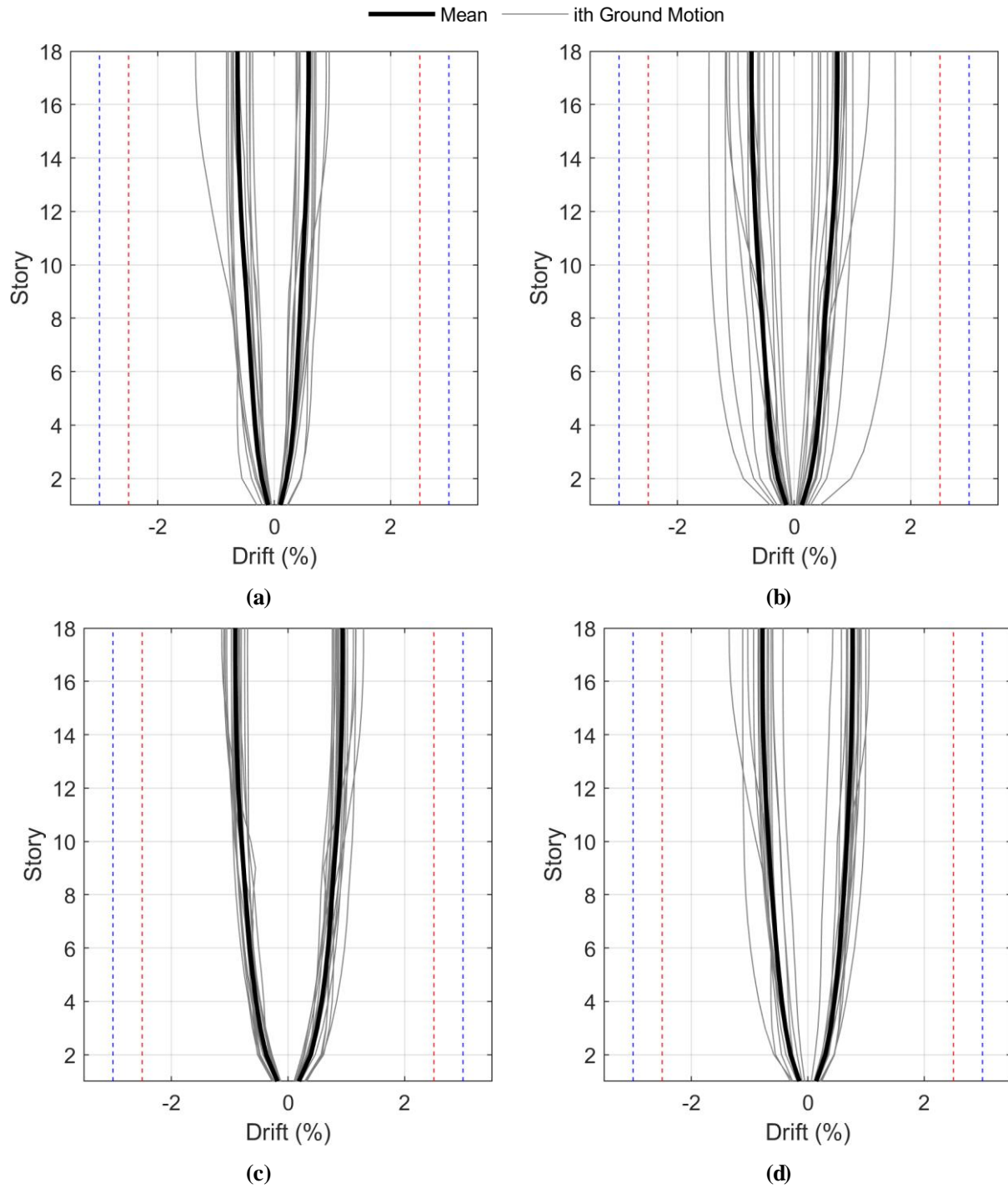


Figure 6.24 Wall direction interstory drift results for the CC 18 story model at the code shaking level for: a) the SHORT075; b) LONG075; c) SHORT20; and, d) LONG20 ground motion suites.

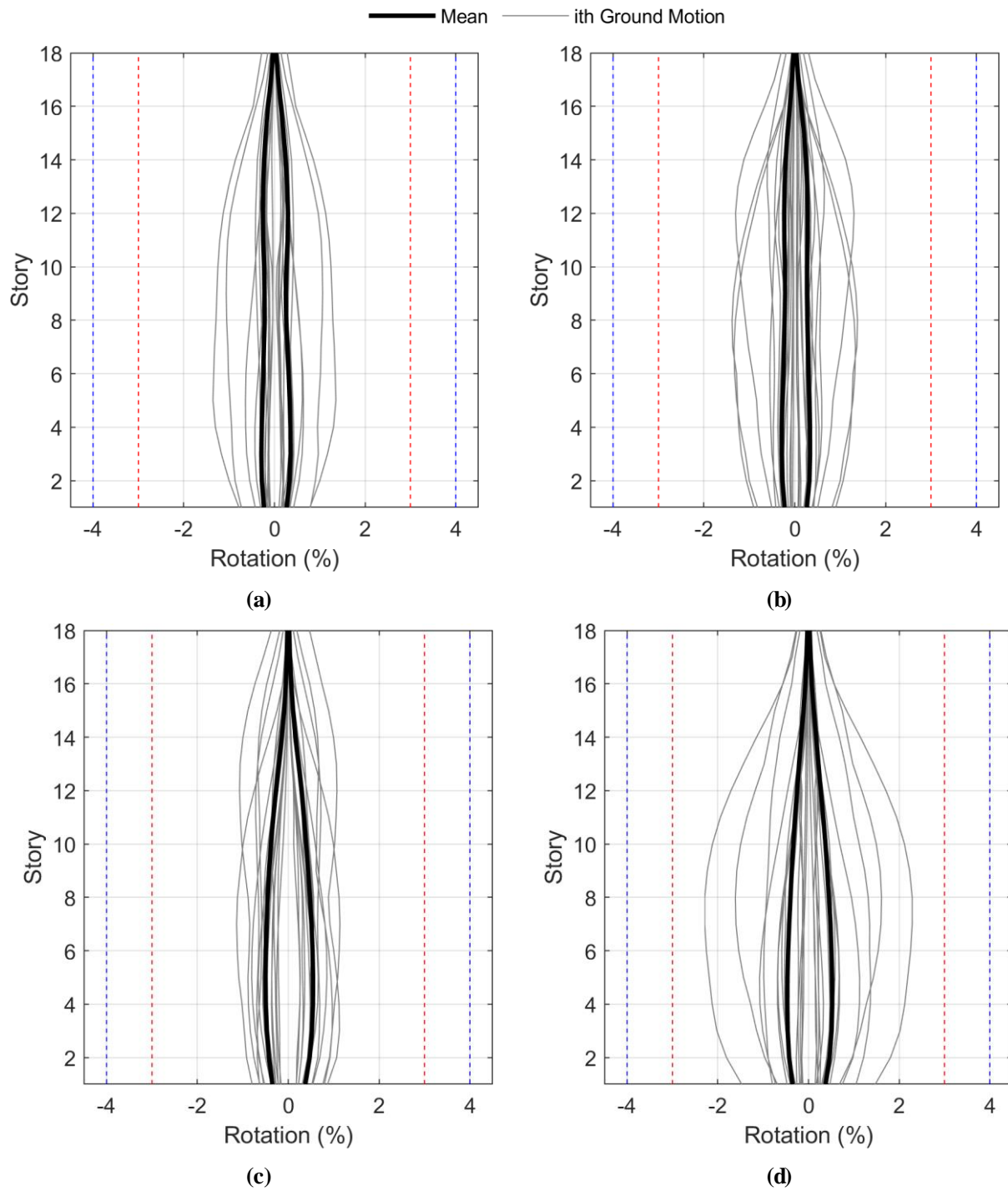


Figure 6.25 Header rotation results for the CC 18 story model at the code shaking level for: a) the SHORT075; b) LONG075; c) SHORT20; and, d) LONG20 ground motion suites.

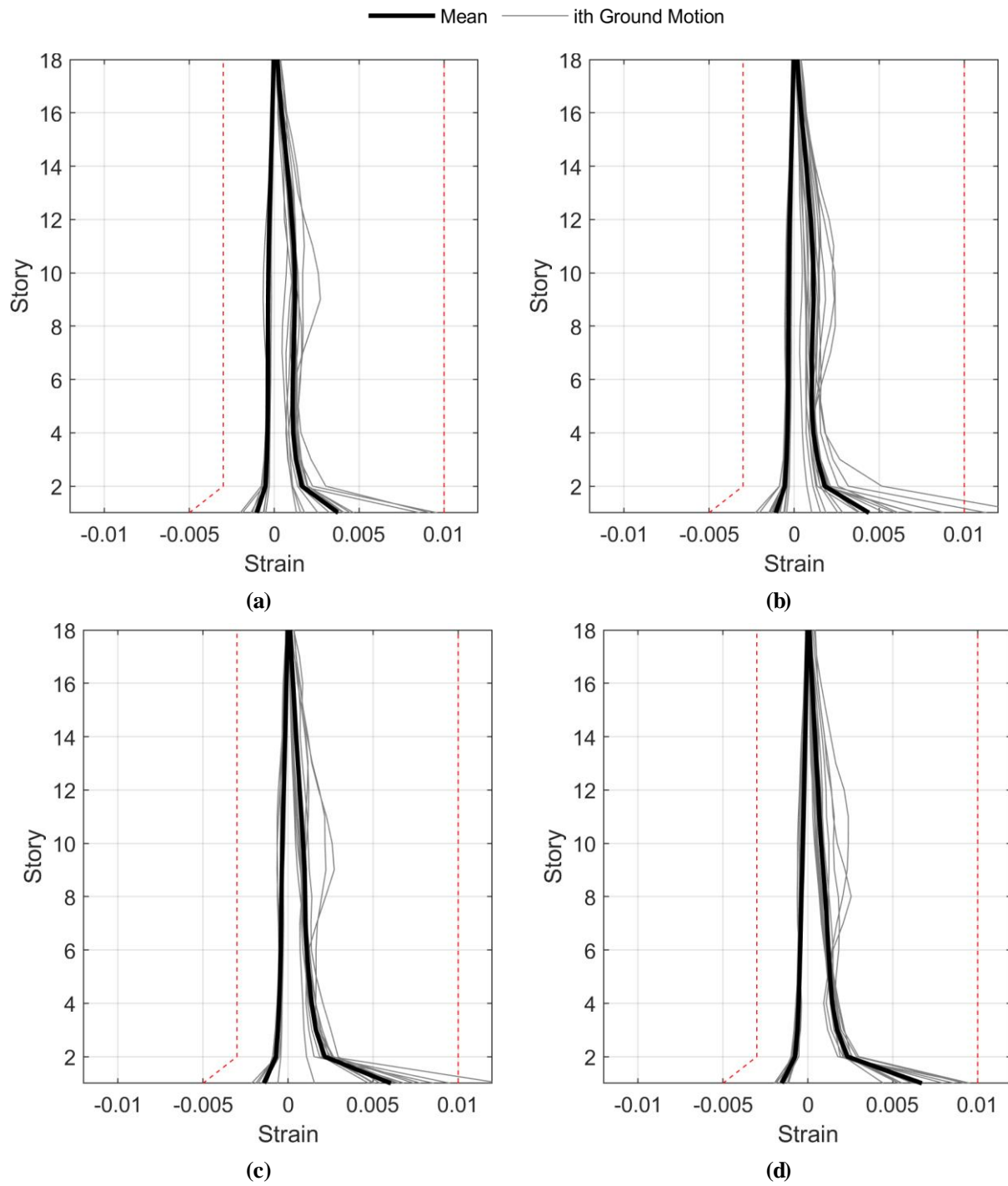


Figure 6.26 Wall strain results for the CC 18 story model at the code shaking level for: a) the SHORT075; b) LONG075; c) SHORT20; and, d) LONG20 ground motion suites.

Lateral-force resisting system force demands

The story force and moment demands are illustrated in Figure 6.27 and Figure 6.28, respectively. These results are presented as the governing results considering both directions of shaking. The overturning moment demands are similar for all four suites, as this is governed by the strength of the walls.

The total shear area of the three walls is 14500 in² (9.36 m²) in the NS direction and 13700 in² (8.84 m²) in the EW direction. This results in total maximum allowable shear forces of 6710 kips (29850 kN) in the NS direction and 6360 kips (28290 kN) in the EW direction following Equation 6-1. The mean shear force demands from Figure 6.27 are well below this limit. Additionally, each wall segment does not exceed its individual maximum allowable shear force from Equation 6-2.

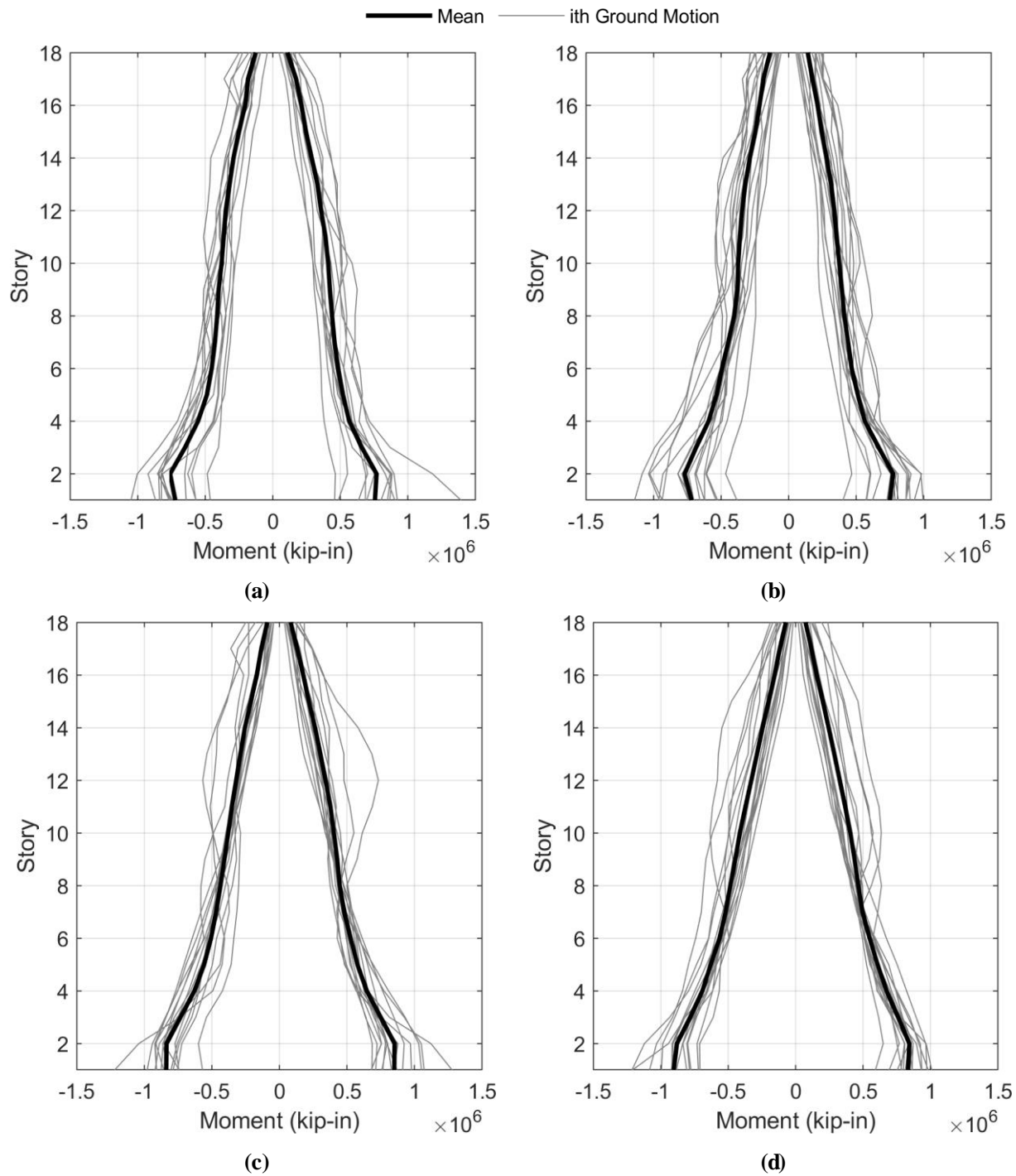


Figure 6.28 Story overturning moment results for the CC 18 story model at the code shaking level for: a) the SHORT075; b) LONG075; c) SHORT20; and, d) LONG20 ground motion suites.

Gravity system results

Figure 6.29 presents the column hinge rotation results over the height of the model. The ASCE 41 collapse prevention rotation limit for this type of column ($\rho > 0.006$ and $P/A_g f'_c < 0.1$) is 6.0%. All results are well below this limit.

6.4.2.2 Collapse and Life Safety Analysis

For the conventional design, collapse is defined as interstory drift exceeding 3%, shear failure in any wall, or gravity system (column or slab) failure. Column failure is defined as a rotation in one or more column springs that exceeds 0.06 rad post-yielding. Slab failure is defined as rotation in a slab spring that exceeds 0.05 rad post-yielding (ASCE 41 collapse prevention criteria for these elements).

The empirical and lognormal fitted CDF curves for the CS075 and CS20 motion suites are presented in Figure 6.30a and b, respectively. The median collapse scaling level (expressed as a percent of the 2% in 50 year hazard level) and collapse probability at the 2% in 50 year scaling level are summarized in Table 6.6

The median collapse scaling levels for the LONG suites was ~20% lower than the comparable SHORT suites – the 2% in 50 year collapse probabilities were ~40 and ~60% lower for the SHORT075 and SHORT20 suites, respectively, compared to the corresponding LONG suites. The CS20 suites were more demanding than the CS075 suites (high collapse probabilities at the 2% in 50 year level and lower median collapse scaling levels.) This indicates that the nonlinear model behavior, which governed displacements, ultimately lead to collapse, rather than the increased force demands from the higher modes.

Next, the LS exceedance results were considered. Following ASCE-41, the header rotation was limited to 0.02 rad (for non-confined headers), the column rotation limit was reduced to 0.045 rad, and the column connection rotation limit was reduced to 0.035 rad; the interstory drift limit was also reduced to 2.5% (NRCC, 2015). With these new criteria, the CDFs were rederived (Table 6.7 and Figure 6.31). As expected, the median LS exceedance levels were lower than the collapse level and the probabilities of exceedance at 2% in 50 year shaking were increased. However, the same

general trends remained: the LONG suites were more demanding than the SHORT, and the CS20 suites governed the results.

Comparing the collapse results between the ductile model (Table 6.4 and Figure 6.21) to the CC model (Table 6.6 and Figure 6.30) shows that the CC design was less resilient to collapse than the more ductile design. The governing median collapse level (from the LONG20 suite) was 174 for the ductile model and 156 for the CC model indicating that the ductile model required higher levels of shaking to induce collapse. The probability of collapse at the 100% shaking level was also higher for the CC model: 12.7 vs 5.6%. The scaling levels required to exceed LS were also slightly less for the CC model.

It can also be observed that the difference between LS exceedance and collapse is smaller for the CC model compared to the ductile model. The governing median collapse scaling level was only 5% higher than the median LS exceedance level for the CC model; it was 12% higher for the ductile model. This is because the collapse prevention and LS criteria are more similar for the CC, indicating a lower reserve capacity against collapse. This means that even if both designs met the same LS criteria, the CC design would still be more likely to collapse under a larger than expected level of shaking. Accordingly, although code-level drift demands may have been similar between the two models subjected to the same ground motion suites (e.g. Figure 6.15 vs. Figure 6.24), the CC model has a lower margin against collapse and may not perform to risk-targeted performance requirements (e.g. FEMA P695 collapse margin ratios).

Suite	Median Collapse Scaling Level (% of 2% in 50 year level)		
	Long Duration Suite	Short Duration Suite	Short/Long
075	169	200	1.18
20	156	189	1.17
	P[Collapse] at 2% in 50 year shaking level (%)		
075	9.5	0.8	0.08
20	12.7	2.0	0.16

Table 6.6 Median collapse scaling level and probability of collapse at the 2% in 50 year shaking level for the 18 story CC models.

Suite	Median LS Exceedance Scaling Level (% of 2% in 50 year level)		
	Long Duration Suite	Short Duration Suite	Short/Long
075	153	186	1.22
20	149	173	1.16
	P[LS] at 2% in 50 year shaking level (%)		
075	12.8	3.7	0.29
20	15.6	4.9	0.31

Table 6.7 Median life safety exceedance scaling level and probability of life safety exceedance at the 2% in 50 year shaking level for the 18 story CC models.

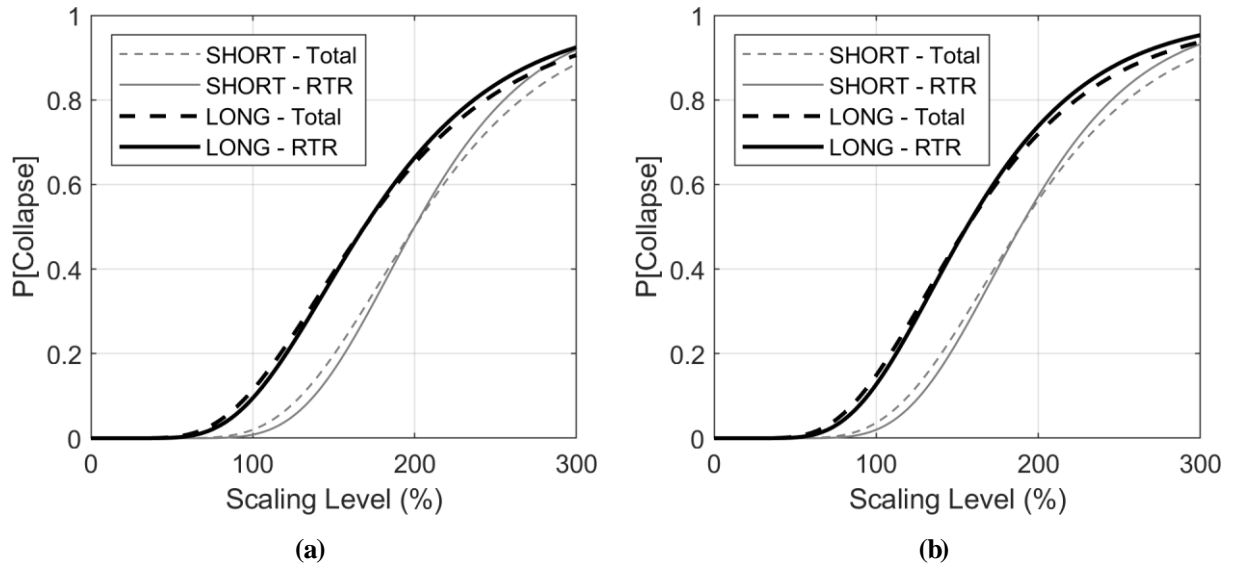


Figure 6.30 Collapse results for the CC 18 story model: a) SHORT075 and suites lognormal CDFs with total vs. RTR variability; b) SHORT20 and LONG20 suites lognormal CDFs with total vs. RTR variability.

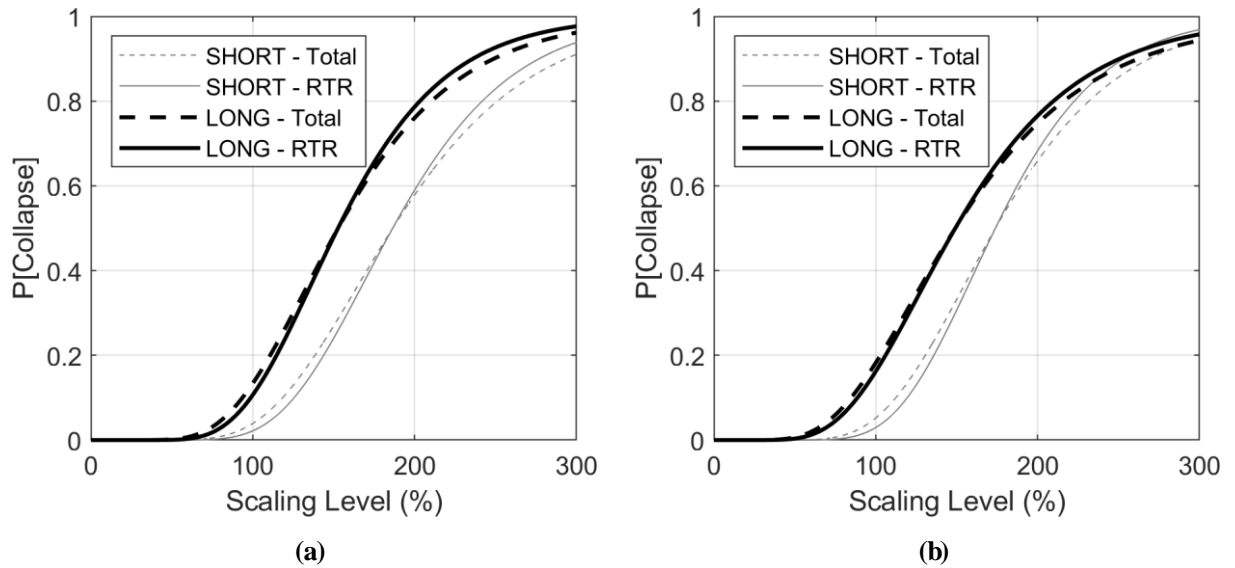


Figure 6.31 LS exceedance results for the CC 18 story model: a) SHORT075 and suites lognormal CDFs with total vs. RTR variability; b) SHORT20 and LONG20 suites lognormal CDFs with total vs. RTR variability.

6.5 Conclusions

This chapter aimed to study the effect of ground motion duration using two, 3D, 18 story models: one designed a ductile structure, the other using conventional construction. These models included both the lateral force resisting system, as well as the gravity resisting columns and slabs, so that the performance of the gravity system could also be assessed. IDA was performed with these models using four suites of CS matched motions (two suites: long and short duration; and two conditioning periods). The trends observed for the CC model were similar to the analysis results presented in Chapter 4, with the longer motions imposing greater demands at the larger shaking intensities. Accordingly, it was deemed not necessary to rerun another sensitivity study considering ductile-designed models.

The longer motions also tended to produce results with larger record-to-record variability, despite the input motions both matching the same target record spectral variability. This is because the shorter records tend to produce the majority of the damage over a single short pulse. The motions are scaled either intense enough to damage/induce collapse, or not, and the majority of the records induce collapse at similar scaling levels. Whereas, the longer motions contain multiple pulses with unique intensities/frequency content (e.g. Figure 2.8); thus, collapse can occur at largely different shaking levels for different motions. In the following chapter we will see that structural response variability has a large effect on determining the safety and/or collapse risk of a structure, which may be another potential reason long duration motion might require unique design considerations.

In these studies, both code-level and collapse level (determined through IDA) performance was considered. The results tended to show that the designs met code performance and had adequate margins against collapse. However, the aim of this chapter was simply to study the effect

of the different ground motion suites – not to assess the safety of the structures as per modern building code standards.

In the next chapter, these results will be further investigated in an effort to make recommendations to account for the effect of ground motion duration on the design of RC shearwall buildings in modern building codes. These results are generated with CS matched motions that captured the target mean and record-to-record spectral variation and, thus, are expected to demonstrate appropriate record-to-record variation in the results.

Chapter 7: Effect of Ground Motion Duration on Prescriptive Building Codes

In the previous chapters, the difference in performance between RC shearwall buildings was assessed when the building models were subjected to either long or short duration ground motion suites. The implications towards both NBCC and ASCE 7 were briefly discussed – however, this was not the main objective of the studies in this chapter.

In this chapter, the results from Chapter 6 and their effect on modern building codes will be investigated. The aim of this chapter is to quantify the effect of ground motion duration on modern, prescriptive building codes and to provide recommendations for the design of RC shearwall buildings in subduction zones (e.g. Southwestern BC).

7.1 Modern Standards

The major modern design standards for new construction in North America were introduced in Section 2.1; these are summarized in Table 7.1 including the shaking level(s) considered and overarching performance objectives.

Standard	Shaking Level(s) ¹	Performance Objectives
NBCC 2015	2%/50	Protect the life safety of building occupants
ASCE 7-16	2/3MCE _R (ELFP) MCE _R (NTHA)	<10% P[collapse] at MCE _R 1% collapse risk in 50 years ²
FEMA P695	IDA ³	Acceptable CMR <10% P[collapse] at MCE _R level
LATBSDC / PEER TBI	MCE _R (collapse prevention) 50%/30 (serviceability)	Meet or exceed ASCE 7 performance

¹Probability of exceedance in percent / number of years

²Implicitly assumed if other performance objectives are met

³IDA involves NTHA considering a wide range of shaking intensities

Table 7.1 Modern North American seismic design standards summary.

7.2 Reduction Factor Calibration

Seismic force reduction factors (R or $R_d R_o$) should be calibrated to limit the probability of collapse to an acceptable amount at the design shaking level and to provide a suitable margin against collapse (collapse margin ratio, CMR) for larger than expected levels of shaking (FEMA, 2009).

To assess the design level collapse probability, a suitable number of motions that represent the design hazard level are run through nonlinear time history analysis (NTHA) of a numerical structural model. The probability of collapse is simply the ratio of collapses to the total number of records. Collapse is typically defined as model instability, numerical inconvergence, or exceedance of a non-simulated failure mode (ASCE/SEI, 2016; FEMA, 2009).

To define a CMR, a suite of motions must be run through the model at incrementally increasing shaking levels in order to find the median collapse shaking level; i.e. the level of shaking where 50% of the motions cause collapse (simulated or otherwise). The CMR is then the difference between the median collapse scaling level and the design level. This represents the reserve capacity of the structure to tolerate larger than expected levels of shaking.

7.2.1 Record-to-record Variability

The CMR relies on a reliable estimate of the median collapse shaking level, as well as the variability in results. This variability comes from both record-to-record variation and modelling uncertainties (FEMA, 2009). The record-to-record variation results from differences in ground motion characteristics (e.g. non-stationary properties, pulses, duration, etc.) as well as the variability of spectral amplitudes in ground motion suites. The appropriate variability in spectral amplitudes is what is targeted in the proposed ground motion modification methodology from Chapter 5. The other ground motion characteristics should be accounted for from proper ground

motion selection (i.e. magnitude, distance, soil properties, event type – all of which influence duration – which are typically obtained through PSHA deaggregation).

Two systems could have the same probability of collapse at the design shaking level (e.g. maximum considered earthquake, MCE), but if one shows much more variability between records, it would have a lower CMR – this is illustrated for two hypothetical system collapse cumulative distribution functions (CDF; low variability: System 1; high variability: System 2) in Figure 7.1a. Also, two hypothetical systems could have the same CMR, but different collapse probabilities at other shaking levels based on their observed variability – this is illustrated in Figure 7.1b.

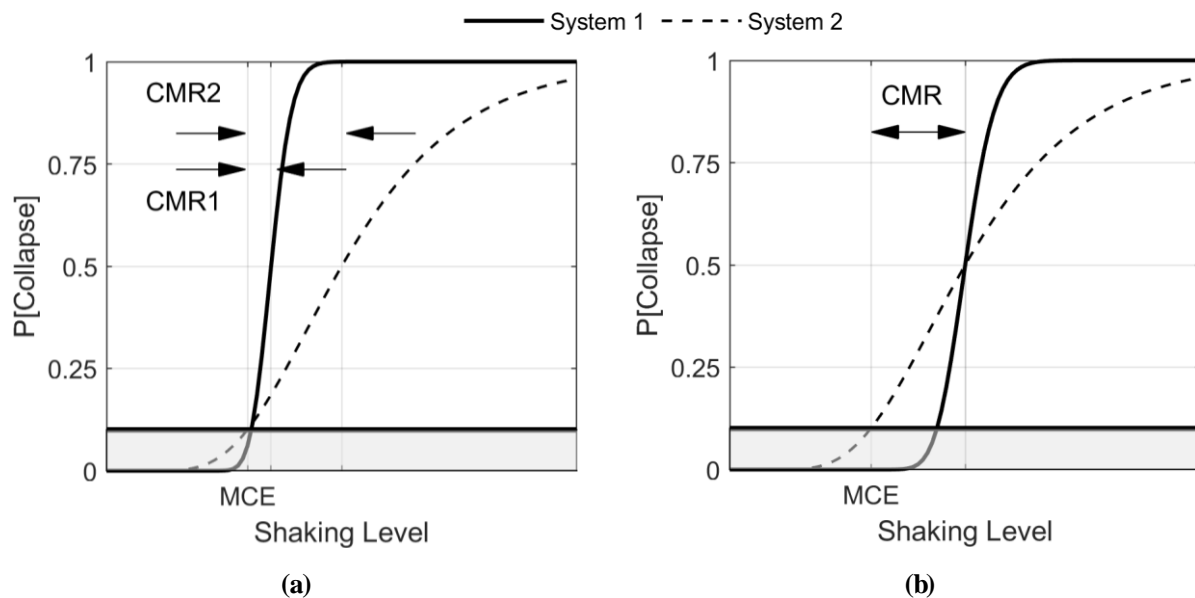


Figure 7.1 Theoretical CDFs for two systems of different variability with: a) same P[Collapse] at the MCE shaking level; and, b) same CMR.

7.2.2 R-Factor Calibration

In Table 7.2, the collapse statistics (median collapse scaling level and observed record-to-record lognormal standard deviation: β_{RTR}) from the two 3D models in Chapter 6 are summarized for the four suites of CS matched motions. Since both the mean and variation of the motion suites

was matched, these results should capture the appropriate mean and variation in collapse level. The average short/long median collapse scaling level was ~1.2, which also agrees with the 2D model sensitivity study from Chapter 4.

The average β_{RTR} of the SHORT suites is 0.30; the average for the LONG suites was 0.36. However, these standard deviations only account for the record-to-record variability, and thus, should be further adjusted for the uncertainty in design-requirements and test-data, as well as modeling related uncertainties (FEMA, 2009). The resulting total lognormal standard deviation (β_{TOT}) is computed as:

$$\beta_{TOT} = \sqrt{\beta_{RTR}^2 + \beta_{DR}^2 + \beta_{TD}^2 + \beta_{MDL}^2} \quad (7-1)$$

where β_{DR} is the design requirement uncertainty, β_{TD} is the test data uncertainty, and β_{MDL} is the modeling related uncertainty (FEMA, 2009).

Because the design, testing, and modeling of reinforced concrete shearwalls is well established, it was assumed that each of these uncertainties is very low (β values of 0.1 were selected for each.) This resulted in an average $\beta_{TOT,SHORT}$ of 0.35 for the SHORT suites and $\beta_{TOT,LONG} = 0.40$ for the LONG suites.

Suite	Ductile		CC	
	Median (% of 2%/50 year)	β_{RTR}	Median (% of 2%/50 year)	β_{RTR}
SHORT075	230	0.31	200	0.29
LONG075	183	0.38	169	0.40
SHORT20	206	0.29	189	0.31
LONG20	174	0.34	156	0.34

Table 7.2 Collapse statistics for the 3D ductile and conventional construction (CC) 3D models.

From Table 7.1, it can be seen that all the standards specify a collapse probability at the design shaking level (~2% in 50 years) to be less than or equal to 10%, except for the NBCC, which does not explicitly quantify a collapse probability. If we design a system to meet this target (i.e. specify a seismic force reduction factor that results in designs that meet this collapse probability) and subject it to a suite of incrementally scaled short duration motions (with properly matched mean and variation) we would expect the SHORT CDF in Figure 7.2 ($\beta_{TOT,SHORT} = 0.35$). However, if this structure was subjected to a similar suite of long duration records, we would expect a $\beta_{TOT,LONG}$ of ~0.40 and a median collapse scaling level: μ_{LONG} , around 1/1.2 times the original short duration suite median collapse scaling level: μ_{SHORT} . This would result in the LONG CDF in Figure 7.2. Note that this CDF has a much higher probability of collapse at 100% of the design shaking level (~25%) - which would be unacceptable performance - and a reduced CMR.

To solve this, we could simply increase the design shaking level of the LONG CDF. If we design the system for a 10% probability of collapse at 125% of the design shaking level, we would effectively shift the LONG CDF to the right as shown in Figure 7.3. Now, when subjected to long duration records at the old design level, the system meets the collapse probability limit of 10% and has a similar CMR to the previous SHORT CDF. By simply decreasing the seismic force modification factor: R_{LONG} , by 20% ($1/1.25 = 0.8$); i.e. the old 100% design level is now 80% of the new design shaking level; we would accomplish this. Now a system designed with R_{LONG} , subjected to long duration records, would have better or equal performance to a similar system designed with the existing R , when subjected to short duration records.

To apply this to the NBCC, the existing reduction factor due to system ductility: R_d , could be reduced by 20% for systems in regions with significant subduction interface hazards (e.g. the

West Coast of BC) to account for the increase in energy demands due to longer shaking durations, which essentially reduces the system's effective ductility capacity.

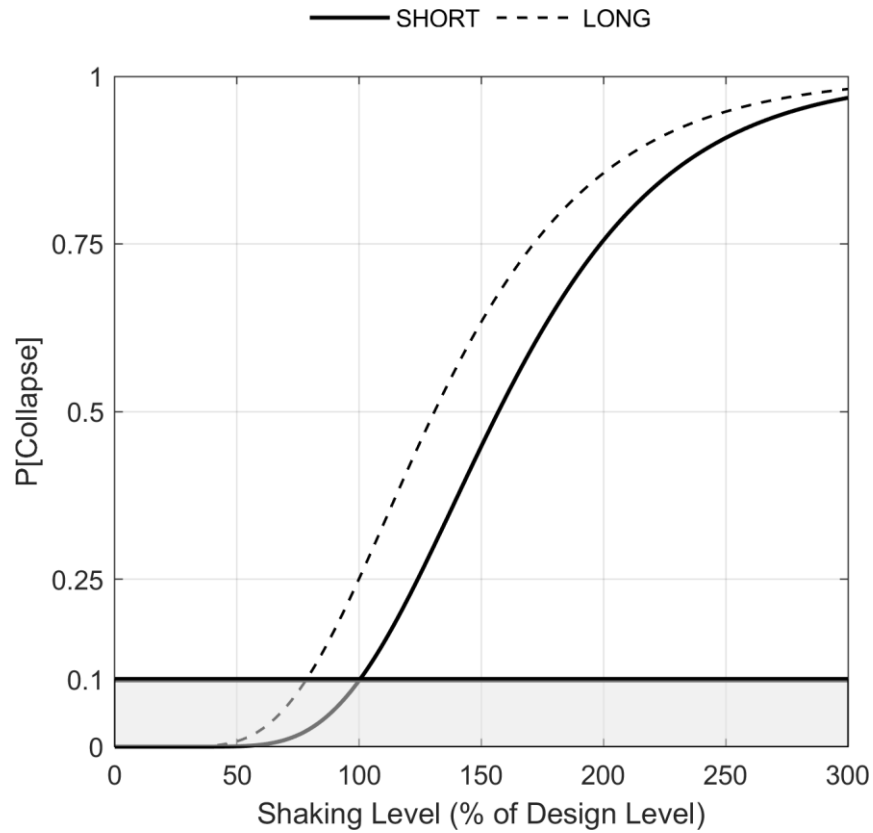


Figure 7.2 CDFs of 1) a system designed for 10% P[Collapse] at the design shaking level subjected to short duration records ($\beta_{TOT,SHORT} = 0.35$); and, 2) the same systems subjected to long duration records ($\beta_{TOT,LONG} = 0.40$; $\mu_{LONG} = \mu_{SHORT}/1.2$).

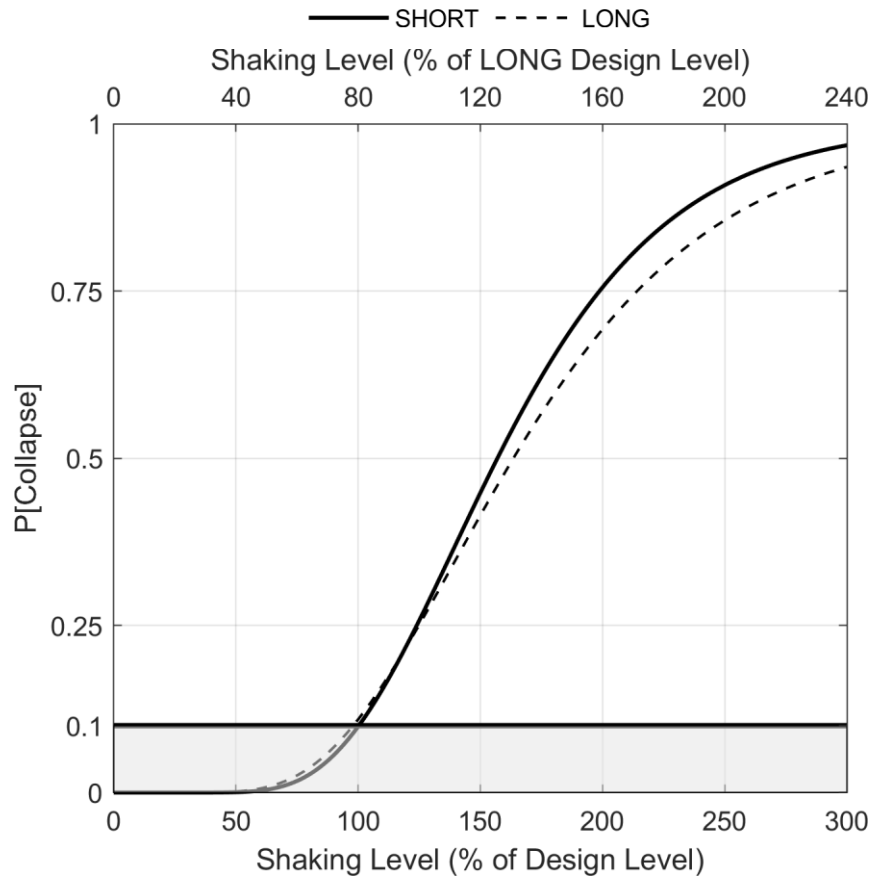


Figure 7.3 CDFs of 1) a system designed for 10% P[Collapse] at the design shaking level subjected to short duration records ($\beta_{TOT,SHORT} = 0.35$); and, 2) a system designed for 10% P[Collapse] at 125% of the design shaking level subjected to long duration records ($\beta_{TOT,LONG} = 0.40$).

7.2.3 Collapse Risk Check

ASCE 7-16 also has an implicit goal of achieving a 1% or less collapse risk in 50 years for new structures; since the LATBSDC and PEER guidelines state that their objective is to match or exceed the performance of code-designed buildings, they also implicitly have this goal (Table 7.1). To check if the recommendations from the previous section are adequate, this objective should also be considered.

First, the hazard curves (annual exceedance frequency vs. level of shaking) for the three earthquake sources in Southwestern BC were obtained from PSHA for Vancouver at $T = 2.0$ s using the 2015 GSC seismic hazard model (see Section 2.2). Southwestern BC has three potential earthquake sources: shallow crustal, subduction intraslab, and subduction interface. The crustal and subduction intraslab rates were combined and denoted as crustal, as these earthquake types are similar in duration and accelerogram shape. The two resulting source curves and total hazard curve are illustrated in Figure 7.4, where shaking level is expressed as a percentage of the total 2% in 50 year $S_a(2.0$ s).

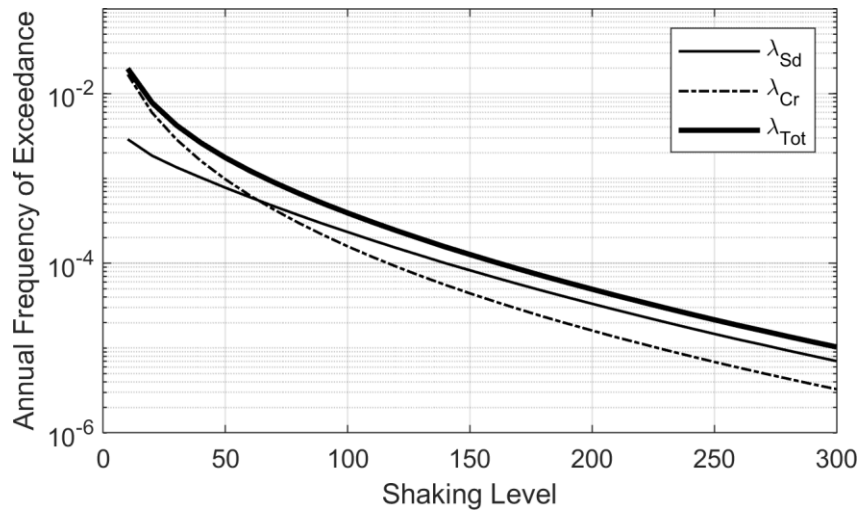


Figure 7.4 Subduction interface, crustal (combined crustal + intraslab), and total hazard curves for Vancouver, BC, for $T = 2.0$ s. Shaking level is expressed the percentage of the 2% in 50 year hazard level.

Next, two sets of collapse fragility curves for two theoretical structures were created. The first structure assumes an unadjusted R-factor – meaning that using short duration crustal records the system obtains a 10% probability of collapse at the design level of shaking (LS): $P[\text{Collapse}|LS = \text{Design Level}] = 0.1$. Two corresponding collapse CDFs were derived from the assumed response to the two shaking types:

1. **CDF_{CR}**: μ_{CR} set to achieve a 10% $P[\text{Collapse}|LS = \text{Design Level}]$ and $\beta_{CR} = 0.35$.

2. CDF_{SD}: μ_{SD} set to $\mu_{CR}/1.2$ and $\beta_{SD} = 0.40$.

The CDF means and standard deviations are from the results of Section 7.2.2. These theoretical CDFs are illustrated in Figure 7.5a (similar to Figure 7.2).

These CDFs can be combined with the hazard curves from Figure 7.4 and integrated over all levels of shaking to obtain a rate of collapse: λ_i , for each source: i , using:

$$\lambda_i = \int P[\text{Collapse}_i|LS] * d\lambda_{LS,i} \quad (7-2)$$

where $P[\text{Collapse}_i|LS]$ is the probability of collapse for source i at a given level of shaking: LS – i.e. the collapse CDF – and $d\lambda_{LS,i}$ is the derivative of the hazard curve for source i at LS .

This is solved numerically as:

$$\lambda_i = \sum_{j=10\%}^{300\%} \int -P[\text{Collapse}_i|LS] * [\lambda_{LS,i}(j) - \lambda_{LS,i}(j - 10\%)] \quad (7-3)$$

The total annual rate of collapse is then the sum of the rates of the two sources and the total probability of collapse in 50 years: P , is computed following the temporal Poisson probability model with the total collapse rate and $T = 50$ years:

$$P = 1 - \exp\left(-T \sum_{i=1}^2 \lambda_i\right) \quad (7-4)$$

For the system illustrated in Figure 7.5a, this results in $P = 1.1\%$, which is above the ASCE 7-16 target of 1%.

Next, the system was “redesigned” using $0.8 * R$, which results in a collapse probability of 10% at the design shaking level when using subduction interface records. The two CDFs for this system are illustrated in Figure 7.5b. Note that now the system has significant overstrength when

subjected to shallow crustal records, as seen by the very low collapse probability at the design level for the crustal CDF.

Applying Equations 7-3 and 7-4 yields a $P = 0.6\%$, which now meets the 1% maximum collapse risk target. This, in addition to the $<10\%$ collapse probabilities at the design shaking, mean that both ASCE 7-16 objectives are met.

Note that hazard curves are period-dependent, and thus, these results would change for other possible periods. For this system, $T = 2.0$ s was selected because the CS20 motion suites results governed the collapse behavior of the numerical models. At shorter periods, the crustal sources would contribute more to the total hazard, and the original R-factor may be suitable.

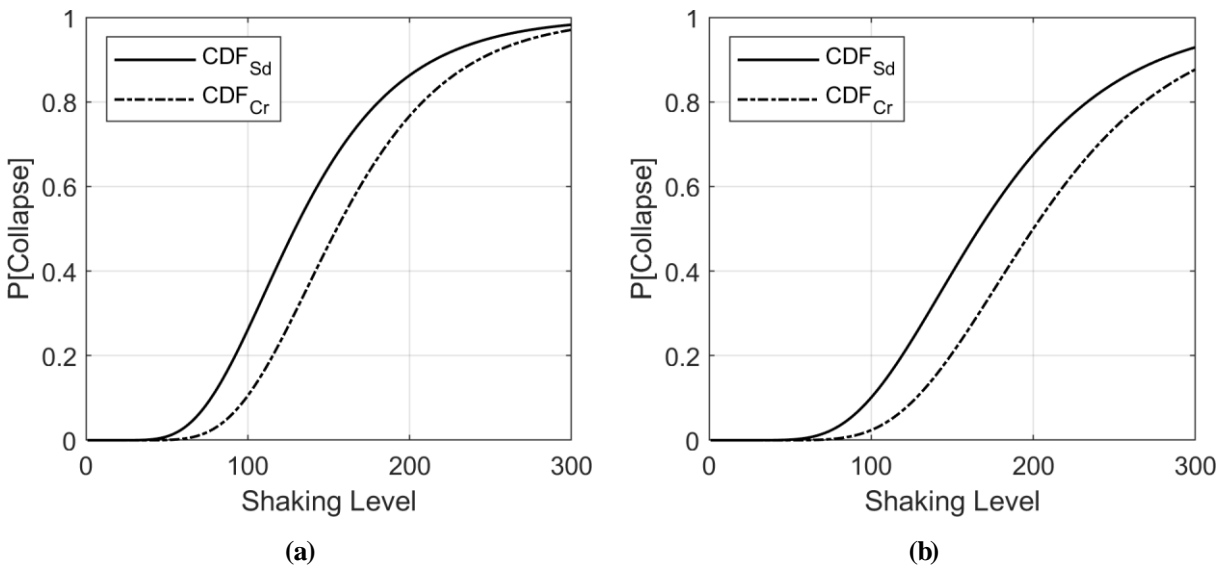


Figure 7.5 Crustal and subduction interface CDFs for a system calibrated to a) $P[\text{Collapse} \mid \text{Design Shaking}] = 10\%$ for crustal records; and, b) $P[\text{Collapse} \mid \text{Design Shaking}] = 10\%$ for subduction interface records.

7.2.4 Implications for NBCC and ASCE 7

From the results presented in the previous sections, it can be seen that long duration ground motions can lower the median collapse scaling level, which both lowers the CMR and increases the probability of collapse at the 2% in 50 year shaking level. This was illustrated for two theoretical CDFs in Figure 7.2: one short duration CDF, and one long duration CDF. In Figure 7.2, the R factor of the hypothetical building system is calibrated so that a typical short duration ground motion suite produces a certain mean and standard deviation to achieve a 10% probability of collapse at the 2% in 50 year shaking level (i.e. it is calibrated to meet FEMA P695 performance objectives). From the results of the previous sections, it can be assumed that an equivalent long duration suite would produce a median collapse scaling level of $\sim 1/1.2$ of that from the short duration suite along with an increase in record-to-record variability. It can then be seen that the long duration CDF has a much lower CMR and a probability of collapse much greater than 10% at the 2% in 50 year shaking level, suggesting that this design is unacceptable.

In Canada, new buildings are designed for 2% in 50 year probability of exceedance shaking levels, which gives them a very low probabilities of collapse when checked at this shaking level and large CMRs (NRCC, 2015). This was the case for reinforced concrete shearwall buildings when subjected to both long and short duration ground motion suites. This is in contrast to ASCE 7 (ASCE/SEI, 2016) which specifies a lateral static force equal to $2/3$ of MCE_R level when using an equivalent lateral force procedure (ELFP) for design. Therefore, it follows that a building designed following ASCE 7 could pass FEMA P695 safety criteria when considering a suite of short duration motions (theoretical short duration curve in Figure 7.2); but it could have an unacceptably large probability of collapse at the 2% in 50 year shaking level and/or a very low CMR when subjected to long duration ground motions (theoretical long duration curve in Figure

7.2). This means that when developing R factors for building systems, it will be necessary to include ground motion duration if the factors are intended to be used to design structures in tectonic regimes capable of producing long duration ground motions.

7.3 Component Factor Calibration

Along with system level performance, modern seismic design standards also specify component level performance criteria. Components are classified into one of two types (LATBSDC, 2017; PEER, 2017; ASCE/SEI, 2016);

1. **Force Controlled:** these are brittle components/responses that are controlled by force demands (i.e. once a certain force demand is exceeded, the element will fail shortly thereafter, with little capacity for additional plastic deformation). Examples of this would be shear failure in RC shearwalls, axial failure in columns, and shear failure in non-ductile coupling beams.
2. **Deformation Controlled:** these are ductile components/responses that are controlled by deformation demands (i.e. they reach failure at a certain deformation limit, which may be well past yielding). Examples include flexural failure of RC shearwalls and shear failure of ductile coupling beams.

Deformation controlled actions are modelled and allowed to yield and behave plastically; force controlled actions are modelled and required to remain elastic (LATBSDC, 2017; PEER, 2017; ASCE/SEI, 2016).

The commentary language of ASCE 7-16 provides details about how the force and deformation controlled responses are calibrated (ASCE/SEI, 2016). Accordingly, this is the standard that will be followed in the following sections.

7.3.1 Force Controlled

Following the PEER TBI guidelines (PEER, 2017), for force controlled actions, ASCE 7-16 requires:

$$\lambda F_u \leq \varphi F_{n,e} \quad (7-5)$$

where λ is a calibration parameter, F_u is the average demand on the component/action, φ is the material strength reduction factor from the material standard used for design, and $F_{n,e}$ is the nominal strength of the component calculated using expected material properties (ASCE/SEI, 2016).

To calibrate λ , ASCE 7-16 assumes that any failure of a force-controlled component will result in partial or complete collapse (and acknowledges that this is a conservative assumption), and then, based on φ , selects a λ to limit probability of collapse to 10% at MCE_R shaking (Table 7.1). This, first, requires an estimate in the variability and uncertainty in demand and capacity. ASCE 7-16 assumes variability and uncertainty in force controlled action capacity and demand as summarized in Table 7.3 and Table 7.4, respectively. In these tables, ASCE 7-16 differentiates between general and well-defined mechanisms; however, in the end, the resulting λ values are similar, so the average was taken.

Demand Dispersion (β_D)		Variability/Uncertainty in Demand
General	Well-defined	
0.40	0.20	Record-to-record variability
0.20	0.20	Force demand uncertainty
0.13	0.06	Variability from estimating demands using only 11 ground motions
0.46	0.29	Total

Table 7.3 ASCE 7-16 assumed variability and uncertainty values for component force demand (reproduced from ASCE/SEI, 2016, Table C16-3).

Capacity Dispersion (β_C)		Variability/Uncertainty in the Final As-built Component
General	Well-defined	
0.30	0.30	Variability in strength equation for $F_{n,e}$ (from available data)
0.10	0.10	Variability in strength equation for $F_{n,e}$ (extrapolation beyond available data)
0.20	0.20	Uncertainty in as-built strength due to construction quality and possible errors
0.37	0.37	Total

Table 7.4 ASCE 7-16 assumed variability and uncertainty values for component capacity (reproduced from ASCE/SEI, 2016, Table C16-3).

ASCE 7-16 ultimately derives a λ/ϕ ratio of 2.0 to limit the probability of collapse to 10% at the MCE_R shaking level. Thus, Equation 7-5 is rewritten as:

$$2.0I_eF_u \leq \phi F_e \quad (7-6)$$

where I_e is the seismic risk category factor (equal to 1.0 for regular structures) and F_e is the strength of the component calculated using expected material properties.

This is illustrated in Figure 7.6, which plots the demand and capacity probability distribution functions (PDFs) for a mean demand normalized to 1.0 with $\beta_D = 0.375$ (average of total from Table 7.3) and a mean capacity of 2.0 times the mean demand with $\beta_C = 0.37$ (from Table 7.4). The total probability that the demand exceeds the capacity of the component in this figure is ~10%.

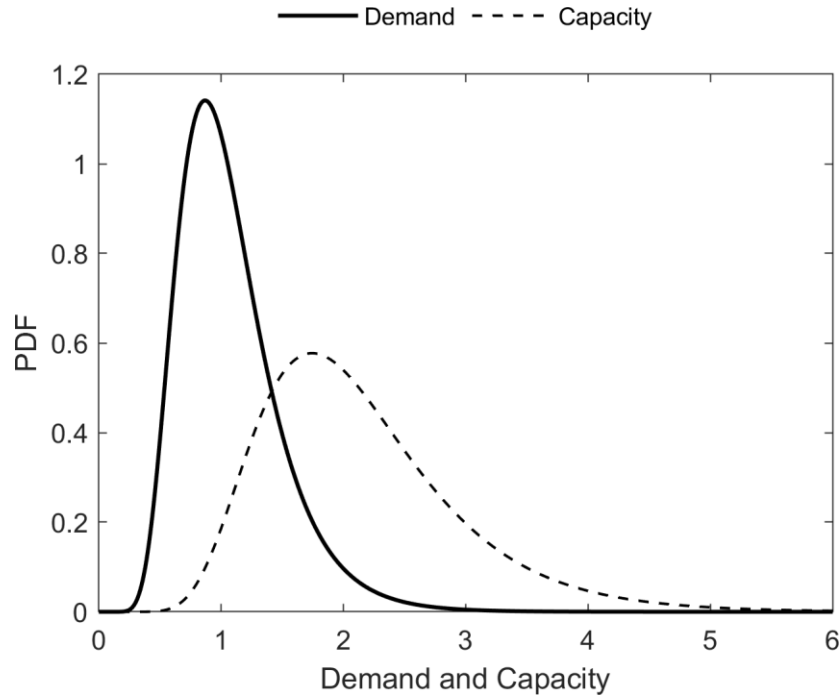


Figure 7.6 . Illustration of lognormal PDFs for component force capacity and demand (normalized to an average capacity of 1.0); the average component capacity is calibrated to achieve a probability of collapse = 10% at the MCE_R.

Following this methodology, the demand dispersion of the shear in the walls was extracted for the ductile and CC models for the four suites CS matched motions from Section 6.4. This was performed for each model for each motion suite by computing the shear force variability for the walls at each story, and then taking the average over all 18 stories. The average demand lognormal standard deviation was 0.30 for the SHORT suites and 0.34 for the LONG suites. These values fall between the assumed ASCE 7-16 values for record-to-record variation for general and well-defined mechanisms (Table 7.3), which means that the λ/φ ratio of 2.0 recommended in ASCE 7-16 would be suitable for both motion types.

Table 7.6 summarizes the results for the moment demands in the columns. The results also fall into the ASCE 7-16 range, which means that the recommended $\lambda/\varphi = 2.0$ will be sufficient.

Suite	Ductile	CC
SHORT075	0.25	0.31
SHORT20	0.32	0.32
SHORT Average	0.30	
LONG075	0.31	0.33
LONG20	0.35	0.37
LONG Average	0.34	

Table 7.5 Demand dispersion (β_D) at the 100% shaking level (2% in 50 year probability of exceedance) for wall shear in the ductile and CC models subjected to four suites of motions.

Suite	Ductile	CC
SHORT075	0.18	0.28
SHORT20	0.25	0.31
SHORT Average	0.26	
LONG075	0.26	0.32
LONG20	0.35	0.36
LONG Average	0.32	

Table 7.6 Demand dispersion (β_D) at the 100% shaking level (2% in 50 year probability of exceedance) for column rotation in the ductile and CC models subjected to four suites of motions.

7.3.2 Deformation Controlled

In ASCE 7-16, the deformation limits for deformation controlled actions are calibrated similarly to force limits in force controlled actions:

$$\lambda D_u \leq D_e \quad (7-7)$$

where D_u is the inelastic deformation demand, D_e is the expected inelastic deformation capacity, and λ is the deformation capacity/demand ratio required for adequate performance.

Similar to Table 7.3 and Table 7.4, Table 7.7 and Table 7.8 summarize the variability and uncertainty in deformation demand and capacity for deformation controlled actions in ASCE 7-16, respectively. Note that deformation capacity is assumed to be much more uncertain than force capacity when comparing these tables. This is because there are many tested and calibrated equations for estimating component force capacities, whereas test data on components deformed to failure is quite rare.

Demand Dispersion (β_D)	Variability/Uncertainty in Demand
0.40	Record-to-record variability
0.20	Force demand uncertainty
0.13	Variability from estimating demands using only 11 ground motions
0.46	Total

Table 7.7 ASCE 7-16 assumed variability and uncertainty values for component deformation demand (reproduced from ASCE/SEI, 2016, Table C16-5).

Capacity Dispersion (β_C)	Variability/Uncertainty in the Final As-built Component
0.60	Variability in prediction equation for deformation capacity (from available data)
0.20	Uncertainty in prediction equation for deformation capacity (extrapolation beyond data)
0.20	Uncertainty in as-built deformation capacity due to construction quality and errors
0.66	Total

Table 7.8 ASCE7-16 assumed variability and uncertainty values for component deformation (reproduced from ASCE/SEI, 2016, Table C16-5).

From the values in these tables, ASCE 7-16 calculates a $\lambda = 3.0$ (i.e. deformation capacity equal to 3.0 times the mean deformation demand) to achieve a probability of collapse of 10% at MCE_R level shaking. Because this would be very conservative, ASCE 7-16 recommends a lower $\lambda = 2.0$ to allow a 25% probability of collapse, acknowledging that failure of a deformation controlled component will not likely lead to structural collapse. However, if no alternate load path is available and failure of the component would likely lead to local or global collapse, then $\lambda = 3.0$ should be used. The demand and capacity PDFs resulting from these values are illustrated in Figure 7.7.

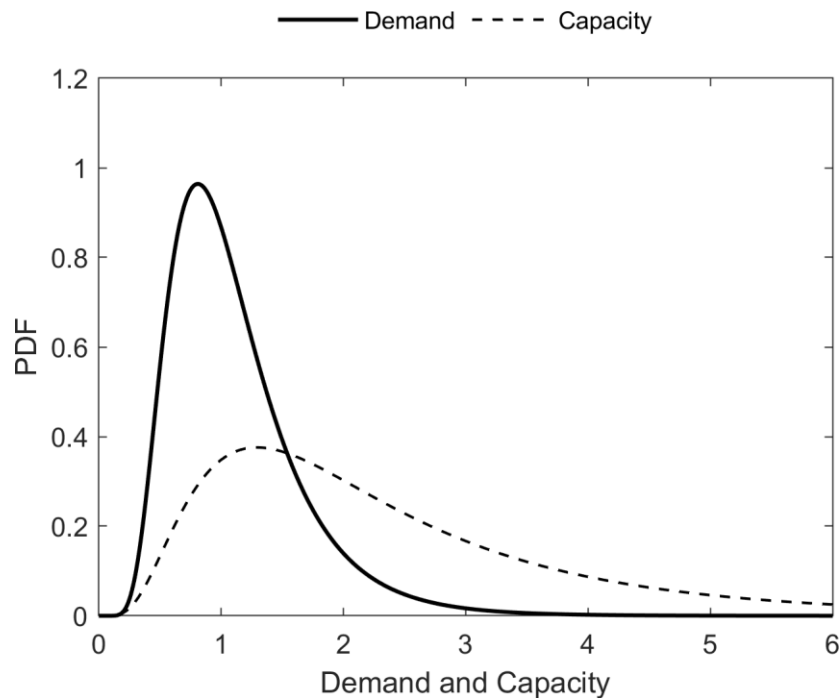


Figure 7.7 . Illustration of lognormal PDFs for component deformation capacity and demand (normalized to an average capacity of 1.0); the average component capacity is calibrated to achieve a probability of collapse = 25% at the MCE_R .

Table 7.9 and Table 7.10 summarize the lognormal standard deviations observed for the deformation controlled actions in the 3D models from Chapter 6: wall plastic hinge rotation

(rotation in the first story) and header deformation (average over the model height). The SHORT suites are all much less variable than the corresponding LONG suites and are well below the ASCE 7-16 assumed value of 0.40.

More variability was observed in the LONG suites, particularly for the ductile model. Even for the ductile model, however, the observed values are below 0.40 - with the exception of wall plastic hinge rotation under the LONG075 suite, which was only just above this value ($\beta_D = 0.44$). This means that the ASCE 7-16 deformation capacity/demand limit of 2.0 should be suitable for both motion types, especially since the majority of the variability comes from deformation capacity uncertainties (Table 7.8).

Suite	Ductile	CC
SHORT075	0.37	0.23
SHORT20	0.28	0.16
SHORT Average	0.26	
LONG075	0.44	0.30
LONG20	0.39	0.30
LONG Average	0.36	

Table 7.9 Demand dispersion (β_D) at the 100% shaking level (2% in 50 year probability of exceedance) for wall plastic hinge rotation in the ductile and CC models subjected to four suites of motions.

Suite	Ductile	CC
SHORT075	0.35	0.24
SHORT20	0.26	0.19
SHORT Average	0.26	
LONG075	0.39	0.26
LONG20	0.37	0.25
LONG Average	0.32	

Table 7.10 Demand dispersion (β_D) at the 100% shaking level (2% in 50 year probability of exceedance) for header deformation in the ductile and CC models subjected to four suites of motions.

7.4 Conclusions

In this chapter, the effect of ground motion duration on prescriptive building codes was investigated for RC shearwall buildings. First, the performance objectives of modern North American standards were highlighted. All the standards tended to limit the probability of collapse at the maximum considered earthquake, and either explicitly assess or implicitly imply a total collapse risk, or margin of safety against collapse, at greater than expected levels of shaking. These standards all set component-level performance requirements in addition to the global collapse requirements.

The results from the 3D numerical models from Chapter 6 were used to assess the effect of duration on these performance objectives. These results were generated with CS matched motions; and thus, should properly reflect the mean and variability in structural response.

It was concluded that structures in regions with the potential for long duration shaking (i.e. large subduction interface events) should be designed to stricter seismic standards (e.g. lower seismic force reduction factors). This is because the longer duration shaking leads to earlier collapse potential. A factor of 0.8 was recommended for the RC shearwall buildings modelled in Chapter

6. This led to acceptable collapse probabilities when subjected to design level, long duration records, as well as acceptable total 50 year collapse probabilities when computed using all possible earthquake types and shaking intensities.

The component level seismic safety factors for force and deformation controlled actions were also assessed, including a discussion of the ASCE 7-16 methodology for deriving such factors. It was found that the longer motions tended to have more variable component-level results, which should require larger factors – however, because the majority of the demand/capacity uncertainty came from other sources, the ASCE 7-16 factors appear suitable for both motion types.

Chapter 8: Conclusion

8.1 Research gaps

Since the 1970's, there has been a vast amount of research into the effect of ground motion duration on the response of different structural systems including site reconnaissance, physical testing, and numerical modelling. However, it hasn't been until recently that researchers have begun to employ nonlinear time history analysis (NTHA) using more sophisticated mathematical models that are able to simulate all responses affected by duration (such as cyclic and non-cyclic degradation modes and cumulative P-delta effects). Although the behavior and design of coupled RC shearwall systems is largely understood, the effect of ground motion duration on the behavior of this type of system has not yet been adequately investigated.

Another missing link in the current state-of-knowledge is the effect of different earthquake shaking types on the safety of modern, code-designed, buildings. Recently, this issue has become a focus of several research groups. A large part of the research presented in this dissertation was to investigate the current building design standards for RC shearwall buildings and to assess their reliability to produce safe designs when subjected to a range of shaking types (i.e. subduction interface events vs. shallow crustal events).

To implement the studies required for this research, it was essential to be able to produce hazard-consistent ground motions suites that would represent design level crustal and subduction interface earthquakes. The selection and modification of relatively rare, large magnitude, subduction interface records is another a gap in current structural and earthquake engineering research and practice.

8.2 Summary and Conclusions

The main goal of this research was to add to the state-of-knowledge of the effect of ground motion duration – particularly as it pertains to the performance of RC shearwall buildings – and to close some of the research gaps previously discussed. Three sub-goals of this work were:

1. develop a method to properly select and modify ground motion records for use in the assessment of ground motion duration;
2. provide modelling recommendations to ensure numerical simulations are adequately capable of capturing the effect of ground motion duration on the response of RC shearwall structures, and;
3. consider an approach to include ground motion duration into prescriptive modern building codes methods.

This work utilized 2D and 3D nonlinear numerical models to study the effect of duration on RC shearwall models. Two different types of RC construction were assessed: conventional construction and ductile construction; the former to represent existing structures, and the latter to represent modern construction. The collapse probabilities of the two model types (2D and 3D) and two construction types were influenced by the duration of the input ground motion time histories: longer motion suites tended to induce collapse at lower shaking intensities compared to shorter duration motion suites.

The development of a methodology to match the mean and variance of a ground motion suites to a target was also considered. Currently, the conditional spectra (CS) approach, which requires matching a mean spectrum as well as a target standard deviation, are considered most appropriate for capturing record-to-record variation in analysis results, which is necessary for risk analysis. However, when applying such methods for subduction interface records, practitioners

and researchers are often limited by the number of available records for this shaking type, especially when trying to account for geophysical parameters (e.g. soil conditions, magnitudes, distances, etc.). The ground motion suite matching methodology developed as part of this research overcomes these limitations and is useful for developing hazard-consistent suites of motions, subduction interface or otherwise.

From the results of these structural analyses, it was hypothesized that structures designed to meet current building code objectives using analysis results generated from (typical) short duration, crustal ground motion suites, could fail to meet code performance targets when subjected to longer duration motions. This hypothesis appeared to be correct – and accordingly, it was proposed to lower seismic force reduction factors for buildings designed in subduction tectonic regimes. The factor reduction was calibrated so that both long and short motions suites would predict acceptable collapse probabilities at a maximum considered earthquake level, and would provide designs with an adequate long-term (i.e. 50 year) total collapse risk considering all possible shaking scenarios (i.e. larger or smaller compared to the design level).

Component level seismic safety factors were also investigated. It was observed that the longer motion suites produced component-level responses that were more variable than similar suites of shorter records. Since the safety of these components depends largely on both capacity and demand means and variations/uncertainties, it was necessary to assess if current provisions were adequate. Ultimately, it appeared that current requirements would be adequate to produce safe designs when subjected to assessments conducted using either short and long ground motion suites.

The major findings and contributions of this dissertation are:

1. This is the first study into the effect of ground motion duration on RC shearwall structures using nonlinear fiber models and 3D analyses.
2. This study showed that code-level performance of this type of structure is not significantly influenced by shaking duration; however, collapse risk (requiring very high levels of shaking) is affected by the duration of shaking: longer duration motion suites tend to induce collapse at lower shaking intensities.
3. A method to develop input ground motion suites that match a target mean and conditional standard deviation was also developed and implemented. This type of suite is essential for assessing the safety and collapse risk of structural systems, which depend on both mean results and the distribution (variability) in analysis results.
4. The effect of ground motion duration on design code provisions was also investigated. It was found that structures designed to meet current building code life safety objectives could fail to meet other code performance (i.e. collapse risk) targets when subjected to long duration motions. Accordingly, it was proposed to lower seismic force reduction factors for buildings designed in subduction tectonic regimes capable of producing long duration ground motions.
5. The effect of ground motion duration on component level seismic safety factors was also investigated. Despite the increased variability in component demands observed under structures subjected to long duration motions, it appeared that current code component factors could adequately meet the performance objectives required for new construction.

This dissertation focused on RC coupled shearwall buildings in the Cascadia Subduction Zone; however, a similar methodology could be applied to other structural systems or other subduction zones.

8.3 Recommended Research

There are still many gaps in the knowledge of the effect of ground motion duration in general and on its effect of the design/analysis of RC concrete shearwall buildings. Some of these gaps are related to modelling uncertainties and others are related to input ground motion section.

In terms of modelling, some topics for further research may include:

- **Effect of foundation/soil structure interaction.**

The models developed as a part of this research were all fixed at the base and did not account for soil-structure interaction (SSI). Whether this could influence the effect of different types of ground motions currently is not known. Subduction interface records tend to produce more energy at longer periods, while shorter crustal records have higher energy at lower periods. SSI could amplify or de-amplify some of this energy, resulting in further differences between these two shaking types.

If using nonlinear soil models, ratcheting may also occur from inelastic displacements in the soil – ratcheting being one of the main mechanisms behind the effect of ground motion duration.

- **Effect of shear-flexure interaction in the shearwalls.**

Although this research did briefly look at the effect of replacing fiber models with 2D wall models capable of simulating shear-flexure interaction (Appendix C), this study was limited. Further work, including, but not limited to, 3D modelling, to agree or disagree with the conclusions made would be useful,

- **Effect on taller or shorter building heights.**

This research compared building systems with heights from 6 to 30 stories, noting similar trends between the effect of ground motion duration on the different models, however with

effects being amplified in the shorter models. Thus, studies using even shorter buildings may be warranted.

The 3D analyses in Chapter 6 were only conducted using 18 story models; the results from these more sophisticated models seemed to correlate with the results of the 2D models. However, in taller buildings, torsional effects may become more significant. Thus, additional studies using 3D models of taller (>30 stories) structures would also be highly useful.

- **Effect on combined systems.**

This work only considered coupled shearwall systems. However, this type of system could be combined with other lateral force resisting systems, such as exterior moment frames. The effect of ground motion duration on such combined systems would also be useful for further investigation including assessing the appropriateness of seismic force reduction factors for such systems.

- **Effect on high-strength concrete.**

In order to design taller buildings, engineers quite often have to rely on high-strength concrete in order to meet the seismic shear demands on these buildings. However, high-strength concrete is typically more brittle than traditional concrete. The effect of ground motion duration on shearwall systems designed with high-strength concrete would also be warranted.

In terms of input ground motion selection and modification, further topics for research may include:

- **Effect of subduction intraslab records.**

This research focused on the difference in structural response between short and long duration motions, or, alternatively, between crustal and large magnitude subduction interface records. However, as noted in Chapter 2, subduction zones can also produce intraslab events deep within the subducting slab. Due to their large depth, moderate magnitudes, and faulting mechanisms, records from this type of event may have characteristics (e.g. duration, frequency content, etc.) that differ from both crustal and interface events. Because this type of event largely governs the short-period hazard in Southwestern BC, the effect subduction intraslab records has on structural response should not be ignored.

- **Effect of vertical ground motions.**

In the studies conducted as part of this research, only horizontal records, or record pairs, were applied to the models. The effect of modelling vertical mass and applying tri-direction records should also be considered – particularly its effect on the gravity system (slabs and columns), which may be sensitive to the increased demands from vertical accelerations.

- **Effect on ground motion matching techniques.**

The methodology proposed to develop ground motion suites relied on spectral matching to match motions to modified variable target spectra, with time domain matching methods being employed. However, the application of time domain spectral matching to long duration subduction motions could be investigated. These methods add as few wavelets as possible to the input acceleration time series in order to match spectral acceleration targets.

Due to the long duration of subduction interface records, adding a few localized wavelets may not appropriately preserve the non-stationary characteristics of the input records. Thus, alternatives such as frequency domain spectral matching (which tends to produce more uniform modifications over the length of an input record) should also be investigated. Frequency domain spectral matching would not change the theory or application of the methodology, but may be better suited towards long duration record matching.

Bibliography

- Ab-Kadir, M. A., Zhang, J., Mashros, N., Hassan, A., & Mohd, N. Z. (2014). Experimental and Numerical Study on Softening and Pinching Effects of Reinforced Concrete Frame. *IOSR Journal of Engineering*, 4(1).
- Abrahamson, N. A., Gregor, N., & Addo, K. (2016). BC Hydro ground motion prediction equations for subduction earthquakes. *Earthquake Spectra*, 32(1), 23-44.
- ACI. (2008). *Building Code Requirements for Structural Concrete ACI 318*. Farmington Hills, MI: American Concrete Institute.
- Afshari, K., & Stewart, J. P. (2016). Physically Parameterized Prediction Equations for Significant Duration in Active Crustal Regions. *Earthquake Spectra*, 32(4), 2057-2081. doi:<http://dx.doi.org/10.1193/063015EQS106M>
- Ancheta, T. D., Darragh, R. B., Stewart, J. P., Seyhan, E., Silva, W. J., Chiou, B. S., . . . Kishida, T. (2013). Peer NGA-West2 database. *Pacific Earthquake Engineering Research Center (PEER)*.
- Arias, A. (1970). A measure of earthquake intensity. *Seismic Design for Nuclear Power Plants*, 438 – 483.
- ASCE/SEI. (2016). Minimum design loads for buildings and other structures. *American Society of Civil Engineers/Structural Engineering Institute*.
- ASCE/SEI. (2017). Seismic Evaluation and Retrofit of Existing Buildings. *American Society of Civil Engineers/Structural Engineering Institute*.
- ATC. (2010). *Modeling and acceptance criteria for seismic design and analysis of tall buildings*. PEER/ATC 72-1.

- Atik, A. L., & Abrahamson, N. (2010). An improved method for nonstationary spectral matching. *Earthquake Spectra*, 26(3), 601-617.
- Atik, A. L., & Abrahamson, N. A. (2010). An improved method for nonstationary spectral matching. *Earthquake Spectra*, 26(3), 601-617.
- Atkinson, G. M., & Adams, J. (2013). Ground motion prediction equations for application to the 2015 Canadian national seismic hazard maps. *Canadian Journal of Civil Engineering*, 40(10), 988-998.
- Atkinson, G. M., & Boore, D. M. (1995). Ground-motion relations for eastern North America. *Bulletin of the Seismological Society of America*, 85(1), 17-30.
- Atkinson, G. M., & Boore, D. M. (2003). Empirical ground-motion relations for subduction-zone earthquakes and their application to Cascadia and other regions. *Bulletin of the Seismological Society of America*, 93(4), 1703-1729.
- Atkinson, G. M., & Macias, M. (2009). Predicted ground motions for great interface earthquakes in the Cascadia subduction zone. *Bulletin of the Seismological Society of America*, 99(3), 1552-1578.
- Baker, J. W., & Cornell, C. A. (2006). Correlation of response spectral values for multicomponent ground motions. *Bulletin of the seismological Society of America*, 96(1), 215-227.
- Baker, J. W., & Cornell, C. A. (2006). Spectral shape, epsilon and record selection. *Earthquake Engineering and Structural Dynamics*, 35(9), 1077-1095.
- Baker, J. W., & Jayaram, N. (2008). Correlation of spectral acceleration values from NGA ground motion models. *Earthquake Spectra*, 24(1), 299-317.
- Baker, J. W., & Jayaram, N. (2008). Correlation of spectral acceleration values from NGA ground motion models. *Earthquake spectra*, 24(1), 299-317.

- Barney, G. B., Shiu, K. N., Rabbit, B. G., Fiorato, A. E., Russell, H. G., & Corley, W. G. (1980). *Behavior of coupling beams under load reversals (RD068. 01B)*. Skokie, IL.: Portland Cement Association.
- Bazzurro, P., & Luco, N. (2006). Do scaled and spectrum-matched near-source records produce biased nonlinear structural responses. *8th National Conference on Earthquake Engineering*. San Francisco, CA.
- Bebamzadeh, A., Fairhurst, M., & Ventura, C. E. (2017). Correlation of spectral values in worldwide subduction zone earthquakes. *16th World Conference on Earthquake Engineering*. Santiago, Chile.
- Beresnev, I. A. (2002). Source Parameters Observable from the Corner Frequency of Earthquake Spectra. *Bulletin of the Seismological Society of America*, 92(5), 2047–2048.
- Bertero, V. V., Mahin, S. A., & Herrera, R. A. (1978). Aseismic design implications of near-fault San Fernando earthquake records. *Earthquake Engineering and Structural Dynamics*, 6(1), 31-42.
- Bommer, J. J., & Martinez-Pereira, A. (1999). The effective duration of earthquake strong motion. *Journal of Earthquake Engineering*, 30(2), 127-172.
- Boore, D. M., & Atkinson, G. A. (2008). Ground-motion prediction equations for the average horizontal component of PGA, PGV, and 5%-damped PSA at spectral periods between 0.01 s and 10.0 s. *Earthquake Spectra*, 24(1), 99-138.
- Bozorgnia, Y., Abrahamson, N. A., Atik, L. A., Ancheta, T. D., Atkinson, G. A., Baker, J. W., . . . Darragh, R. (2014). NGA-West2 research project. *Earthquake Spectra*, 30(3), 973-987.
- Brown, J., & Kunnath, S. K. (2000). *Low Cycle Fatigue Behavior of Longitudinal Reinforcement in Reinforced Concrete Bridge Columns*. State University of New York at Buffalo, Buffalo,

- N.Y: NCEER Technical Report 00-0007, National Center for Earthquake Engineering Research.
- Brune, J. N. (1970). Tectonic stress and the spectra of seismic shear waves from earthquakes. *Journal of Geophysical Research*, 75(26), 4997-5009.
- Calado, L., Castiglioni, C. A., & Carydis, P. (2002). Shaking table tests for seismic performance evaluation of steel frames. *12th European Conference on Earthquake Engineering*. London.
- Carballo, J. E., & Cornell, C. A. (1998). Input to nonlinear structural analysis: modification of available accelerograms for different source and site characteristics. *6th US National Conference on Earthquake Engineering*. Seattle, WA.
- Carballo, J. E., & Cornell, C. A. (2000). Probabilistic seismic demand analysis: spectrum matching and design. *Reliability of Marine Structures Program, Department of Civil Engineering, Stanford University*.
- Carlton, B., & Abrahamson, N. A. (2014). Issues and approaches for implementing conditional mean spectra in practice. *Bulletin of the Seismological Society of America*, 104(1), 503-512.
- Chai, Y. H. (2005). Incorporating low-cycle fatigue model into duration-dependent inelastic design spectra. *Earthquake Engineering and Structural Dynamics*, 34(1), 83-96.
- Chandramohan, R. (2016). Duration of earthquake ground motion: influence on structural collapse risk and integration in design and assessment practice. *Ph.D. Dissertation. Stanford University*.

- Chandramohan, R., Baker, J. W., & Deierlein, G. G. (2016a). Impact of hazard-consistent ground motion duration in structural collapse risk assessment. *Earthquake Engineering and Structural Dynamics*, 45(8), 1357-1379.
- Chandramohan, R., Baker, J. W., & Deierlein, G. G. (2016b). Quantifying the influence of ground motion duration on structural collapse capacity using spectrally equivalent records. *Earthquake Spectra*, 32(2), 927-950.
- Chandramohan, R., Baker, J. W., Deierlein, G. G., & Lin, T. (2013). Influence of ground motion spectral shape and duration on seismic collapse risk. *10th International Conference on Urban Earthquake Engineering*. Tokyo Institute of Technology, Tokyo, Japan.
- Chang, G. A., & Mander, J. B. (1994). *Seismic Energy Based Fatigue Damage Analysis of Bridge Columns: Part I – Evaluation of Seismic Capacity*. State University of New York, Buffalo: NCEER Technical Report No. NCEER-94-0006.
- Chen, X., & Abercrombie, R. E. (2020). Improved approach for stress drop estimation and its application to an induced earthquake sequence in Oklahoma. *Geophysical Journal International*, 233, 233–253.
- Clough, R. W., & Johnston, S. B. (1966). Effect of stiffness degradation on earthquake ductility requirements. *Proceedings of Japan Earthquake Engineering Symposium*, (pp. 227-232). Tokyo, Japan.
- Cosenza, E., & Manfredi, G. (1997). *The improvement of the seismic-resistant design for existing and new structures using damage criteria*. Balkema, Rotterdam: Seismic Design Methodologies for the Next Generation of Codes.

- Cosenza, E., Iervolino, I., & Manfredi, G. (2004). On ground motion duration and engineering demand parameters. *International Workshop on Performance-based Seismic Design, Concepts and Implementation*. Bled, Slovenia.
- COSMOS. (2008). *Strong-motion Virtual Data Center (VDC)*. available at <http://www.strongmotioncenter.org> : The Consortium of Organizations for Strong-Motion Observation Systems .
- Dhakal, R., & Maekawa, K. (2002). Modelling for postyield buckling of reinforcement. *Journal of Structural Engineering*, 128(9), 1139-1147.
- Dutta, A., & Mander, J. B. (2001). Energy based methodology for ductile design of concrete columns. *Journal of Structural Engineering*, 127(12), 1374-1381.
- Eshelby, J. D. (1957). The determination of the elastic field of an ellipsoidal inclusion, and related problems. *Proceedings of the Royal Society of London. Series A. Mathematical and physical sciences*, 241(1226), 376-396.
- Estrella, X., Guindos, P., & Almazán, J. L. (2019). Ground motions for FEMA P-695 application in subduction zones. *Latin American Journal of Solids and Structures*, 16(9).
- FEMA. (2009). Quantification of building seismic performance factors. *FEMA-P695, Federal Emergency Management Agency*.
- Fujiwara, H., Aoi, S., Kunugi, T., & Adachi, S. (2004). Strong-motion Observation Networks of NIED: K-NET and KiK-net. *Cosmos Report*.
- Furgo Consultants Inc. (2015). *EZ-FRISK 8.00*. Furgo N.V.
- Galano, L., & Vignoli, A. (2000). Seismic behavior of short coupling beams with different reinforcement layouts. *ACI Structural Journal*, 97(6), 876-885.

- Ghofrani, H., & Atkinson, G. M. (2014). Ground-motion prediction equations for interface earthquakes of M7 to M9 based on empirical data from Japan. *Bulletin of earthquake engineering, 12*(2), 549-571.
- Gogus, A., & Wallace, J. W. (2015). Seismic safety evaluation of reinforced concrete walls through FEMA P695 methodology. *Journal of Structural Engineering, 141*(10). doi:04015002
- Goldfinger, C., Nelson, C. H., Morey, A. E., Johnson, J. E., Patton, J. R., Karabanov, E., . . . Enkin, R. J. (2012). Turbidite event history: Methods and implications for Holocene paleoseismicity of the Cascadia subduction zone. *US Geological Survey Professional Paper, 1661*.
- Green, M. C., & Karsh, J. E. (2012). *Tall Wood – The Case for Tall Wood Buildings*. Vancouver, BC.
- Gutenberg, M., & Richter, C. F. (1944). Frequency of earthquakes in California. *Bulletin of the Seismological Society of America, 34*(4), 185-188.
- Halchuk, S., Allen, T. I., Adams, J., & Rogers, G. C. (2014). *Fifth generation seismic hazard model input files as proposed to produce values for the 2015 National Building Code of Canada*. Geological Survey of Canada, Open File 7576.
- Hancock, J., & Bommer, J. J. (2006). A state-of-knowledge review of the influence of strong-motion duration on structural damage. *Earthquake Spectra, 22*(3), 827-845.
- Hancock, J., Bommer, J. J., & Stafford, P. J. (2008). Numbers of scaled and matched accelerograms required for inelastic dynamic analyses. *Earthquake engineering & structural dynamics, 37*(14), 1585-1607.

- Hancock, J., Watson-Lamprey, J., Abrahamson, N. A., Bommer, J. J., Markatis, A., McCoy, E., & Mendis, R. (2006). An improved method of matching response spectra of recorded earthquake ground motion using wavelets. *Journal of Earthquake Engineering*, 10(1), 67-89.
- Heo, Y., Kunnath, S. K., & Abrahamson, N. A. (2010). Amplitude-scaled versus spectrum-matched ground motions for seismic performance assessment. *Journal of structural engineering*, 137(3), 278-288.
- Hossain, A. (2013). Seismic Performance of concrete buildings reinforced with superelastic shape memory alloy rebars. *M.A.Sc. Thesis. University of British Columbia Okanagan, Kelowna, BC.*
- Housner, G. W. (1952). *Spectrum intensities of strong-motion earthquakes*. Pasadena, Ca.: Division of Engineering, California Institute of Technology.
- Ibarra, L. F., & Krawinkler, H. (2005). *Global collapse of frame structures under seismic excitations*. John A. Blume Earthquake Engineering Center, Stanford University: PEER Projecy 3192002.
- Ibarra, L. F., Medina, R. A., & Krawinkler, H. (2005). Hysteretic models that incorporate strength and stiffness deterioration. *Earthquake Engineering and Structural Dynamics*, 34(12), 1489-1511.
- Iervolino, I., Manfredi, G., & Cosenza, E. (2006). Ground motion duration effects on nonlinear seismic response. *Earthquake Engineering and Structural Dynamics*, 35(1), 21-38.
- Jayaram, N., Baker, J. W., Okano, H., Ishida, H., McCann Jr, M. W., & Mihara, Y. (2011). Correlation of response spectral values in Japanese ground motions. *Earthquake and Structures*, 2(4), 357-376.

- Jayaram, N., Lin, T., & Baker, J. W. (2011). A computationally efficient ground-motion selection algorithm for matching a target response spectrum mean and variance. *Earthquake Spectra*, 27(3), 797-815.
- Kanamori, H. (1978). Quantification of earthquakes. *Nature*, 271(5644), 411-414.
- Kinoshita, S. (1998). Kyoshin Net (K-net). *Seismological Research Letters*, 69(4), 309-332.
- Kolaj, M., Halchuk, S., Adams, J., & Allen, T. I. (2020). *Sixth Generation seismic hazard model of Canada: Input files to produce values proposed for the 2020 National Building Code of Canada*. Geological Survey of Canada, Open File 8630.
- Kolozvari, K., & Wallace, J. (2016). Practical nonlinear modeling of reinforced concrete structural walls. *Journal of Structural Engineering*, 142(12). doi:G4016001
- Kolozvari, K., Orakcal, K., & Wallace, J. (2018). New openses models for simulating nonlinear flexural and coupled shear-flexural behavior of RC walls and columns. *Computers and Structures*, 196, 246-262.
- Kutner, M. H., Nachtsheim, C., & Neter, J. (2004). *Applied linear regression models*. McGraw-Hill/Irwin.
- Kwan, A. K., & Zhao, Z. Z. (2002). Testing of coupling beams with equal end rotations maintained and local joint deformation allowed. *Proceedings of the Institution of Civil Engineers-structures and Buildings*, 152(1), 67-78.
- LATBSDC. (2005). *An alternative procedure for seismic analysis and design of tall buildings located in the Los Angeles Region*. Los Angeles, Ca.
- LATBSDC. (2017). *An alternative procedure for seismic analysis and design of tall buildings located in the Los Angeles Region*. Los Angeles, Ca.

- Lignos, D. (2008). *Sidesway collapse of deteriorating structural systems under seismic excitations*. Ph.D. Dissertation, Stanford University.
- Lin, T., Haselton, C. B., & Baker, J. W. (2013). Conditional spectrum-based ground motion selection. Part I: Hazard consistency for risk-based assessments. *Earthquake engineering & structural dynamics*, 42(12), 1847-1865.
- Lowes, L. N., Mitra, N., & Altoontash, A. (2003). *A Beam-column Joint Model for Simulating the Earthquake Response of Reinforced Concrete Frames*, PEER Report 2003/10. University of California, Berkeley, C.A.: Pacific Earthquake Engineering Center (PEER).
- Luco, N., Lui, T. J., & Rukstales, K. S. (2017). A risk-targeted alternative to deterministic capping of maximum considered earthquake ground motion maps. *16th World Conference on Earthquake Engineering*. Santiago, Chile.
- Mander, J. B., Priestley, M. J., & Park, R. (1998). Theoretical stress-strain model for confined concrete. *Journal of Structural Engineering*, 114(8), 1804-1826.
- Manfredi, G., & Pecce, M. (1997). Low cycle fatigue of RC beams in NSC and HSC. *Engineering Structures*, 19(3), 217-223.
- McKenna, F., Fenves, G. L., Scott, M. H., & Jeremic, B. (2000). *Open System for Earthquake Engineering (OpenSees)*. Berkeley, C.A.: Pacific Earthquake Engineering Research Center.
- Mitchell, D., Paultre, P., Tinawi, R., Saatcioglu, M., Tremblay, R., Elwood, K., . . . Devall, R. (2010). Evolution of seismic design provisions in the National building code of Canada. *Canadian Journal of Civil Engineering*, 37, 1157-1170.
- Naish, D. (2007). Testing and Modeling of Reinforced Concrete Coupling Beams. *Doctoral dissertation, University of California, Los Angeles, Ca.*

- Naish, D., Fry, A., Klemencic, R., & Wallace, J. (2013). Reinforced concrete coupling beams-Part I: testing. *ACI Structural Journal*, 110(6), 1057-1066.
- National Research Council of Canada. (1941). *National Building Code of Canada*. Ottawa, Ont.
- National Research Council of Canada. (1953). *National Building Code of Canada*. Ottawa, Ont.
- National Research Council of Canada. (1965). *National Building Code of Canada*. Ottawa, Ont.
- National Research Council of Canada. (1970). *National Building Code of Canada*. Ottawa, Ont.
- National Research Council of Canada. (1995). *National Building Code of Canada*. Ottawa, Ont.
- National Research Council of Canada. (2005). *National Building Code of Canada*. Ottawa, Ont.
- National Research Council of Canada. (2010). *National Building Code of Canada*. Ottawa, Ont.
- National Research Council of Canada. (2015). *National Building Code of Canada*. Ottawa, Ont.
- NEHRP Consultants Joint Venture. (2011). Selecting and Scaling Earthquake Ground Motions for Performing Response-History Analyses. *NISTGCR-11-917-15*.
- Noh, N. M., Liberatore, L., Mollaioli, F., & Tesfamariam, S. (2017). Modelling of masonry infilled RC frames subjected to cyclic loads: State of the art review and modelling with OpenSees. *Engineering Structures*, 150, 599-621.
- Orakcal, K., & Wallace, J. (2006). Flexural modeling of reinforced concrete walls-experimental verification. *ACI Materials Journal*, 103(2), 196-206.
- Pan, Y. (2018). *Effect of Ground Motion Duration on the Seismic Performace and Collapse of Timber Structures*. PhD Thesis, University of British Columbia, Vancouver, B.C.
- Paulay, T. (1980). Earthquake-resisting Shearwalls - New Zealand Design. *ACI Journal*, 77(3), 144-152.
- Paulay, T., & Binney, J. R. (1974). Diagonally reinforced coupling beams of shear walls. *Shear in Reinforced Concrete, SP-42, American Concrete Institute*, 579-598.

- PEER. (2010). *Guidelines for performance-based seismic design of tall buildings*. University of California, Berkeley.
- PEER. (2014). *PEER Ground Motion Database*. available at <http://ngawest2.berkeley.edu>: Pacific Earthquake Engineering Research Center.
- PEER. (2017). *Guidelines for performance-based seismic design of tall buildings*. University of California, Berkeley.
- Pugh, J. (2012). *Numerical Simulation of Walls and Seismic Design Recommendations for Walled Buildings*. PhD Thesis, University of Washington, Seattle, W.A.
- Raghunandan, M., & Liel, A. B. (2013). Effect of ground motion duration on earthquake-induced structural collapse. *Structural Safety*, *41*, 119-133.
- Rahnama, M., & Manuel, M. (1996). The effect of strong motion duration on seismic demands. *11th World Conference on Earthquake Engineering*. Acapulco, Mexico.
- Rezaeian , S., Petersen , M. D., Moschetti , M. P., Harmsen , S. C., & Frankel , A. D. (2014). Implementation of NGA-West2 ground motion models in the 2014 US National Seismic Hazard Maps. *Earthquake Spectra*, *30*(3), 1319-1333.
- Seifried, A. E. (2013). Response compatibilization and impact on structural response assessment. *Doctoral dissertation, Stanford University, Ca.*
- Shahnewaz, M., Pan, Y., Shahria, A. M., & Tannert, T. (2020). Seismic Fragility Estimates for Cross-Laminated Timber Platform Building. *Journal of Structural Engineering*, *146*(12). doi: 04020256
- Shen, Y. L., Schneider, J., Tesfamariam, S., Stiemer, S. F., & Mu, Z. G. (2013). Hysteresis behavior of bracket connection in cross-laminated-timber shear walls. *Construction and Building Materials*, *48*, 980-991.

- Sivaselvan, M. V., & Reinhorn, A. M. (2000). Hysteretic models for deteriorating inelastic structures. *Journal of Engineering Mechanics*, 126(6), 633-640.
- Song, J. K., & Pincheira, J. A. (2000). Spectral displacement demands of stiffness-and strength-degrading systems. *Earthquake Spectra*, 16(4), 817-851.
- Stephens, J. E., & Yao, J. T. (1987). Damage assessment using response measurements. *Journal of Structural Engineering*, 113(4), 787-801.
- Strasser, F. O., Arango, M. C., & Bommer, J. J. (2010). Scaling of the source dimensions of interface and intraslab subduction-zone earthquakes with moment magnitude. *Seismological Research Letters*, 81(6), 941-950.
- Tang, J. P., & Yao, J. T. (1972). Expected fatigue damage of seismic structures. *Journal of the Engineering Mechanics Division*, 98(3), 695-709.
- Tassios, T. P., Moretti, M., & Bezas, A. (1996). On the behavior and ductility of reinforced concrete coupling beams of shear walls. *Structural Journal*, 93(6), 711-720.
- Tsai, W. T. (1988). Uniaxial Compressional Stress-Strain Relation of Concrete. *Journal of Structural Engineering*, 114(9), 2133-2136.
- Ulugtekin, D. (2010). *Analytical modeling of reinforced concrete panel elements under reversed cyclic loadings*. M.S. Thesis. Bogazici University, Istanbul, Turkey.
- Vamvatsikos, D., & Cornell, A. C. (2002). Incremental dynamic analysis. *Earthquake engineering & structural dynamics*, 31(3), 491-514.
- Ventura, C. E., Bebamzadeh, A., & Fairhurst, M. (2019). *Ground Motion Selection for the UBC Campus*. University of British Columbia: VC Structural Dynamics Ltd. Prepared for Infrastructure Development Project Services.

- Xiao, Y., Esmaeily-Ghasemabadi, A., & Wu, H. (1999). High-strength concrete short beams subjected to cyclic shear. *Structural Journal*, 96(3), 392-399.
- Yassin, M. H. (1994). *Nonlinear Analysis of Prestressed Concrete Structures under Monotonic and Cyclic Loads*. PhD Thesis, University of California, Berkeley.
- Yathon, J., Adebar, P., & Elwood, K. J. (2017). A detailed inventory of non-ductile concrete shear wall buildings. *Earthquake Spectra*, 33(2), 605-622.
- Yathon, J., Adebar, P., & Elwood, K. J. (2017). A Detailed Inventory of Non-Ductile Concrete Shear Wall Buildings. *Earthquake Spectra*, 33(2), 605-622.
- Zareian, F., Lignos, D. G., & Krawinkler, H. (2010). Evaluation of seismic collapse performance of steel special moment resisting frames using FEMA P695 (ATC-63) methodology. *Structures Congress*, 1275-1286.
- Zhao, J. X., Zhang, J., Asano, A., Ohno, Y., Oouchi, T., Takahashi, T., . . . Fukushima, Y. (2006). Attenuation relations of strong ground motion in Japan using site classification based on predominant period. *Bulletin of the Seismological Society of America*, 96(3), 898-913.
- Zhao, J., & Sritharan, S. (2007). Modeling of strain penetration effects in fiber-based analysis of reinforced concrete structures. *ACI Structural Journal*, 104(2), 133-141.

Appendix A: Ground Motion Suite Metadata for Duration Intensity Metric Study

Name	Scale Factor	Magnitude (M_w)	Distance (km)	Vs30 (m/s)	Type
KOBE_TAZ000	0.76	6.90	42.6	312	Cr
IMPVALL_H-BRA315	2.62	6.53	44.3	209	Cr
CHICHI06_CHY035-N	3.58	6.30	60.5	474	Cr
Maule_LACH.HN-N	1.48	8.80	183.0	-	Sd
CHICHI06_CHY034-N	3.41	6.30	63.4	379	Cr
CHALFANT_A-BEN270	3.89	6.19	32.8	271	Cr
CHICHI_CHY054-N	3.96	7.62	80.1	172	Cr
Tohoku_CHB0171103111446-NS	4.25	9.00	201.6	281	Sd
Maule_stgolafloida1002271-NS	3.58	8.80	174.0	685	Sd
CHICHI_TCU056-N	2.92	7.62	40.5	273	Cr
NORTHR_SYL360	0.69	6.69	24.2	441	Cr
Maule_STL.HN-N	3.1	8.80	178.0	-	Sd
Tohoku_MYG0091103111446-EW	1.52	9.00	111.3	954	Sd
CHICHI_CHY107-W	4.21	7.62	82.2	176	Cr
Hokkaido_HKD0680309260450-EW	2.46	8.00	130.6	299	Sd
NORTHR_UCL360	2.67	6.69	25.6	398	Cr
Tohoku_MYG0171103111446-EW	1.06	9.00	100.9	168	Sd
CHICHI_TCU046-E	4.23	7.62	69.4	466	Cr
STELIAS_059v2009	4.16	7.54	160.5	275	Cr
CHICHI_TCU042-E	2.65	7.62	78.8	273	Cr
NORTHR_RRS318	0.97	6.69	20.6	282	Cr
KOBE_SKI000	3.68	6.90	0.0	256	Cr
CHICHI_TCU046-N	4.66	7.62	69.4	466	Cr
NORTHR_CCN090	2.53	6.69	26.7	278	Cr
CHICHI03_CHY028-N	2.97	6.20	32.8	543	Cr
SANSALV_NGI180	1.2	5.80	14.5	350	Cr
IMPVALL_H-E03140	1.98	6.53	30.3	163	Cr
CHICHI_HWA041-N	4.11	7.62	81.3	273	Cr
SUPERST_B-KRN270	3.26	6.54	21.3	208	Cr
ITALY_B-CTR270	2.13	6.20	13.9	600	Cr
NORTHR_STM090	1.87	6.69	28.5	336	Cr
Tohoku_NIG0121103111446-NS	3.94	9.00	193.6	287	Sd
IMPVALL_H-AGR003	2.07	6.53	10.3	275	Cr
CHICHI_TCU055-E	2.08	7.62	36.7	273	Cr
MTLEWIS_HVR090	3.49	5.60	18.3	282	Cr
LOMAP_LGP000	0.61	6.93	25.4	478	Cr
LOMAP_STG000	1.45	6.93	32.4	371	Cr
SUPERST_B-CAL315	4.5	6.54	32.9	206	Cr
CHICHI_TCU-N	1.9	7.62	37.1	473	Cr
CHICHI_TCU105-E	3.2	7.62	51.4	576	Cr

Tohoku_SIT0031103111446-EW	2.27	9.00	163.6	122	Sd
Tohoku_TKY0241103111446-NS	2.79	9.00	177.5	-	Sd
CHICHI03_TCU122-E	2.92	6.20	25.7	476	Cr
CHICHI06_CHY037-N	3.72	6.30	71.3	212	Cr
Hokkaido_HKD0760309260450-NS	1.58	8.00	98.1	178	Sd
CHICHI_CHY107-N	4.02	7.62	82.2	176	Cr
SUPERST_B-POE360	2.44	6.54	14.4	208	Cr
CHICHI_TCU033-E	2.71	7.62	93.4	423	Cr
LOMAP_HSP000	0.94	6.93	51.3	371	Cr
CHICHI_TCU122-E	2.63	7.62	23.2	476	Cr
NORTHR_LDM334	1.56	6.69	21.1	629	Cr
CHICHI_TCU040-N	3.65	7.62	69.5	362	Cr
CHICHI03_TCU138-N	3.91	6.20	29.8	653	Cr
PALMSPR_DSP000	2.45	6.06	15.1	345	Cr
SMART1_40E01NS	3.53	6.32	67.4	275	Cr
CHICHI_CHY008-N	3.93	7.62	69.7	211	Cr
IMPVALL_H-E04140	1.45	6.53	28.9	209	Cr
BAJA_CPE161	1.5	5.50	7.0	660	Cr
ERZIKAN_ERZ-EW	1.25	6.69	12.7	275	Cr
CHICHI_TCU067-N	1.14	7.62	29.8	434	Cr
CHICHI_TCU026-E	4.29	7.62	106.5	474	Cr
CHICHI_TCU042-N	2.6	7.62	78.8	273	Cr
Tohoku_TKY0161103111446-NS	2.54	9.00	188.7	-	Sd
CHICHI_ILA042-E	4.17	7.62	136.1	209	Cr
Maule_stgoentro1002271-L	2.69	8.80	175.8	-	Sd
IMPVALL_H-E12230	4.87	6.53	33.5	197	Cr
CHICHI_TCU055-N	2.18	7.62	36.7	273	Cr
LIVERMOR_A-DVD246	4.57	5.80	29.4	339	Cr
Tohoku_FKS0101103111446-EW	1.7	9.00	56.3	719	Sd
CHICHI06_CHY030-E	4.22	6.30	62.0	205	Cr
Maule_ANTU.C.HN-N	2.63	8.80	167.0	-	Sd
CHICHI_TCU082-N	1.92	7.62	37.1	473	Cr
CHICHI_HWA039-N	3.84	7.62	75.5	375	Cr
NORTHR_STM360	2.22	6.69	28.5	336	Cr
Tohoku_MYG0091103111446-NS	1.55	9.00	111.3	954	Sd
LANDERS_IND090	4.1	7.28	60.1	345	Cr
CHICHI_TCU138-W	2.35	7.62	25.5	653	Cr
Tohoku_TKY0161103111446-EW	2.45	9.00	188.7	0	Sd
CHICHI_TCU036-E	2.74	7.62	68.3	273	Cr
Tohoku_KNG2011103111446-EW	3.24	9.00	273.3	-	Sd
NORTHR_BLD090	3.83	6.69	33.2	297	Cr
CHICHI_TCU098-N	4.17	7.62	100.1	375	Cr
CHICHI_TCU051-N	2.49	7.62	39.4	273	Cr
IMPVALL_H-E05140	1.74	6.53	29.5	206	Cr
CHICHI_CHY036-E	1.36	7.62	44.7	233	Cr
CHICHI_TCU089-E	2.05	7.62	10.7	553	Cr
SMART1_45M01EW	2.43	7.30	78.6	275	Cr

Tohoku_GNM0081103111446-NS	3.86	9.00	186.3	410	Sd
ITALY_A-STU270	1.91	6.90	31.8	1000	Cr
LOMAP_G06000	4.77	6.93	39.5	663	Cr
COALINGA_H-Z07000	3.23	6.36	41.4	371	Cr
CHICHI_TCU082-E	2.2	7.62	37.1	473	Cr
CHICHI_TCU049-E	2.27	7.62	39.7	487	Cr
CHICHI_CHY047-W	3.87	7.62	55.5	273	Cr
Hokkaido_HKD1090309260450-NS	2.01	8.00	65.3	342	Sd
CHICHI_TCU038-E	3.19	7.62	73.6	273	Cr
KOBE_TAZ090	0.81	6.90	42.6	312	Cr
NORTHR_JEN022	1.24	6.69	21.8	373	Cr
NORTHR_0655-022	1.24	6.69	21.8	526	Cr
SUPERST_B-WSM090	3.41	6.54	21.5	194	Cr
Maule_curico1002271-EW	1.68	8.80	36.5	537	Sd
LOMAP_AGW000	4.34	6.93	43.8	240	Cr
CHICHI_TCU076-E	2.18	7.62	17.9	615	Cr
MANJIL_184327	2.46	7.37	79.5	275	Cr
Hokkaido_HKD0750309260450-NS	2.03	8.00	110.2	422	Sd
Geiyo_EHM0080103241528-EW	1.72	6.40	61.2	561	Scr
SHonshu_EHM0080103241528-EW	1.72	6.40	61.2	561	Scr
CHICHI06_CHY039-N	4.64	6.30	79.8	201	Cr
CHICHI03_CHY035-N	4.35	6.20	42.9	474	Cr
LOMAP_PRS090	2.62	6.93	99.3	595	Cr
NORTHR_VEN360	4.53	6.69	70.6	271	Cr
CAPEMEND_FOR000	3.74	7.01	31.0	457	Cr
GREECE_H-KAL-NS	2.59	6.20	11.2	339	Cr
NORTHR_0655-292	0.77	6.69	21.8	526	Cr
Tohoku_TCG0071103111446-EW	4.76	9.00	117.5	765	Sd
LANDERS_ABY000	4.29	7.28	75.5	271	Cr
CHICHI_CHY046-N	2.69	7.62	55.8	442	Cr
PugetSound_OLY0B-2	4.76	6.70	109.0	-	Scr
NORTHR_JEN292	0.77	6.69	21.8	373	Cr
CHICHI_TCU-E	2.3	7.62	37.1	473	Cr
Tohoku_CHB0111103111446-NS	2.37	9.00	151.9	270	Sd
Tohoku_TKY0051103111446-NS	3.79	9.00	218.6	352	Sd
LOMAP_AGW090	4.16	6.93	43.8	240	Cr
CHICHI06_CHY028-N	3.66	6.30	51.6	543	Cr
SUPERST_B-PTS315	1.52	6.54	18.4	349	Cr
CHICHI_TAP095-N	3.46	7.62	158.6	215	Cr
NORTHR_5082A-235	2.44	6.69	26.2	392	Cr
IMPVALL_I-ELC270	2.33	6.95	15.7	213	Cr
KOCAELI_YPT060	1.76	7.51	25.1	297	Cr
CHICHI_TCU010-E	3.94	7.62	132.6	474	Cr
Tohoku_YMN0091103111446-EW	3.84	9.00	289.7	756	Sd
Tohoku_CHB0091103111446-EW	2.77	9.00	173.6	197	Sd
CHICHI_CHY032-N	3.92	7.62	62.2	193	Cr
IMPVALL_H-E12140	3.87	6.53	33.5	197	Cr

HECTOR_11625090	3.39	7.13	118.8	345	Cr
SMART1_45I01NS	2.68	7.30	77.9	275	Cr
Tohoku_GNM0131103111446-EW	3.41	9.00	197.0	316	Sd
CHICHI_TCU056-E	2.64	7.62	40.5	273	Cr
CHICHI_TCU070-N	2.01	7.62	48.5	401	Cr
LANDERS_ABY090	3.45	7.28	75.5	271	Cr
Hokkaido_HKD0840309260450-NS	1.38	8.00	92.1	510	Sd
CHICHI_TCU105-N	3.23	7.62	51.4	576	Cr
LOMAP_A2E090	3.96	6.93	72.9	271	Cr
LOMAP_G03090	1.66	6.93	35.9	350	Cr
CHICHI_TCU015-E	3.38	7.62	101.9	426	Cr
KERN_TAF111	3.84	7.36	46.2	385	Cr
Tohoku_TKY0251103111446-NS	3.47	9.00	177.4	-	Sd
LANDERS_BRS090	4.15	7.28	95.0	371	Cr
NORTHR_WPI316	1.19	6.69	27.8	286	Cr
Tohoku_KNG2051103111446-NS	3.39	9.00	269.6	-	Sd
LOMAP_CLD285	3.35	6.93	35.5	295	Cr
Tohoku_CHB0241103111446-NS	2.05	9.00	172.9	264	Sd
CHICHI_TCU061-E	2.67	7.62	42.8	273	Cr
LOMAP_SVL270	2.59	6.93	45.6	268	Cr
CHICHI_HWA-N	4.53	7.62	81.5	273	Cr
LANDERS_DSP000	4.13	7.28	28.2	345	Cr
Tohoku_GNM0101103111446-EW	4.17	9.00	164.0	326	Sd
VICT_CHI102	2.73	6.33	38.3	275	Cr
KOCAELI_Izt180	2.82	7.51	16.9	811	Cr
SMART1_45I01EW	2.49	7.30	77.9	275	Cr
CHICHI_TCU061-N	2.61	7.62	42.8	273	Cr
NORTHR_GLE170	4.38	6.69	29.8	446	Cr
LANDERS_PSA090	3.92	7.28	42.5	208	Cr
CHICHI_HWA011-E	3.13	7.62	80.0	273	Cr
Tohoku_CHB0281103111446-NS	3.4	9.00	168.9	-	Sd
Tohoku_CHB0141103111446-EW	3.07	9.00	187.8	237	Sd
NORTHR_MRP180	3.37	6.69	36.0	405	Cr
NORTHR_TEM090	4.51	6.69	37.1	376	Cr
IMPVALL_H-EMO000	1.5	6.53	21.8	186	Cr
CHICHI_TAP043-E	4.84	7.62	140.6	273	Cr
Tohoku_MYG0151103111446-EW	0.99	9.00	99.2	279	Sd
Mich_CALE9701_111_S00E	3.05	7.10	29.3	800	Scr
Tohoku_AOM0111103111446-NS	4.61	9.00	193.9	357	Sd
KOCAELI_Izt090	2.47	7.51	16.9	811	Cr
KOCAELI_GBZ270	4.34	7.51	49.7	792	Cr
Tohoku_CHB0041103111446-NS	3.14	9.00	126.8	414	Sd
Tohoku_NIG0121103111446-EW	4.67	9.00	193.6	287	Sd
WESTMORL_WLF225	3.96	5.90	8.9	191	Cr
MANAGUA_B-MAN180	4.45	5.20	7.6	289	Cr
Tohoku_TCG0161103111446-NS	3.49	9.00	100.9	693	Sd
CHICHI_TCU065-N	0.73	7.62	27.9	306	Cr

LOMAP_HDA165	1.68	6.93	48.4	216	Cr
CAPEMEND_FOR090	4.1	7.01	31.0	457	Cr
Tohoku_TKY0041103111446-NS	3.62	9.00	215.6	380	Sd
CHICHI_TCU029-E	3.82	7.62	79.6	474	Cr
Hokkaido_HKD1030309260450-NS	2.32	8.00	121.4	603	Sd
CHICHI_WGK-E	1.79	7.62	33.0	259	Cr
CHICHI04_TCU116-N	4.84	6.20	41.7	493	Cr
IMPVALL_H-AGR273	1.78	6.53	10.3	275	Cr
Tohoku_MYG0041103111446-EW	1.54	9.00	112.2	303	Sd
NORTHR_LDM064	1.06	6.69	21.1	629	Cr
Tohoku_FKS0121103111446-EW	2.45	9.00	59.9	259	Sd
SUPERST_B-IVW360	1.61	6.54	30.8	208	Cr
SMART1_45C00EW	2.58	7.30	77.7	275	Cr
SMART1_45O02EW	3.66	7.30	79.0	275	Cr
CHICHI_TCU053-E	2.68	7.62	42.0	455	Cr
Tohoku_CHB0021103111446-NS	3.04	9.00	171.2	436	Sd
Tohoku_AOM0211103111446-NS	3.38	9.00	196.4	312	Sd
NORTHR_5082-235	2.28	6.69	26.2	414	Cr
CHICHI_ILA042-N	4.85	7.62	136.1	209	Cr

**Appendix B: Additional Plots for 6 and 30 Story Models for Period Elongation
Study**

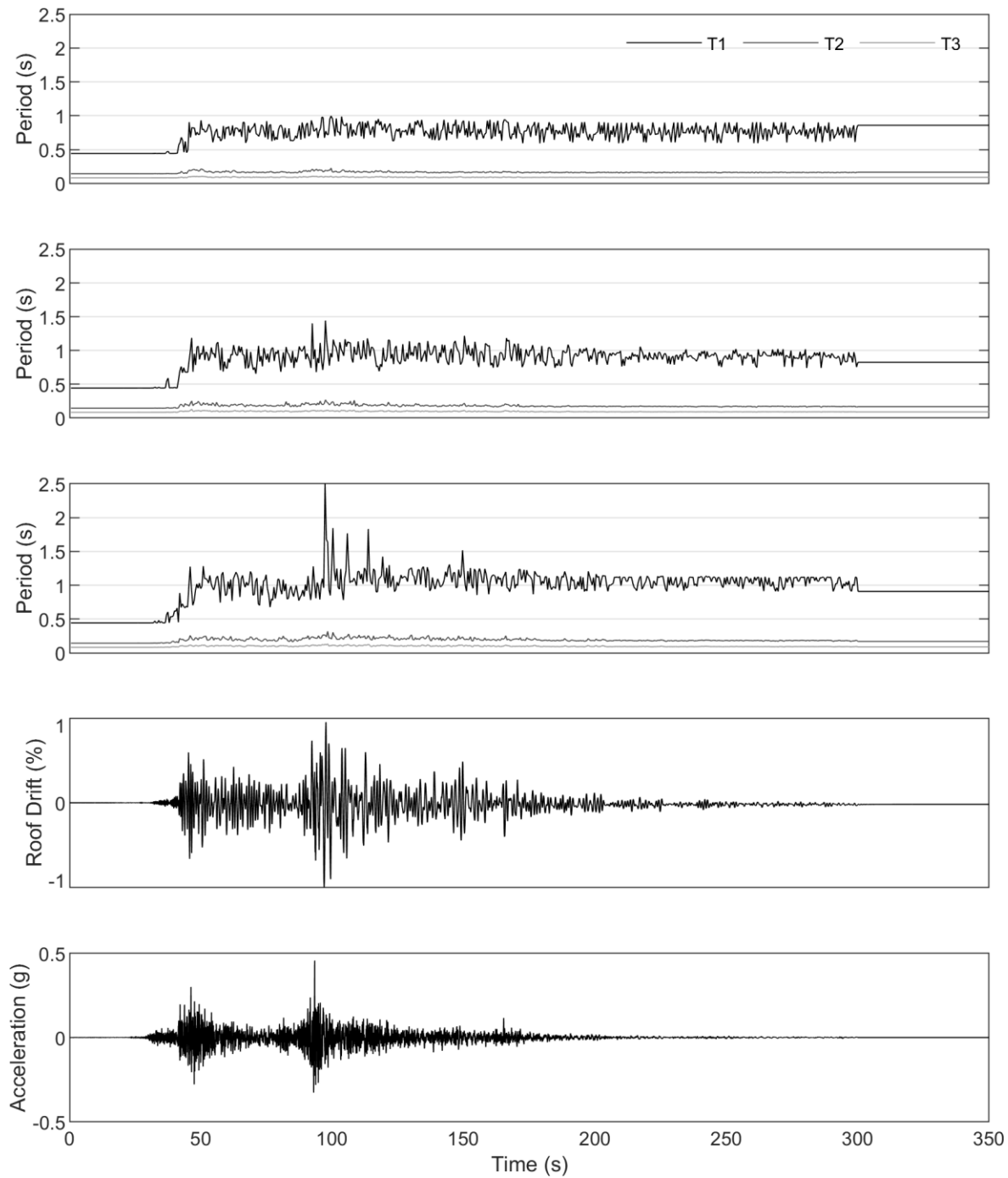


Figure B.1 First three periods of 6 story RC shear wall model subjected to the Tohoku-MYG009 NS ground motion; from top to bottom: scaled to 100%, 150%, and 200% ; roof drift time history response under the 200% shaking level; and input acceleration time history scaled to 100% Vancouver 2% in 50 year target UHS.

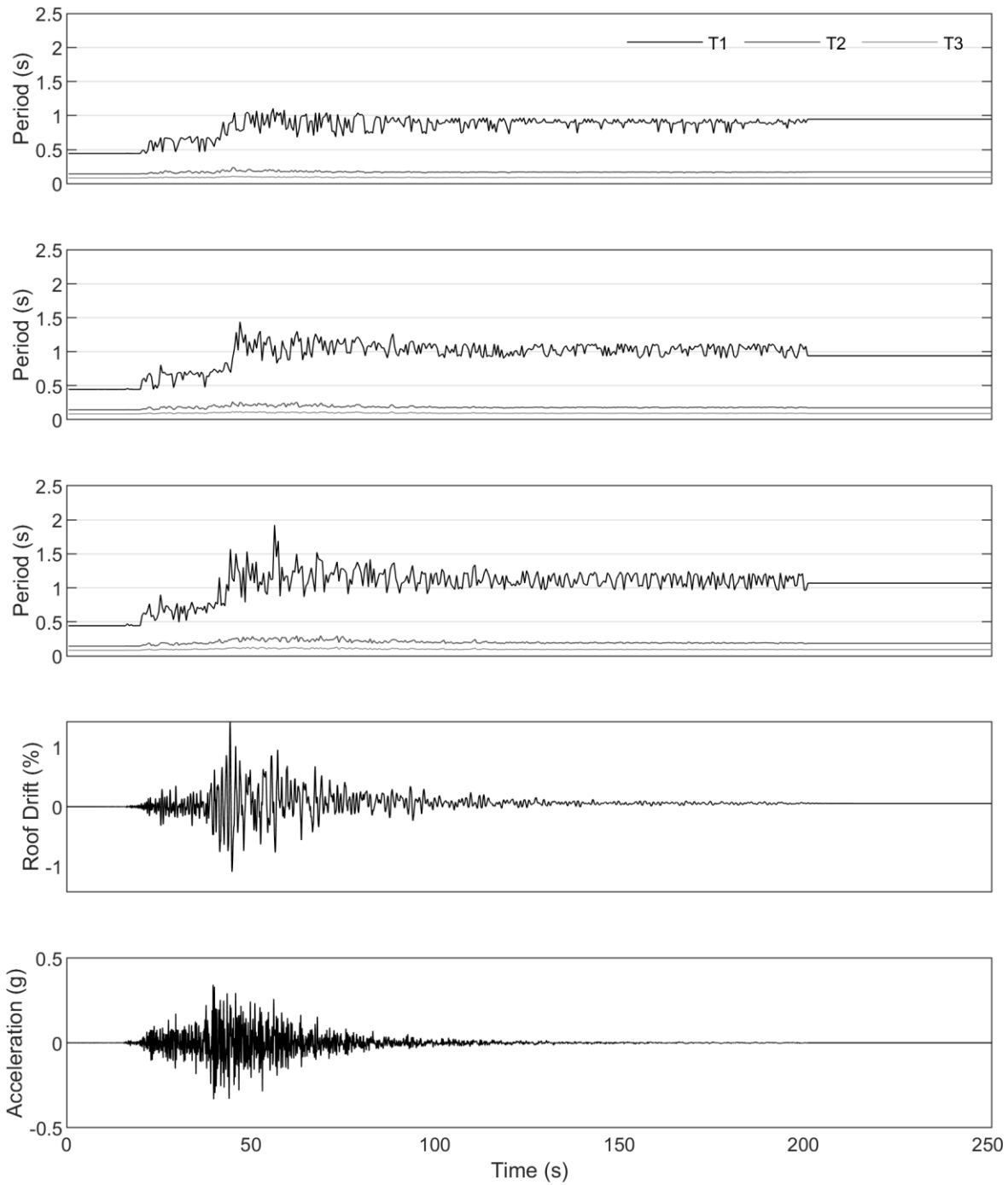


Figure B.2 First three periods of 6 story RC shear wall model subjected to the Hokkaido-HKD125 NS ground motion; from top to bottom: scaled to 100%, 150%, and 200%; roof drift time history response under the 200% shaking level; and input acceleration time history scaled to 100% Vancouver 2% in 50 year target UHS.

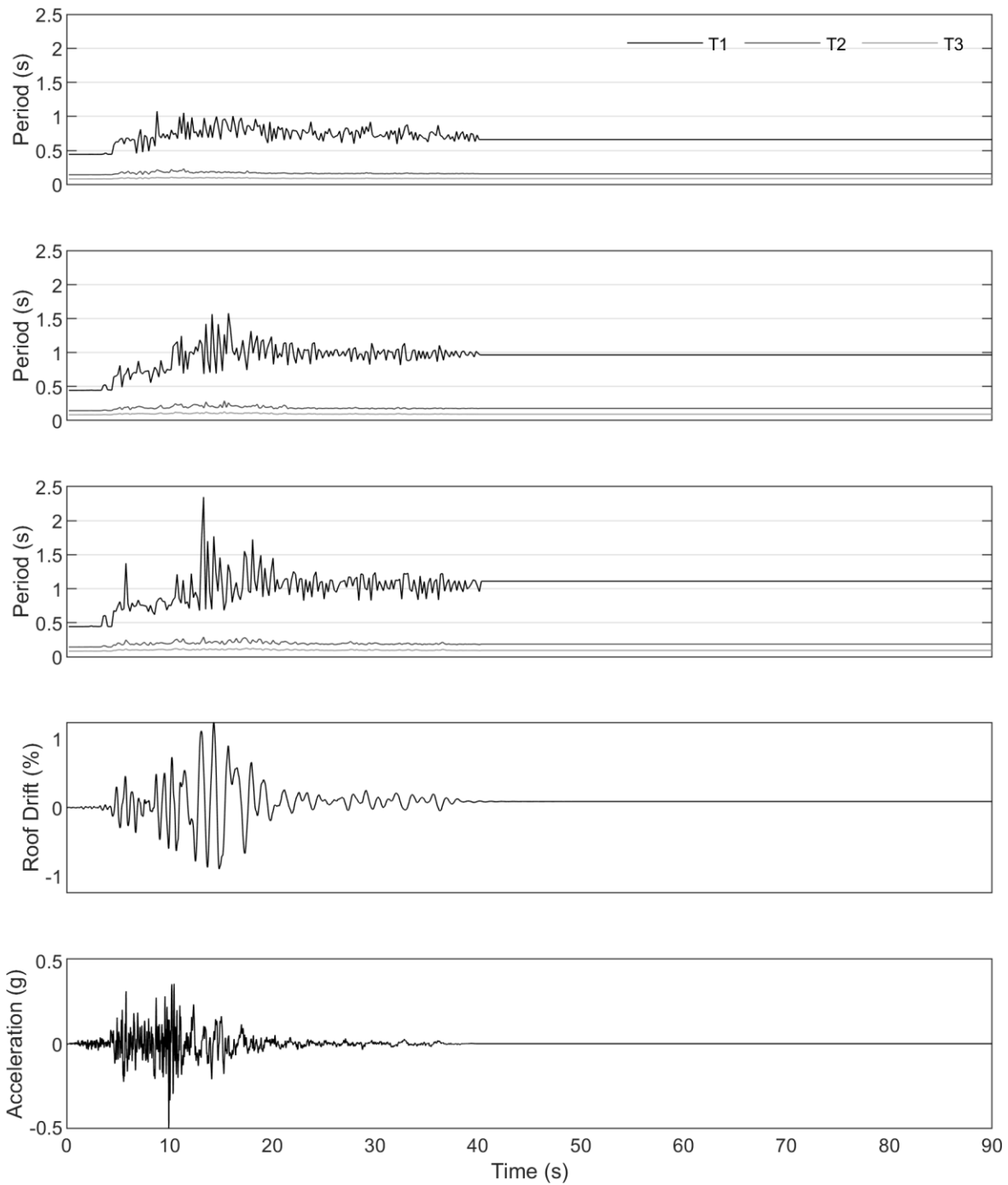


Figure B.3 First three periods of 6 story RC shear wall model subjected to the Northridge-STM360 ground motion; from top to bottom: scaled to 100%, 150%, and 200%; roof drift time history response under the 200% shaking level; and input acceleration time history scaled to 100% Vancouver 2% in 50 year target UHS.

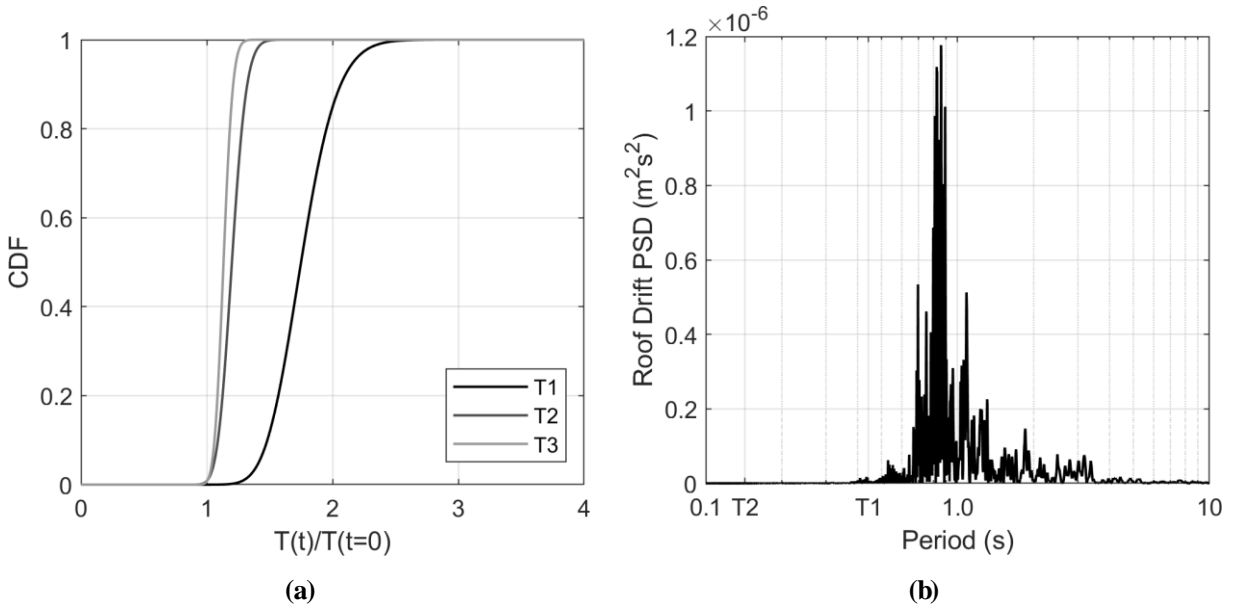


Figure B.4 (a) First three period cumulative distribution function; and, (b) power spectral density of roof drift of 6 story RC shear wall model subjected to the Tohoku-MYG009 NS ground motion scaled to 100%.

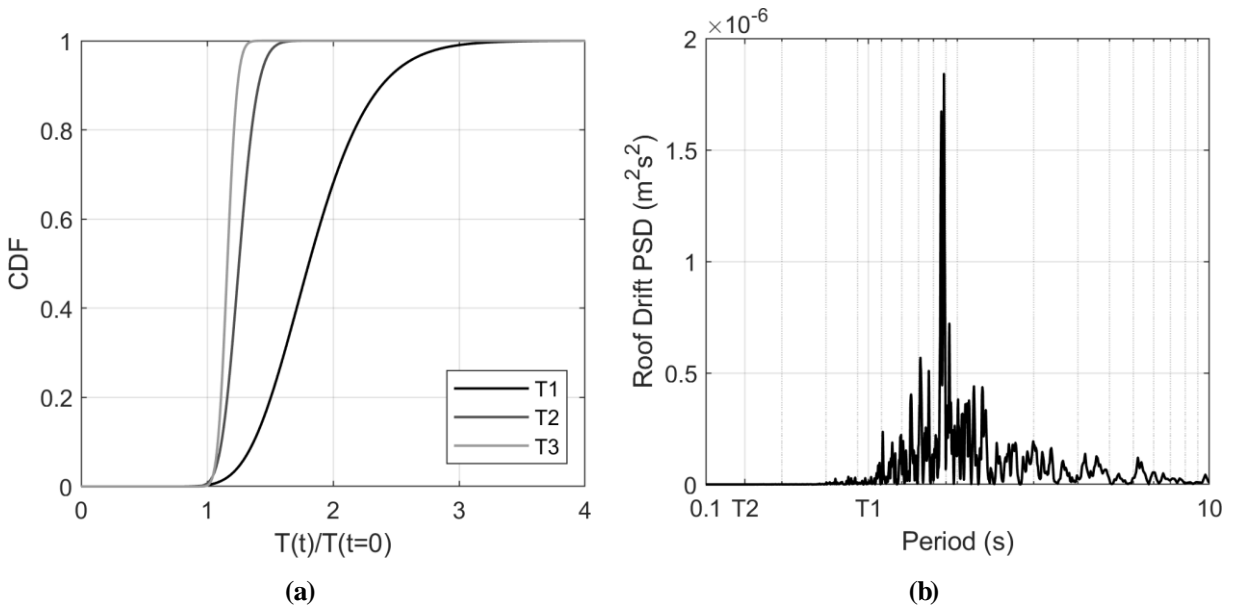


Figure B.5 (a) First three period cumulative distribution function; and, (b) power spectral density of roof drift of 6 story RC shear wall model subjected to the Hokkaido-HKD125 NS ground motion scaled to 100%.

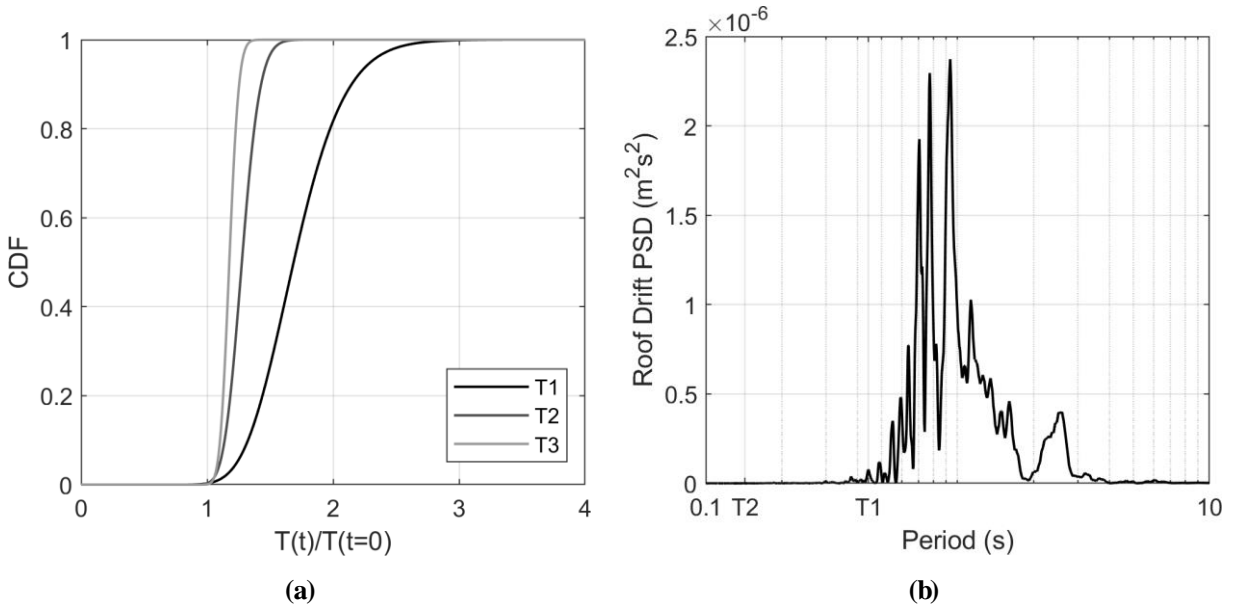


Figure B.6 (a) First three period cumulative distribution function; and, (b) power spectral density of roof drift of 6 story RC shear wall model subjected to the Northridge-STM360 groundmotion scaled to 100%.

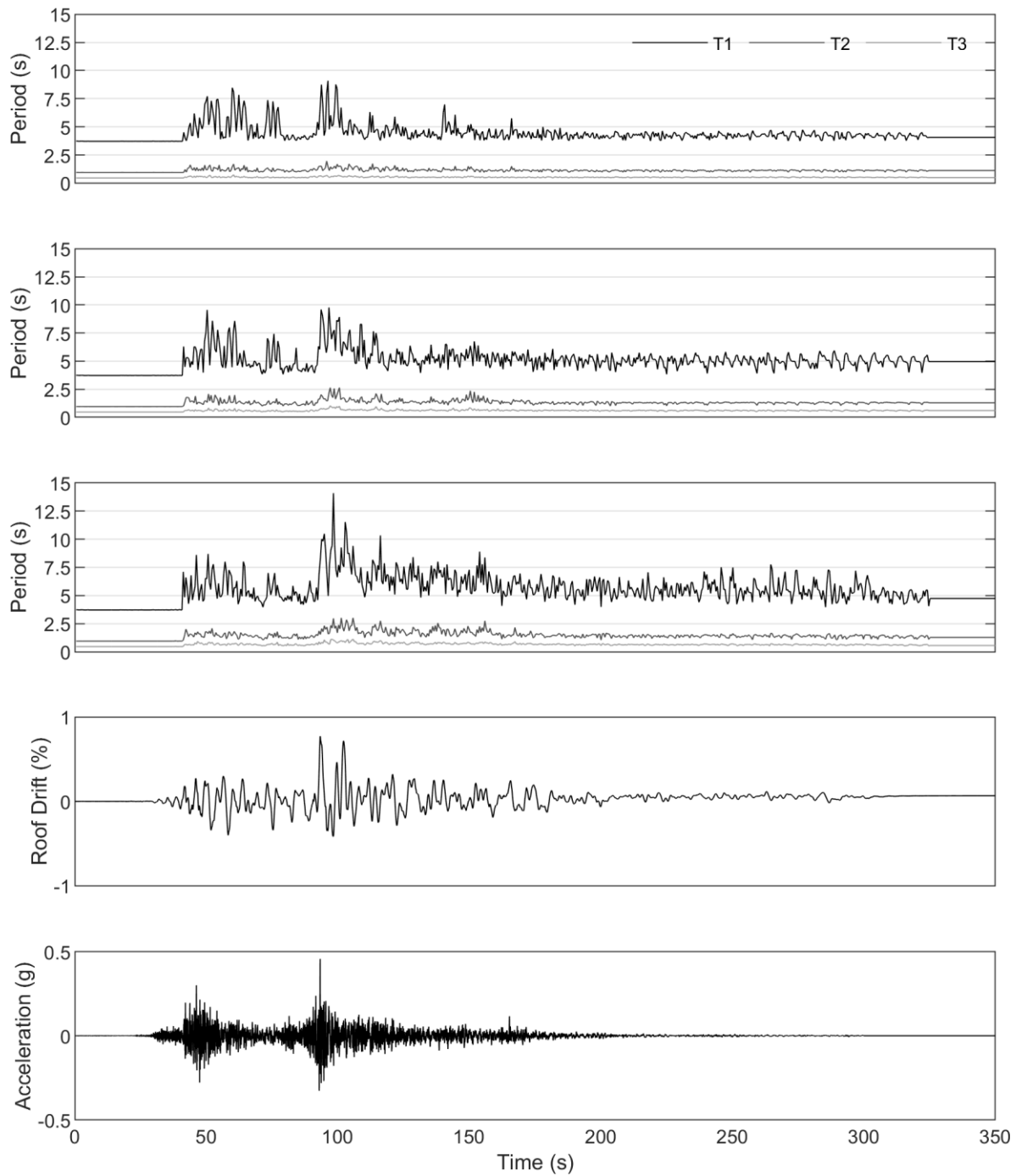


Figure B.7 First three periods of 30 story RC shear wall model subjected to the Tohoku-MYG009 NS ground motion; from top to bottom: scaled to 100%, 150%, and 200%; roof drift time history response under the 200% shaking level; and input acceleration time history scaled to 100% Vancouver 2% in 50 year target UHS.

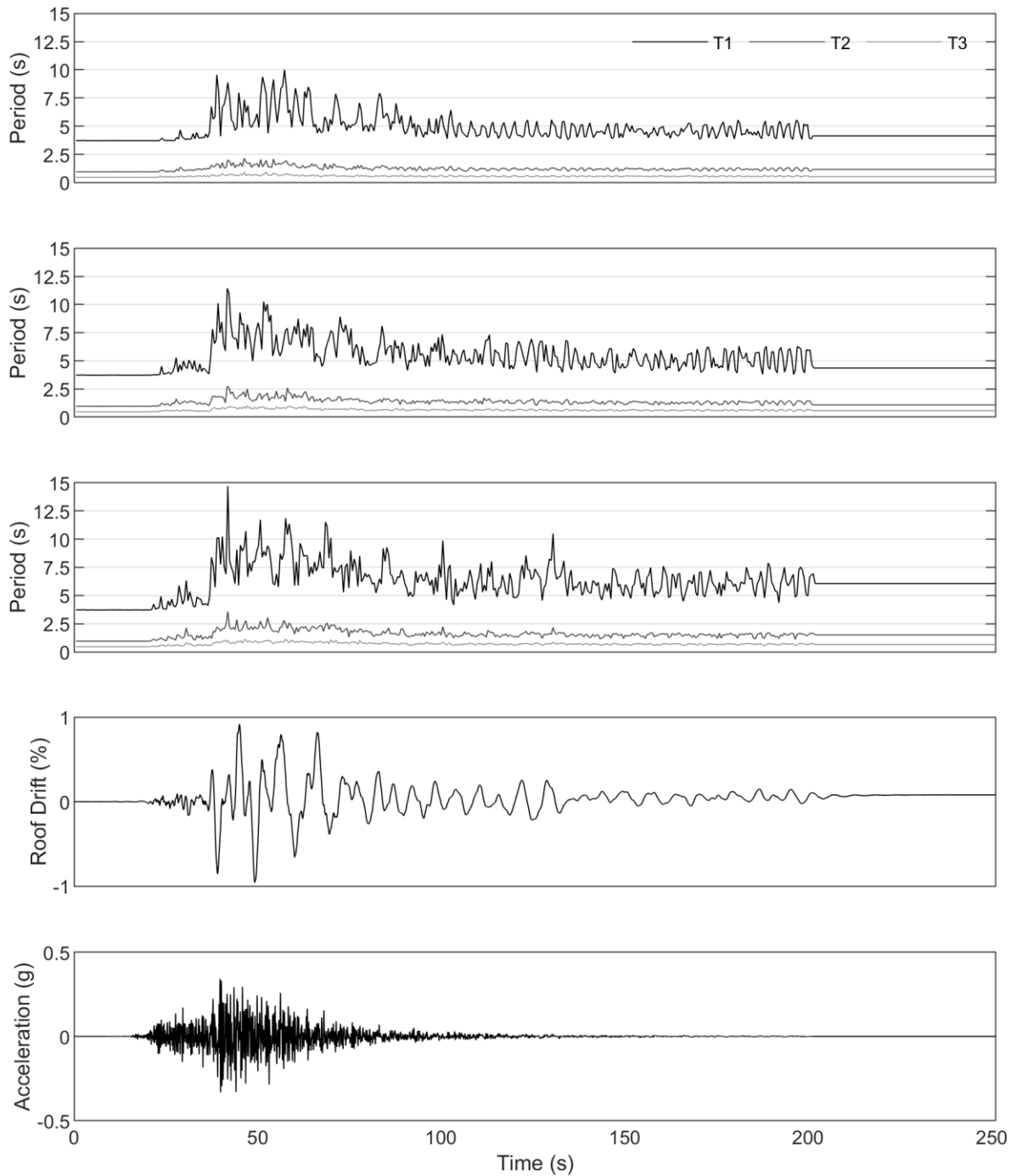


Figure B.8 First three periods of 30 story RC shear wall model subjected to the Hokkaido-HKD125 NS ground motion; from top to bottom: scaled to 100%, 150%, and 200%; roof drift time history response under the 200% shaking level; and input acceleration time history scaled to 100% Vancouver 2% in 50 year target UHS.

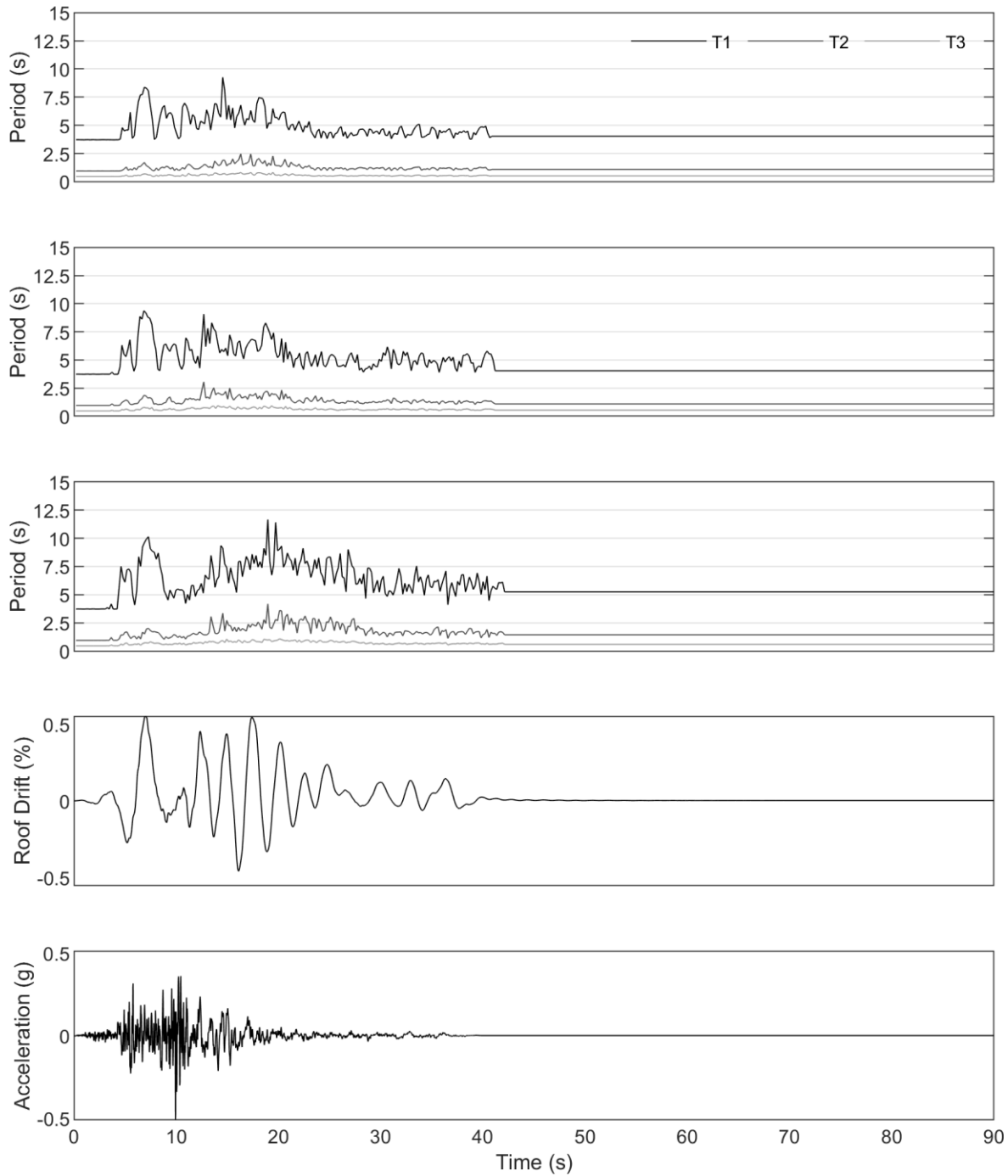


Figure B.9 First three periods of 30 story RC shear wall model subjected to the Northridge-STM360 ground motion; from top to bottom: scaled to 100%, 150%, and 200%; roof drift time history response under the 200% shaking level; and input acceleration time history scaled to 100% Vancouver 2% in 50 year target UHS.

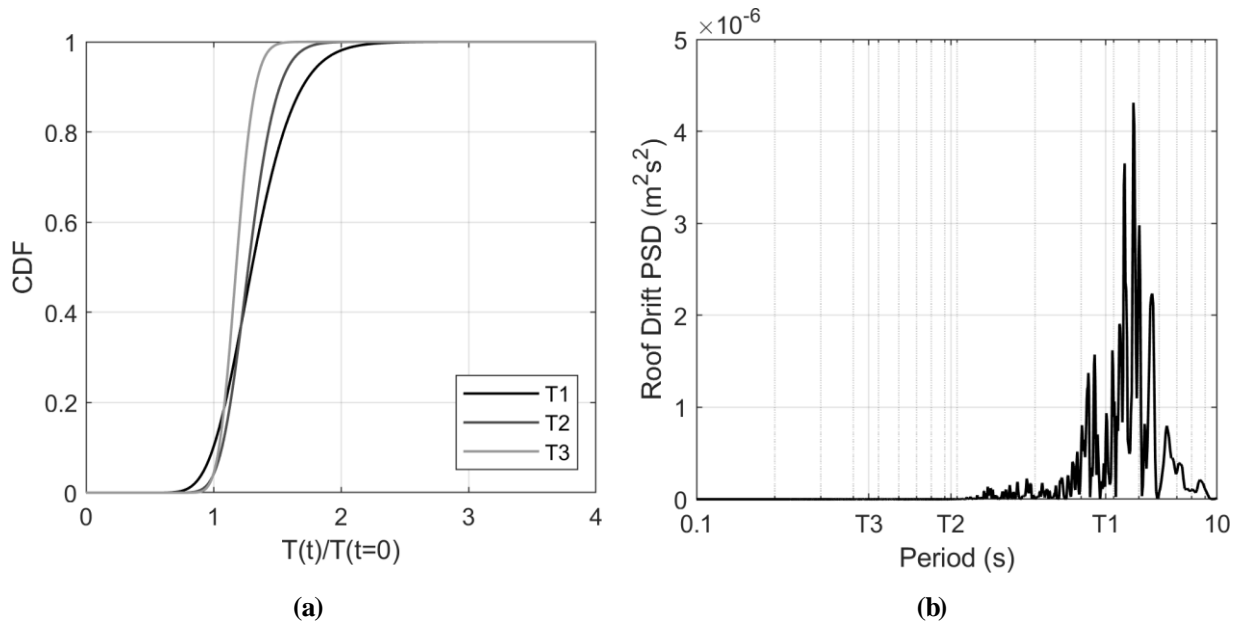


Figure B.10 (a) First three period cumulative distribution function; and, (b) power spectral density of roof drift of 30 story RC shear wall model subjected to the Tohoku-MYG009 NS ground motion scaled to 100%.

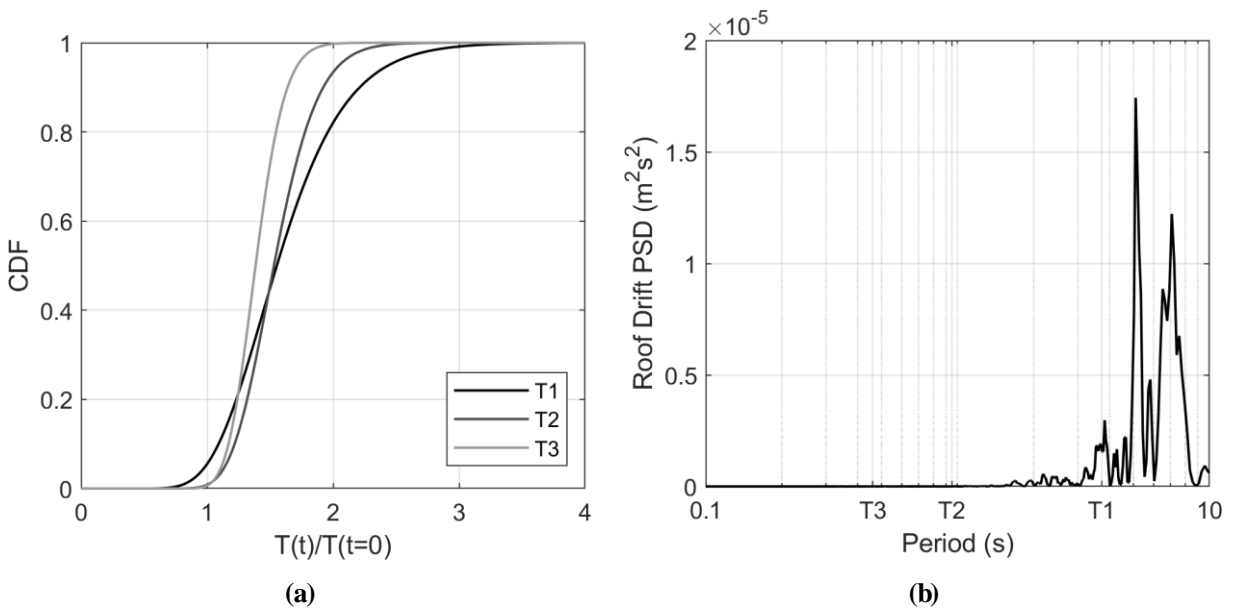


Figure B.11 (a) First three period cumulative distribution function; and, (b) power spectral density of roof drift of 30 story RC shear wall model subjected to the Hokkaido-HKD125 NS ground motion scaled to 100%.

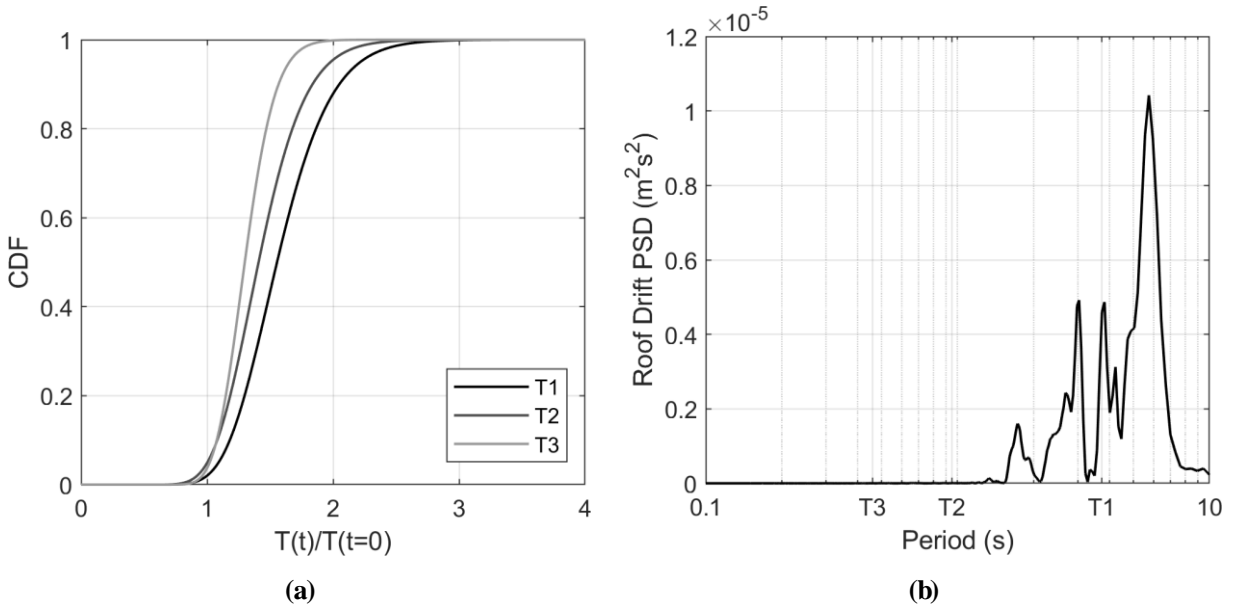


Figure B.12 (a) First three period cumulative distribution function; and, (b) power spectral density of roof drift of 30 story RC shear wall model subjected to the Northridge-STM360 ground motion scaled to 100%.

Appendix C: Flexure-shear Coupling

The models in Chapter 4 utilized fiber sections to model the axial/flexural response of the walls, with elastic, uncoupled shear springs to simulate the shear response. This is generally considered acceptable for approximating the response of slender RC shearwalls and has been used to successfully simulate the response of such walls (ATC, 2010; Orakal and Wallace, 2006). However, fiber section models with uncoupled shear springs may underestimate compression strains at boundary regions (Orakal and Wallace, 2006) and may overestimate the lateral capacity of moderate aspect ratio shearwalls (Kolozvari et al., 2018; Kolozvari and Wallace, 2016).

Kolozvari et al. (2018) developed a shear-flexure interaction (SFI) element model for RC shearwalls by modifying the existing Multiple-Vertical-Line-Element Model (MVLEM). The MVLEM simulates the flexural/axial response of shearwalls, similarly to a fiber element, but with a series of uniaxial macro-fibers connected to rigid element at their top and base, rather than more discretized fibers. The Shear-flexure Interaction Multiple-Vertical-Line-Element Model (SFI-MVLEM) by Kolozvari et al. (2018) replaces the macro-fibers in a MVLEM with 2D RC panels defined by the Fixed-Strut-Angle-Model (FSAM). The FSAM panel element smears 2D stresses over its area and is able to capture the interaction between shear and flexural stresses (Ulugtekin, 2010). The SF-MVLEM has been implemented into OpenSees as the *SFI_MVLEM* element; the FSAM 2D material has been implemented as the *FSAM* material. The *FSAM* takes a steel and a concrete material model as arguments; the *ConcreteCM* uniaxial material is used to define the concrete stress-strain relationship based on the complete model by Chang and Mander (1994); the steel material can be any existing uniaxial material.

To see if SFI in the shearwalls would have affected the results of the previous sections, the 18 story model was modified by replacing the fiber elements with *SFI-MVLEM* elements, while

holding all other aspects constant. The wall boundary elements were modelled with six layers, with the exterior layers using an unconfined concrete material model and the other four layers using a confined concrete model. The other portions of the wall were modelled with six layers of unconfined concrete. The transverse and longitudinal steel is smeared across each layer based on the percentage of reinforcement in each direction.

The steel reinforcement model remained unchanged from the previous model iteration (see Figure 4.6c). The *ConcreteCM* material model was used to model concrete with the same stress-strain relationship as the previous concrete models (see Figure 4.6a and b). The Tsai (1988) shape parameter - used to define the post yielding shape of the relationship - was set to 4 for confined concrete, 11 for unconfined concrete, and 1.2 for concrete in tension. The parameters were chosen to try to best mimic the behavior of the previous *Concrete02* concrete models (see Figure 4.6a and b). These new material models are illustrated in Figure C.1.

The modified 18 story model was subjected to NTHA using three of the SHORT records and three of the LONG records from Chapter 4, as summarized in Table C.1. The analyses were run at the 100% and 150% shaking levels to see if the difference in behavior was dependent on the degree of nonlinearity (the larger shaking level to induce more nonlinearity in the wall elements). The roof drift time histories of the models subjected to the 6 ground motions are presented in Figure C.2 to Figure C.7. In general, both models behaved similarly, with peak roof drifts of the SFI_MLVEM model within 85-110% of those from the fiber model. This implies that the fiber elements, even without SFI, were adequate for predicting the building behavior.

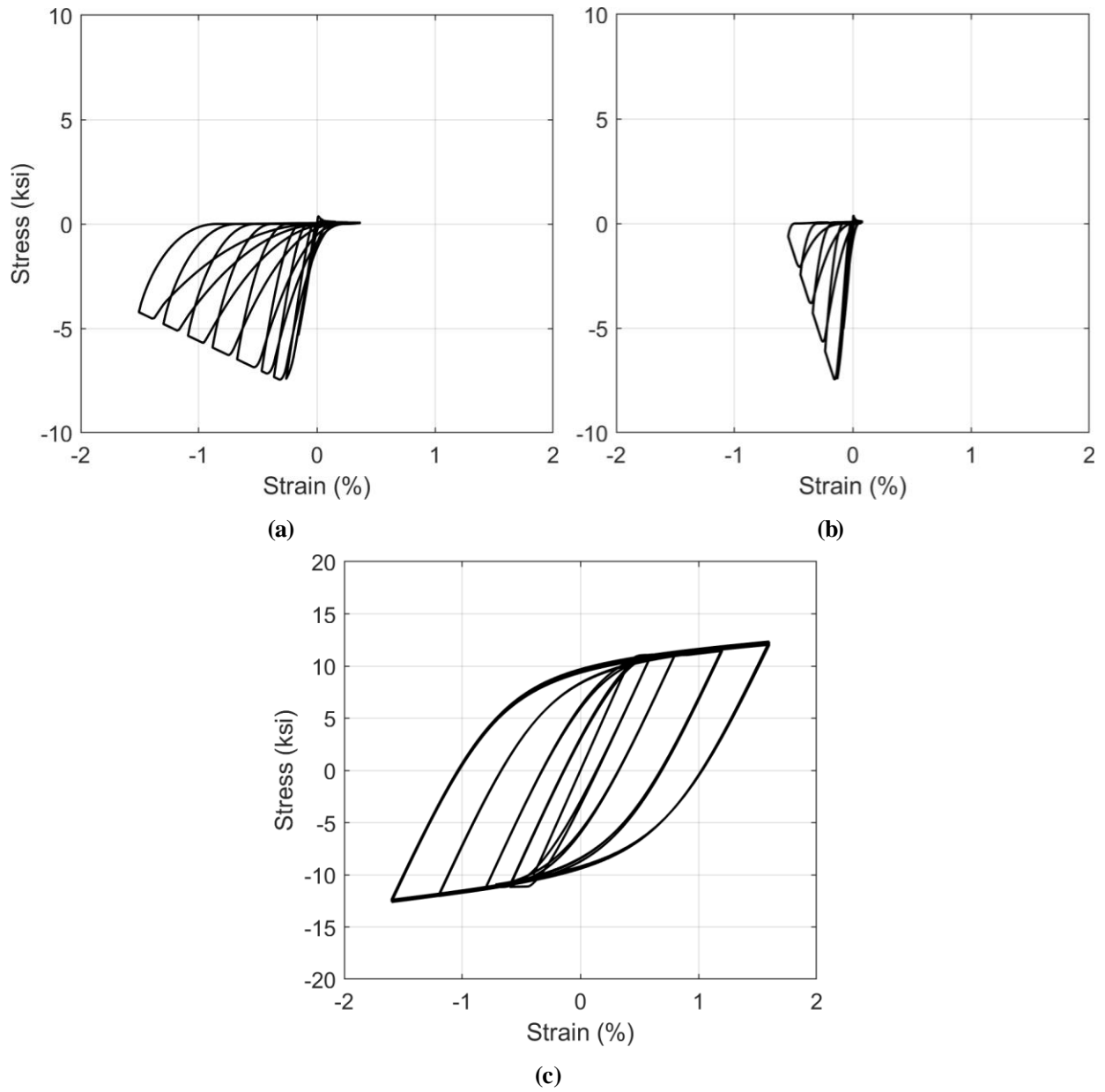
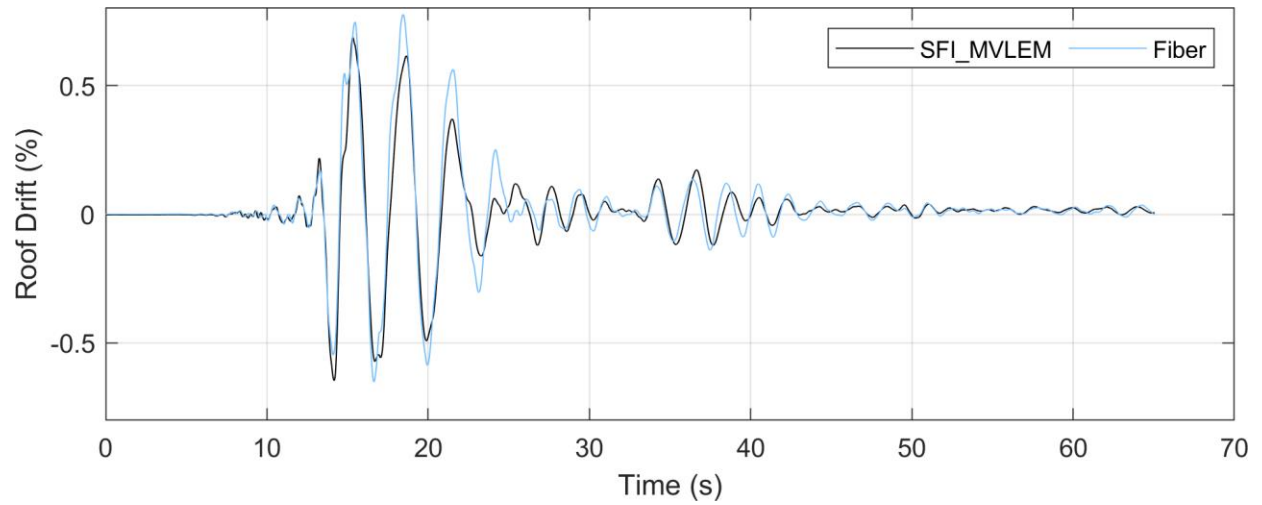


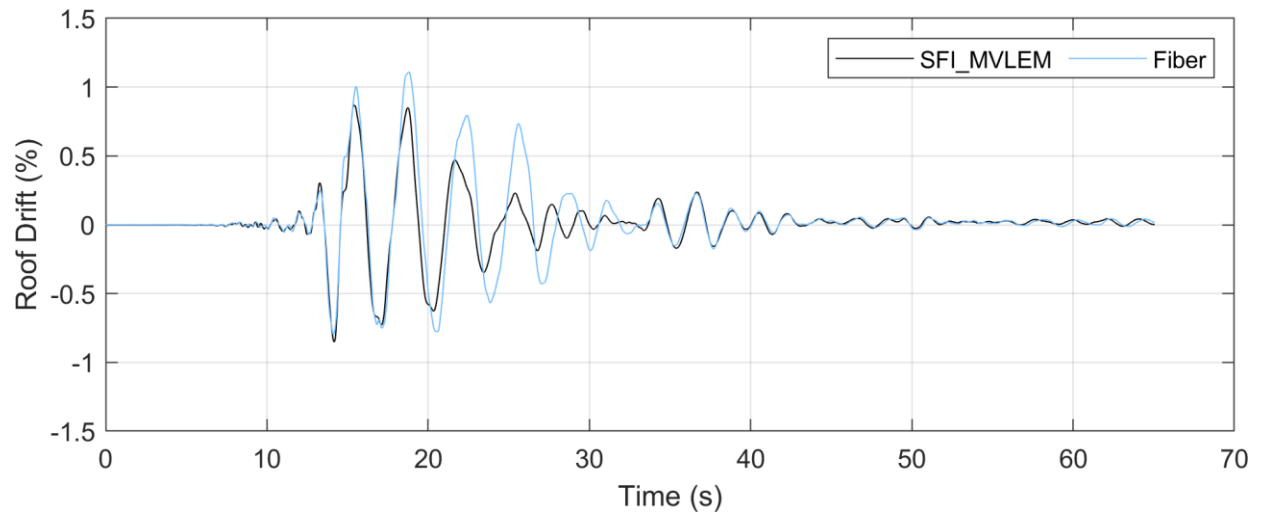
Figure C.1 Material models: 1) confined concrete (*ConcreteCM*); b) unconfined concrete (*ConcreteCM*); c) steel (*ReinforcingSteel*).

Event	Record	Type	Magnitude (M_w)	Year
Chi-Chi, Taiwan	CHY028	SHORT	6.3	1999
Northridge, Ca.	CCN090	SHORT	6.7	1994
Superstition Hills, Ca.	PTS315	SHORT	6.5	1987
Tohoku, Japan	TKY016	LONG	9.1	2011
Hokkaido, Japan	HKD127	LONG	8.0	2003
Kobe, Japan	SKI000	LONG	6.9	1995

Table C.1 Long and short duration records selected for SFI vs fiber element study.

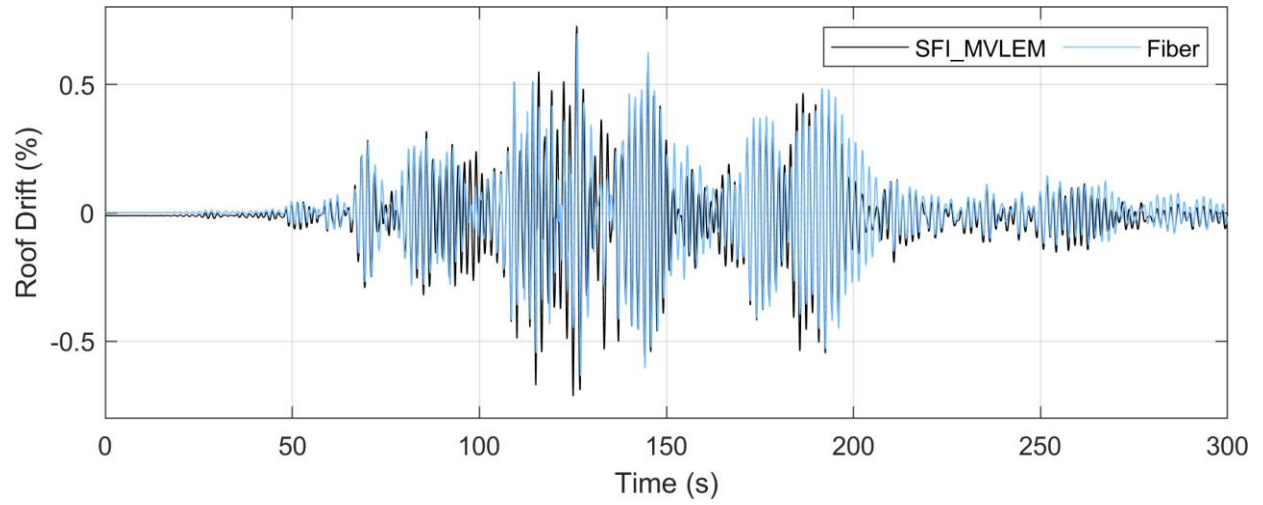


(a)

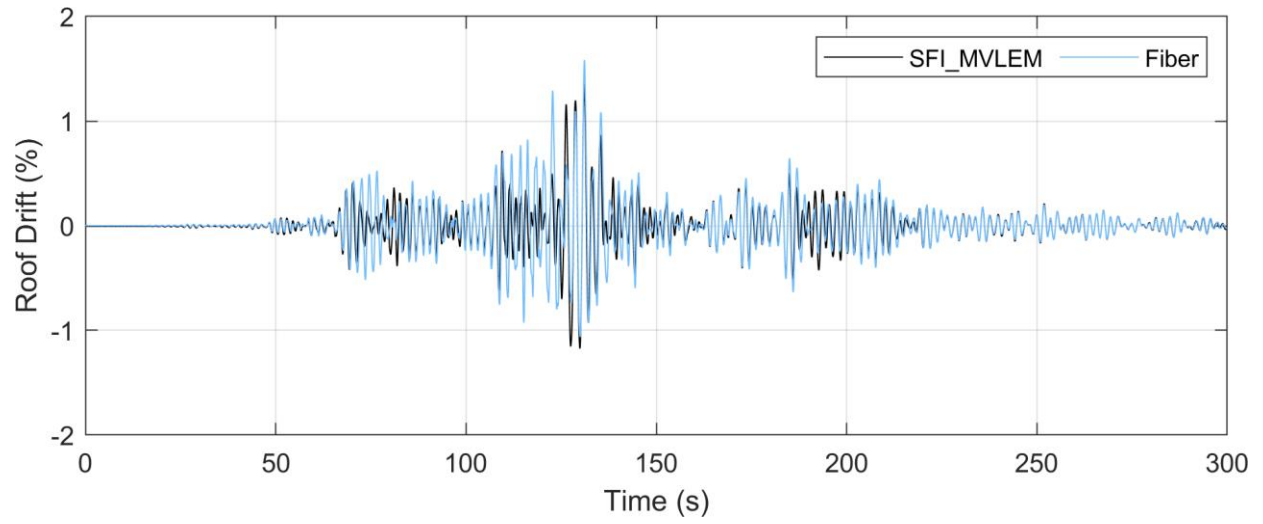


(b)

Figure C.2 Roof drift time history responses of the SFI_MVLEM and Fiber models subjected to the Chi-Chi CHY028 record at: a) 100% shaking level; and, b) 150% shaking level.

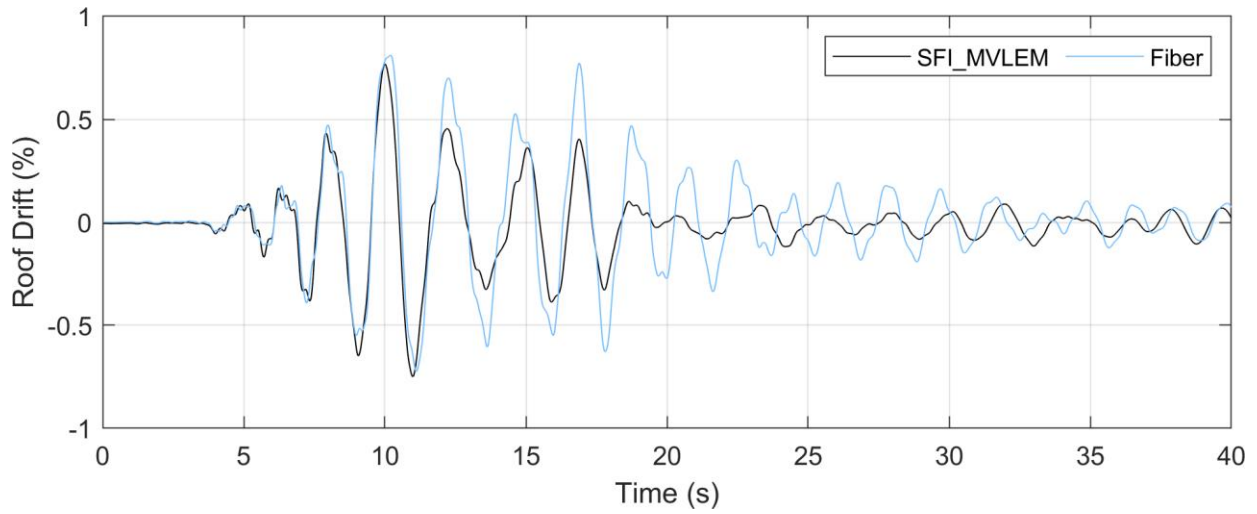


(a)

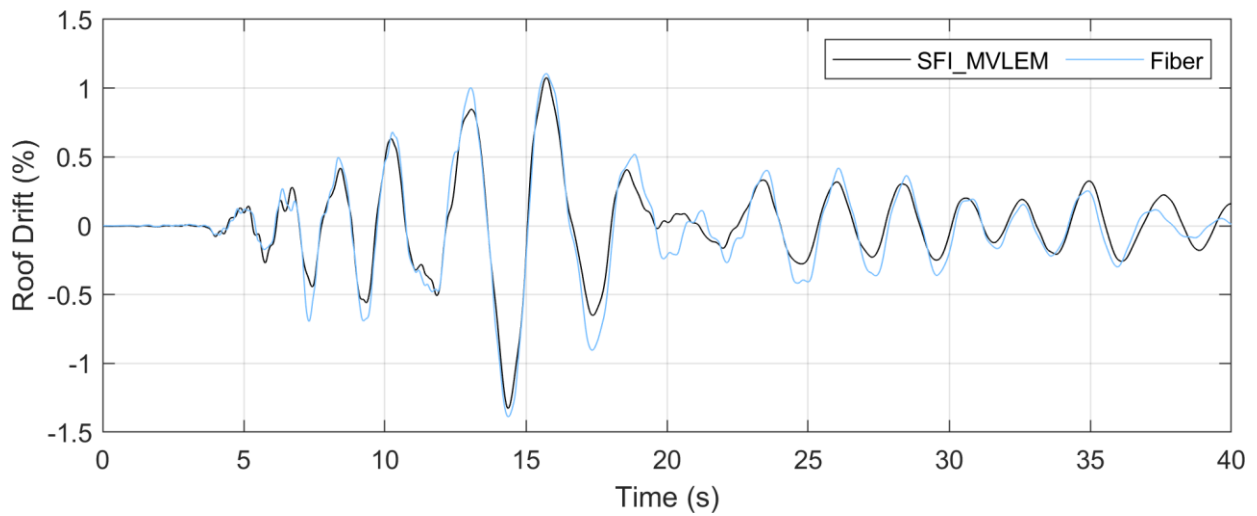


(b)

Figure C.3 Roof drift time history responses of the SFI_MVLEM and Fiber models subjected to the Tohoku TKY016 record at 100% shaking level.

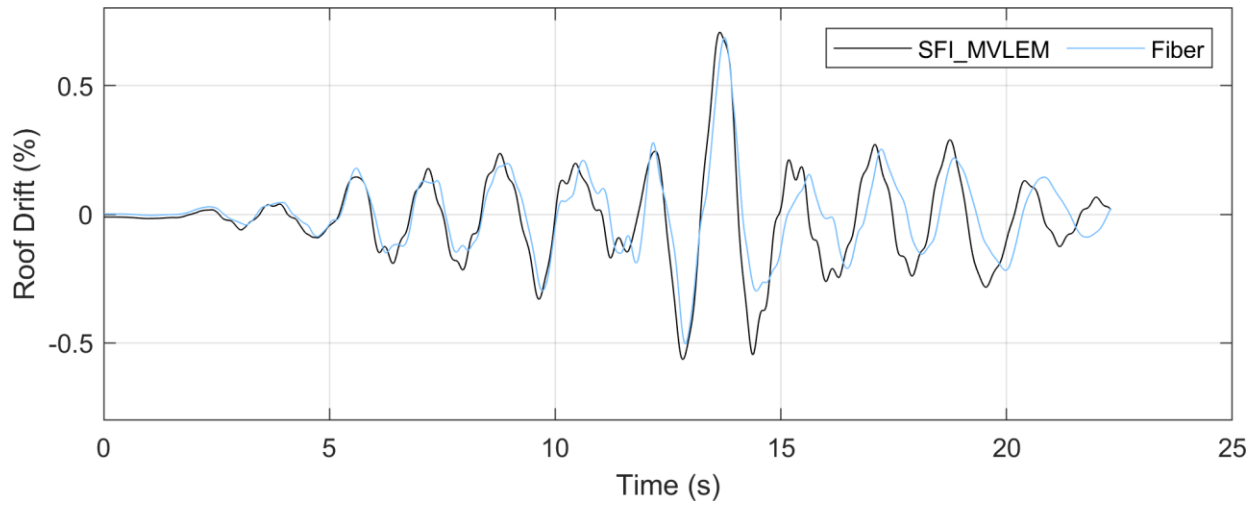


(a)

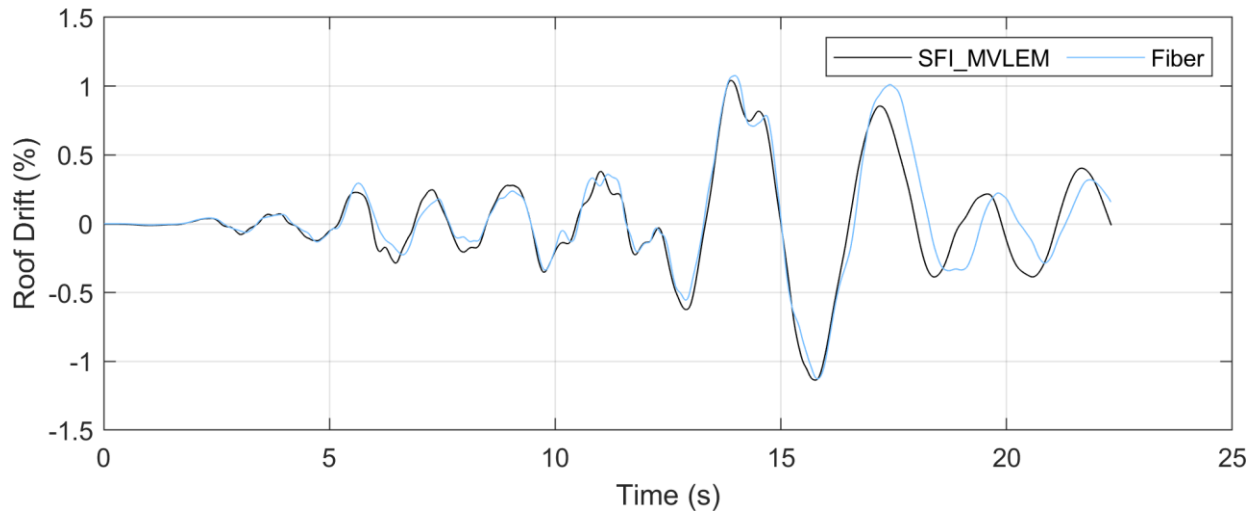


(b)

Figure C.4 Roof drift time history responses of the SFI_MVLEM and Fiber models subjected to the Northridge CCN090 record at: a) 100% shaking level; and, b) 150% shaking level.

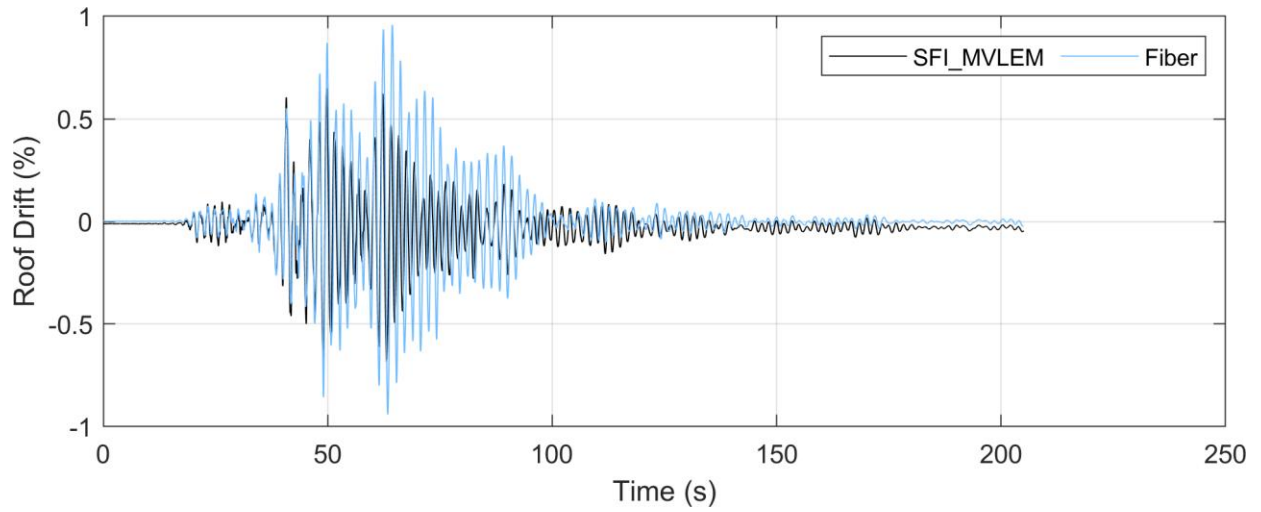


(a)

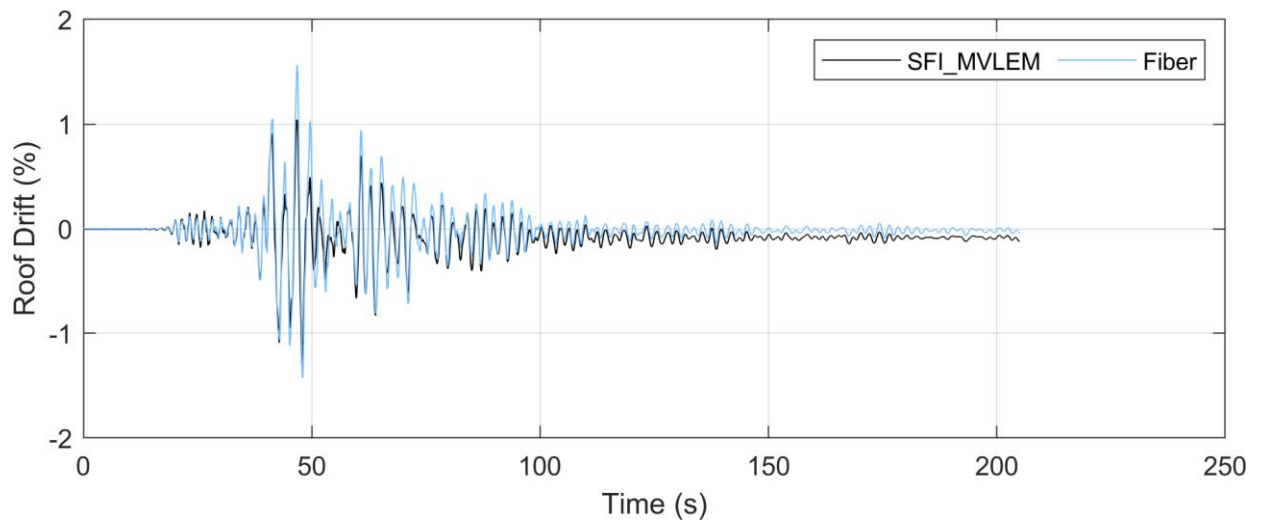


(b)

Figure C.5 Roof drift time history responses of the SFI_MVLEM and Fiber models subjected to the Superstition Hills PTS315 record at: a) 100% shaking level; and, b) 150% shaking level.

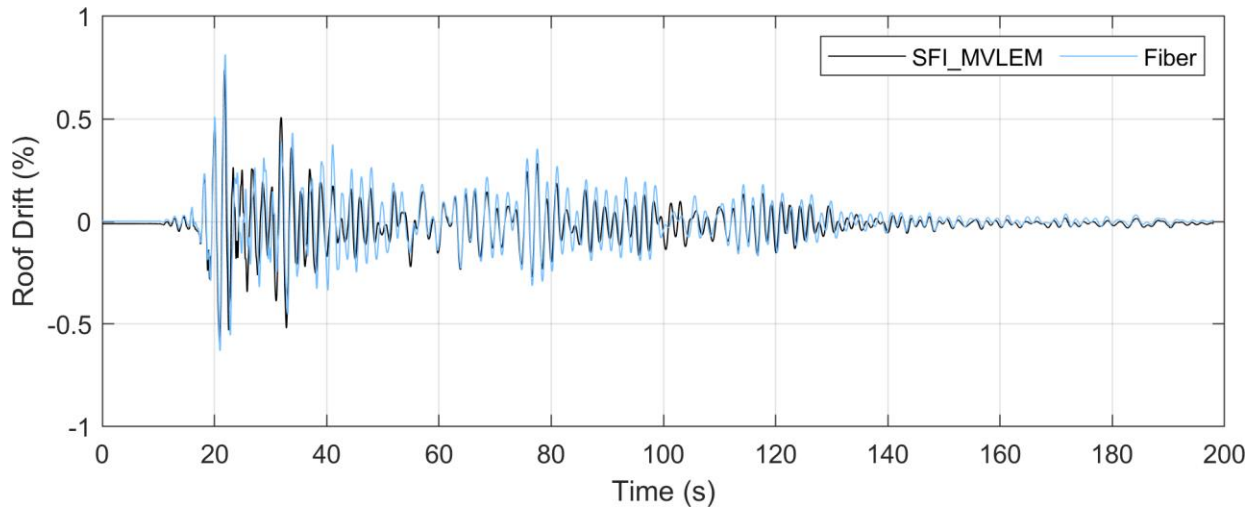


(a)

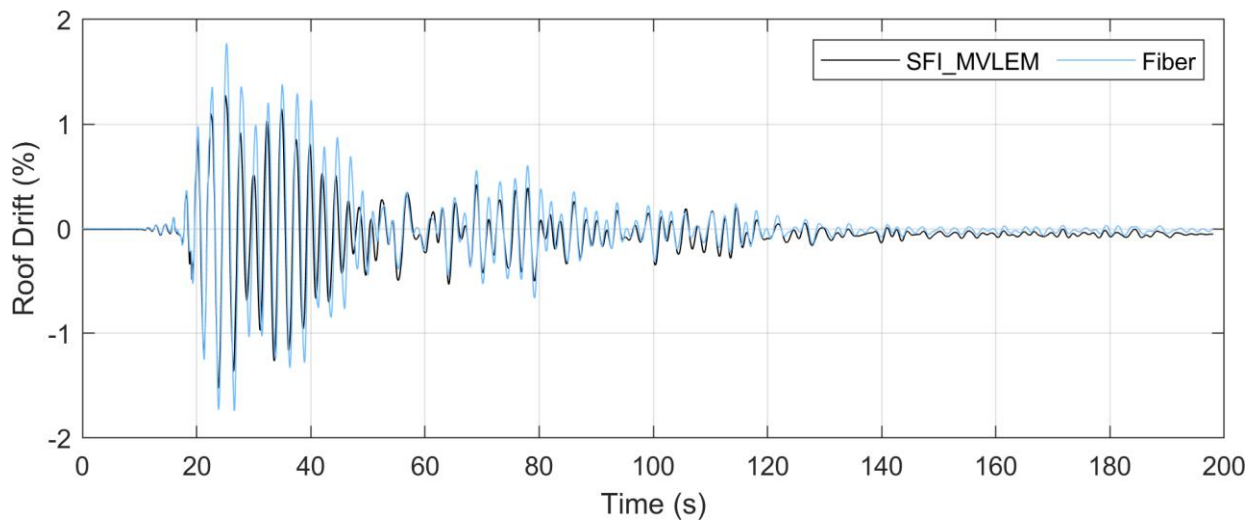


(b)

Figure C.6 Roof drift time history responses of the SFI_MVLEM and Fiber models subjected to the Hokkaido HKD127 record at: a) 100% shaking level; and, b) 150% shaking level.



(a)



(b)

Figure C.7 Roof drift time history responses of the SFI_MVLEM and Fiber models subjected to the Kobe SKI000 record at: a) 100% shaking level; and, b) 150% shaking level.

Appendix D: Additional Code-level Analysis Results for 2D Models

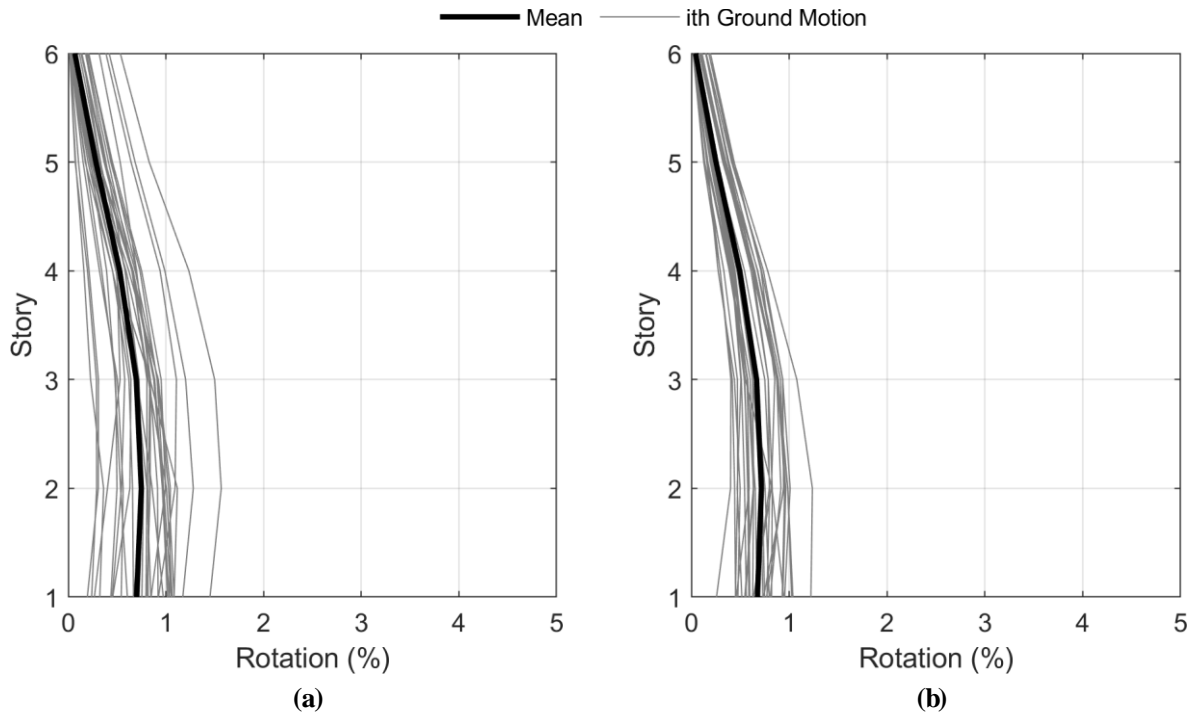


Figure D.1 Coupling beam rotation results for the 6 story model at the code shaking level for (a) the long duration suite and (b) the short duration suite.

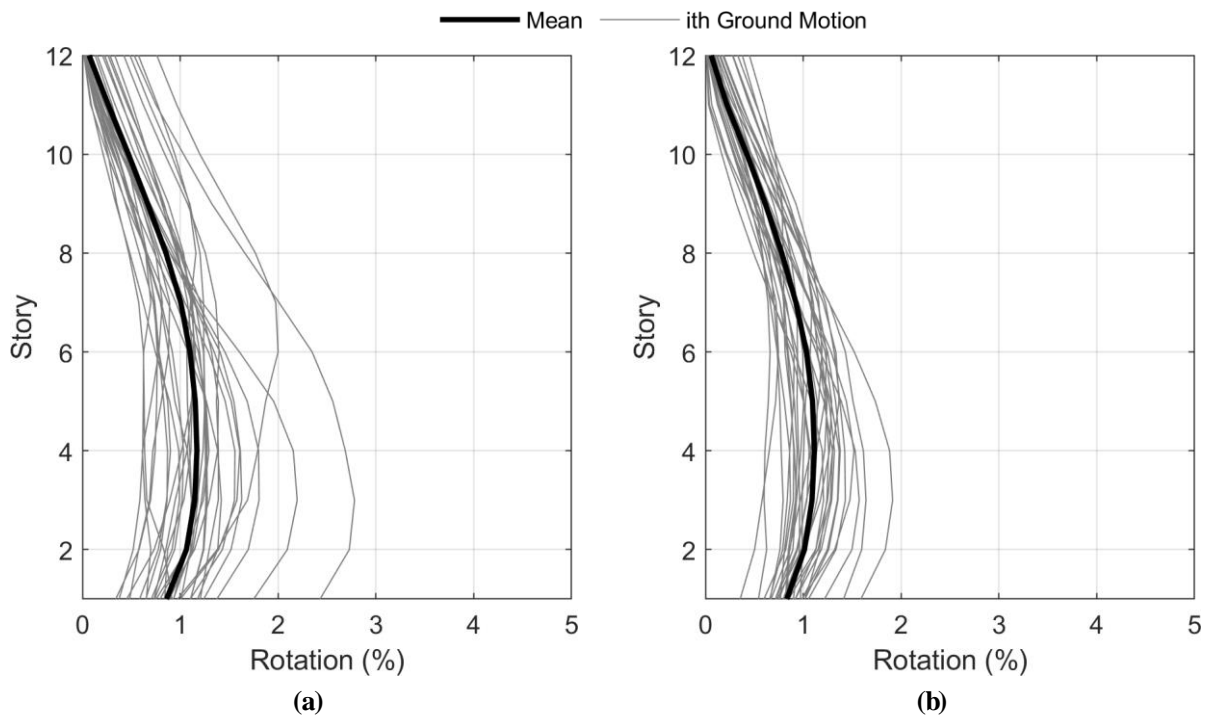


Figure D.2 Coupling beam rotation results for the 12 story model at the code shaking level for (a) the long duration suite and (b) the short duration suite.

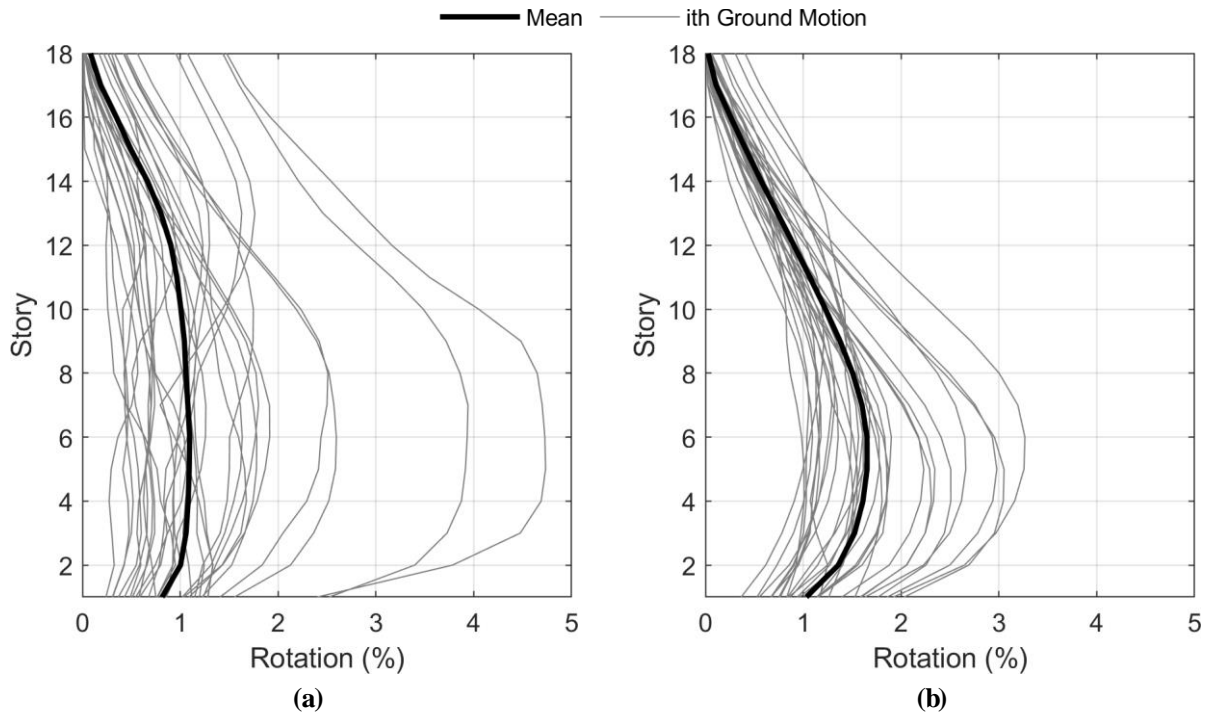


Figure D.3 Coupling beam rotation results for the 18 story model at the code shaking level for (a) the long duration suite and (b) the short duration suite.

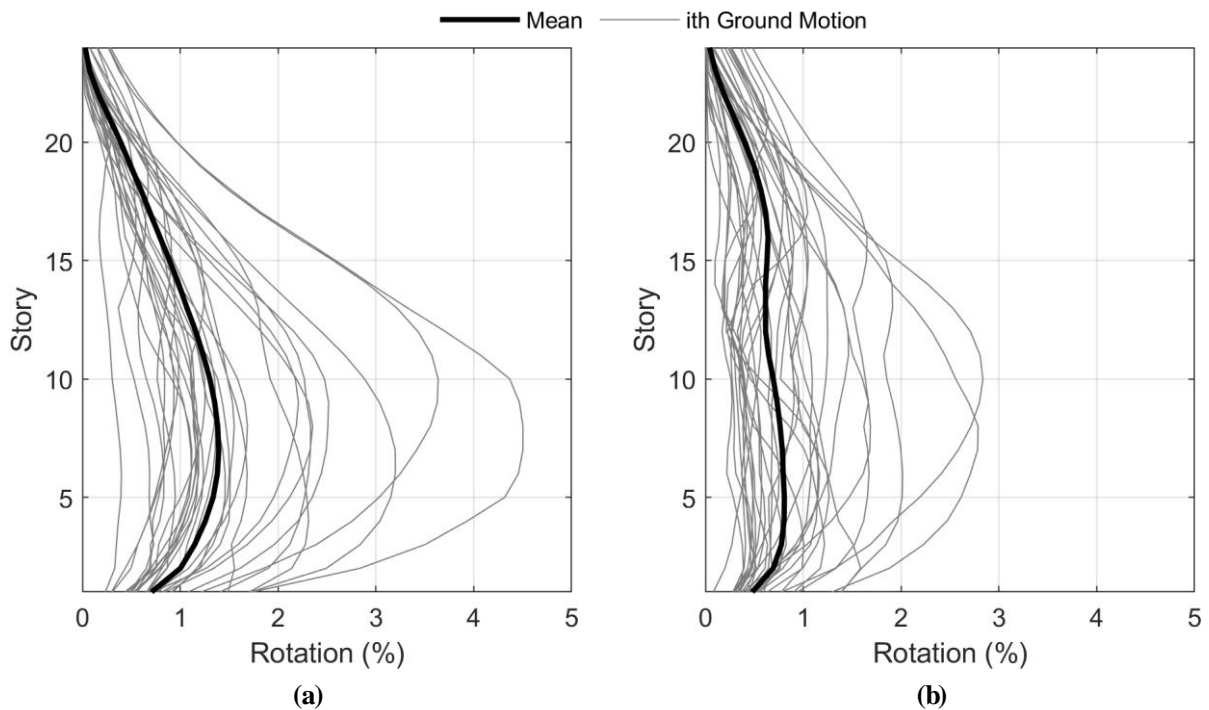


Figure D.4 Coupling beam rotation results for the 24 story model at the code shaking level for (a) the long duration suite and (b) the short duration suite.

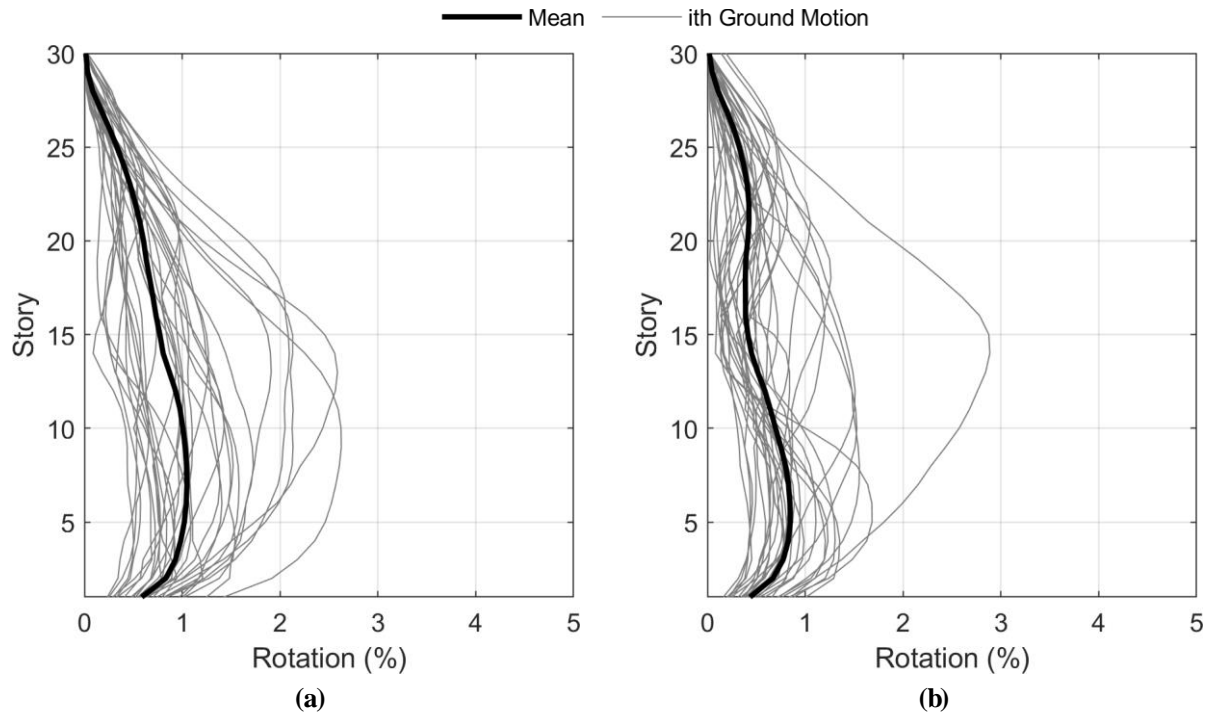


Figure D.5 Coupling beam rotation results for the 30 story model at the code shaking level for (a) the long duration suite and (b) the short duration suite.

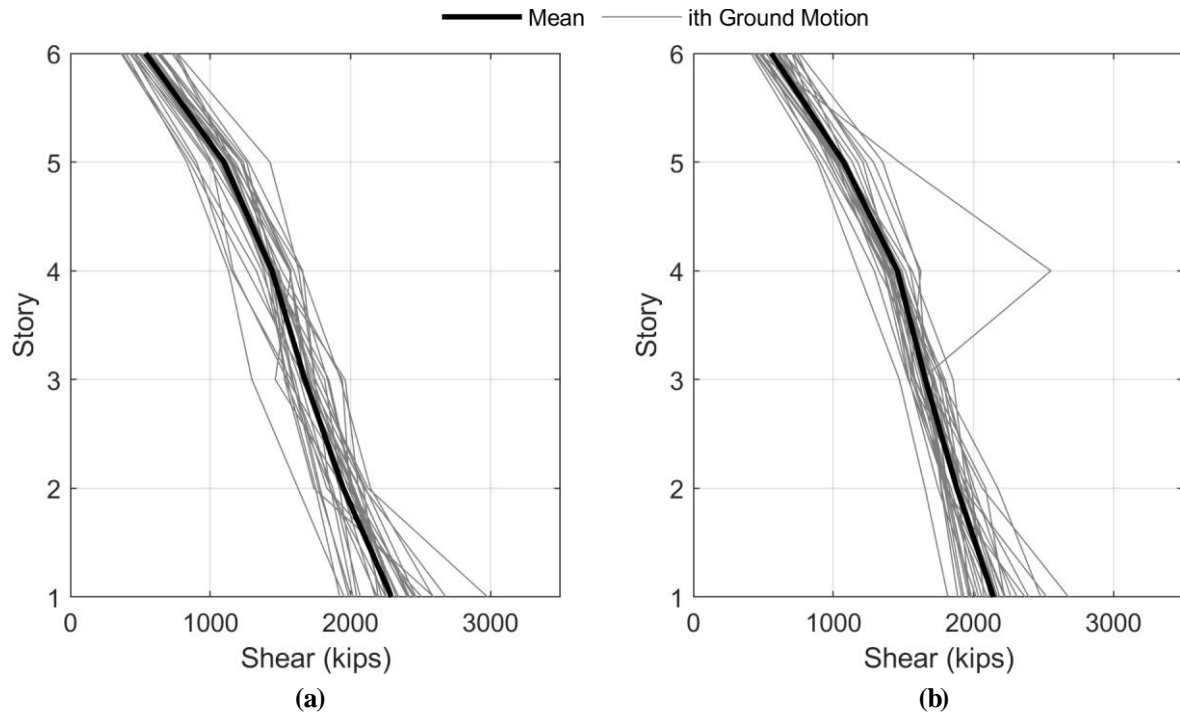


Figure D.6 Story shear results for the 6 story model at the code shaking level for (a) the long duration suite and (b) the short duration suite.

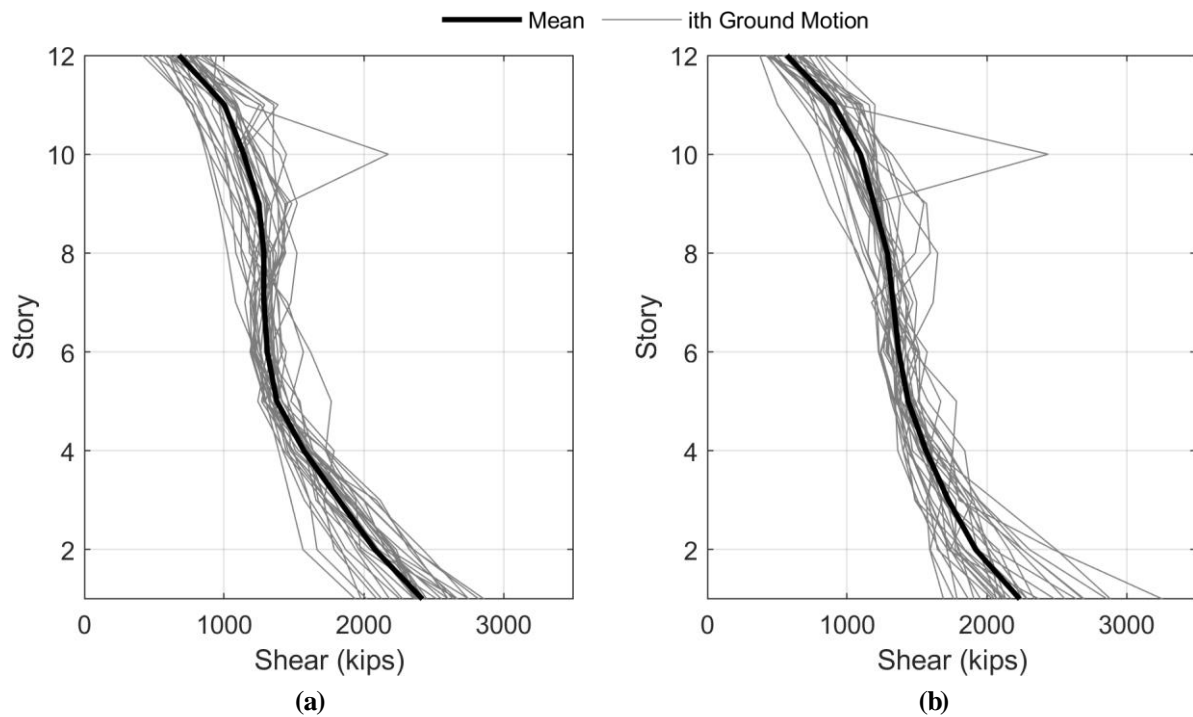


Figure D.7 Story shear results for the 12 story model at the code shaking level for (a) the long duration suite and (b) the short duration suite.

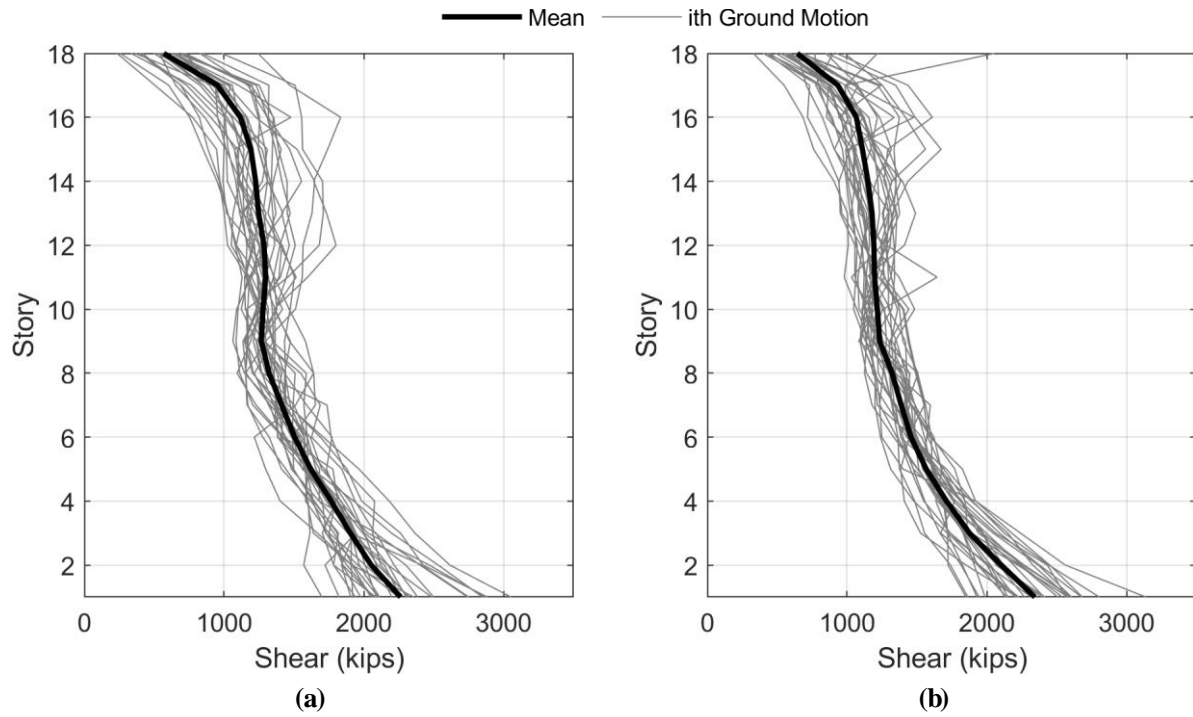


Figure D.8 Story shear results for the 18 story model at the code shaking level for (a) the long duration suite and (b) the short duration suite.

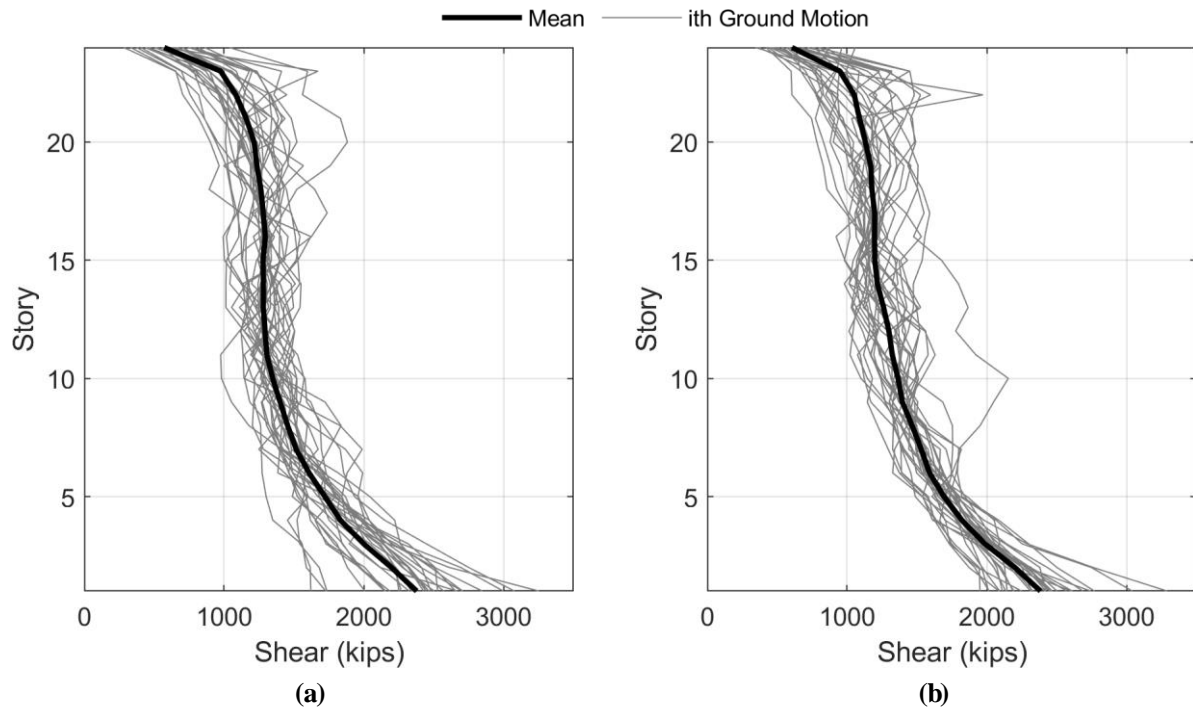


Figure D.9 Story shear results for the 24 story model at the code shaking level for (a) the long duration suite and (b) the short duration suite.

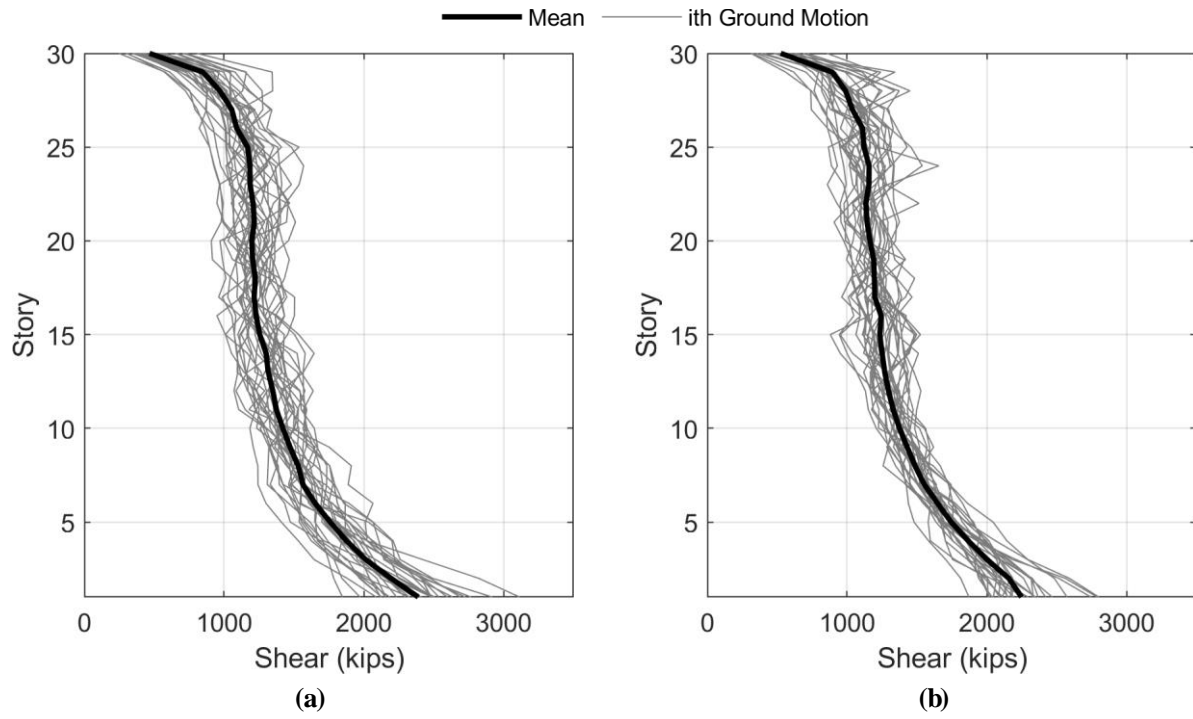


Figure D.10 Story shear results for the 30 story model at the code shaking level for (a) the long duration suite and (b) the short duration suite.

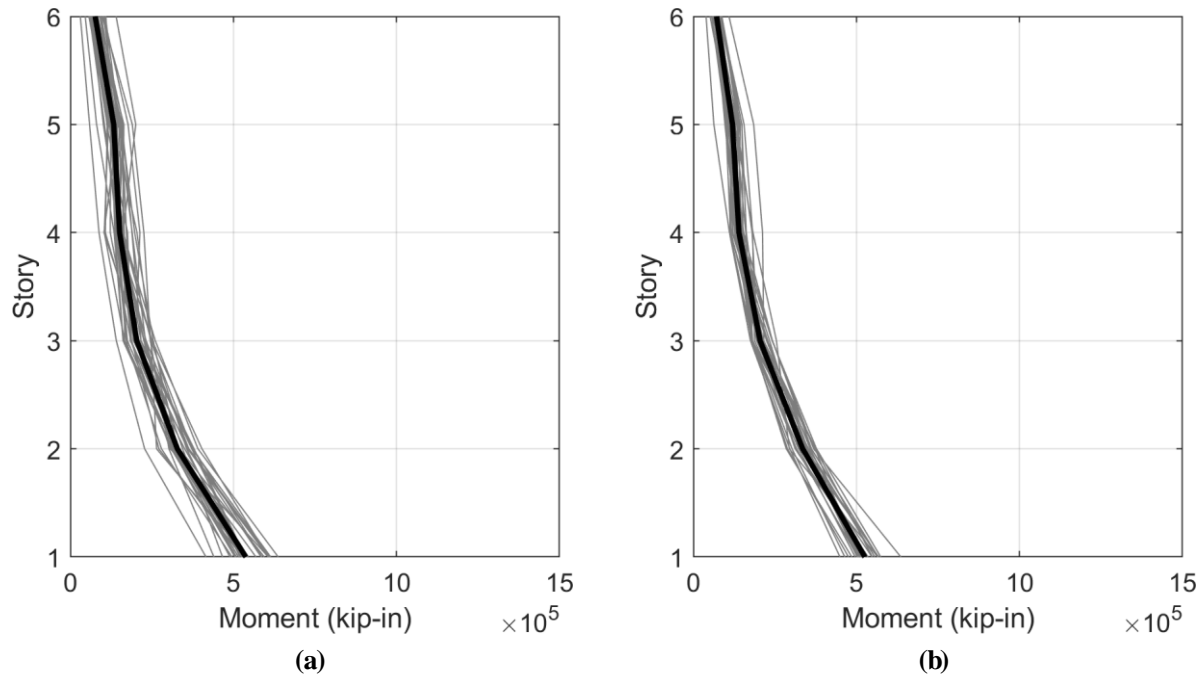


Figure D.11 Story moment results for the 6 story model at the code shaking level for (a) the long duration suite and (b) the short duration suite.

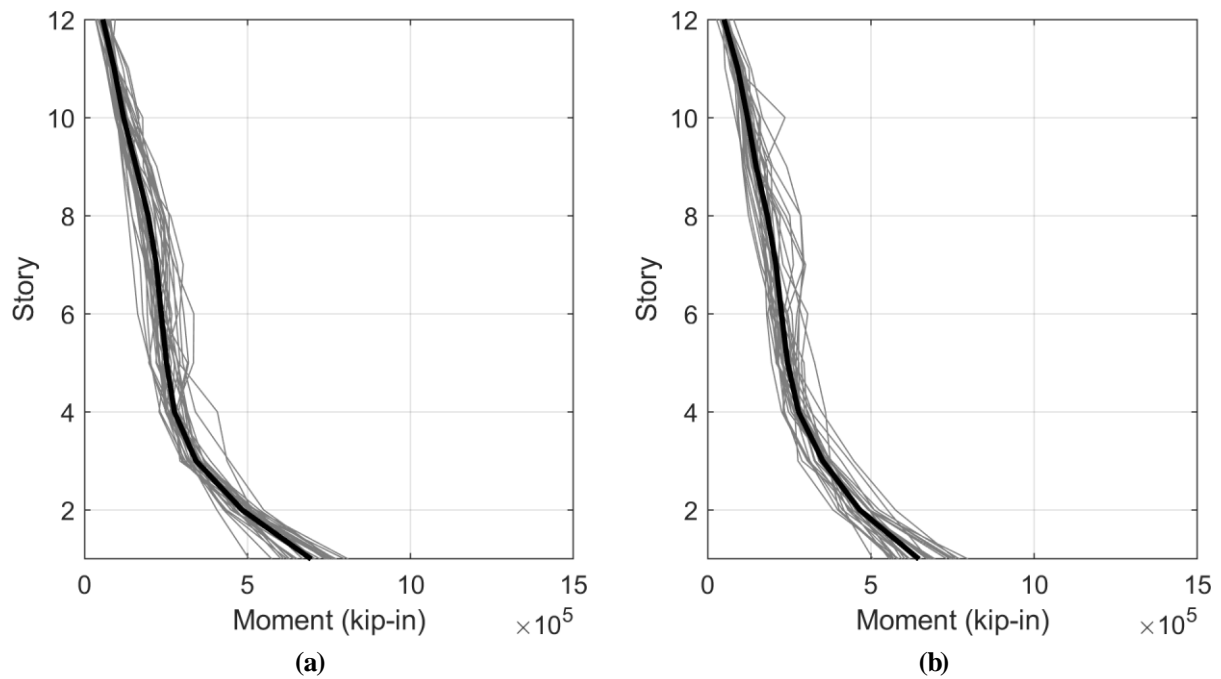


Figure D.12 Story moment results for the 12 story model at the code shaking level for (a) the long duration suite and (b) the short duration suite.

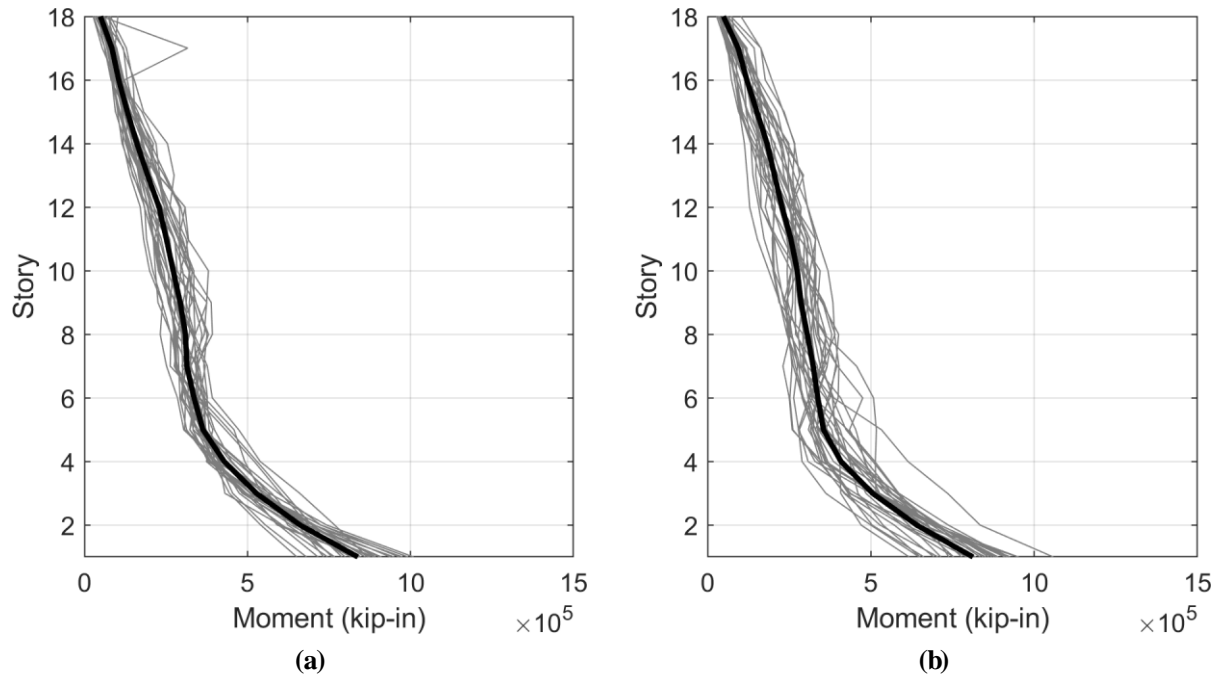


Figure D.13 Story moment results for the 18 story model at the code shaking level for (a) the long duration suite and (b) the short duration suite.

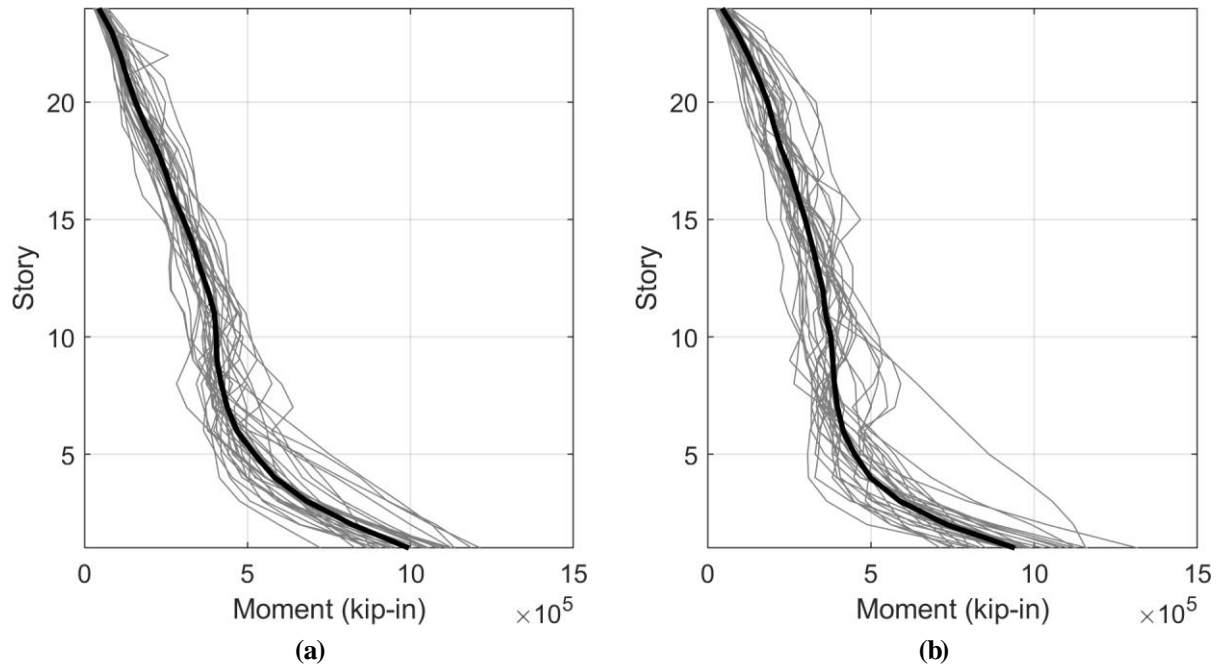


Figure D.14 Story moment results for the 24 story model at the code shaking level for (a) the long duration suite and (b) the short duration suite.

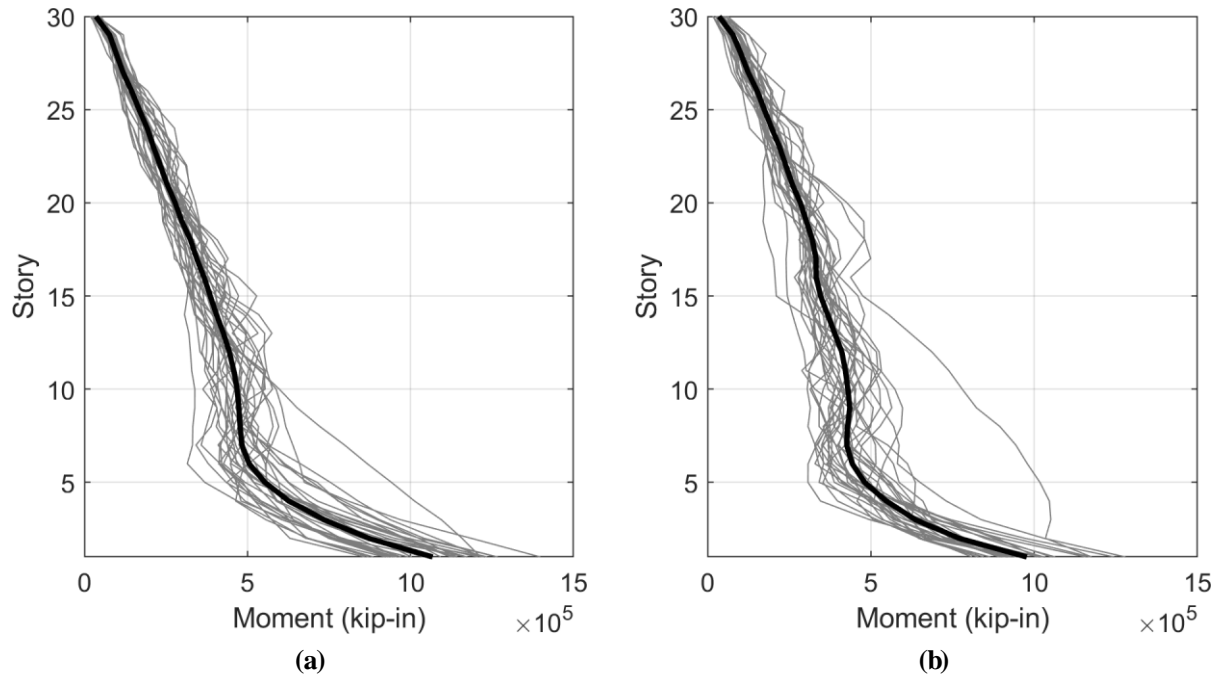


Figure D.15 Story moment results for the 30 story model at the code shaking level for (a) the long duration suite and (b) the short duration suite.